

Photocopy and Use Authorization

In presenting this thesis in partial fulfillment of the requirements for an advanced degree at Idaho State University, I agree that the Library shall make it freely available for inspection. I further state that permission to download and/or print my thesis for scholarly purposes may be granted by the Dean of the Graduate School, Dean of my academic division, or by the University Library. It is understood that any copying or publication of this thesis for financial gain shall not be allowed without my written permission.

Signature _____

Date _____

Narrowing Pulse Widths Using Helium-3 at the Transient Reactor Test Facility (TREAT)
– An Evaluation of the Helium-3 Negative Reactivity Injection (HENRI) System

By

Cody Christopher Race

A thesis

submitted in partial fulfillment

of the requirements of the degree of

Master of Science in the Department of Nuclear Science and Engineering

Idaho State University

Summer 2022

COMMITTEE APPROVAL

To the Graduate Faculty:

The members of the committee appointed to examine the thesis of Cody Race find it satisfactory and recommend that it be accepted.

Dr. Chad Pope,

Major Advisor

Dr. George Imel,

Committee Member

Nick Woolstenhulme,

Committee Member

Dr. Bruce Savage,

Graduate Faculty Representative

To my father, Terry Race, if you could be here, I know you'd be proud.

Acknowledgments

First, I would like to thank Nick Woolstenhulme who had the trust in me as a young engineer to carry his project to the next level of design and fabrication. I would also like to thank Dr. Chad Pope for his continual push to complete this work and get it on paper, and his patience over the way to many years it took to get this done. Lastly, I would like to thank Wynn Monk for pushing me to pursue my master's degree, something I wasn't sure I would ever do and John Carter for his constant reminders to get this work done. I appreciate all the time and effort that they have all put forward in order to help me succeed in my current career and future success.

Vita

Cody Race was born on August 5, 1992 in Twin Falls, Idaho. He graduated high school in 2011 from Shoshone High School and applied to Idaho State University (ISU). Cody graduated in 2016 with undergraduate degrees in Nuclear Engineering and Mechanical Engineering. At the completion of his undergraduate degree, Cody entered the workforce at the Idaho National Laboratory (INL) to help with the restart efforts for the Transient Reactor Test (TREAT) Facility. Cody decided to go back to pursue his Master's degree in Nuclear Engineering and was accepted into ISU's program in 2017.

Table of Contents

List of Figures	vi
List of Tables	xii
Abstract	xiv
1 INTRODUCTION	1
2 BACKGROUND	3
2.1 TREAT Facility Description.....	3
2.2 TREAT Reactor Control	5
2.3 Reactivity Insertion Accident (RIA) Testing of LWR fuels	12
2.4 RIA Capabilities of Worldwide Reactors	20
2.5 Current RIA Capabilities of the TREAT Reactor.....	34
2.6 Clipping Studies for TREAT	37
3 INPUT DESIGN DESCRIPTION	48
3.1 Driver Tank.....	48
3.2 Gas Thimble.....	49
3.3 Transfer Line.....	51
4 METHODS ANALYSIS	52
4.1 Requirements	52
4.2 Monte Carlo N- Particle Transport Description.....	52

4.3	MCNP Geometry Descriptions	55
4.4	Computational Fluid Dynamics	63
4.5	Reactivity Calculations	69
4.6	Model Inaccuracy Calculations.....	86
5	RESULTS & DISCUSSION.....	94
5.1	Rod Positions	94
5.2	Model Inaccuracies Evaluation.....	95
5.3	Quantity and Location of Modules	98
	5.3.1 Double HENRI Locations.....	99
	5.3.2 Quad HENRI Locations	102
5.4	Worth of HENRI System	104
5.5	Annular Evaluation	109
6	SUMMARY AND CONCLUSIONS	118
7	FUTURE WORK.....	118
8	REFERENCES	120
9	APPENDICIES	123

List of Figures

Figure 1: Plan view of TREAT core (half slot).	4
Figure 2: Isometric view of TREAT [34].	5
Figure 3: Examples of shaped Pulses at TREAT [11].	7
Figure 4: Examples of exponential Pulses at TREAT [11].	7
Figure 5: Simplified cross section of a TREAT control rod.	9
Figure 6: Cross section of TREAT control rod fuel assembly.	9
Figure 7: Cross section showing the interfaces of a control rod fuel assembly and control rod with the TREAT core [1].	10
Figure 8: Outcomes during a RIA event flow chart [9].	15
Figure 9: Impact of pulse width on high burnup fuel [9].	18
Figure 10: RIA power pulse schematic showing the relationship between power, energy deposition, and radial average peak fuel enthalpy [36].	19
Figure 11: Cross section view of SPERT CDC (left) and actual image of the drained core (right) [13].	21
Figure 12: Cross section view of a PBF core [37].	23
Figure 13: Cross section view radially (left) and axially (right) of the IGR reactor [16].	25
Figure 14: Cross section view radially (left) and axially (right) of the NSRR reactor [17].	27
Figure 15: Sample NSRR test capsule [17].	27
Figure 16: CABRI core, 1: Experimental water loop, 2: Irradiation channel, 3: Control rods, 4: Transient rods, 5: Fuel assemblies [18].	29
Figure 17: CABRI helium-3 transient injection system [18].	29
Figure 18: Cross section of 236 element ACRR [20].	31

Figure 19: Detail of the dry irradiation cavity [20].....	31
Figure 20: Comparison of contemporary reactor transient conditions.	33
Figure 21: Energy deposition comparison of pulse type reactors worldwide.....	33
Figure 22: Plot of TREAT reactor power and energy based on initial study from 1998 [10].	35
Figure 23: Plot of TREAT reactor power and energy, transient 2930, July 2019.....	35
Figure 24: Energy deposition comparison of pulse type reactors worldwide with TREAT.....	36
Figure 25: Comparison of contemporary reactor transient conditions with TREAT.	36
Figure 26: Pulse comparison for various clipping speeds of 4.5% k/k reactivity insertion pulse [11].	39
Figure 27: Pulse comparison between a natural pulse and a clipped pulse to an energy deposition of 500 MJ. [11].....	39
Figure 28: Pulse comparison for initial reactivity insertion on a clipped pulse [11].	40
Figure 29: Comparison of pulse widths of clipping techniques compared to BWR and PWR pulse width ranges.....	41
Figure 30: Overview of the borated tube clipping concept [11].	42
Figure 31: Schematic of the FAST Shutdown System for TREAT [26]	45
Figure 32: TREAT core with concept helium-3 graphite dummy elements (left) and the concept helium-3 graphite dummy assemblies (right) [11].	46
Figure 33: Conceptual cartridge type assembly for a helium-3 clipping module [11].	47
Figure 34: Schematic of the components that make up the HENRI system used in this evaluation.	48
Figure 35: Schematic of driver tank with fast acting valve.	49
Figure 36: Schematic of gas thimble with vacuum line.....	50

Figure 37: Schematic of transfer line.....	51
Figure 38: West view of the MCNP model of the TREAT core at centerline. Hodoscope slot is on the right.....	57
Figure 39:Top view of the MCNP model of the TREAT core at centerline.....	57
Figure 40: MCNP TREAT half slot core model.....	58
Figure 41:MCNP TREAT full slot core model.....	59
Figure 42: MCNP printout of the cross section of the HENRI system inside a control rod element (air filled).....	61
Figure 43: MCNP printout of the axial cross section of the HENRI system inside a control rod element (air filled).	62
Figure 44:Approximate locations of the CFD data output.....	63
Figure 45: Neutron density comparison at TS00	66
Figure 46:Neutron density comparison at TS01	66
Figure 47: Neutron comparison at TS03.....	67
Figure 48: Neutron density comparison at TS03	67
Figure 49: Neutron density comparison at TS04	68
Figure 50: Neutron density comparison at TS04	68
Figure 51:Temperature spectrum shift comparison for helium-3 and uranium-235.....	71
Figure 52: Flux tally map of a full slot TREAT core.	74
Figure 53: Example Shannon entropy and k_{eff} convergence plot for quantity and location models.	76
Figure 54: Flow of the iterative process used to determine the worth of the HENRI system along with the final driver tank pressures.	78

Figure 55: Example fmesh tally for qualitative results.....	79
Figure 56: Example Shannon entropy and k_{eff} convergence plot for reactivity worth calculation models.....	80
Figure 57: Computer generated geometry used for the cosine tally card test.....	82
Figure 58: ENDF/B-VII.1 helium-3 neutron total energy dependent cross section data vs energy.	84
Figure 59: Example fmesh used for as qualitative evidence for the annular evaluation.	85
Figure 60: Example Shannon entropy and k_{eff} convergence plot for annular models	86
Figure 61: Compensation Rod Derived Bias (Method 1)	90
Figure 62: Compensation rod 1 comparison between MCNP predictions and measured rod worth.	92
Figure 63: Percent deviation between MCNP predicted rod worth and measured rod worth data.	93
Figure 64: Relative inaccuracies for a positive reactivity addition for TREAT in MCNP compared to actual measured values.	97
Figure 65: Relative inaccuracies for a negative reactivity addition for TREAT in MCNP compared to actual measured values.	97
Figure 66: Reactivity effects from HENRI modules being placed in dual locations in TREAT.	101
Figure 67: Reactivity effects of HENRI modules placed in a configuration of four in the TREAT core.	103
Figure 68: Comparison plot of the various driver tank pressures and their reactivity insertion ability over 5 milliseconds.....	105

Figure 69: Reactivity worth of the HENRI system at 500 psig driver tank updated outputs from CFD.	107
Figure 70: Comparison of the timestep truncated data used as compared to the output CFD data to show inclusion of deviations.	108
Figure 71: Mean free path compared to energy for helium-3.	110
Figure 72: Visual of zones and the respective surfaces.	113
Figure 73: Helium-3 savings compared to the neutron population at each surface.	114
Figure 74: Efficiency curve for helium-3 usage vs reduction in neutrons.	115
Figure 75: MCNP HENRI model cross section showing air zones and helium-3 zones.	116
Figure 76: Annular HENRI evaluation compared to the non-annular HENRI worth evaluation.	117

List of Tables

Table 1: Maximum operating conditions for TREAT pulses [1].	8
Table 2: Control rod characteristics of TREAT.	11
Table 4: Pulse width and core-wide maxima of fuel pellet radial average enthalpy and enthalpy increase for various scenarios of REA and RDA estimates [9].	20
Table 5: Pulse characteristics for ACRR core [22].	30
Table 6: Summary of cases performed during a study to determine best ways to create prototypic RIA events in TREAT.	40
Table 7: Configuration of MCNP runs on HPC	54
Table 8: Summary of configurations used in the study of location and quantity	75
Table 9: Rod Locations for Bias Study, Method #2	91
Table 10: Rod Positions of Control Rods for Evaluations.	95
Table 11: MCNP Predicted Values vs Actual Rod Worth Measured Values (Positive Reactivity)	96
Table 12: MCNP Predicted Values vs Actual Rod Worth Measured Values (Negative Reactivity)	96
Table 13: CFD pressure data with calculated atomic density for each timestep.	99
Table 14: F12 & O12 Reactivity Change Results.	100
Table 15: F10 & O10 Reactivity Change Results.	100
Table 16: Quad HENRI Reactivity Reduction Results.	102
Table 17: 500 PSIG Driver Tank Reactivity Results as a Function of Time.	106
Table 18: 5 Millisecond Neutron Density per Section with Average	109
Table 19: Helium-3 Mean Free Path vs. Energy.	111

Table 20: Summation of MCNP F6 Tally up to 0.32609 eV Energy	112
Table 21: Helium-3 Savings vs Neutron Reduction	114

Narrowing Pulse Widths Using Helium-3 at the Transient Reactor Test Facility (TREAT)

- An Evaluation of the Helium-3 Reactivity Injection (HENRI) System

Thesis Abstract – Idaho State University (2022)

The Transient Reactor Test (TREAT) Facility at the Idaho National Laboratory (INL) has been revitalized from a 23-year standdown to study fuel behavior of nuclear fuels and materials. Testing of light water reactor (LWR) reactivity insertion accidents (RIA) has created a need for TREAT to generate pulses with a full width at half max (FWHM) in the 45 to 75 millisecond range as compared to the current 93 millisecond pulse width. A helium-3 clipping system is being evaluated for its effectiveness in reducing the pulse width of the TREAT core. A Monte-Carlo-N-Particle (MCNP) transport code, using a conceptual module design, it was determined that a system that included 4 modules, placed within the modular TREAT core, filled with an initial pressure of 500 psig was sufficient to reach the desired clipping rate to reduce the pulse width of the TREAT core within the desired range. The results will help guide final design of the system.

Key Words: Transient Reactor, Pulse Width, RIA, TREAT, MCNP, Helium-3 Clipping

1 INTRODUCTION

The Transient Reactor Test Facility (TREAT) is an air-cooled, graphite moderated experimental reactor that was designed to test nuclear reactor fuels and materials under transient situations. The reactor is located in the desert between Arco, Idaho and Idaho Falls, Idaho at the Materials and Fuels Complex (MFC) within the Idaho National Laboratory (INL) complex. After 23 years of being in cold standby, resumption activities commenced for TREAT in 2014 and it was restarted in late 2017 with the goal to once again provide crucial behavioral data for the next generation of nuclear fuels and materials.

Due to the modularity of the TREAT core, it is capable of various transient types, shaped bursts (shaped) or excursion/peak bursts (natural). Shaped transients are produced by a step insertion of reactivity followed by various reactivity additions or removals at various rates to produce the desired shape. TREAT's natural transients can produce pulses with an integrated power of approximately 2,100 MJ which can be terminated either by the reactor's natural temperature feedback or by "clipping" the pulse using four boron carbide transient rods that travel up to 140 inches per second over a 40 inch stroke. TREAT can produce a pulse with a full width at half maximum (FWHM) of approximately 89-92 milliseconds.

Since return to service, TREAT is being tasked with performing transient studies that it was not originally designed to support as a result of other reactor shutdowns and a desire for specific data gathering objectives. The new mission involves performing transient testing that improves the materials and fuels used for the current nuclear fleet as well as to provide data for novel concepts in the metal-cooled and nuclear thermal propulsion areas. Historically, TREAT was used to support sodium fast reactor programs and was never adapted to specifically address

light water reactor (LWR) reactivity insertion accidents (RIA) which requires pulses with a FWHM of around 45 milliseconds to 75 milliseconds. Because of TREAT's new mission, a new concept for clipping pulses is required to provide prototypic and representative environments to gather data that can be used for qualification of materials and fuels.

Many clipping concepts have been evaluated for TREAT but only one, requiring the use of module thimbles filled with helium-3 gas, has been requested for further evaluation. This project involved understanding the kinetics of the reactor with use of these modules to support design efforts at TREAT. The evaluations required understanding the following:

- How many modules would be required to support target reactivity clips.
- The best locations of these modules
- Worth of the system at various driving pressures
- Evaluation of an annular design to support helium-3 usage efficiency.

Due to many test reactors either being decommissioned or not being well suited to perform the accident conditions for LWR reactors, TREAT is being tasked with an upgrade to meet the need. This thesis will support initial design and scoping activities for a helium-3 injection system that will be used at TREAT. The scope of this evaluation includes determining the quantity of modules required in the core, the locations of those modules for best performance, a scoping calculation for the reactivity worth of the entire system, as well as an evaluation to determine if a cylindrical module could be converted to an annular type design to save the amount of helium-3 needed for the system, which would drastically reduce cost. Since its inception in the 1950's TREAT has had one main mission; understand the behavior of reactor fuel under reactor accident

conditions. With this upgrade, TREAT will be able to continue its mission and provide reactor fuel data that the world is desiring.

2 BACKGROUND

2.1 TREAT Facility Description

TREAT is an air cooled, graphite moderated experiment reactor facility designed to expose nuclear reactor fuels and materials to extreme transient conditions. Fuel meltdowns, water-cladding interactions, thermal interactions between overheated fuel and coolant, and ceramic fuel transient behavior are a few of the extreme conditions that can be produced and studied at the facility. TREAT achieved initial criticality in February of 1959 after ten months of construction. [1] TREAT went through three building upgrades between 1972 and 1982 before being placed in cold standby in 1994. TREAT was recently restarted in 2017 to fill a gap in capability of transient testing in the United States [2].

The TREAT core is a modular design that is able to accommodate 361 nominal 3.9 inch square fuel assemblies with chamfered corners to allow airflow, in a 19 x 19 positional grid. The standard fuel assembly contains a four-foot central fuel section, with an atom ratio of carbon to uranium of 10,000 to 1. The assemblies contain two, two-foot long graphite reflectors that are located on the top and bottom of each assembly. The total assemblies are approximately nine feet tall and wrapped in a Zircaloy-3 can. Although the TREAT core is capable of housing 361 fuel elements, space is generally required for control/shutdown rods, transient rods, an experiment, dummy elements for flux shaping, and in some cases slotted assemblies for use of the hodoscope [3]. The slotted assemblies can be placed from the north end of the grid to the center location, known as a half slotted core, or placed from the north end of the grid to the south end of the grid,

omitting the experiment position, also known as a full slotted core. Figure 1 provides a generic TREAT half slotted core configuration with graphite dummy fuel assemblies in the corners.

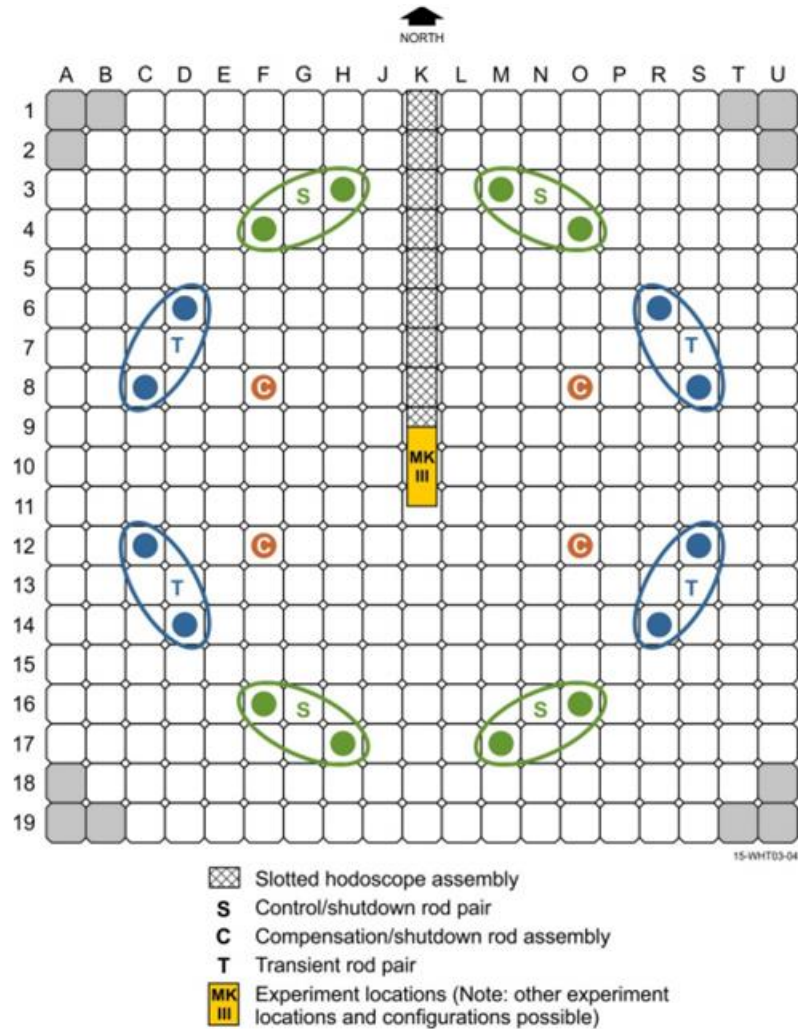


Figure 1: Plan view of TREAT core (half slot).

The TREAT core is surrounded by a permanent graphite reflector, that was repurposed from Chicago Pile 1 and 2, that has a cross section of approximately two feet. Surrounding the reflector, which also provides shielding, is a high-density concrete shell that is approximately five feet thick. The inner surface contains $\frac{1}{4}$ inch steel plate. The top of the core, approximately four feet above the top of the fuel assemblies, contains a one-foot thick rotating shield plug that provides shielding and allows access to every location in the core. Above the rotating shield plug are

removable high-density concrete shield blocks [1]. Figure 2 provides a detailed isometric view of the TREAT core.

2.2 TREAT Reactor Control

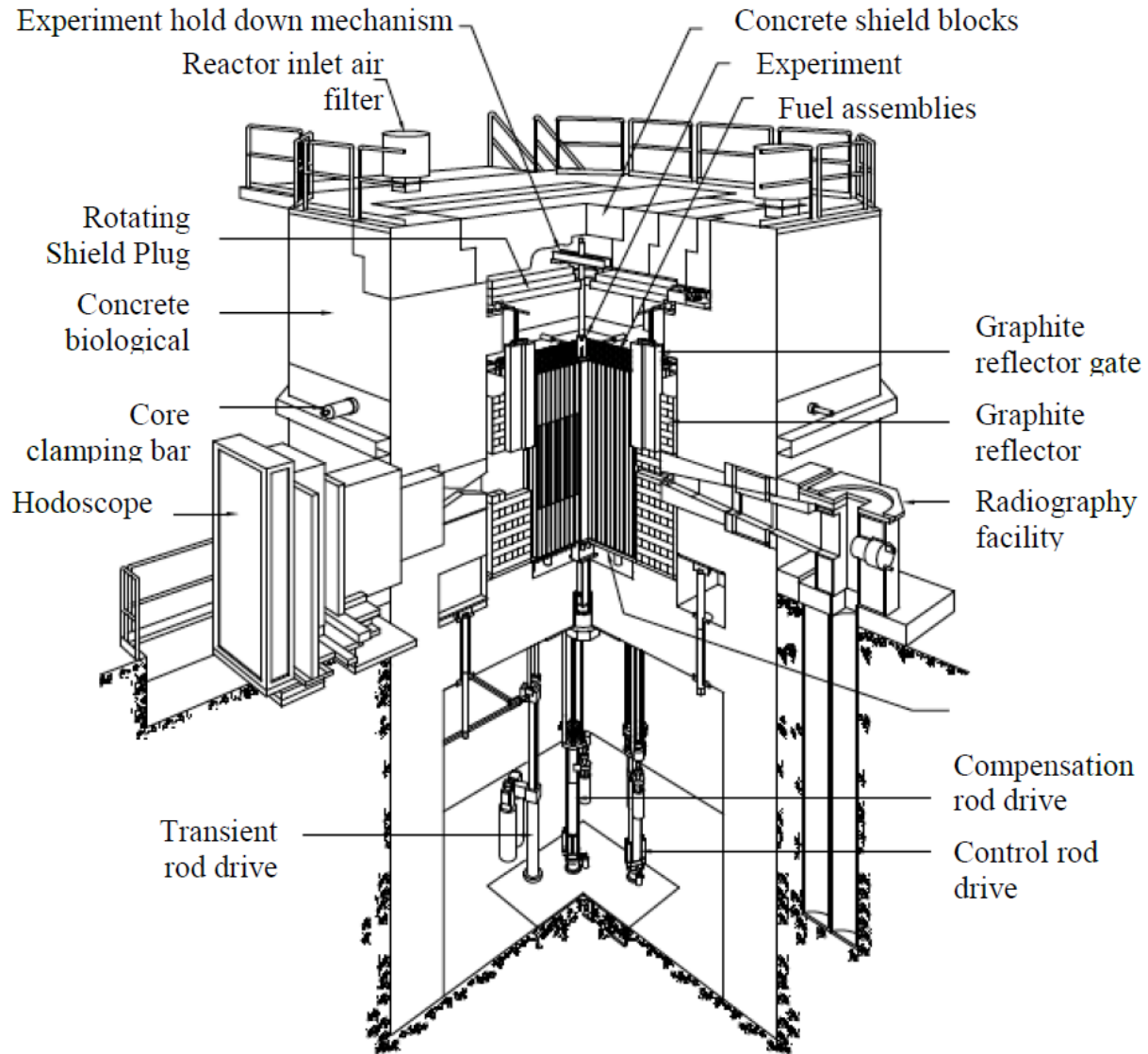


Figure 2: Isometric view of TREAT [38].

Due to the modularity of the TREAT core, it is capable of various transient types, exponential/peak bursts (natural) or shaped bursts (shaped) as seen in Figure 4 and Figure 3.

Exponential bursts can be categorized as a temperature-limited or rod-and-temperature-limited excursion, with the later excursion type “clipping” the transient via control rods short of the time-integrated flux that would result in shutdown by the temperature coefficient. Exponential bursts are initiated by inserting a step insertion of reactivity, which limits the peak power of a pulse, with the maximum reactivity used to initiate the burst being limited so that even if control rods fail to operate properly, the maximum fuel temperature will not exceed 600°C. For the temperature limited pulses, the pulse is terminated by a negative temperature coefficient produced by the graphite-uranium fuel composition. When initiation of the core operation occurs, the temperature within the reactor increases due to a power increase. The temperature rise causes an increase in the reactor neutron energy spectrum for uranium-235 in the fuel. With the increased neutron energy spectrum the neutron absorption rate of the ^{235}U decreases based on its inverse relationship to the neutron energy. With the fuel absorbing less neutrons, the core has a greater potential to leak neutrons from the core resulting in a decrease in the reactivity and termination of a pulse [4].

Shaped bursts are produced with an insertion of reactivity, similar to exponential type bursts, followed by various insertions or removals of reactivity at specific rates to achieve the desired transient shape. The shaped pulses are controlled by a computer, also known as the Automatic Reactor Control System (ARCS), providing an infinite number of shaped transients, only limited by reactivity within the transient rods and kinetics of the reactor.

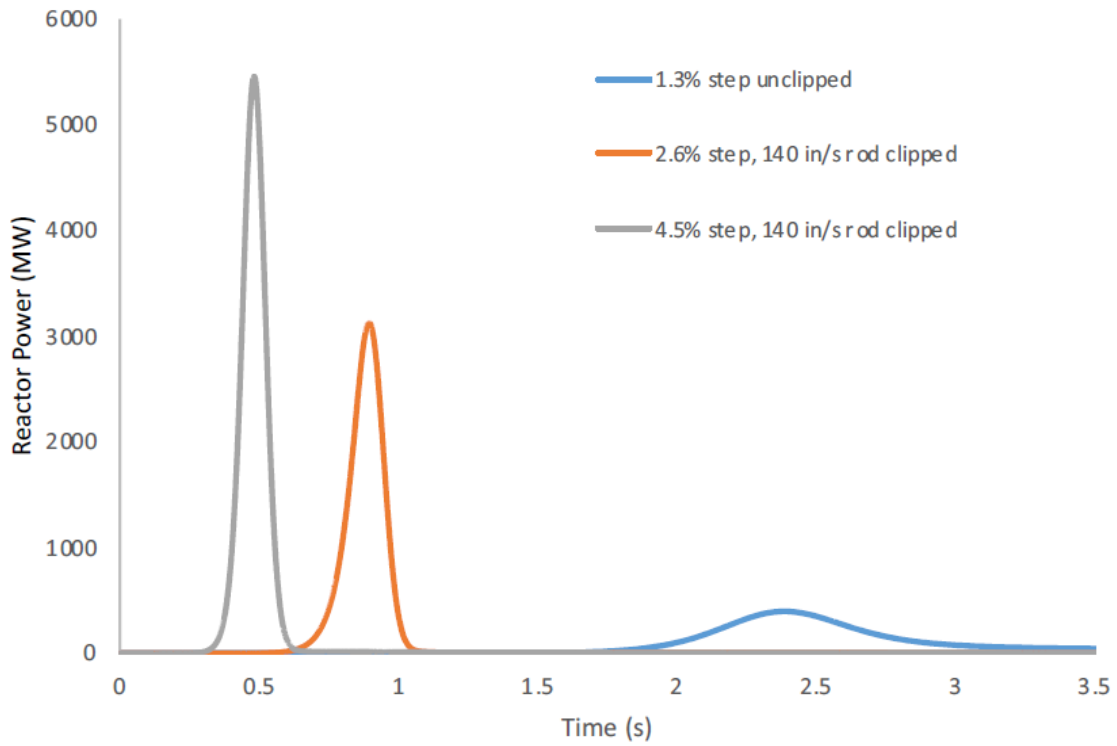


Figure 4: Examples of exponential Pulses at TREAT [12].

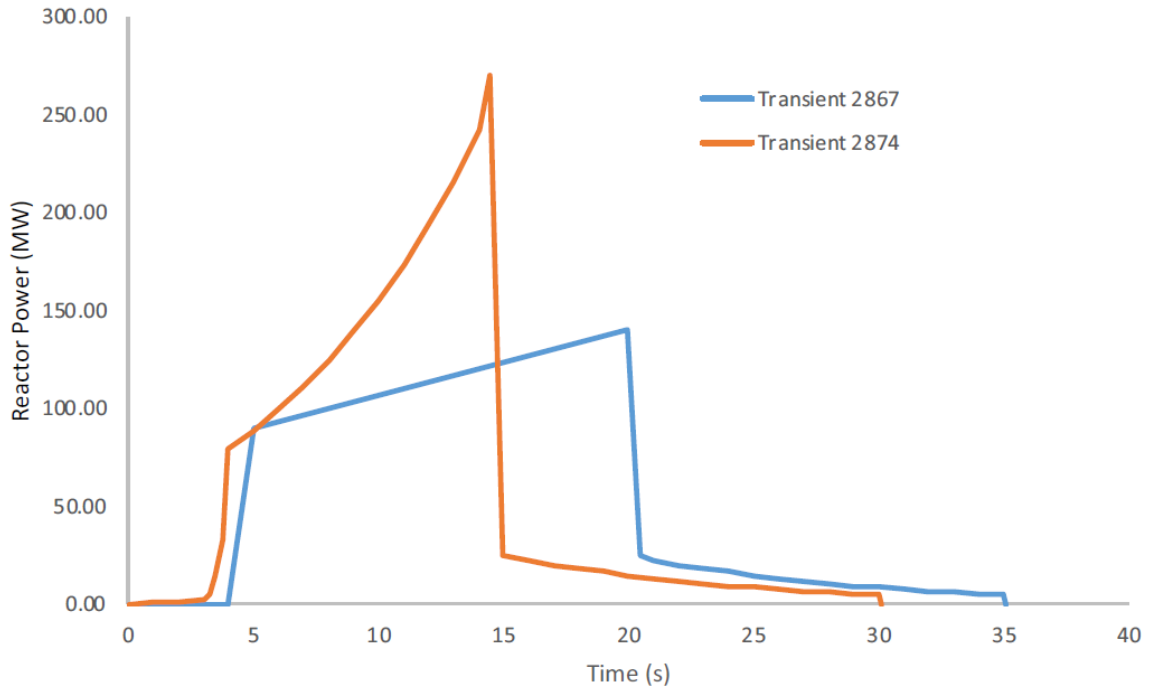


Figure 3: Examples of shaped Pulses at TREAT [12].

Of the above transients, the rod-and-temperature limited, “clip” type excursions are the most typical type of transient ran at TREAT. This is because the energy in the tail of a temperature-limited transient is typically not useful for the desired test. Table 1 provides the characteristics of each type of transient [3].

Table 1: Maximum operating conditions for TREAT pulses [1].

Transient	Shaped	Unshaped
Integrated Power	*	2100 MJ
Peak Power	*	16,000 MW
Fuel Temperature	600°C	600°C
Reactor Period	0.100 sec.	0.023 sec.
Excess Reactivity	6.20%	4.70%

* Depends on transient shape performed

TREAT controls the above transient pulse types using 20 control rods. Each control rod is made of four cylindrical sections that are threaded together. The top section is comprised of a poison made of boron carbide (B₄C) powder, which is compacted to a density of 1.6 g/cc. The second section is a Zircaloy follower filled with graphite. The purpose of this section is to minimize streaming. The last two sections are made up of a carbon steel follower that is filled with graphite, and then connects to the drive mechanism. Figure 5 provides a simplified cross section of a control rod. The control rods are housed in a control rod fuel assembly, Figure 6, where they are guided in their travel by Graphitar™ bearings within the assembly. Two other Graphitar™ bearings are located in the thimble below the grid plate. The control rod fuel assembly and control rod shielding plug interlock to provide a continuous hole for control rod travel. Figure 7 shows a cross section view of how the control rod and control rod fuel assembly interface with the core [1].

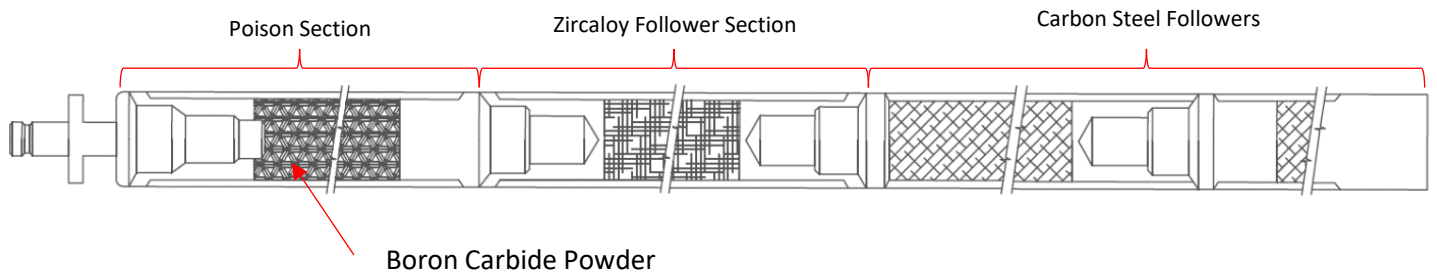


Figure 5: Simplified cross section of a TREAT control rod.

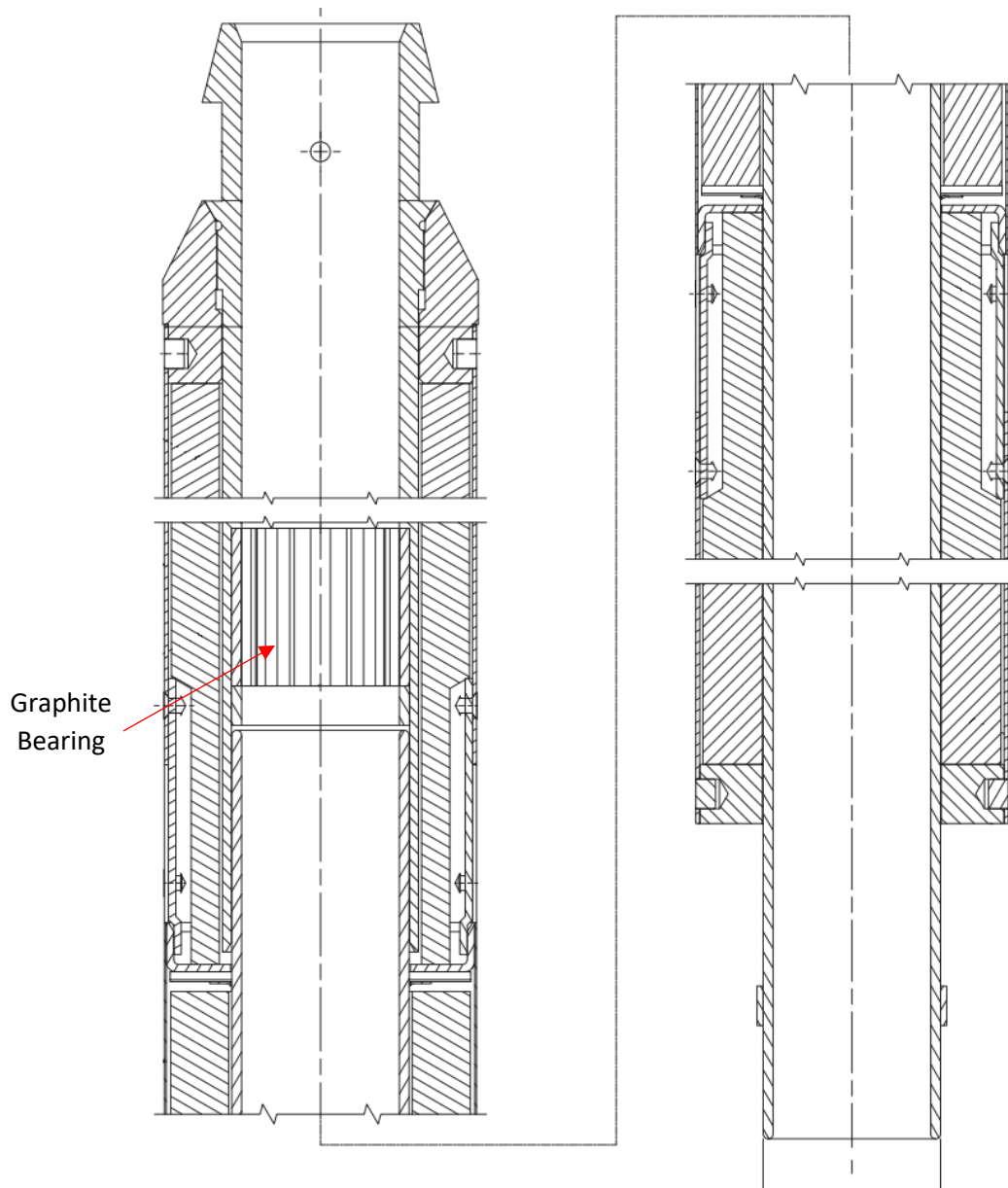


Figure 6: Cross section of TREAT control rod fuel assembly.

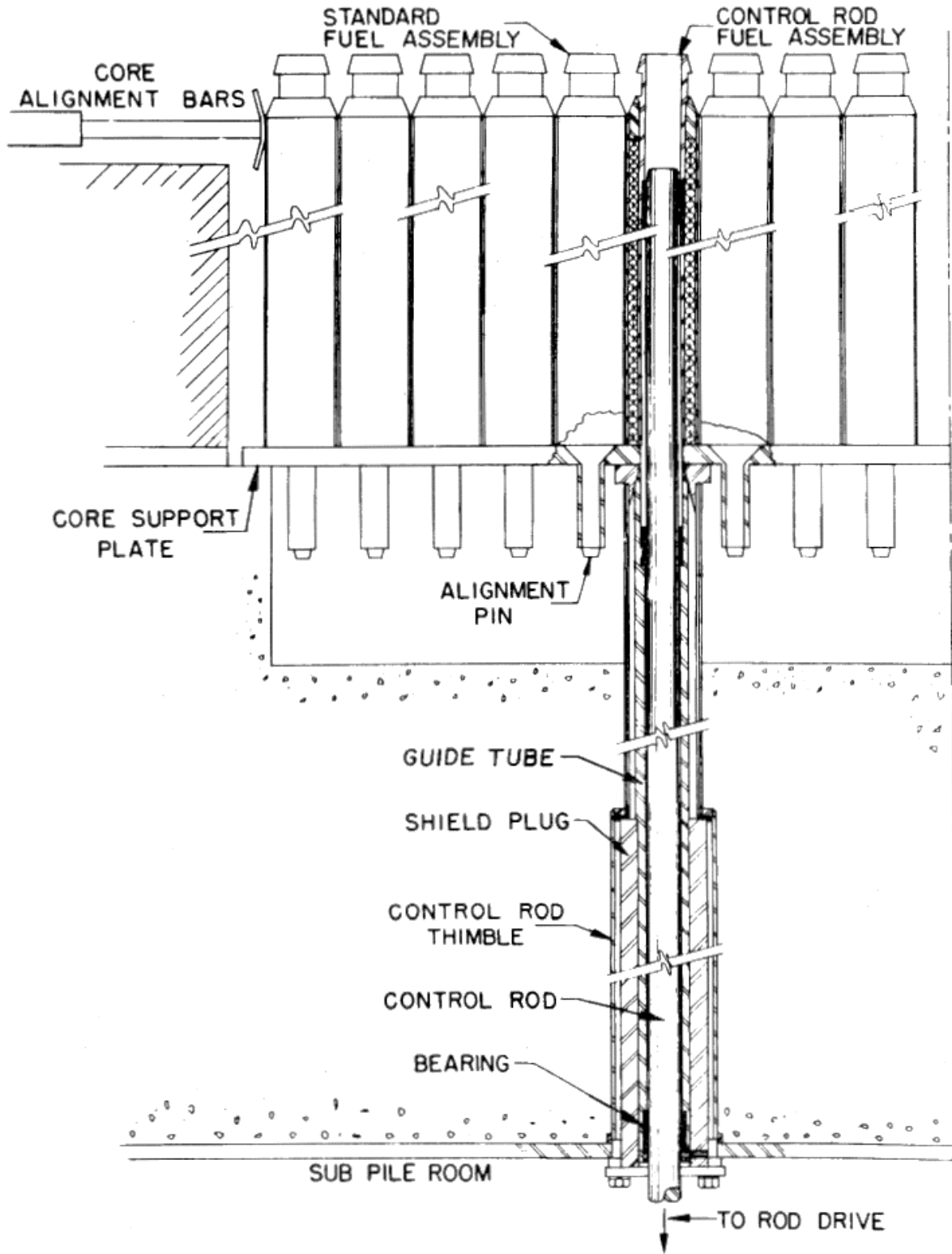


Figure 7: Cross section showing the interfaces of a control rod fuel assembly and control rod with the TREAT core [1].

As shown in Figure 1, eight of these control rods are attached to the four control/shutdown drives, four are attached to the compensation/shutdown rod drives, and eight are connected to the transient rod drives. The control/shutdown rod drives are composed of a pneumatic accelerated fast scram cylinder combined with a motor-driven lead screw mechanism for re-latching and positioning of the rods. The drives can insert the rods at approximately 20 inches per second. A magnetic mechanism latches the rods when needed for operation. There are shock absorbers at the lower end of each drive to control the deceleration of the rods. The compensation/shutdown rod drives are similar to the control/shutdown rod drives, with the only difference being the use of a hydraulic latching mechanism rather than a magnetic latching mechanism. The transient rods are positioned using a 40-inch stroke, oil-operated, hydraulic cylinder with a servocontrol system to control the location of the rod operating piston. All drives are located in the Sub-pile room, under the reactor, and bolted to a steel plate that is embedded in the concrete floor. Appendix A provides detailed diagrams of each rod drive type. Table 2 provides a summary of the various control rods characteristics [1].

Table 2: Control rod characteristics of TREAT.

Type	Nominal Reactivity Worth (Core 1469) [5]	Effective Length [1]	Velocity	
			Reactivity Insertion [5]	Reactivity Removal (Clip/Scram) [5]
Control/Shutdown Rods	0.088 $\Delta k/k$	58 in.	20 in./min.	300 in./sec.
Compensation/Shutdown Rods	0.069 $\Delta k/k$	58 in.	20 in./min.	300 in./sec.
Transient Rods	0.085 $\Delta k/k$	40 in.	Adjustable (0-140 in./sec.)	140 in./sec

Under normal operation, the compensation/shutdown rods are fully withdrawn from the core and remain fully withdrawn during the transient. Transient rods are positioned to the location

needed to perform the desired transient with the control/shutdown rods being banked part way in the core to establish and maintain criticality. When performing a “clipped” transient, the ARCS inserts the transient rods, based on either time or energy, at 140 inches per second to create the desired pulse. When the control/shutdown and compensation/shutdown rods are fully inserted, the poison section extends approximately 4.25 inches above and below the fuel region of the core [1].

2.3 Reactivity Insertion Accident (RIA) Testing of LWR fuels

The design and safety analysis of the current fleet of licensed light water reactors (LWR) has multiple postulated transients and accidents that could challenge the reactor core. These can be broken down into subcategories, undercooling events or overpower events. A reactivity insertion accident (RIA) is classified as an overpower event in which there is a sudden and rapid insertion of positive reactivity [6].

There are many scenarios in Boiling Water Reactors (BWRs) and Pressurized Water Reactors (PWRs) that could lead to an inadvertent insertion of reactivity. The main contributors that would lead to a RIA event in a power reactor include control system failure, control element ejections, and events caused by coolant or moderator removal. Of these events the most severe for both PWRs and BWRs is control rod element ejections. This event is a mechanical failure of control rod drive mechanisms which lead to rapid insertion of reactivity due to the decrease in neutron absorption. This accident is known as a control rod ejection in PWRs and a control rod drop in BWRs [7].

The control rod ejection accident (REA) for PWRs is an accident caused by a break in the control rod housing within the pressure vessel. This leads to a differential in pressure in the coolant which ejects the control rod assembly completely out of the reactor core. This results in a rapid

positive reactivity insertion, resulting in a large localized relative power increase excursion within the core. The most extreme accident of this type happens in approximately 0.1 seconds depending on reactor coolant pressure and extent of the mechanical failure. The most severe REA is a hot zero power (HZIP) condition when there is nearly zero power and the reactor coolant is at normal operating temperature and pressure [7].

The rod drop accident (RDA) for the BWRs is an accident caused by the drive mechanism and control rod blade becoming separated when the blade is fully inserted. The detached blade is assumed to be stuck in this position until it suddenly becomes loose and free falls out of the core. This event is possible at any operating condition, in contrast to the REA in PWRs. RDAs are also much slower than REAs resulting in a lower power surge that is typically slower compared to REAs. The most severe RDA is a cold zero power condition (CZP) when the reactor contains subcooled coolant and is also at nearly zero power [7].

Consequences of RIAs

RIA events for LWRs are design basis accidents which means they have a low probability of occurrence but would have serious consequences if they occur. RIA events create two main safety concerns:

- Loss of long-term cooling ability within the core
- Damage to the pressure boundary or core of the reactor, through the propagation of pressure waves.

Fuel failure is not typically considered a safety concern for a RIA event as it does not imply a loss of cool-ability or the creation of pressure waves. Current studies have focused on fuel

failures during such an event, however, because it is a prerequisite which leads to loss of core cooling geometry and pressure wave generation [8].

The initial effects seen by the reactor fuel, during a RIA event in LWRs, would be an initial temperature and power rise. Solid thermal expansion of the fuel pellets would occur due to the rapid increase in power, resulting in adiabatic like conditions. If the fuel had been operated for long periods of time, i.e. had accrued burn-up, gaseous fission products could also have developed within the fuel. During the expansion phase of the fuel the gasses would escape adding to the pellet deformation as well as adding stress to the fuel cladding, also known as pellet-cladding mechanical interaction (PCMI). During early stages of PCMI if the fuel cladding is lower in temperature, the expansion of the fuel causes a partially brittle mode of cladding failure. Heat transfer from the pellets may elevate the temperature of the cladding such that departure from nucleate boiling (DNB) occurs, in later stages of the transient. The DNB involves formation of a continuous vapor film that insulates the cladding from the coolant at that interface, also known as film boiling. Film boiling may last for up to 15 seconds until rewetting occurs, during which time ballooning and creep rupture could occur, due to elevated temps. During re-wetting it is also possible that the cladding experiences brittle fracture and disruption due to thermal shock between the coolant and high temperature cladding [8].

The final result of the transient, if energy deposition to the fuel is very high, is that cladding may melt and in some cases so could fuel. This leads to a violent thermal interaction between the molten material and coolant, termed the fuel coolant interaction (FCI), causing pressure pulses in the coolant. Figure 8 provides a flow chart for various outcomes that can occur during a RIA event [8].

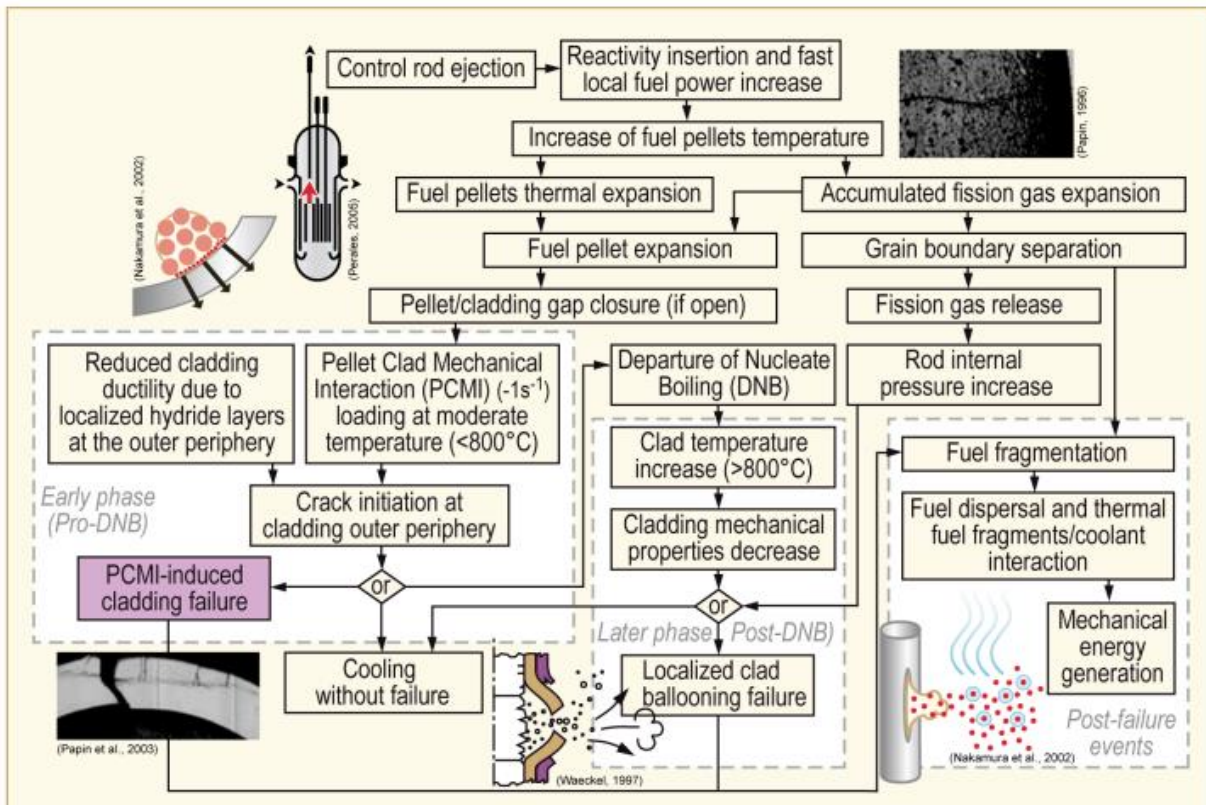


Figure 8: Outcomes during a RIA event flow chart [10].

Pulses Desired for RIA Testing

Thousands of experiments have been performed on fresh (non-irradiated) fuel rods, as well as pre-irradiated fuel in various reactor test facilities to determine the damage mechanisms that can occur during RIA accidents, leading to the events described in the previous section. The main damage mechanisms, summarized from the previous section, observed in the fresh fuel testing are:

- Cladding ballooning and burst
- Embrittlement and failure by high temperature oxidation
- Melting of fuel pellets and/or cladding

All the damage mechanisms above can be attributed to high temperature, specifically the degree of damage correlates to the peak value of the specific enthalpy¹ of the fuel [7].

To test the fuel failures observed during RIA events it is important to understand the variables that lead to such failures. The variables that most affect fuel failure during a RIA include cladding temperature and fuel expansion/ fission gas release. In order to achieve the desired variables within a test reactor there are two main control parameters that can be altered, pulse width and energy deposition. The energy deposition parameter is described as the fuel enthalpy rise in units of energy per gram of fuel [9]. Pulse widths are described in terms of their FWHM value of reactor power as a function of time and is critical as it affects the timing of pellet-to-cladding heat transfer [10].

Getting the correct pulse width is important when studying RIA phenomena. If a pulse is too wide it could produce indications of fuel performance that are overly optimistic and do not reach the critical points that actually occur during a RIA experiment [10]. On the other hand, too

¹ Specific enthalpy refers to the enthalpy per unit mass of the material.

narrow of a pulse also could lead to undesirable testing results. A narrower pulse width induces a faster rate of fuel pellet expansion leading to higher strain in the cladding from PCMI, as well as intensifying the fuel expansion phenomena, through the increase in temperature, increasing the peak hoop stress in the cladding. In addition, this added stress on the cladding occurs before the cladding can reach temperatures at which it is more ductile. This could lead to artificially induced brittle failure of the cladding [9]. Figure 9 shows a diagram of the impact of pulse width for RIA testing, specifically with respect to high burn-up fuels.

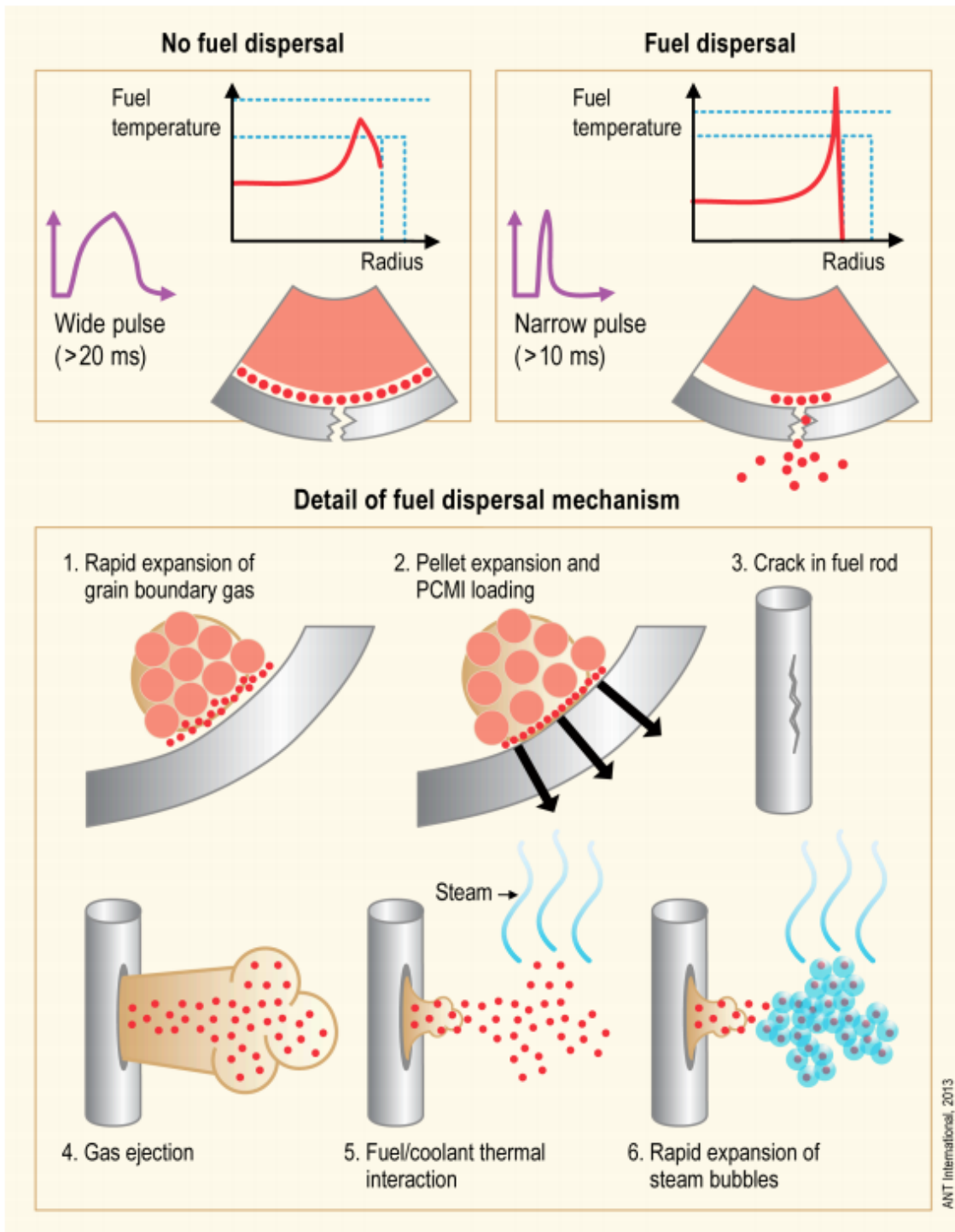


Figure 9: Impact of pulse width on high burnup fuel [10].

Over the last couple of decades three-dimensional kinetics and thermal-hydraulic RIA models have been used to predict values that would lead to RIA phenomena in test reactors. Table 3 below summarizes estimated values for each REA and RDA scenario [7]. Figure 10 shows a RIA power pulse schematic comparing the relationship between power, energy deposition, and radial peak fuel enthalpy.

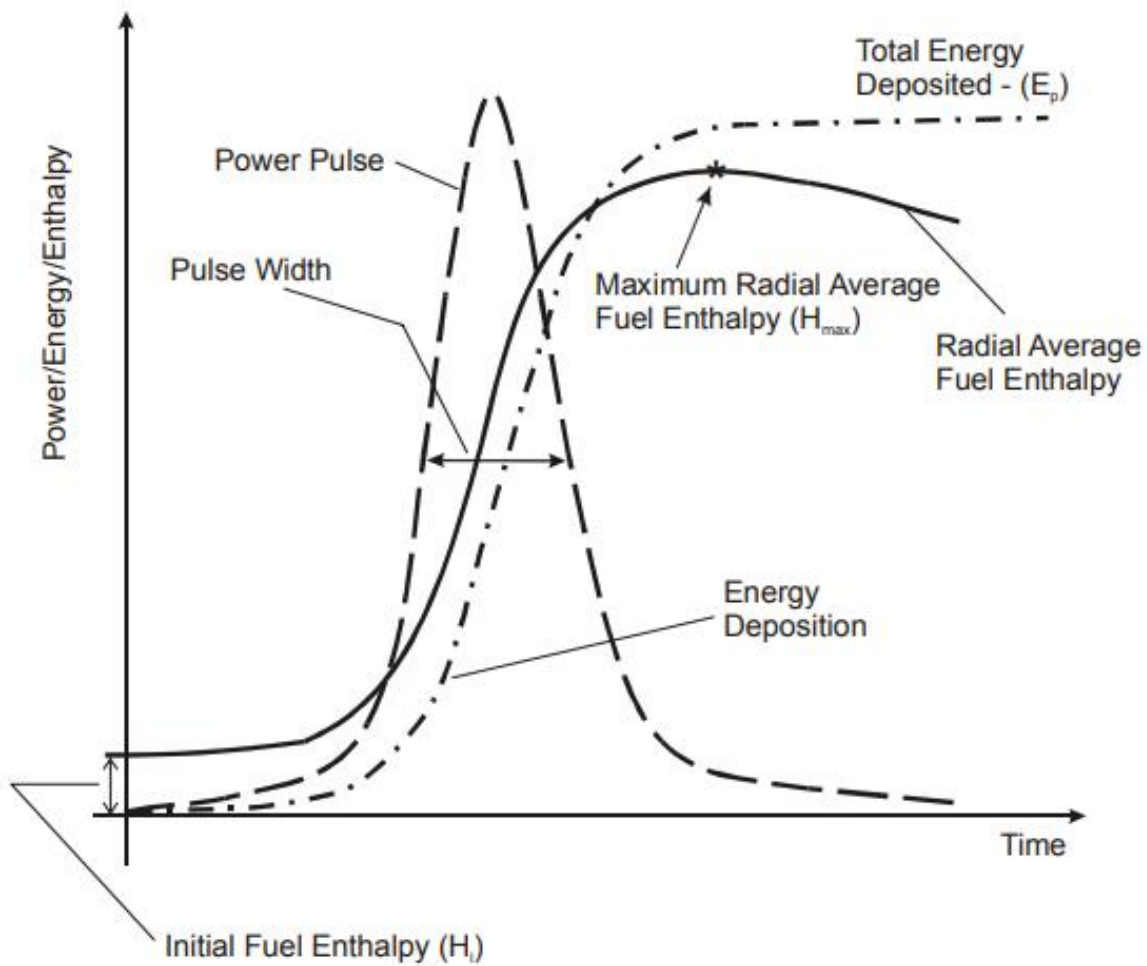


Figure 10: RIA power pulse schematic showing the relationship between power, energy deposition, and radial average peak fuel enthalpy [40].

Table 3: Pulse width and core-wide maxima of fuel pellet radial average enthalpy and enthalpy increase for various scenarios of REA and RDA estimates [7].

Reactor, Accident scenario	Pulse width [ms]	Max fuel enthalpy [J(gUO₂)⁻¹]	Max ent. increase [J(gUO₂)⁻¹]	Rod worth [10⁻⁵]
PWR:				
REA HZP	25 - 65	140 - 320	80 - 250	600 - 850
REA HFP	400 - 4500	230 - 350	10 - 130	40 - 200
BWR:				
RDA CZP	45 - 75	140 - 460	130 - 450	700 - 1300
RDA HZP	45 - 140	160 - 400	90 - 320	600 - 1300

HZP: Hot zero power, **HFP:** Hot full power, **CZP:** Cold zero power

2.4 RIA Capabilities of Worldwide Reactors

Approximately 140 pre-irradiated RIA simulation tests have been done all around the world to better understand the effects of RIA events. There are very few reactors that had or have the capabilities to perform such testing. A brief description of some of those facilities are provided below.

SPERT-IV (CDC)

The Special Power Excursion Reactor Test (SPERT) facility, located in the USA, was a pool type reactor designed and commissioned for the primary purpose of reactor safety research. One of the major testing tasks was to perform power excursion tests using power bursts [11]. SPERT underwent core modifications to achieve desired results. One such core change was the

SPERT Capsule Driver Core (CDC). The core was composed of 1,600 stainless steel-clad fuel rods containing 1,600 grams of UO_2 powder that was 3% enriched. The core allowed a dry center location to allow the insertion of experiment capsules. The core was controlled using eight cruciform shaped control rod blades. The transient was initiated using four transient rod blades that are also cruciform in shape [12]. Figure 11 shows various images of the SPERT-IV-CDC.

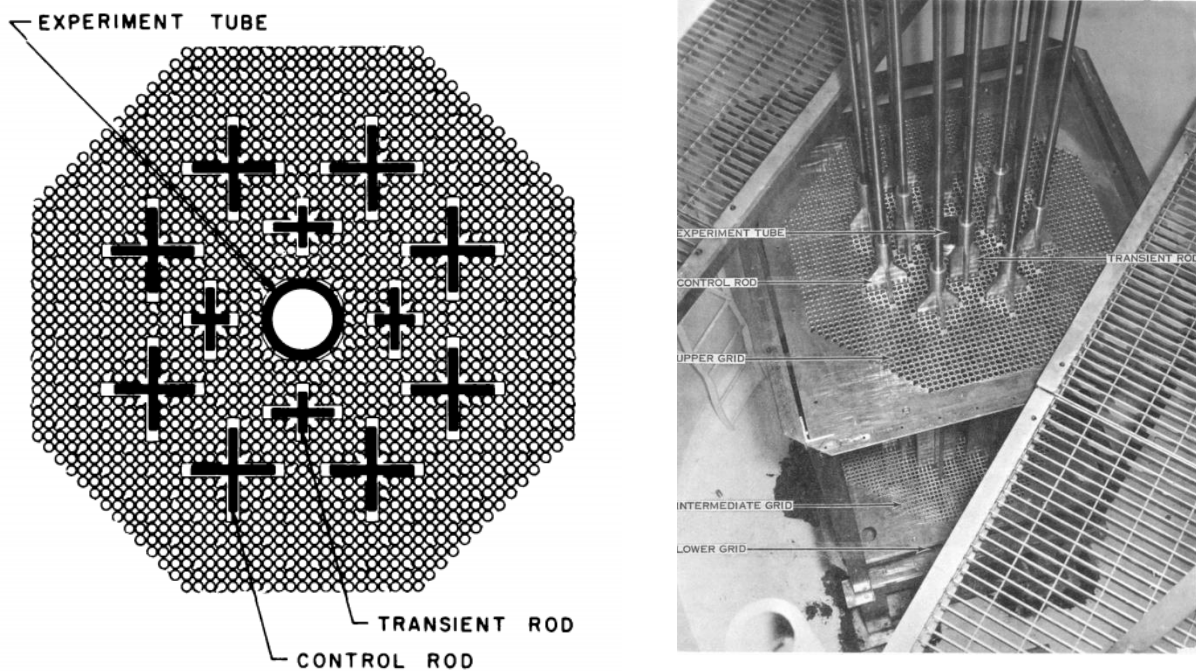


Figure 11: Cross section view of SPERT CDC (left) and actual image of the drained core (right) [14].

SPERT-CDC tested 10 BWR cold start-up events between 1969-1970. The fuel rods that were tested had burnups anywhere between 1-32 MWd/kgU. During the testing the maximum peak enthalpy reached was 1,181 J/g UO_2 . The SPERT reactor was able to reach FWHM pulse widths of 13-31 milliseconds [7]. SPERT has since been decommissioned.

PBF

The Power Burst Reactor (PBF), located in the USA, was a modular designed reactor core facility with the purpose of understanding the phenomena of rapid destructive heating of fuel assemblies for various reactor types. The reactor was designed specifically to test shock, explosive steam generation, fuel disruption, fission product release, and FCI. PBF was built as none of the existing pulse-type facilities at the time could meet the objectives, which included TREAT (hypothesized to able to only reach 40 millisecond pulse and air cooled limited the amount of tests able to be performed in a day) [13].

PBF, similar to SPERT, was a pool-type reactor that contained approximately 2,400 $U(18)O_2$ -CaO-ZrO₂ ceramic fuel rods. The rods were contained in a square lattice that could hold 26-63 rods. The core also had a center location for experiment insertion. The core contained approximately 100 stainless steel shim rods intermixed within the fuel rods. These shims allowed PBF to reach the desired excess reactivity needed for the specific test. Insertion of the shim rods decreased reactivity of the core. In addition to the fuel rods and shim rods, there are also filler rods and reflector rods. The reflector rods, which reduced the thermal neutron flux peaking at the core reflector interface, are identical to the shim rods but were used on the outside of the core to create a cylindrical boundary. The filler rods were aluminum rods that were used to fill out the core and balance the coolant flow within the square canisters [14].

PBF also contained movable rods, control/reflector and transient rods, that were used to control the reactor. The rods contained a section of boron carbide and contained only slight differences in overall assembly [14]. Figure 12 provides an example cross section view of a PBF core.

PBF performed 3 series of PWR tests on 17 rodlets between 1978-1980. These rodlets contained fuel that was slightly more enriched than commercial PWR fuel rods at 5.7-5.8 wt% ^{235}U . Maximum peak enthalpy reached during these series of tests was 1,193 J/g UO_2 with pulse widths of 11-16 milliseconds [7]. PBF has since been decommissioned.

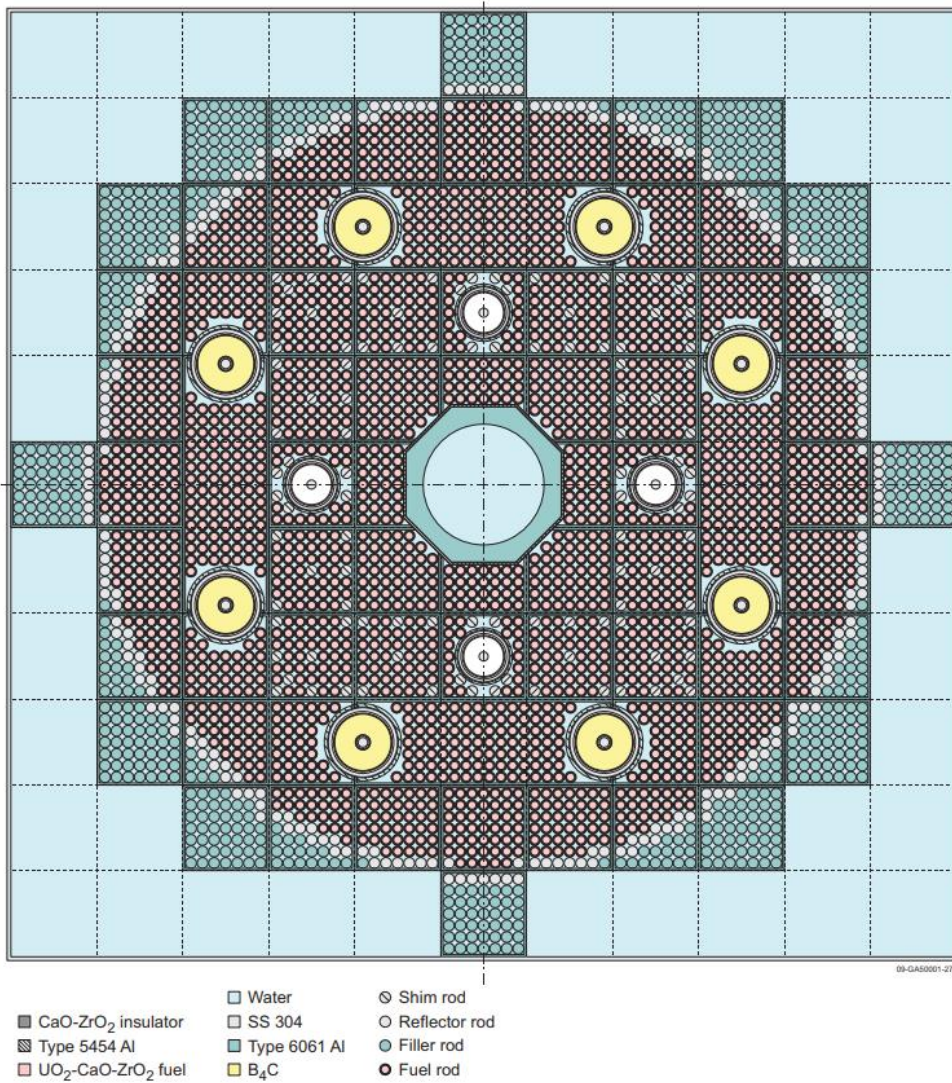


Figure 12: Cross section view of a PBF core [41].

IGR

The Impulse Graphite Reactor (IGR), located in Kazakhstan, is a cubic pulse test reactor with a homogeneous uranium-graphite core. The core is a pile of graphite blocks positioned in columns contained in a reactor vessel. The vessel was placed in a tank of cooling water. The graphite core blocks are saturated in uranium salts with a uranium to graphite ratio of approximately 3:1,000 respectively. The uranium has an enrichment of 90%. The core contains 16 control rods of various sizes that are gadolinium oxide neutron absorbers. There is a central channel within the reactor for various insertion type experiments. Figure 13 shows a cross section view in the axial and radial directions [15].

IGR performed 13 tests on water-water energetic reactor (VVER) fuel, a Russian type reactor similar to a PWR, between 1990 and 1992. Some of the testing contained fuel that was previously irradiated while other testing replaced the high burn-up fuels with fresh fuel resulting in a previously irradiated cladding that contained fresh fuel. The tests were not instrumented during irradiation but characterized prior to and after testing. The pulse width of these tests ranged anywhere from 600-950 milliseconds with a maximum enthalpy of 1,051 J/gUO₂ [7].

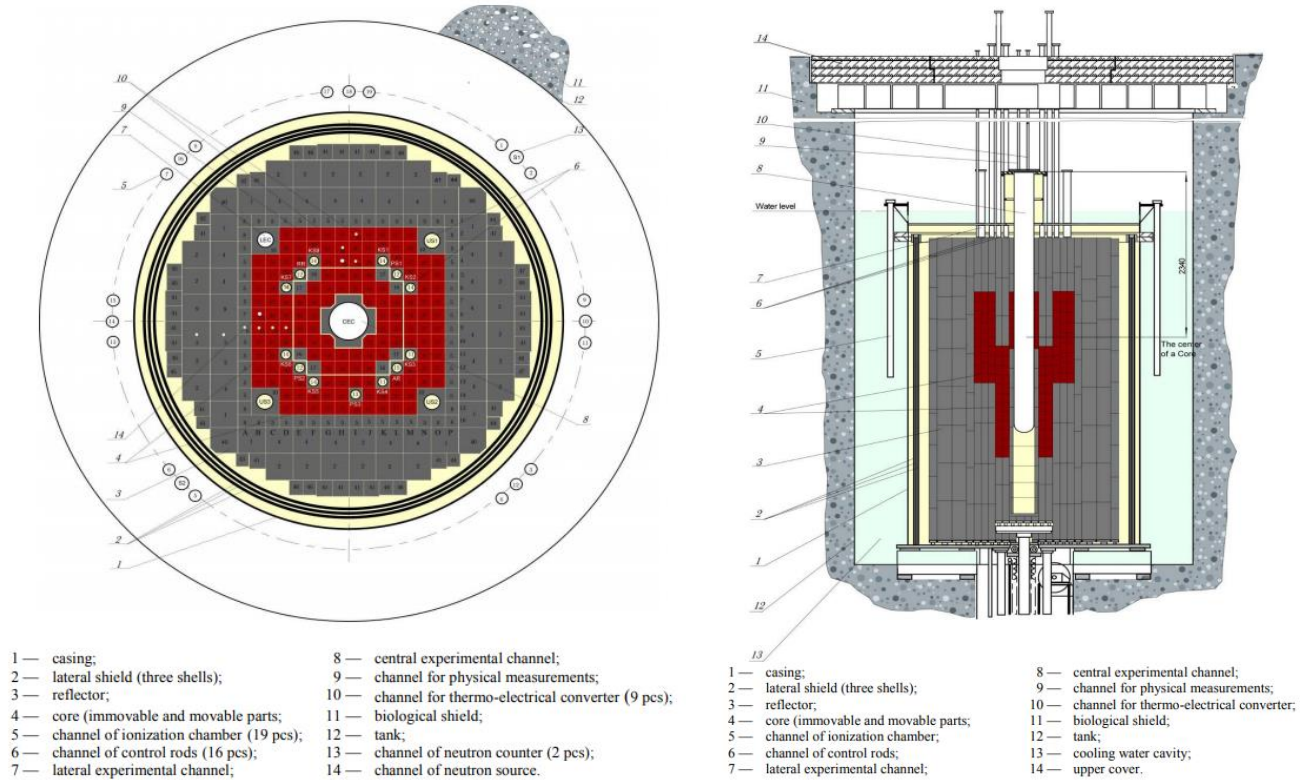


Figure 13: Cross section view radially (left) and axially (right) of the IGR reactor [17].

NSRR

The Nuclear Safety Research Reactor (NSRR), located in Japan, and operated by the Japan Atomic Energy Agency (JAEA), is a pool-type modified TRIGA annular core pulse reactor (TRIGA-ACPR). The core consists of uranium-zirconium hydride fuel moderated elements, approximately 157, 20% enriched, elements make up the core, which also contains 2 safety rods, 6 regulating rods, and 3 transient rods. The core is capable of steady state operations, up to 300 kW, natural pulses, shaped pulses, and a combination of shaped and natural [16]. Figure 14 provides a cross section diagram of the NSRR core in the axial and radial direction.

In order to test materials, instrumented capsules are placed inside the core, see Figure 15. These capsules can create an environment that is desired for the specific testing, for example tests

have been completed with stagnant water at room temperatures and pressures as well as flowing water at elevated temperatures and pressures [16].

Since 1975 NSRR has been able to perform many tests on various fuel types, which makes it very unique compared to the other reactors covered in this paper. NSRR has performed 58 different RIA tests including: 32 PWR type tests, 17 BWR type tests and 9 Mixed oxide fuel (MOX) tests. The majority of the test rods ran in NSRR were previously irradiated and well instrumented. The core has a natural pulse of 4.4 – 7 milliseconds and is able to reach a peak enthalpy of 657 J/g during the tests [7].

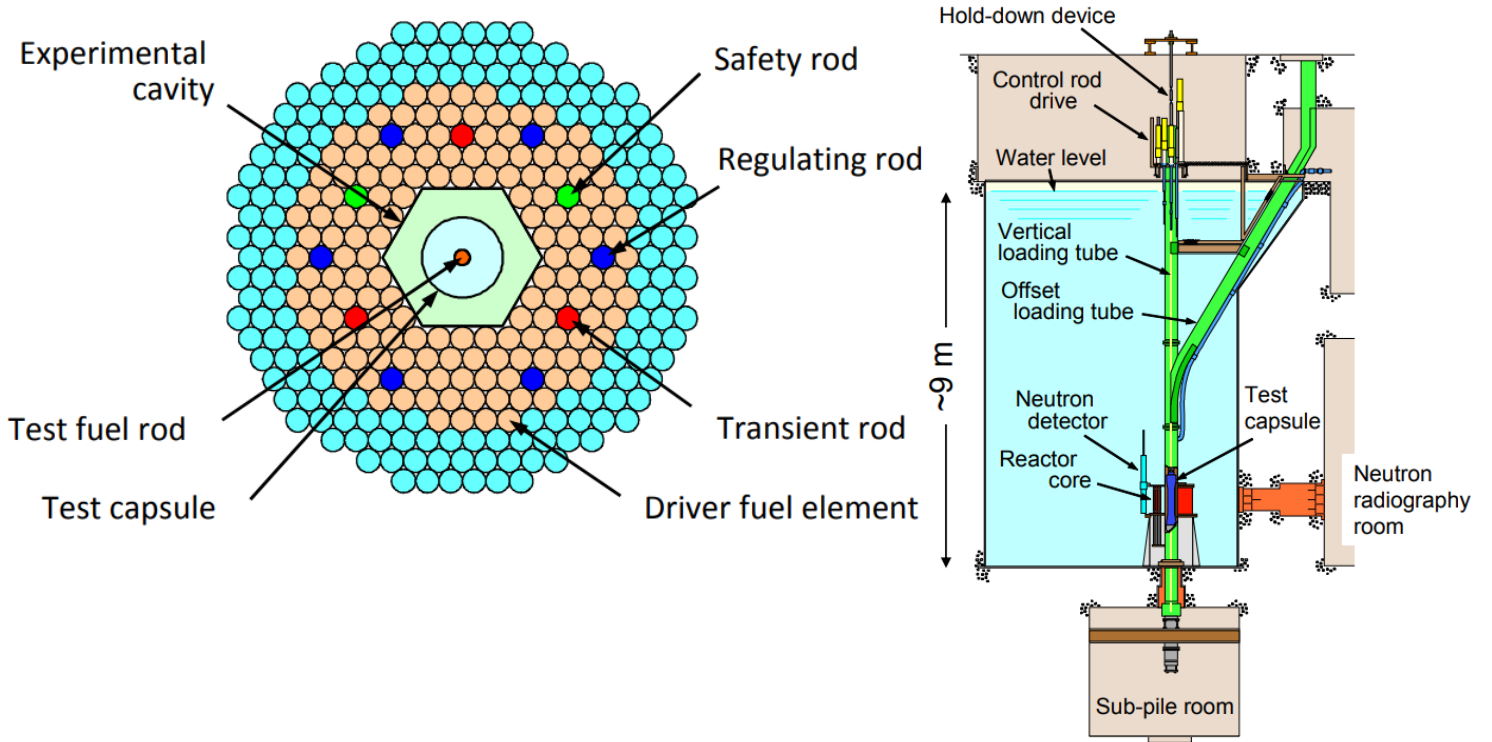


Figure 14: Cross section view radially (left) and axially (right) of the NSRR reactor [18].

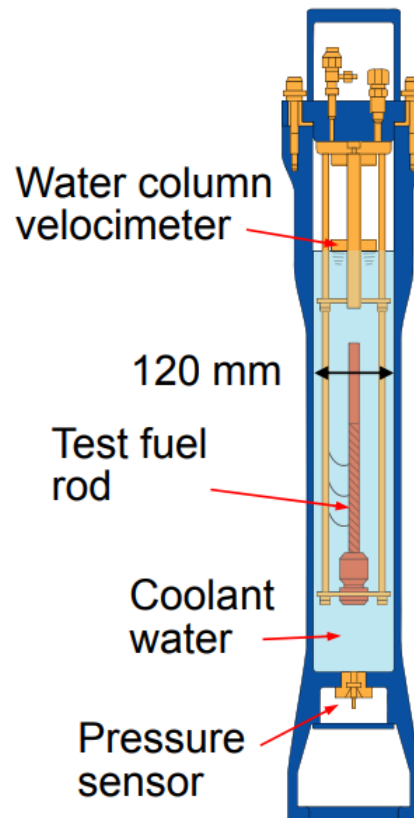


Figure 15: Sample NSRR test capsule [18].

CABRI

The CABRI facility is located at the CEA Cadarache site in southern France. The reactor is a pool type reactor that is moderated and cooled with light water. The fuel for CABRI are 1,487 rods containing UO_2 enriched to 6% and wrapped in stainless steel cladding. The reactor is controlled by hafnium control rods and also contains a helium-3 depressurizing system in order to control transients. The center of the core contains a loop for testing [17] [18]. Figure 16 shows an image of the core components for the CABRI reactor. Up until 2002 the loop was a sodium cooled loop that was used to study the behavior of RIA accidents in fast reactor fuels. In 2002, CABRI went through a 12-year upgrade to change the sodium loop to a water loop to fill a need for LWR RIA testing.

As mentioned above, the CABRI reactor has a unique reactivity injection system used to control transients. The system uses helium-3 which is contained in 24 tubes, that cover approximately the same area of a 5x5 array of the UO_2 rods. The system works by filling the tubes with helium-3 prior to initiation of the transient. The tubes are filled to a pressure of approximately 10 bar. When operating the transient, fast acting valves depressurize the system introducing a very large increase in reactivity creating the pulse [17]. Figure 17 shows a schematic and image of the helium-3 depressurization system used in CABRI.

CABRI performed 14 single, short-rodlet tests, 10 for PWR fuels and 4 for MOX fuels, prior to the refurbishment of 2002. These tests had pulses from 9-75 milliseconds with a maximum fuel enthalpy of 832 J/g [7]. In 2018 the CABRI water loop refurbishment conducted its first successful test; the tests purpose was to ensure all systems of the loop operated as expected.

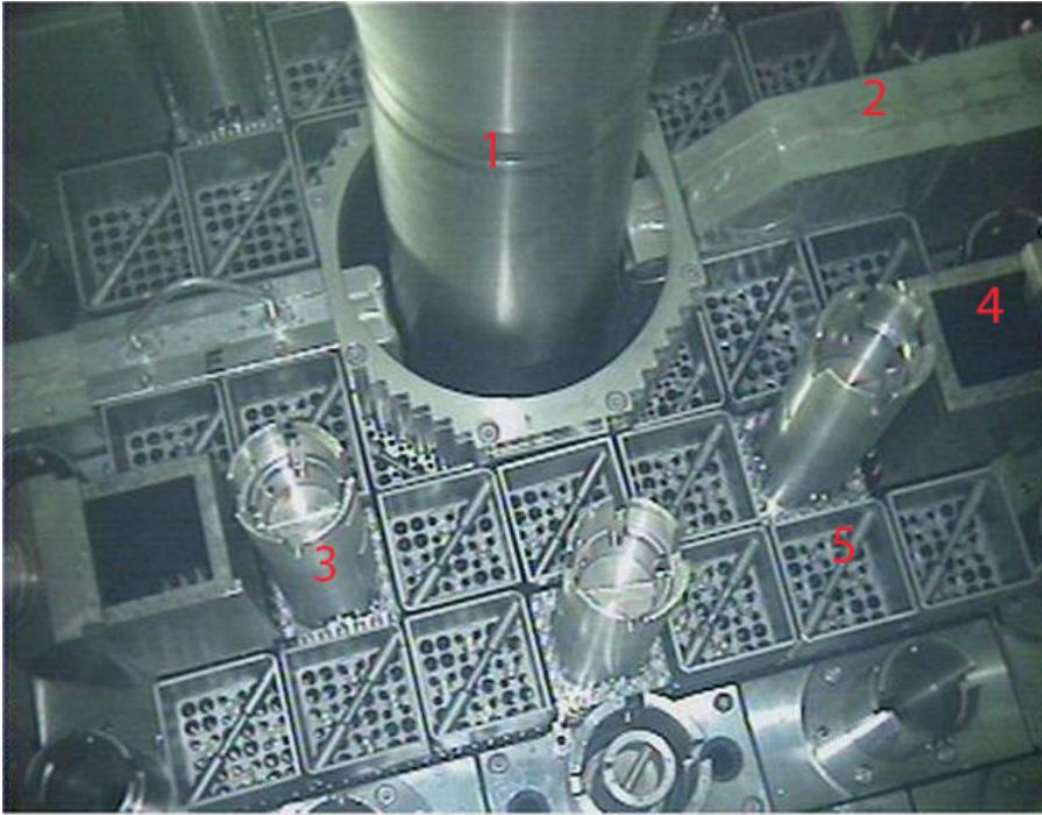


Figure 16: CABRI core, 1: Experimental water loop, 2: Irradiation channel, 3: Control rods, 4: Transient rods, 5: Fuel assemblies [19].

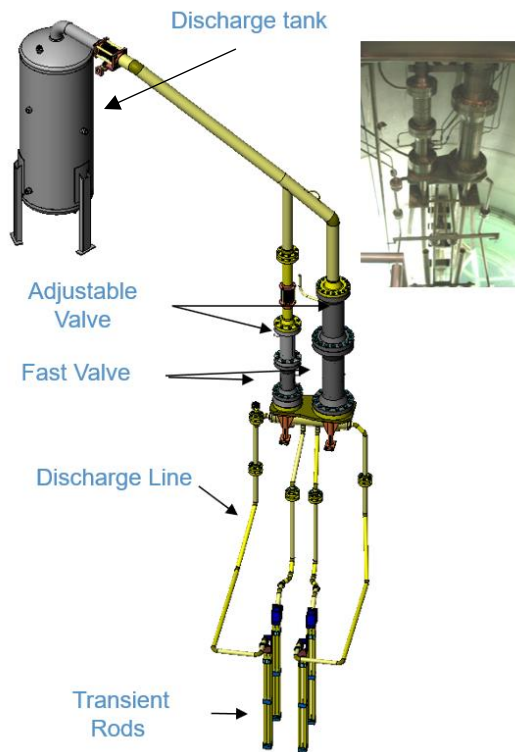


Figure 17: CABRI helium-3 transient injection system [19].

ACRR

The Annular Core Research Reactor (ACRR) is a 28 ft deep 10 ft in diameter, water-moderated pool type reactor located at Sandia National Laboratory in Albuquerque, New Mexico. ACRR contains uranium dioxide/beryllium oxide (UO₂-BeO) fuel elements clad in stainless steel. The fuel is in an annulus hexagonal-like array with a composition of 21.5% UO₂ and 78.5% BeO with a uranium enrichment of 35 wt%. Control of the ACRR is done by two safety rods, three poison transient rods and six control rods, which are part of the nominal 236 elements that make up the ACRR core. In the center of the array is a 23 cm diameter dry irradiation cavity that protrudes out the top of the core [19] [20]. Figure 18 and Figure 19 show the ACRR core and inner experiment cavity respectively. The ACRR core is able to reach pulses from 7 to 28 milliseconds and supply energy depositions in the 3,500 J/g range. Table 5 below provides pulse characteristics for the nominal 236 element core at various reactivity additions [20].

ACRR has not performed RIA testing but does have pulses that might make it conducive to RIA testing which is why it was added. It has performed more than 30 unprotected loss of flow (ULOF) experiments for fast reactor fuels. The main goal of these tests was to capture fuel breakup and motion and data for fresh versus preirradiated rodlets [21].

Table 4: Pulse characteristics for ACRR core [22].

Reactivity Insertion (Dollars)	Pulse Width at Half Maximum (msec)	Peak Power (MW)	Energy Yield (MW-sec)	Approximate Fuel Temperature (°C)
1.50	27.8	1,500	60	220
2.00	13.5	6,900	137	425
2.50	9.3	16,500	210	620
3.00	7.0	30,200	280	850

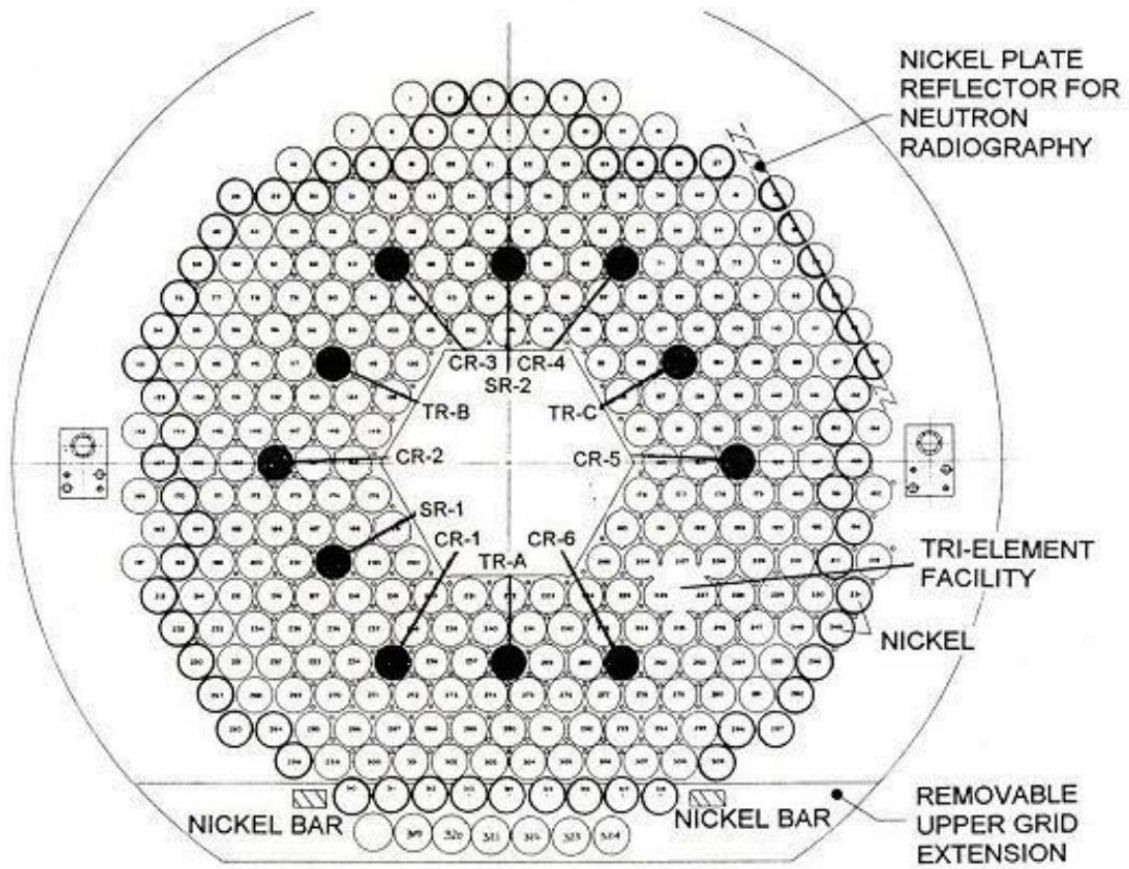


Figure 18: Cross section of 236 element ACRR [21].

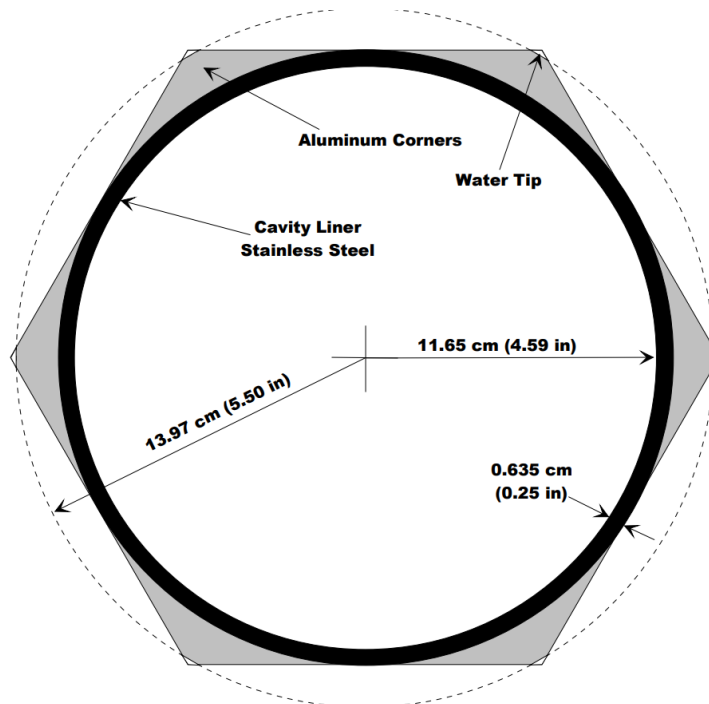


Figure 19: Detail of the dry irradiation cavity [21].

Summary and Comparisons of RIA Capabilities Worldwide

Figure 21 and Figure 20 provide a graphical comparison of the described facilities and the desired pulse widths and energies for BWR and PWR accident scenarios. From the graphs it can be concluded that current capabilities worldwide, either past or present, do not generate desired pulses needed to represent PWR and BWR conditions. The facilities generate either pulses with larger magnitudes of energy deposition, which could lead to experimental data showing early failures of fuels not representative of actual phenomenon, or wider pulses with magnitudes in the power range of PWRs and BWRs, like IGR which could produce experimental data that provides fuel performance being better than what might actually occur. As mentioned previously finding capabilities that produce near BWR and PWR accident scenarios is ideal for understanding the phenomena completely, resulting in better use of fuels in commercial power plants. While some of these facilities appear to present near ideal conditions, such as PBF, many have been decommissioned and are no longer available to support such work, however, they have been discussed and provided as comparison to current available test reactors.

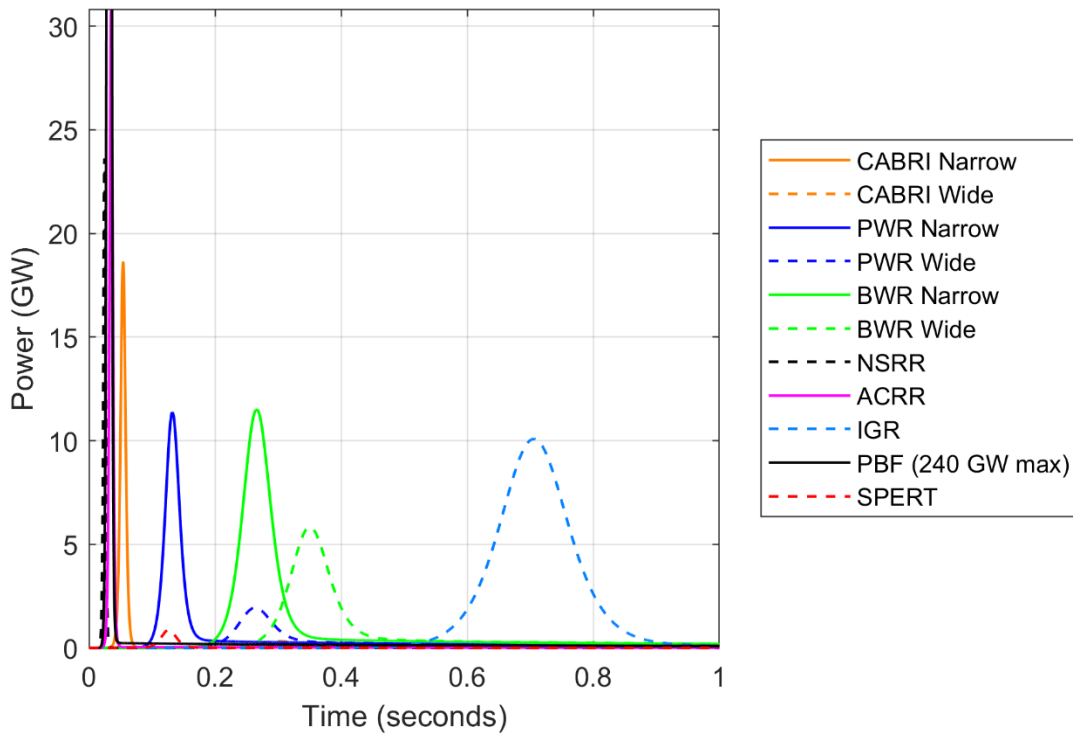


Figure 21: Energy deposition comparison of pulse type reactors worldwide.

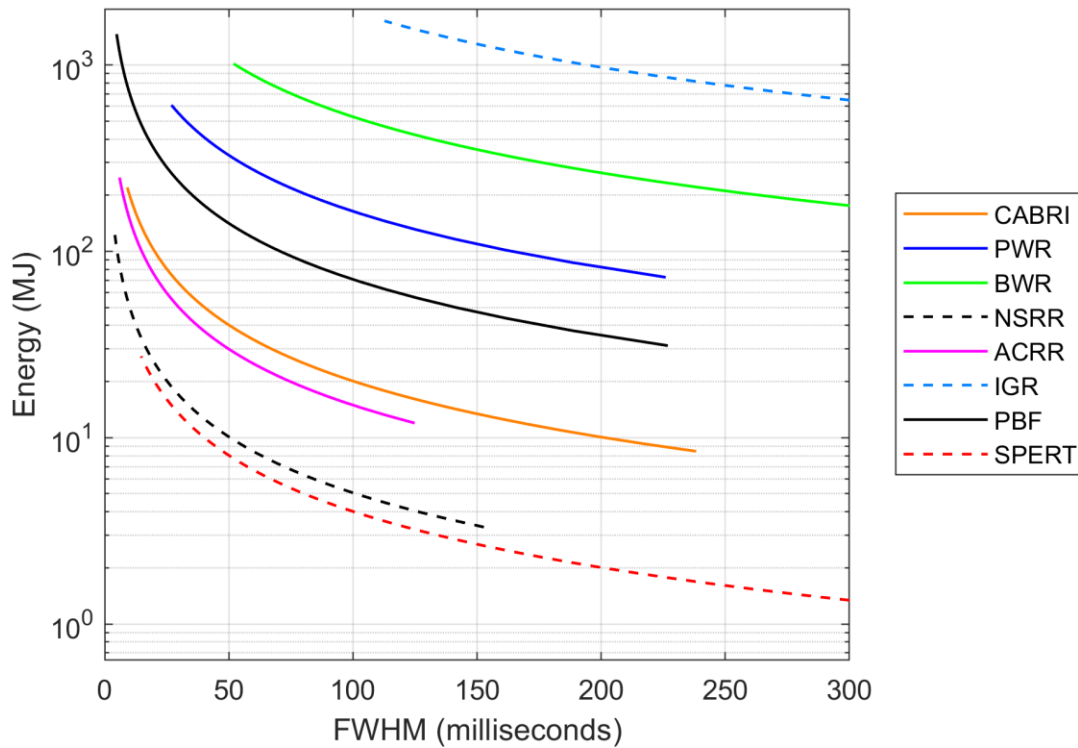


Figure 20: Comparison of contemporary reactor transient conditions.

2.5 Current RIA Capabilities of the TREAT Reactor

Primarily TREAT's contribution to the nuclear world involved research revolving around liquid metal reactor fuel elements, for such reactors as the Experimental Breeder Reactor-II (EBR-II) and the British Prototype Fast Reactor (PFR) [22]. However, TREAT also performed many LWR experiments, specifically water-based experiments under RIA power conditions. This testing supported the development and qualification of the fuel for the Power Burst Facility (PBF) as well as other testing involving aluminum-plate type fuel for research applications. A study was performed in 1998 of the TREAT facility to predict the pulse width of TREAT and show the ability of the reactor to perform more in-depth RIA testing. In the study, based on a simulation using ARCS, it was determined that the minimum pulse that the reactor is capable of was approximately a 71-millisecond pulse with a limit on energy of 1400 MJ, see Figure 22 [23]. In an actual trial transient performed at TREAT in July of 2019, it was shown that in reality TREAT can currently produce a minimum pulse width of approximately 93 milliseconds and produce approximately 900 MJ of energy, see Figure 23. Figure 25 and Figure 24 show the ability of TREAT, natural pulse and clipped pulse, compared to the reactors discussed in the sections above.

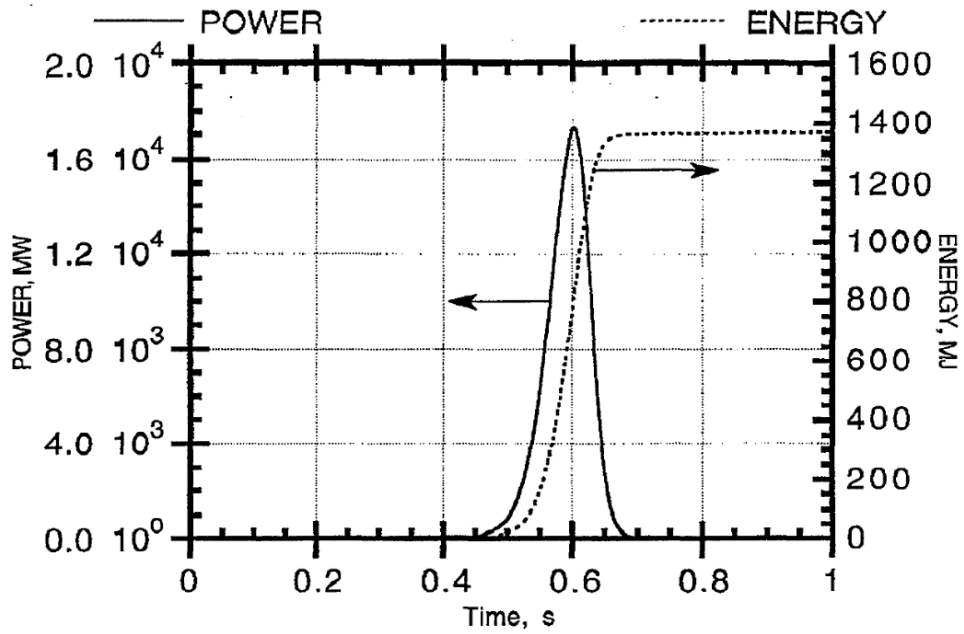


Figure 22: Plot of TREAT reactor power and energy based on initial study from 1998 [11].

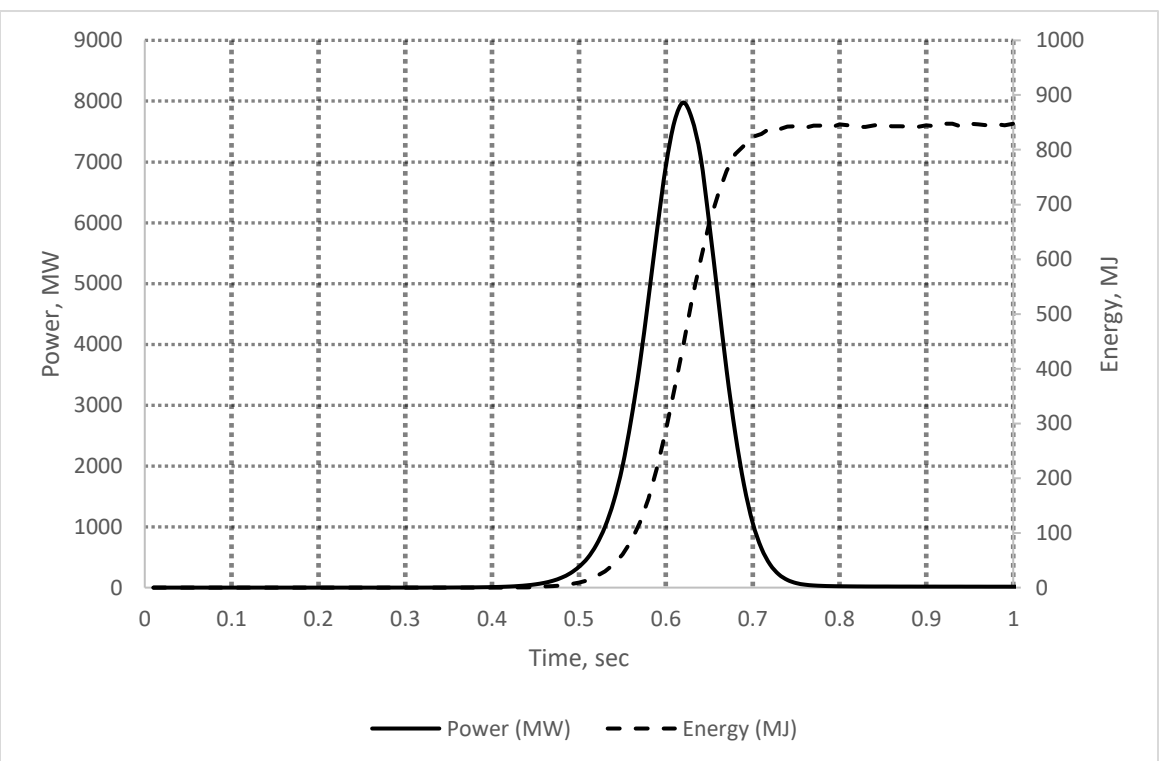


Figure 23: Plot of TREAT reactor power and energy, transient 2930, July 2019.

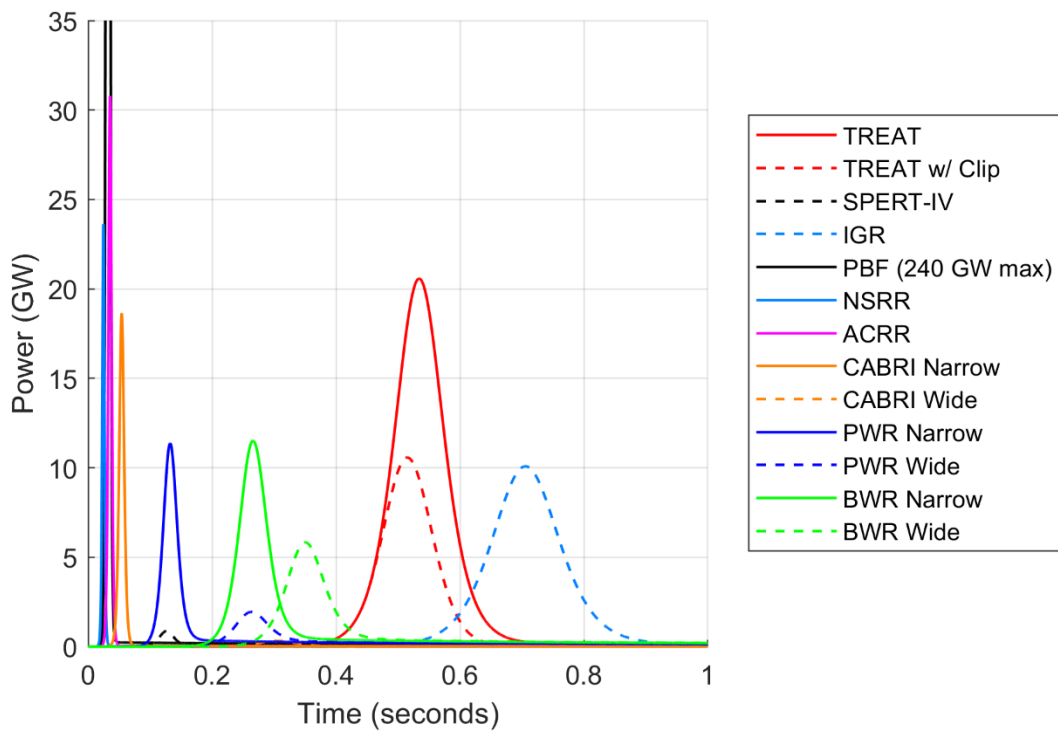


Figure 24: Comparison of contemporary reactor transient conditions with TREAT.

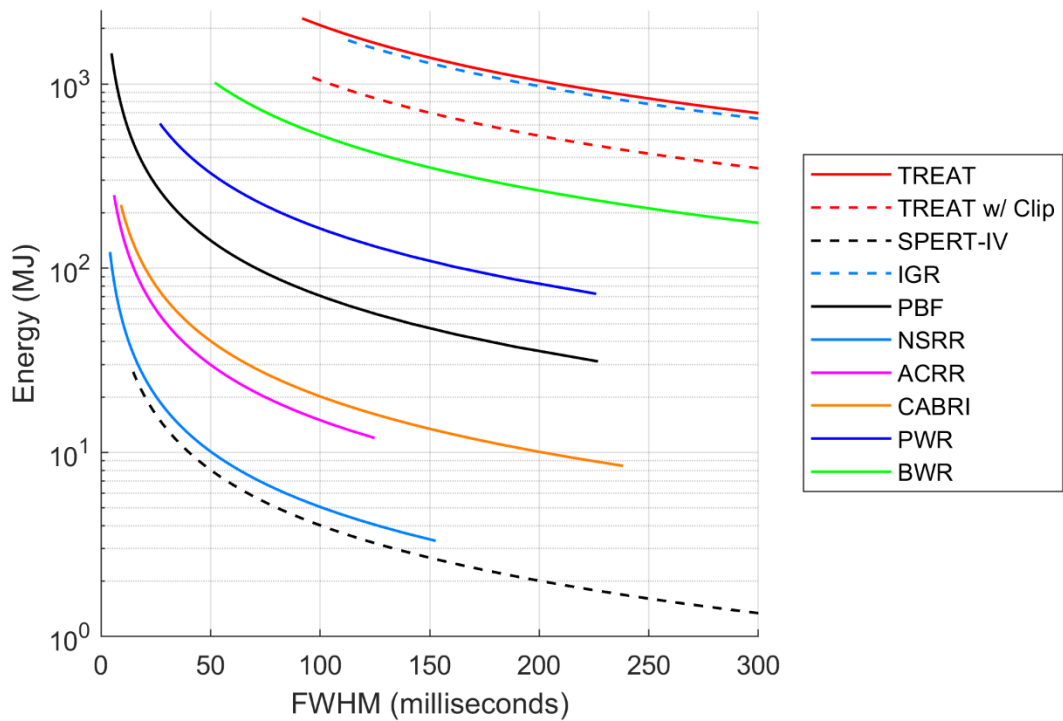


Figure 25: Energy deposition comparison of pulse type reactors worldwide with TREAT.

Once again, similar to Figure 20 and Figure 21 above, while TREAT provides an environment closer to BWR conditions than the reactors discussed in the section above, it still doesn't meet the needs for a more realistic BWR and PWR environment, and in fact could result in experimental data that provides expectations of fuels that are better than might actually be the case.

2.6 Clipping Studies for TREAT

In 2019, there was an extensive point kinetics study, using RELAP5-3D, to determine the best way in which TREAT could produce more prototypic pulses and energies to represent conditions seen during LWR RIA events. Twenty-one cases were looked at during this extensive study varying reactivity insertion, clipping time and speed, and the total peaking factor. Cases 1 through 7 were used to determine the effects of reactivity on the pulse width. Reactivity was increased from 4.0% $\Delta k/k$ to 5.8% $\Delta k/k$ and the pulses were not clipped to see the response of the temperature feedback used to terminate the TREAT pulse. The cases showed that as reactivity insertion increases, the pulse width decreases and the temperature and energy both increase, as expected. Flattening of the core power distribution was looked at in cases 8 through 14. This was done by reducing the total peaking factor, the highest local power density in the core fuel, from 1.82 to 1.60. Reactivity was also varied to provide a comparison between the 1.60 peaking factor to the 1.82 peaking factor studied in cases 1 through 7. Based on the results, energy and pulse width stayed the same, however, the maximum temperature was reduced. Cases 15 and 16 were used to compare a clipped energy case and a natural pulse with a target energy of 500 MJ. Case 15 was the natural pulse at a 1.3% $\Delta k/k$ reactivity and case 16 shows a 2.6% pulse that is clipped. Using the clip, the FWHM was reduced by more than 0.4 seconds. Figure 26 shows a graphical comparison of the two. Cases 17 through 20 study the effects of clipping. This was done in cases

17 through 19 by increasing the speed in which the transient rods are inserted during the clip from 140 in/sec, the current speed of the transient rods, to 250 in/sec. Case 20 used a hypothetical helium-3 injection system, discussed in more detail in the helium-3 clipping section below, for the clip that was able to insert -5% $\Delta k/k$ reactivity in 5 milliseconds [10]. These cases were all performed at a reactivity of 4.45% $\Delta k/k$ which is the maximum initiating reactivity at TREAT with the current 0.023 second period limit [24]. Figure 27 shows the comparison of the various clipping speeds on the pulse width. Case 21 was an increased reactivity insertion, 5.1% $\Delta k/k$ as compared to the 4.45% $\Delta k/k$, with the helium-3 injection system as the clipping mechanism. This provided interesting results in which the pulse width was wider at the higher reactivity insertion than that of the lower, see Figure 28. This showed that during natural transients, a higher insertion reactivity results in a shorter pulse width, however this does not hold up when transients are clipped. Table 6 provides a summary of the study with the variables changed as well as the resulting energy, fuel temperature, and pulse width. It should be noted that current TREAT safety basis requires that fuel temperature stay below 600°C so any of these options chosen, cases outlined on Table 6, would have required modification to the safety basis. Based on these studies minor modifications to the facility, including modifying the transient rod drives to go from a speed of 140 in/sec to 250 in/sec would result in pulse widths in the BWR range, however, it would not allow for PWR pulse widths [10]. Figure 29 is a modified graph of Figure 27 which compares the rod drive clipping speeds and helium-3 injection clip compared to BWR and PWR pulse width ranges.

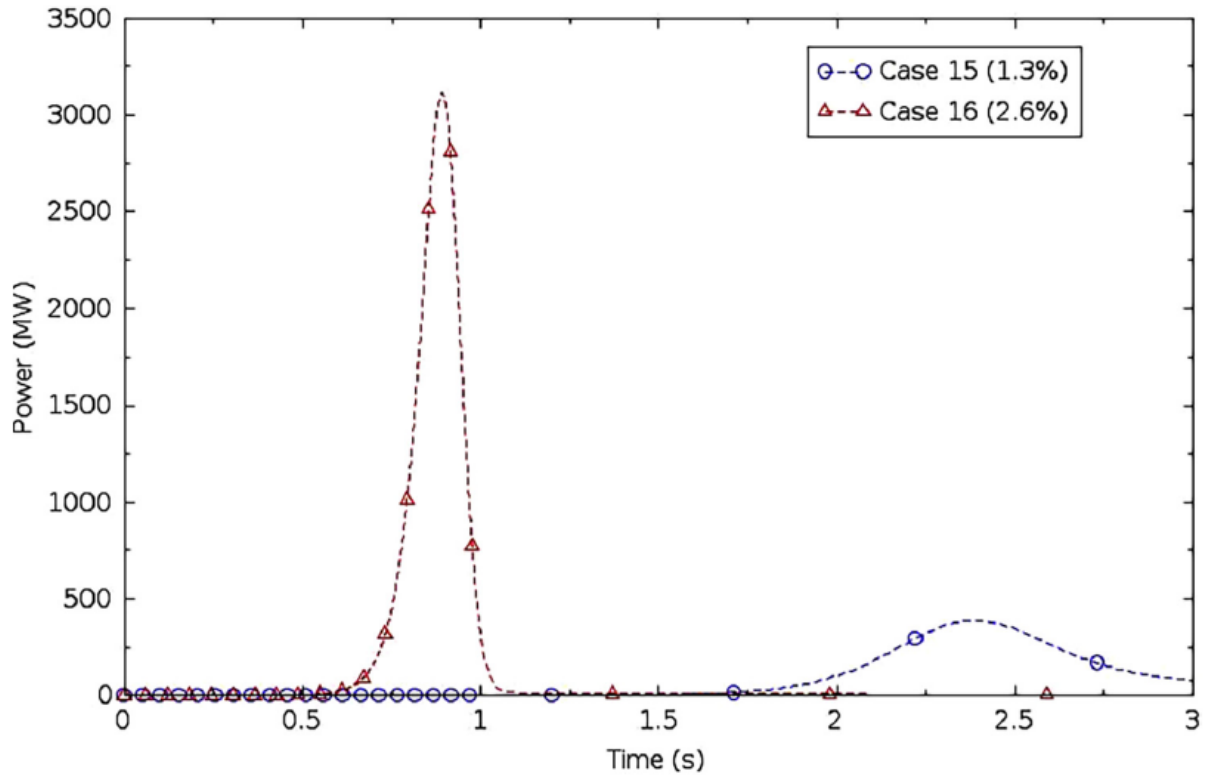


Figure 26: Pulse comparison between a natural pulse and a clipped pulse to an energy deposition of 500 MJ [12].

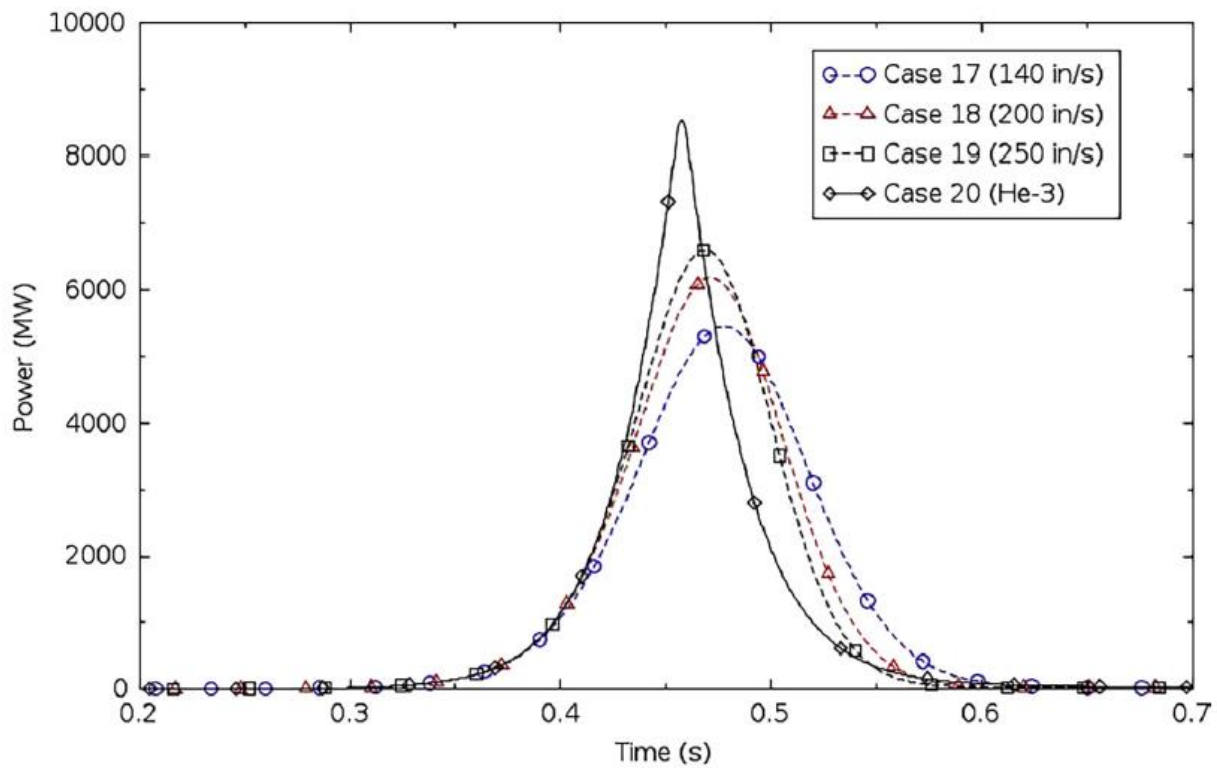


Figure 27: Pulse comparison for various clipping speeds of 4.5% k/k reactivity insertion pulse [12].

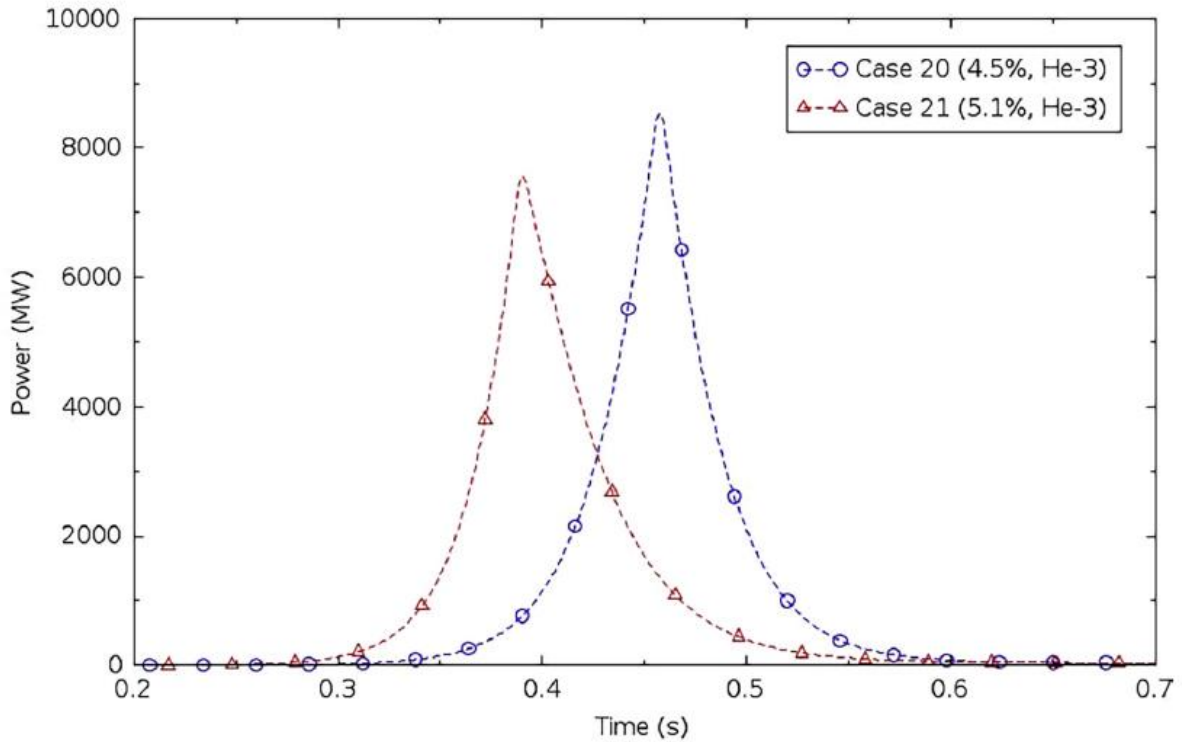


Figure 28: Pulse comparison for initial reactivity insertion on a clipped pulse [12].

Table 5: Summary of cases performed during a study to determine best ways to create prototypic RIA events in TREAT.

Case	Reactivity Insertion ($\Delta k/k$)	Clipping Time/Speed (s)/(in/s)	Total Peaking Factor	Energy Deposition (MJ)	Maximum Fuel Temperature ($^{\circ}\text{C}$)	FWHM (s)
1	0.040	NA/NA	1.82	2266	529	0.1192
2	0.043	NA/NA	1.82	2525	575	0.1103
3	0.046	NA/NA	1.82	2799	621	0.1027
4	0.049	NA/NA	1.82	3086	668	0.0963
5	0.052	NA/NA	1.82	3388	717	0.0909
6	0.055	NA/NA	1.82	3704	766	0.0862
7	0.058	NA/NA	1.82	4035	816	0.0821
8	0.040	NA/NA	1.60	2266	480	0.1192
9	0.043	NA/NA	1.60	2525	521	0.1103
10	0.046	NA/NA	1.60	2799	563	0.1027
11	0.049	NA/NA	1.60	3086	607	0.0963
12	0.052	NA/NA	1.60	3388	651	0.0909
13	0.055	NA/NA	1.60	3704	696	0.0862
14	0.058	NA/NA	1.60	4035	742	0.0821
15	0.013	NA/NA	1.82	500	173	0.5675
16	0.026	0.845/140	1.82	500	173	0.1327
17	0.045	0.364/140	1.82	627	203	0.0954
18	0.045	0.392/200	1.82	626	203	0.0837
19	0.045	0.405/250	1.82	619	202	0.0771
20	0.045	0.455/ ^3He	1.82	627	203	0.0458
21	0.051	0.387/ ^3He	1.82	624	203	0.0496

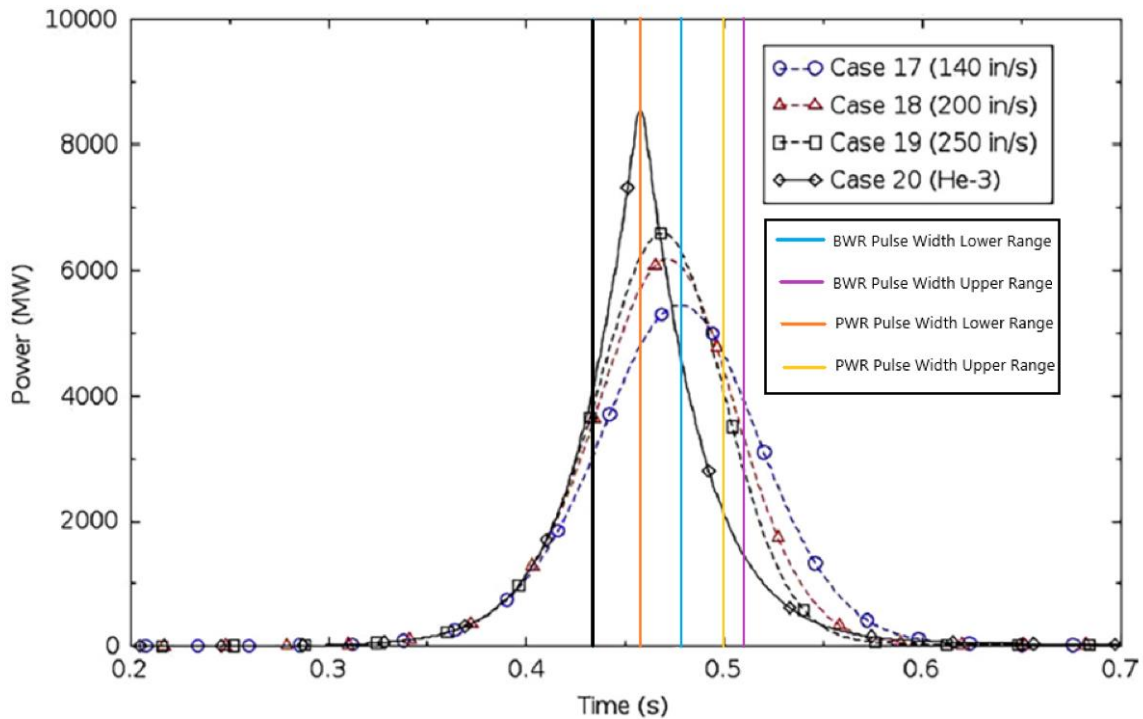


Figure 29: Comparison of pulse widths of clipping techniques compared to BWR and PWR pulse width ranges.

Boron Clipping Concepts

A boron tube concept was evaluated in the 2019 study. This system also used a modified TREAT dummy fuel assembly which contained a cavity that allowed for a rapid insertion of a guided poison piston tube. The piston tube would be held in an “out-of-core” position with the use of a mechanical device, pyrotechnic fasteners, and would be injected into the core using a gas chamber above the rod. The rod would be made of ^{10}B enriched B_4C dispersed in aluminum composite clad plates that make up a square like tube shape. Based on the size constraints of this system it was estimated that the tube could be inserted approximately 8,000 inches per second requiring a deceleration device to catch the tube. The shock absorbers that were required to provide consistent stopping force were a one-time-use. Due to the necessary replacement of the fasteners and shock absorbers, required after every use, this system was not as desirable. Figure 30 provides

a schematic of this concept. Boron-10 gas was also looked at as a potential concept, however, due to its additional hazards it was not considered viable [10].

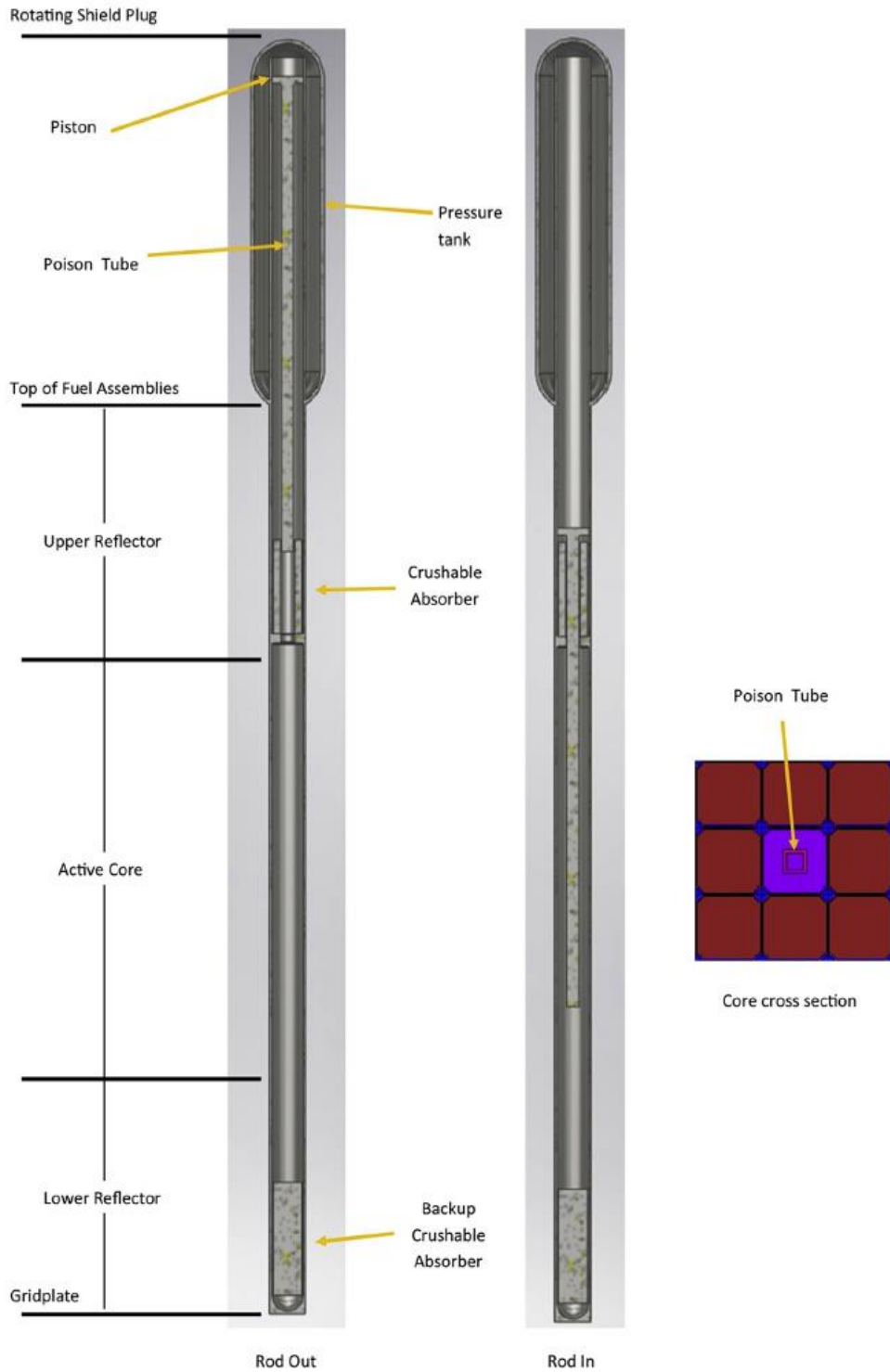


Figure 30: Overview of the borated tube clipping concept [12].

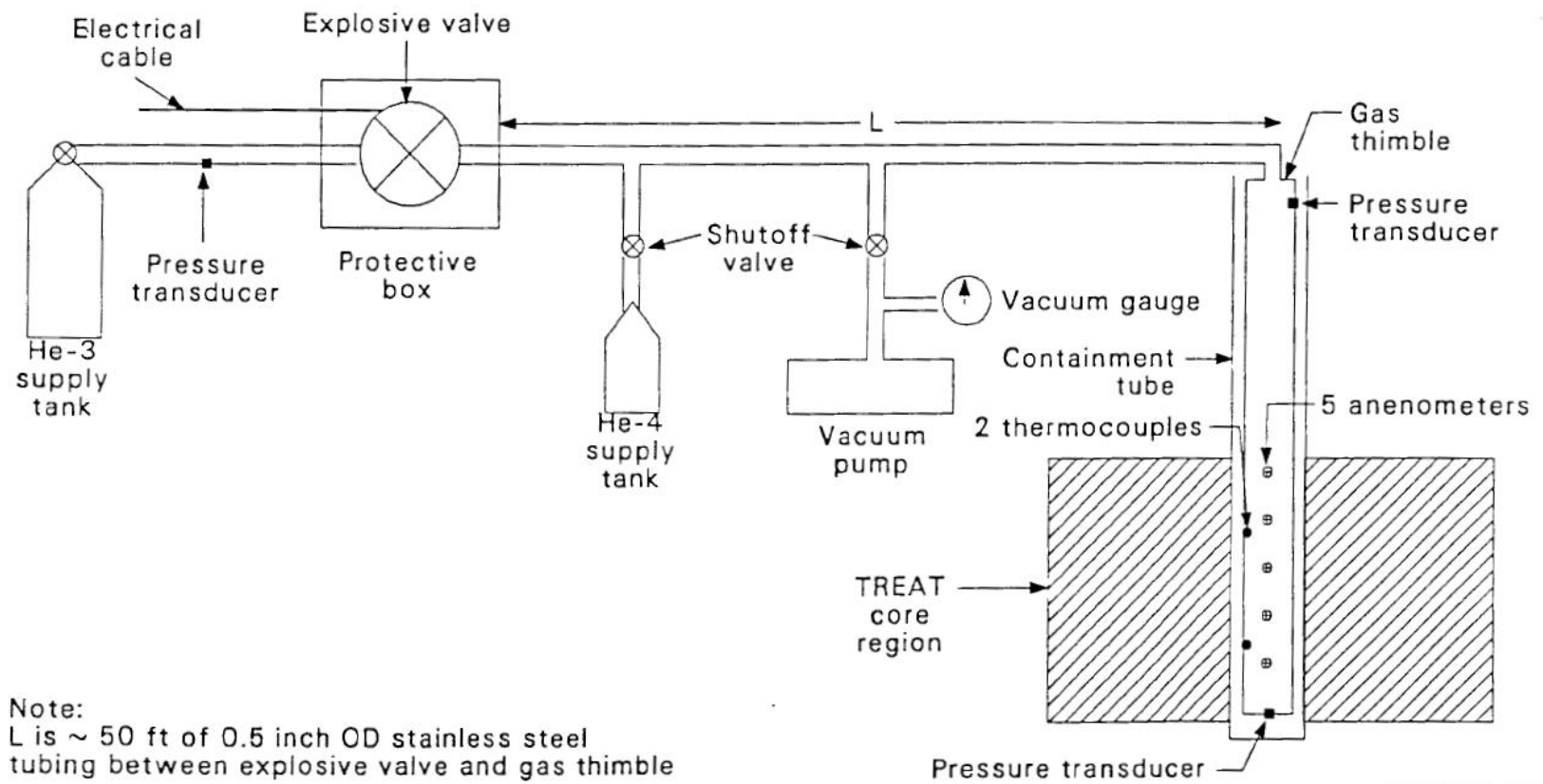
Helium-3 Clipping

Historically a helium-3 injection system had been looked at to allow TREAT to produce more prototypic pulses and energies for PWR and BWR RIA studies. The system was termed the Fast Shutdown System (FSS). The hypothetical system consisted of an electronic detection and a firing system. High pressure storage tanks filled with helium-3 would be placed outside the core and connected to gas thimbles that spanned the full length of the core. Explosive valves would be placed within the piping system to allow the rapid injection of the large absorption cross section gas into the thimbles. Figure 31 shows a schematic of the proposed system. The FSS thimbles and piping would begin at a vacuum state to ensure core performance. After the detection of a LOCA event within the experiment the valves would fire allowing the helium-3 gas to fill the thimbles. The desire was that this would reduce the fission power within TREAT for approximately 1.5 seconds allowing the control rods to complete the shutdown of the reactor. At the completion of the “blowdown” a collection tank would be used to collect the used gas which would contain the helium-3 gas along with some helium-4 gas and small amounts of tritium. The FSS gas thimbles were a tube, 1.27 in. OD and 1.08 in ID, with eight internal ribs to allow for more heat transfer area [25]. While this system was never built, other reactors have used helium-3 systems to alter power. Such reactors include Cabri, as discussed above, and a Russian RBMK critical facility which used a system very similar to the FSS [10].

The 2019 study of TREAT clipping conceptualized a few in core designs for in-core helium-3 gas thimbles, excluding the external components to complete the process of the system. One concept used a graphite dummy fuel assembly, like those used in the TREAT core, that contained zirconium-alloy tubes. These dummy assemblies would replace existing TREAT fuel in the locations required to provide desired clipping effect. Figure 32 provides an example core

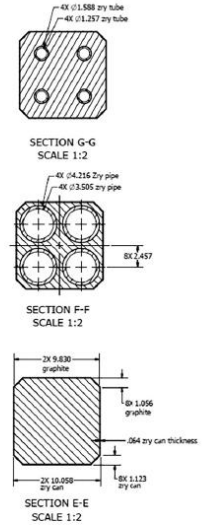
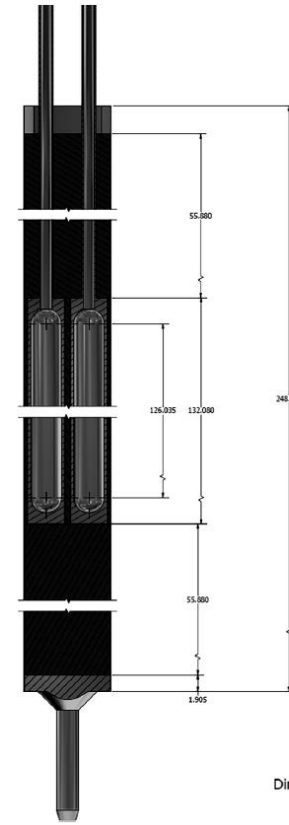
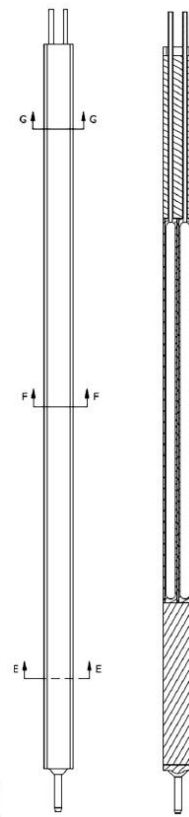
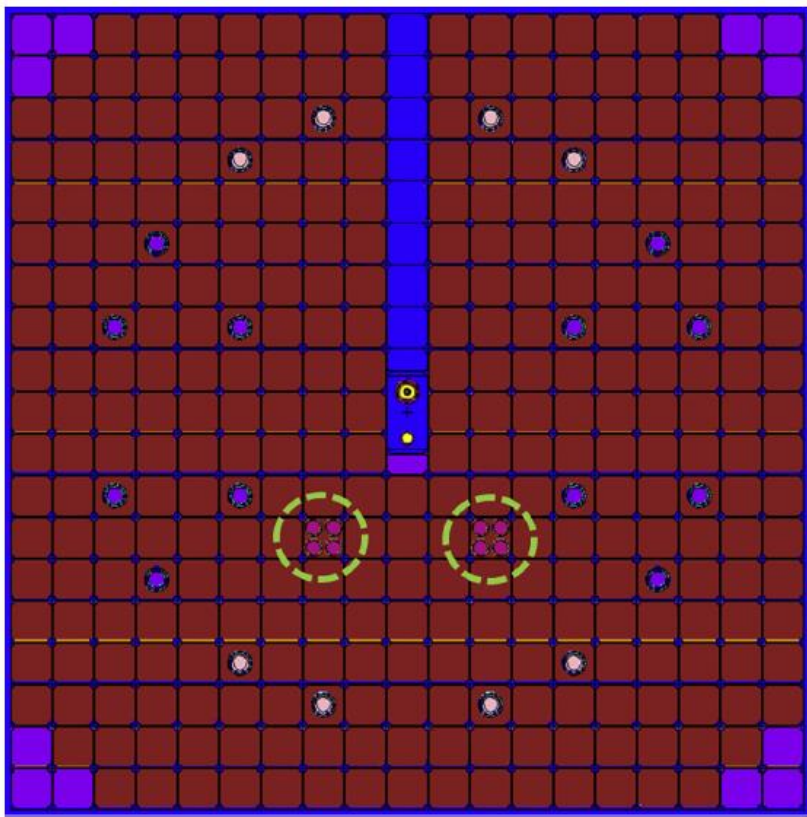
placement of the dummy assemblies as well as the schematic for the system described. The other concept was a cartridge type gas thimble similar to the FSS. Due to the self-shielding of helium-3, this concept used an annular test gas thimble to reduce the amount of helium-3 required to clip a transient and optimize the helium-3 used. A driver tank would be affixed to the top of each thimble to reduce required piping. Rather than an exploding valve, a fast-acting valve would be placed between the driver tank and gas thimble section. Similar to the previous concept, this concept would contain the same cross-sectional area as a TREAT fuel assembly, to allow placement anywhere within the core. Figure 33 provides a simple model of what such a system might look like.

Based on these studies, both modern and historical, helium-3 offered the greatest benefit to the clipping design and performance of a system for LWR RIA studies at TREAT as long as the system was able to produce a $-5.0\% \Delta k/k$ reactivity insertion in 5 milliseconds or less [10].



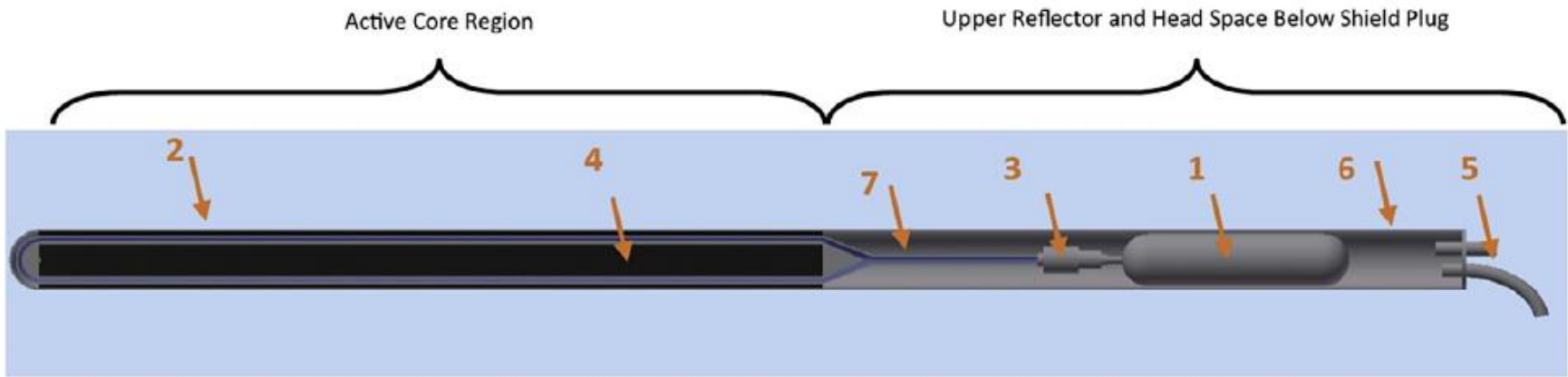
S66-WHT-989-01

Figure 31: Schematic of the FAST Shutdown System for TREAT [25]



Dimensions in cm

Figure 32: TREAT core with concept helium-3 graphite dummy elements (left) and the concept helium-3 graphite dummy assemblies (right) [12].



Labels:

- 1) Driver Tank
- 2) Receiver Chamber
- 3) Fast opening device valve or burst disc.
- 4) Graphite filler
- 5) Feedthroughs for control lines and re-charging line
- 6) Containment vessel
- 7) Connector Tube

Figure 33: Conceptual cartridge type assembly for a helium-3 clipping module [12].

3 INPUT DESIGN DESCRIPTION

The input design for this evaluation is based on the cartridge type helium-3 system, from here on called the Helium Negative Reactivity Insertion (HENRI) system, as shown in Figure 33. The design details needed for this evaluation can be broken down into three main components, the driver tank, gas thimble, and transfer line. Figure 34 shows a simple schematic of the system, each component described in more detail in the sections below.

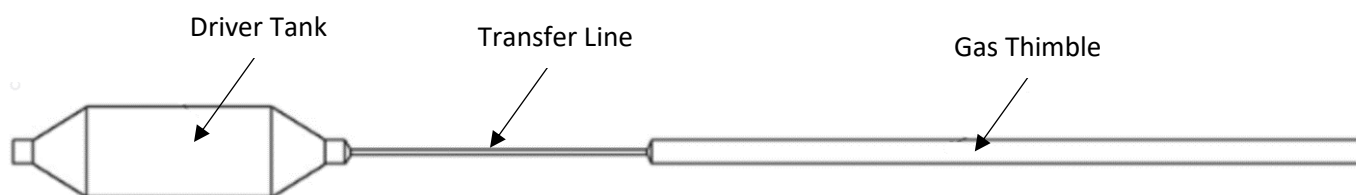


Figure 34: Schematic of the components that make up the HENRI system used in this evaluation.

3.1 Driver Tank

The driver tank holds high pressure helium-3 during reactor operations. The approximate 6-liter driver tank is a nominal 6-inch schedule 40 stainless steel (SS-316) pipe, allowing it to fit within the nominal 10.2” diameter opening of the existing loop handling casks at TREAT. The driver tank pipe is 13.5 inches tall and has a top cap that is welded to the top of the pipe. Prior to operations, the driver tank is filled to the desired pressure required to achieve the necessary helium-3 density in the gas thimble. The driver tank contains a fast-acting valve that when initiated fills the gas thimble with helium-3 to initiate the clip of the transient. The bottom of the tank has a flange that bolts down to form a tight, double O-ring seal to the flange of the transfer line. The driver tank also has various penetrations for charging the tank as well as for instrumentation lead pass throughs. Figure 35 provides a sketch of the tank used in this evaluation. Appendix B has a schematic of the dimensions used for this evaluation. It should be noted that details of the fast-

acting valve and pass throughs are not required for this evaluation and it is assumed that the actual valve used for the final systems will perform as desired.

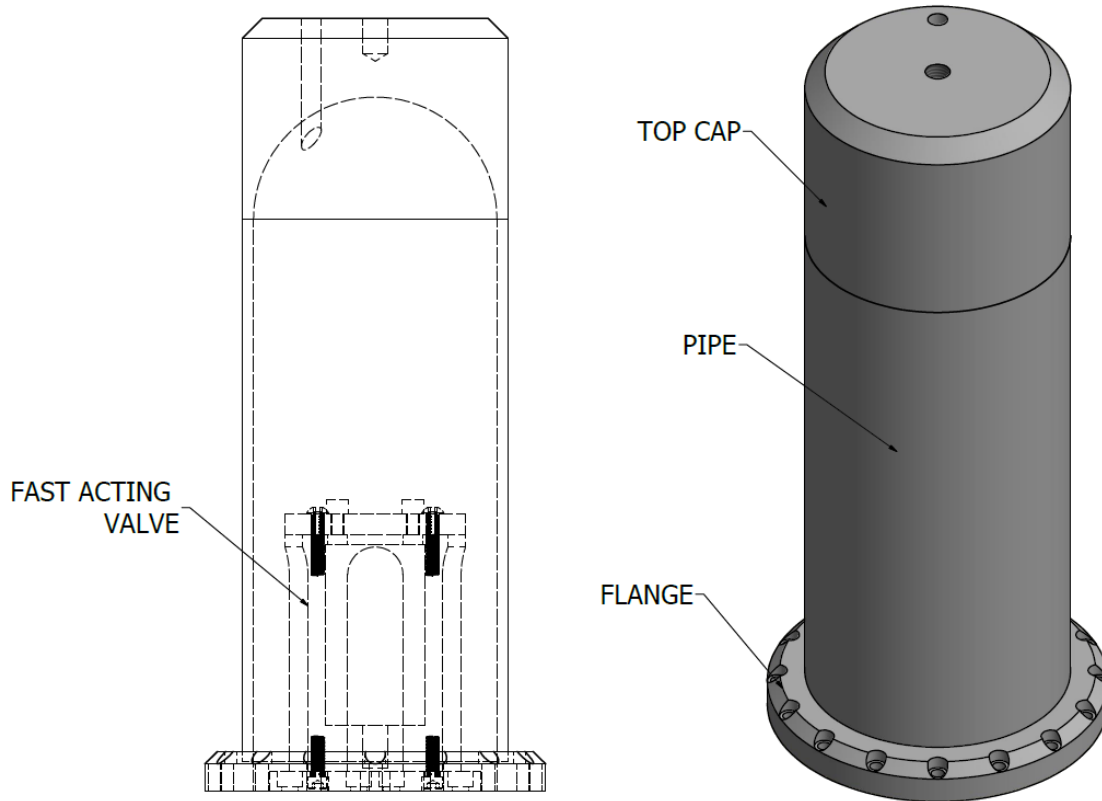


Figure 35: Schematic of driver tank with fast acting valve.

3.2 Gas Thimble

The gas thimble is the cartridge, located in the active region of the core, which holds the flowing helium-3 after the fast-acting valve has been initiated to clip the transient. The gas thimble extends from the top of the active region of the core to just above the core grid plate approximately six feet. To maintain TREAT's modular design and to reduce the amount of design and fabrication work required, the helium-3 system was constrained to fit within a control rod fuel assembly or RE assembly. Both the RE and control rod assemblies have a hollow center allowing for the gas

thimble to be centered in the middle of the assemblies and interface with existing core hardware. This constraint requires the gas thimble to have an outer diameter no larger than 2 inches. The gas thimble was designed to be a nominal 1.5-inch schedule 40 pipe fabricated from Zircalloy-4 metal. A conical end cap is welded to the bottom of the gas thimble as well as an upper end cap to connect the transfer line to the gas thimble. A Zircalloy-4 vacuum line extends out of the bottom of the gas thimble to allow for removal of helium-3 from the system at various times during operation of the system. Figure 36 provides a model of the gas thimble. Appendix B provides the gas thimble schematic of the dimensions used for this evaluation.

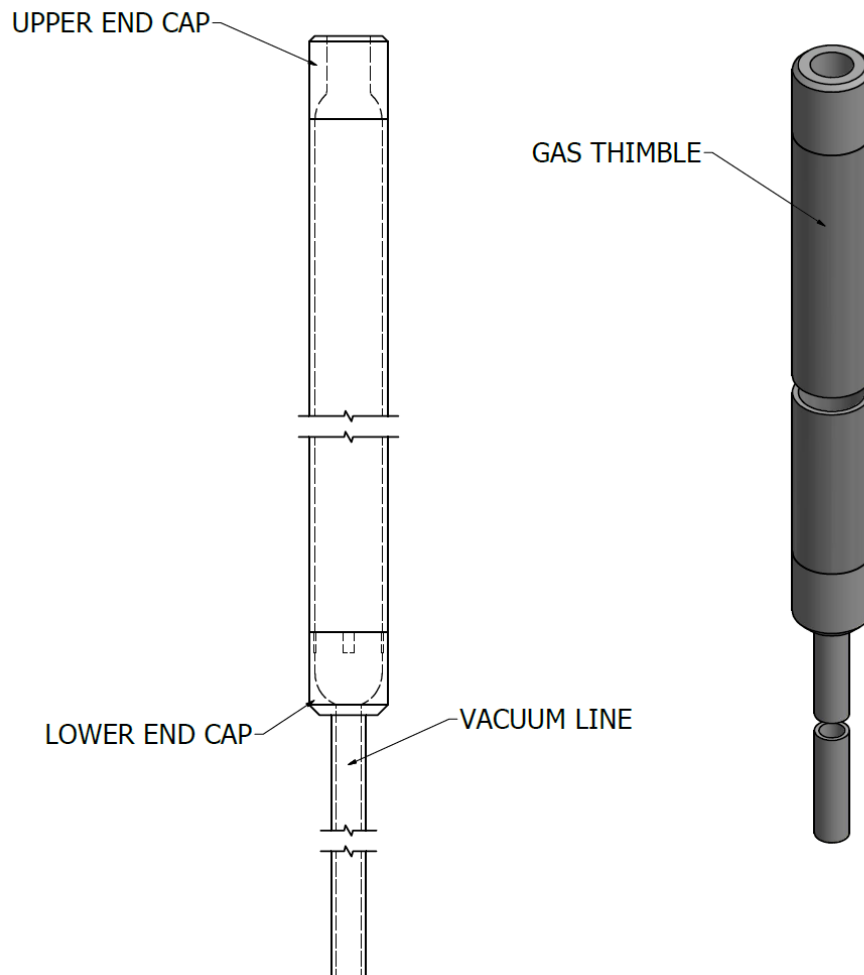


Figure 36: Schematic of gas thimble with vacuum line.

3.3 Transfer Line

The transfer line is a smaller line approximately 2 ft in length that connects the driver tank, located near the top of a fuel assembly, to the gas thimble that is located in the active region of the core. The line is a nominal 1" schedule 40 pipe that is welded to the upper end cap on the gas thimble. A flange is welded to the upper end of the transfer line that has three main functions, provide a sealing surface for the driver tank, a sealing surface for the fast acting valve piston, and a mating feature with the fuel assembly to support the HENRI module. Figure 37 provides a model of the transfer line. Appendix B provides the transfer line schematic of the dimensions used for this evaluation.

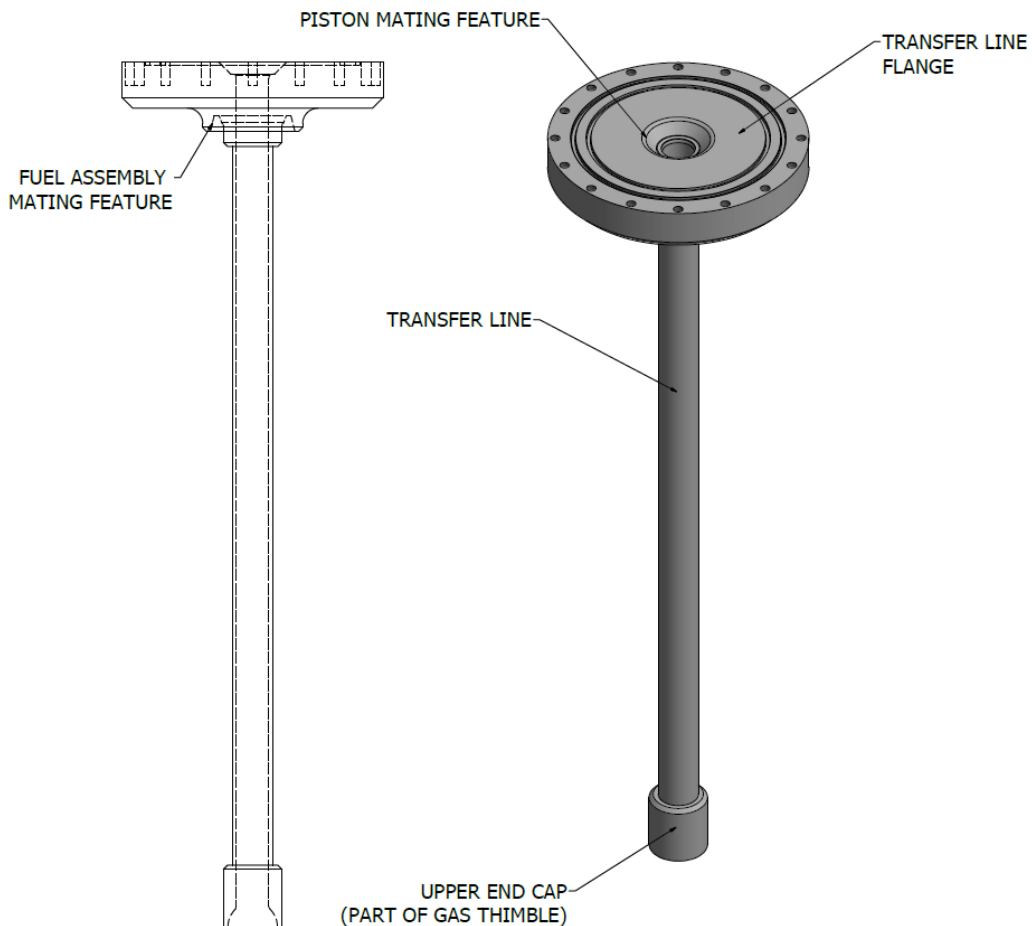


Figure 37: Schematic of transfer line.

4 METHODS ANALYSIS

4.1 Requirements

The requirements for this evaluation were as follows:

1. The HENRI system shall be able to provide a reactivity reduction of 5% $\Delta k/k$ after initiation of the system.
2. The reactivity insertion shall occur within a 5-millisecond timeframe after initiation of the system.
3. A single HENRI module must be able to fit within a control rod fuel assembly or RE assembly used in the TREAT core.

4.2 Monte Carlo N- Particle Transport Description

Monte Carlo N-Particle (MCNP) is a continuous-energy particle transport software which allows for the physics of particles, such as alphas, electrons, photons, and neutrons, to be tracked based on random sampling and statistical methods. The software is also capable of calculating the k_{eff} eigenvalue of systems that contain fissile materials. The Monte Carlo process consists of using a pseudorandom number generator to simulate specific particle histories. The random numbers are used to sample the probability density functions for various particle characteristics (scattering angles, track lengths, etc.). The code follows a large number of particles, chosen at random, from the particles creation and gives them random energy, positions, and direction until they are captured or escapes the modeled system. This process is repeated until enough particle histories have been performed, from a statistical sense, that the particle distributions are well known [26].

The MCNP input deck is set up in three sections, the surface card, data card, and cell card.

The input deck typically contains information about the problem such as:

- Geometry (surface and cell card)
- Materials and cross-sectional data (data card)
- Location and characteristics of the specific particle source (data card)
- Type of tally, or particle tracking, desired (data card)
- Any variance reduction techniques used to improve computing efficiency of the problem. (data card) [26]

MCNP version 6 (MCNP6) was used in this evaluation and can be obtained from the Radiation Safety Information Computational Center (RSICC). MCNP 6 is effective and shown to be beneficial to support scientific and engineering analysis. In addition, all MCNP model inputs used for this evaluation were processed on the high-performance computing system (HPC) located at Idaho National Laboratory. The table below describes the HPC configuration.

Table 6: Configuration of MCNP runs on HPC

Model of Computer	Processor	Operating System
Falcon : SGI ICE®-X Distributed Memory Cluster	<ul style="list-style-type: none"> • 34992 cores • 121 TB total memory • FDR InfiniBand Network (56 Gbit/s), Single-Plane Enhanced Hypercube Topology • LINPACK: 1087.58 TFlops • ECCN4A003.c • 2 Login and 972 Compute Nodes <ul style="list-style-type: none"> ○ 2 Intel Xeon E5-2695 v4 CPUs <ul style="list-style-type: none"> ▪ Broadwell chipset ▪ 18 cores per CPU ▪ 2.10 GHz ○ 128 GB RAM ○ FDR InfiniBand Interconnect 	SUSE Linux Enterprise Server 12 Service Pack 4

MCNP Validation for the HENRI Evaluation in TREAT

Currently there are three separate benchmarks on the TREAT Core in the International Handbook of Evaluated Reactor Physics Benchmark Experiments (IRPhEP). These benchmark models cover the TREAT Start-up core (TREAT-FUND-RESR-001), the M8CAL core (TREAT-FUND-RESR-002), and the M2CAL core (TREAT-FUND-RESR-003) [27]. These benchmarks can be used to validate the MCNP modeling performed for this evaluation. This was not done for this evaluation as this thesis was intended to be a study to provide information about feasibility and support design efforts. Final results to support final design efforts would require validation of the modeling of the TREAT core.

While there are benchmarks for the TREAT core in various configurations, research in both the IRPhEP and International Criticality Safety Benchmark Evaluation Project Handbook (ICSBEP), resulted in no such benchmarks containing helium-3, especially in a core that is graphite moderated and 93% enriched. Since there are no benchmark models it is hard to validate the use of MCNP for helium-3 and its effects on the core. Since this is a scoping study to support feasibility and design efforts the use of MCNP with helium-3 in the TREAT core is acceptable. Once a final system is built and installed at TREAT, various tests will be done while in core to help validate a first of its kind helium-3 benchmark model [28].

4.3 MCNP Geometry Descriptions

The two primary components of the MCNP model used for simulation in this analysis consists of: 1) the TREAT core, coupled with 2) up to four HENRI modules, in various configurations.

TREAT Core Model

The TREAT core model has been baselined and validated through its use at Idaho National Laboratory. This evaluation used the same TREAT baseline model that is used for all safety analyses for experiments. This model has been validated [29] and updated [30] [31] to better represent TREAT reactor physics. This evaluation will briefly describe the model for completeness.

The TREAT MCNP model consists of the core, reflector, concrete biological shield, and various other features (radiography, hodoscope, and graphite thermal column block) within the reflector shield. The core and surrounding shielding and reflector is only modeled from the grid plate in the bottom of the core to the top of the fuel elements, approximately 8ft total. Figure 39

and Figure 38 are snips of the MCNP reactor core model. The colors in the figures represent the materials used in the MCNP model. Below is a list of the main colors seen in the figures and the material they represent.

- Yellow: Concrete – Biological shield
- Green: Air
- Blue: Graphite – Reflectors
- Purple: Fuel Graphite Mixture

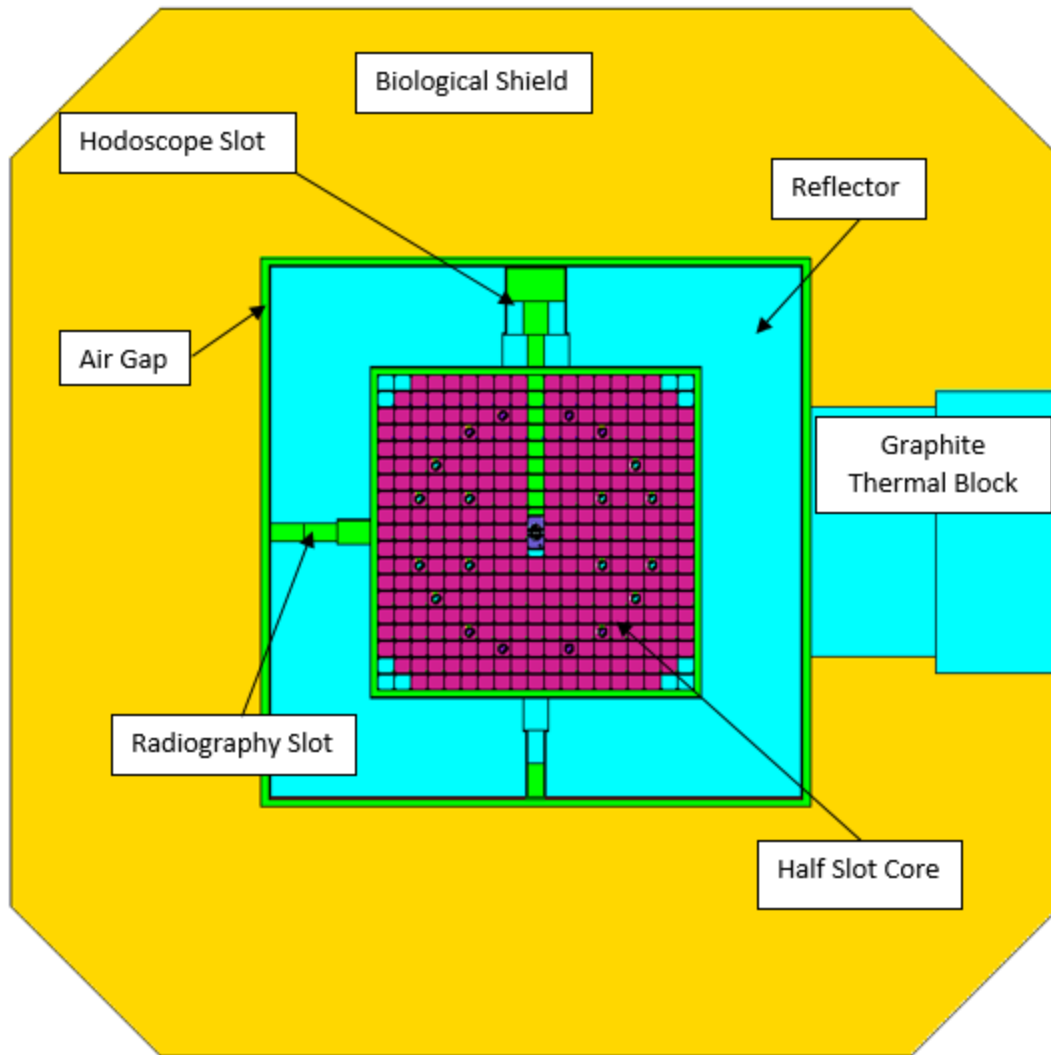


Figure 39: Top view of the MCNP model of the TREAT core at centerline.

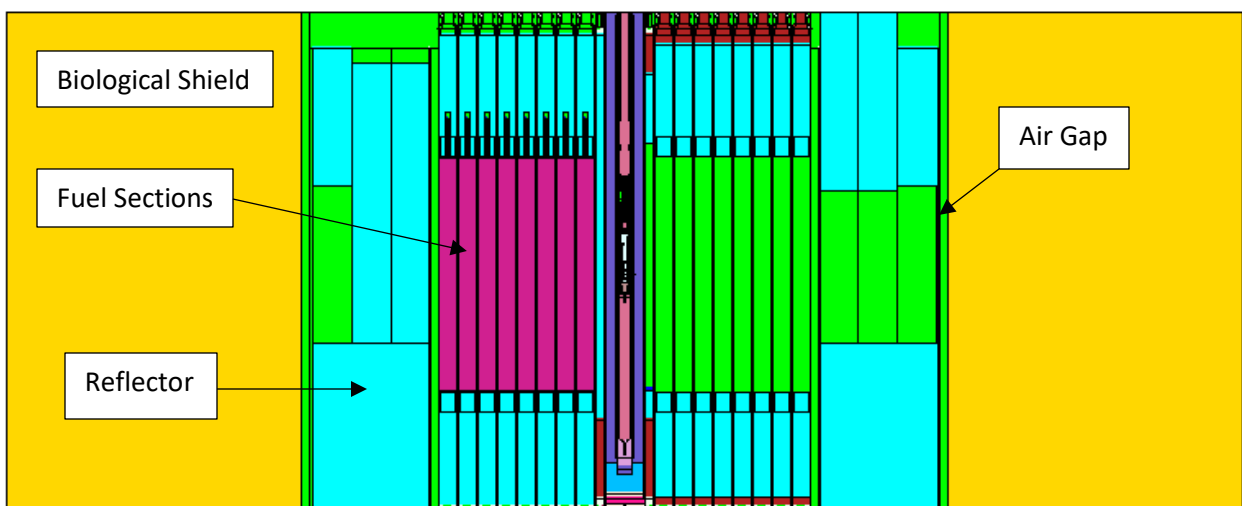


Figure 38: West view of the MCNP model of the TREAT core at centerline. Hodoscope slot is on the right.

The core of the TREAT MCNP model is modeled similar to that shown in Figure 1. It is a 19 by 19 array with dummy elements that make up the corners of the array. The various control rods are also modeled as well as an experiment slot located in the center of the core. Figure 40 and Figure 41 show images of the modeled core using a half slot and full slot respectively.

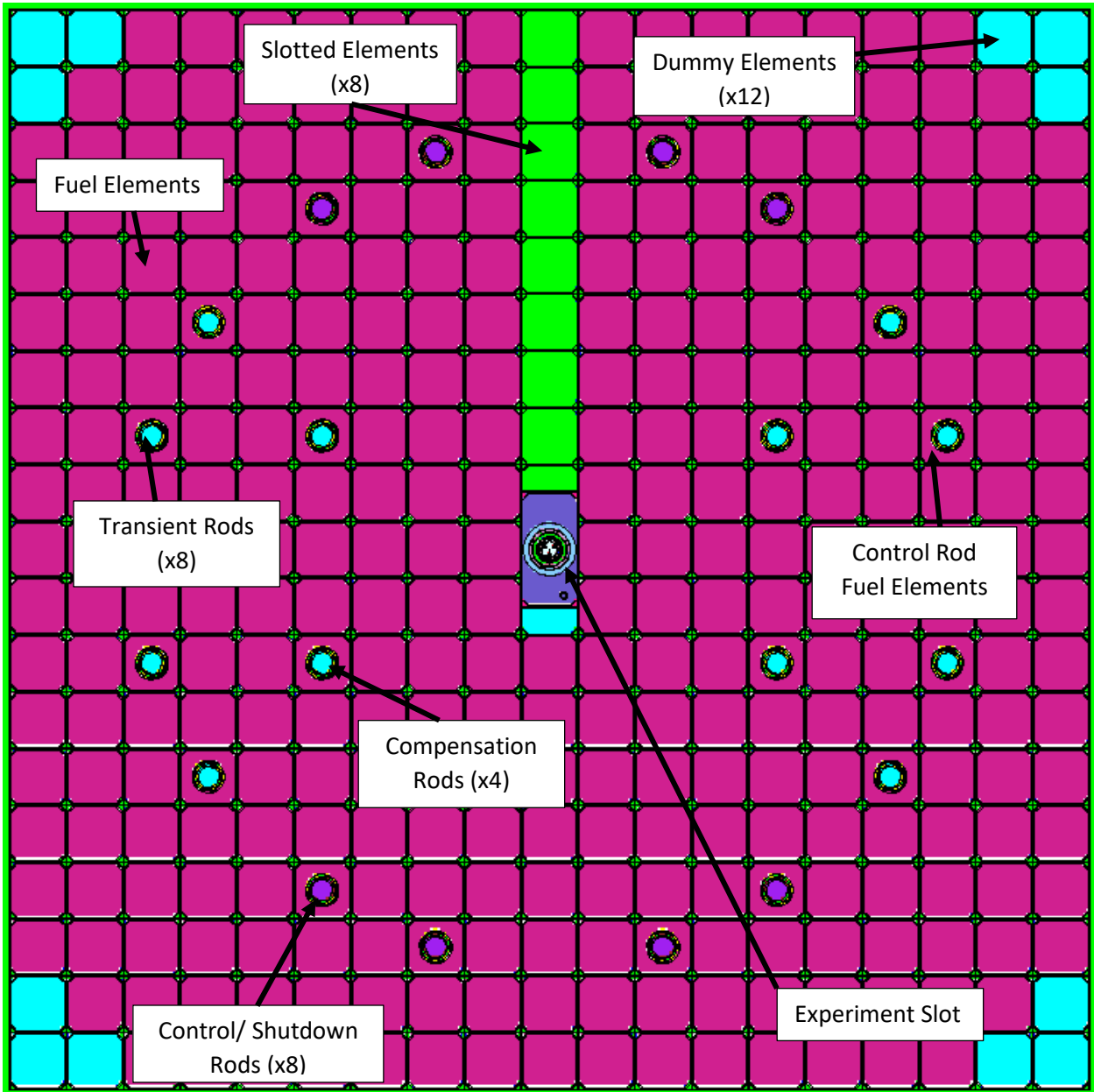


Figure 40: MCNP TREAT half slot core model.

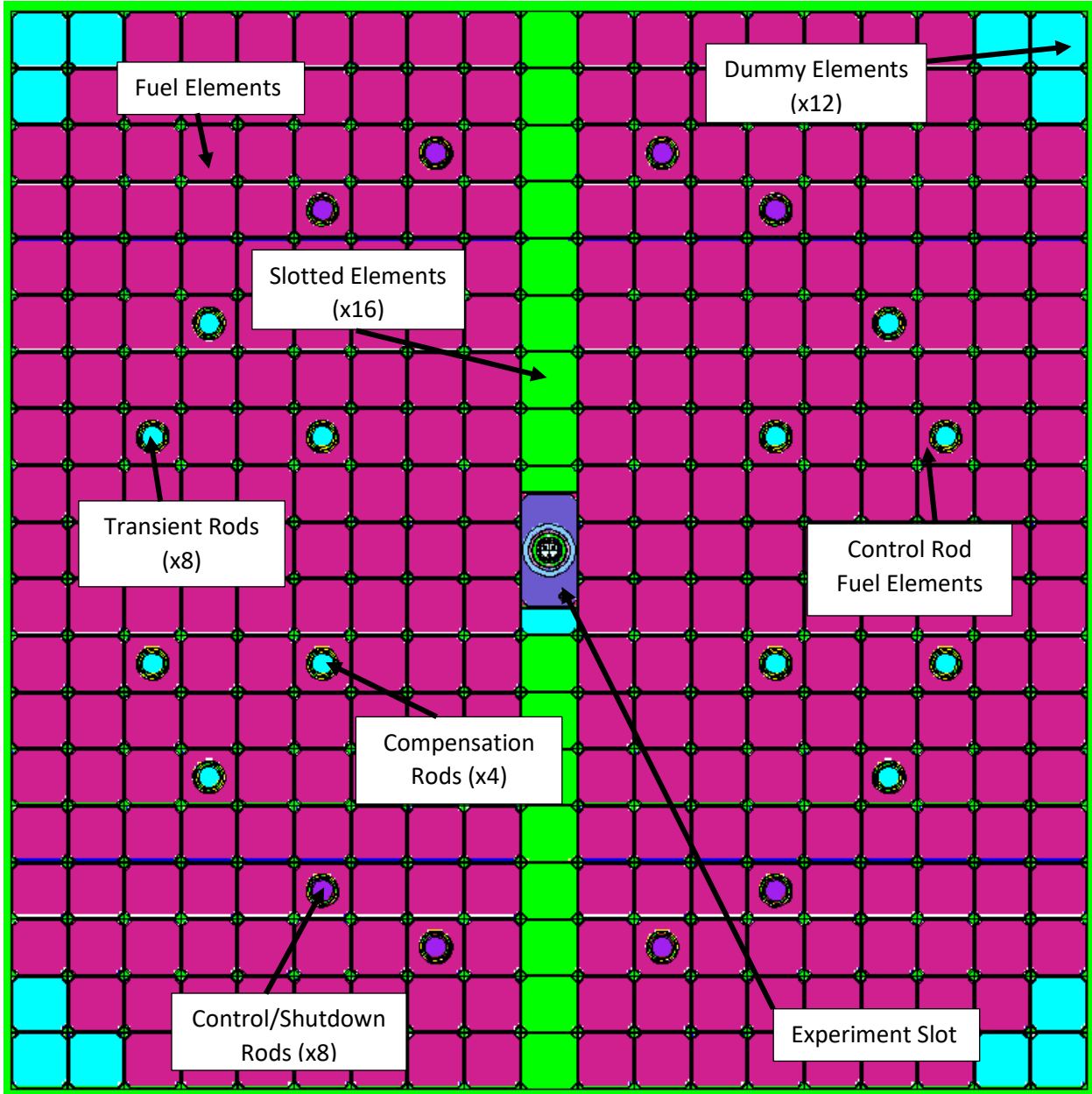


Figure 41:MCNP TREAT full slot core model.

HENRI Model

A model of the HENRI module was also created in MCNP 6 for use in this evaluation. The module was created as a universe (u=15) to allow easy placement within the TREAT MCNP 6 core array. The HENRI model consists of the control rod fuel assembly components as well as the gas thimble portion of the module as shown in Figure 36 and Appendix B. The driver tank, Figure

35, was not included as part of the model since the TREAT MCNP 6 validated core model does not extend past the top of the fuel elements, which is where the driver tank will reside during operation. In addition, the transfer line was also omitted from the module model. Due to the added benefit of the helium-3 in the system, omission of the transfer line was deemed acceptable and conservative for this evaluation. The vacuum line was also not included in the gas thimble model in MCNP, due to the fact that the vacuum line begins after the grid plate which is the lower limit of the TREAT MCNP core model.

The gas thimble modeled in MCNP 6 had some geometric simplifications where they would not have a significant impact on the final calculations. The HENRI gas thimble was modeled as a cylindrical pipe within the control rod fuel assembly. The pipe was an open-faced pipe, beginning at the top of the active core region, and terminating at the grid plate. The end of the pipe was modeled as a simple cap. The pipe model was split axially into six regions that represented the measurement locations of the equivalent Computational Fluid Dynamics (CFD) model which is discussed in greater detail in the next section. Each region was determined by taking the distance between each measurement point and dividing the region at the geometrical mean location. Since the data from the CFD work was limiting, and based on measurement points, these regions were chosen for ease of data inputs. A mathematical gradient of the data between two measurement locations could have been used as well, however, it was determined that it would add computational time for little improvement in the results for these scoping studies. The HENRI module was also divided radially into 7 cylindrical regions, each $\frac{1}{8}$ inch thick to support the annular evaluation, described in greater detail later.

The HENRI module used Zircaloy-4 (m22) for the outer tube. The control rod fuel assembly used the same materials as the other control rod fuel assemblies represented in the core.

Since the HENRI module contained various materials depending on the study being performed, each section below will specify the fill material used at each point in the study scope. No new materials, except for the helium-3 material, had to be added to the existing TREAT core model for this evaluation. Figure 42 and Figure 43 show the various components of the HENRI module modeled in this evaluation.

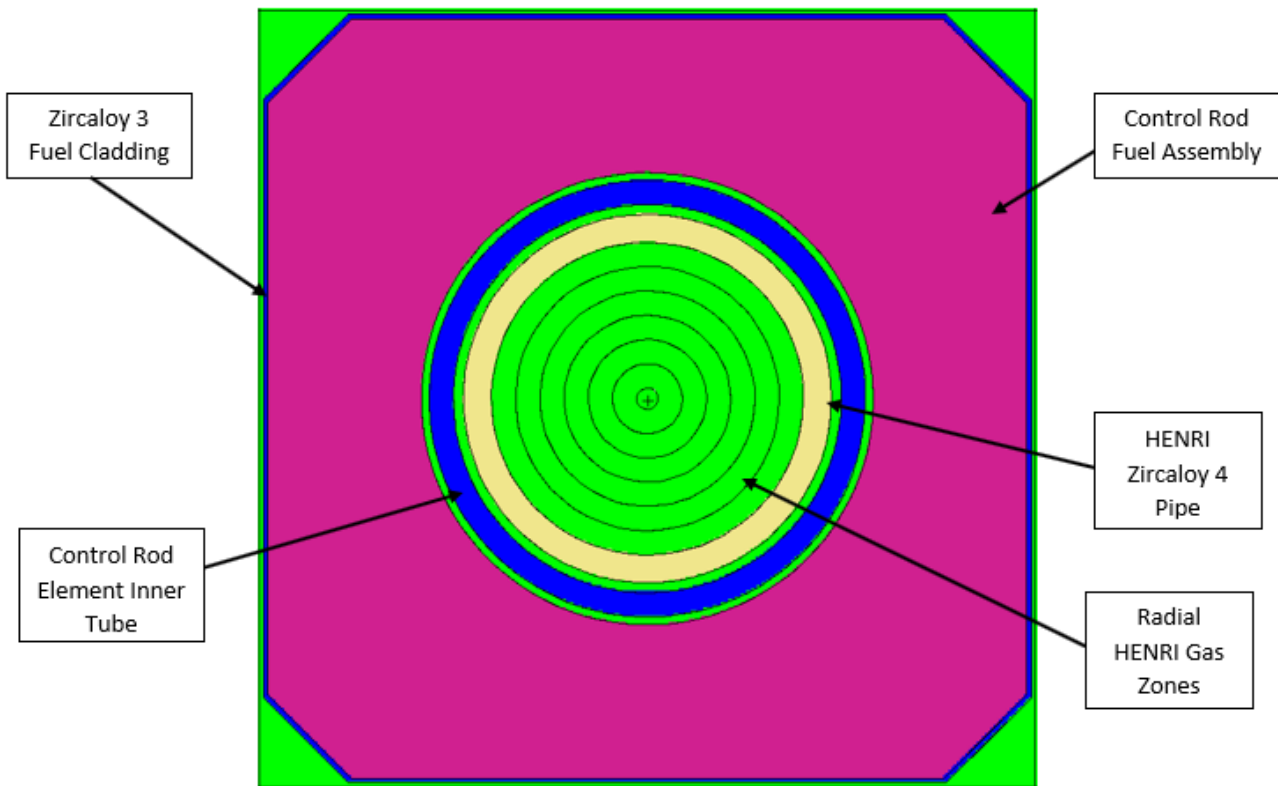


Figure 42: MCNP printout of the cross section of the HENRI system inside a control rod element (air filled).

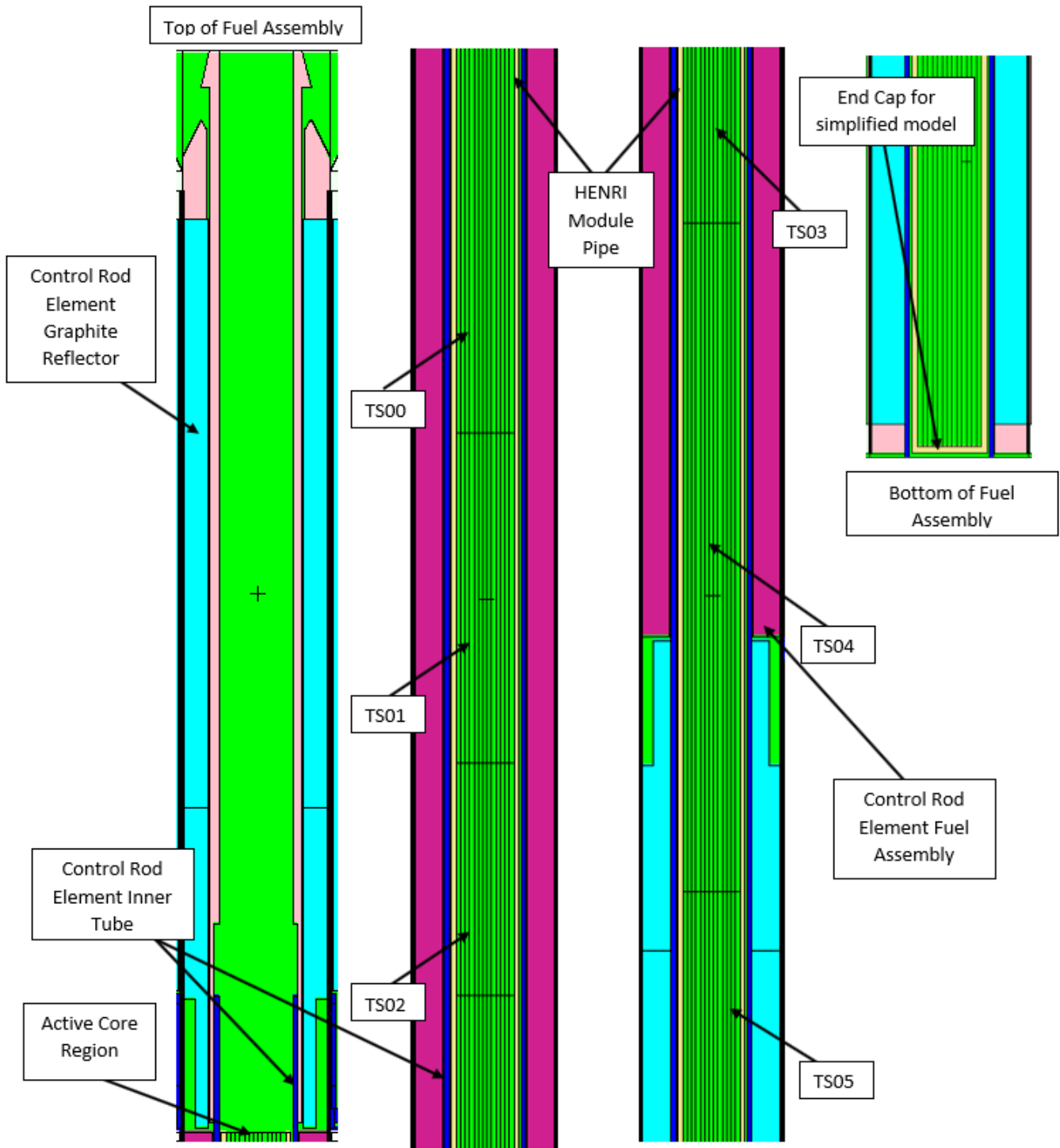


Figure 43: MCNP printout of the axial cross section of the HENRI system inside a control rod element (air filled).

4.4 Computational Fluid Dynamics

Helium-3 pressure data used for this evaluation, was provided by Oregon State University (OSU). A HENRI model, based on the input design discussed above, was produced in STAR-CCM+. STAR-CCM+ is a simulation software that allows for solving multi-physics computational fluid dynamics (CFD) problems [32]. The basic model assumed an initial pressure at room temperature within the driver tank (DTP), the simulation was then ran to model the gas flow through the transfer line and gas thimble. Based on gas flow, the model was used to produce pressure estimates at various locations and timesteps. Figure 44 provides the approximate locations used to gather the pressure data. Only data output from points TS00 through TS05, which correspond to the sections used in the HENRI MCNP model, were used in the evaluation.

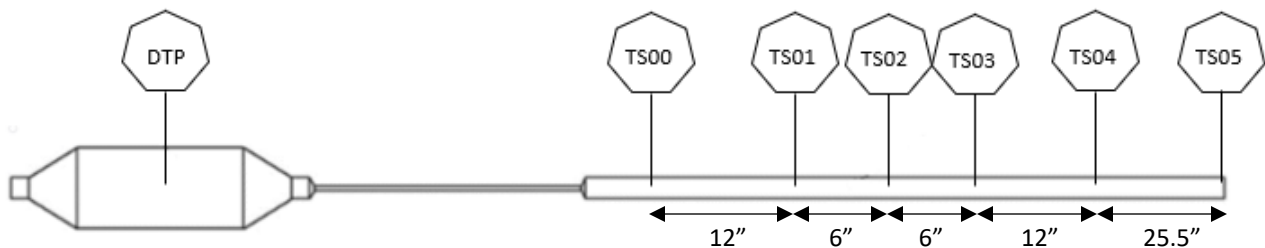


Figure 44: Approximate locations of the CFD data output.

The STAR-CCM+ model was validated using a full scale, out-of-pile, prototype of the HENRI system located at OSU. Validation of the STAR-CCM+ model was performed initially using helium-4 properties, the same gas used in the prototype. Pressure and temperature sensors were placed within the prototype in the same locations to that of the STAR-CCM+ model [33]. Once the STAR-CCM+ model produced results that matched the helium-4 prototype validation experiments, the model was modified to use helium-3 properties. The helium-3 model provided helium-3 pressure data, as a function of position and time within the system. Driver tank pressures were adjusted as needed to provide resulting pressure and temperature data to use in the HENRI

MCNP model. Because pressure is a function of temperature, the STAR-CCM+ model also produced expected temperatures as a function of location and time. Temperature data could not be validated explicitly by the experiment prototype due to the temperatures increasing faster than the resolution of the temperature instrumentation as a result of rapid movement of the gas.

Once the pressure and temperature data was received, the data was converted to a value that could be used as an input in MCNP, in this case hemium-3 density for the various HENRI in-pile cell cards. The densities were then converted to atomic densities with units atoms/barns-cm for each specific location in the HENRI MCNP model. [Equation 1](#) below was used to convert the pressure and temperature values to atomic densities, using the data provided from OSU’s STAR-CCM+ HENRI model.

$$N = \left[\frac{P_{xi}}{R * T_{xi}} \right] * N_a * \frac{1E^{-24} \text{ cm}^2}{b} * \left(\frac{1 \text{ m}}{100 \text{ cm}} \right)^3 \quad [1]$$

where

N = neutron density (atoms/b-cm)

P_{xi} = Pressure at timestep (x) and location (i) (Pascals)

R = Ideal Gas Constant (J/mol-K)

T_{xi} = Temperature at timestep (x) and location (i) (Kelvin)

N_a = Avagadro’s Number (6.022 x 10²³ atoms/mol)

It should be noted that [Equation 1](#) can be used to incorporate the temperature changes for each timestep at each location, however, for this study the neutron densities were determined assuming a 100°C (373 K). While the temperature datum was provided along with the pressure

values from STAR-CCM+, the datum could not be validated so 100°C was chosen as a starting point. Figure 45 through Figure 50 show example comparisons between the neutron densities at 100°C and the neutron densities including the temperature datum from STAR-CCM+ using [Equation 1](#). In most of the locations during the 5-millisecond time region, which is the region of study for the HENRI system, the neutron density at 100°C results in a higher atom density by almost 12%. This means that the neutron density at 100°C in the MCNP models are likely to overestimate the effectiveness of the HENRI system at TREAT. Since this observation was known up front the results of this evaluation took this into consideration as will be discussed in future sections.

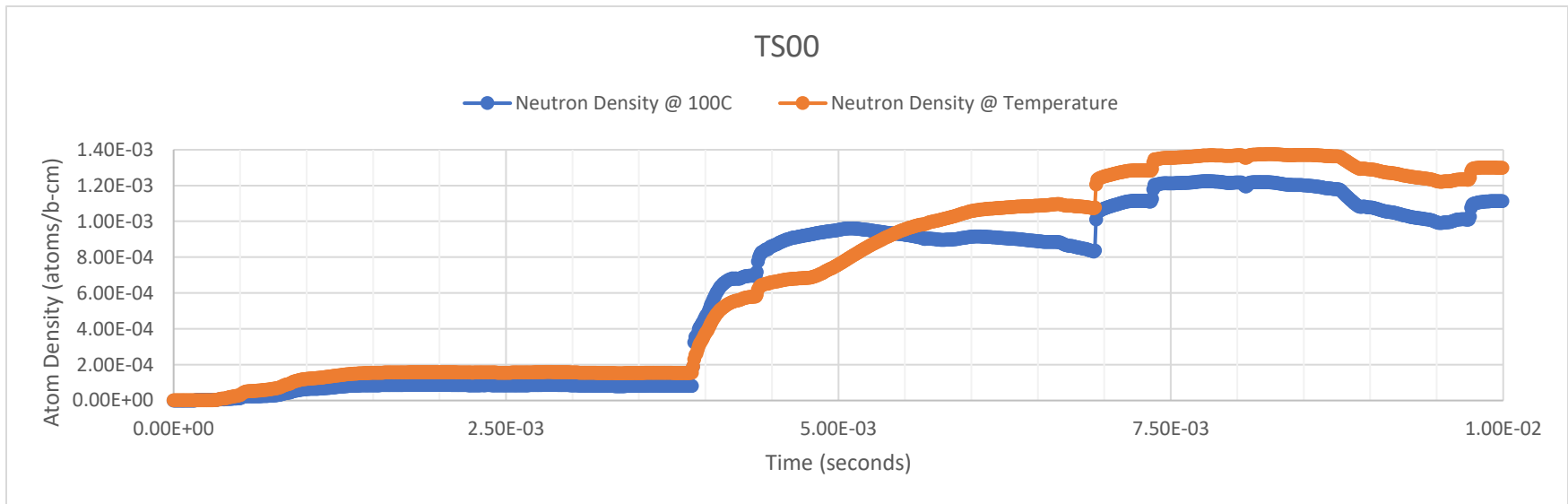


Figure 45: Neutron density comparison at TS00

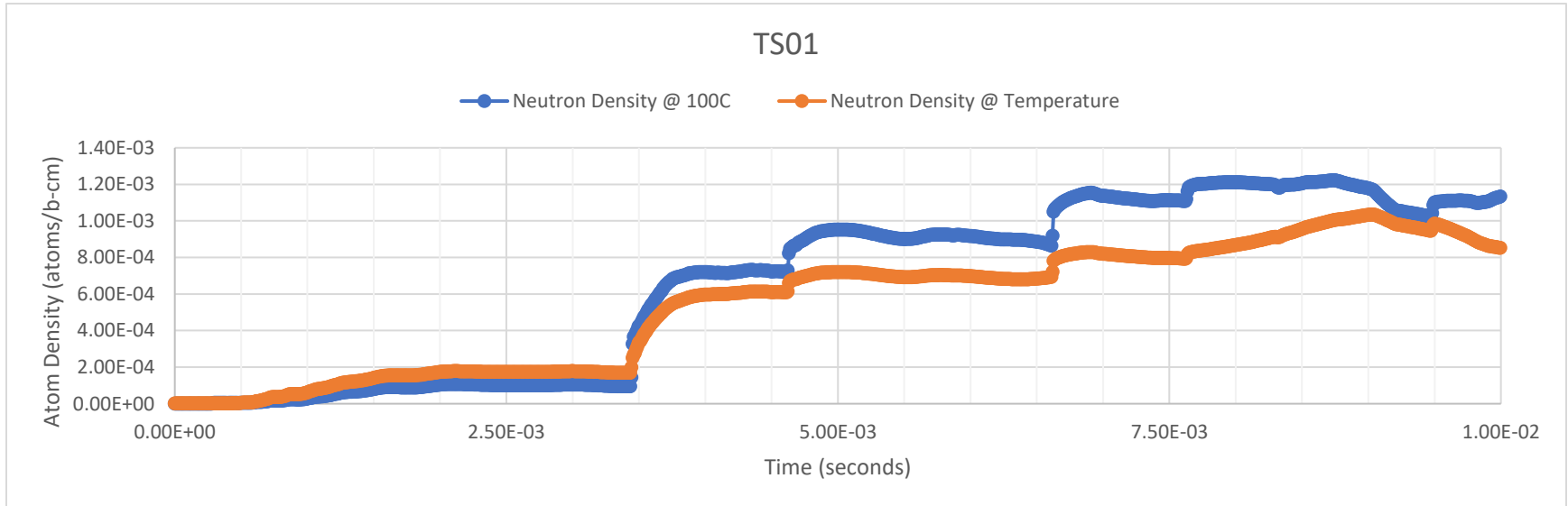


Figure 46: Neutron density comparison at TS01

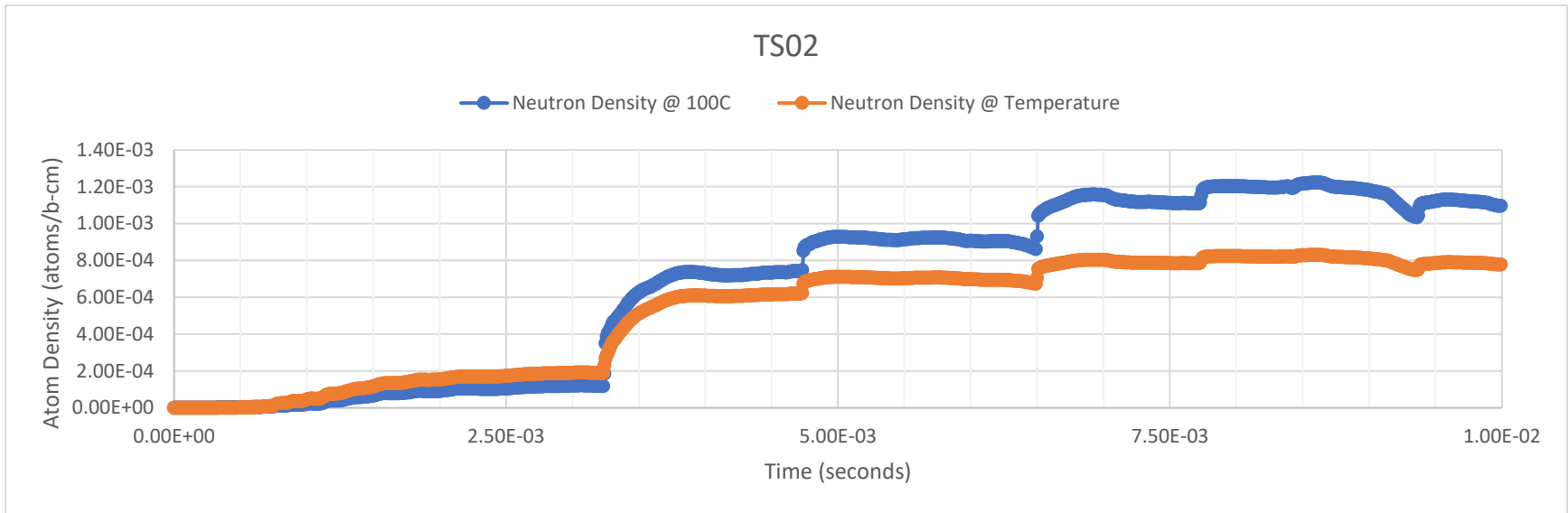


Figure 47: Neutron comparison at TS03

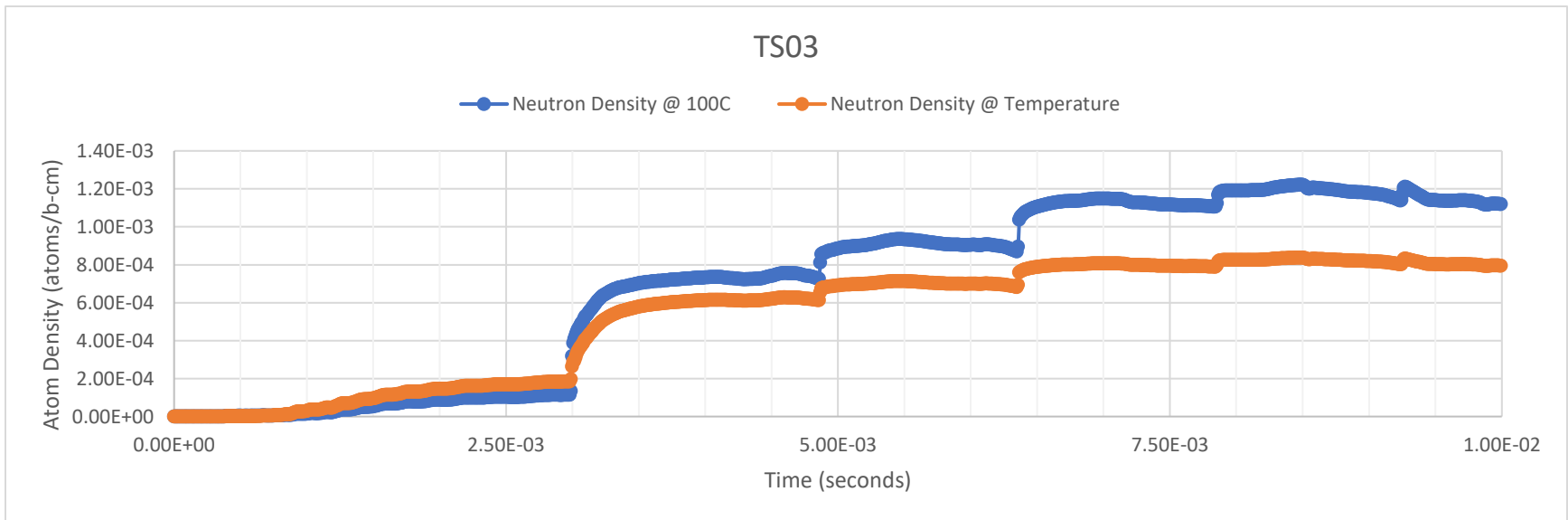


Figure 48: Neutron density comparison at TS03

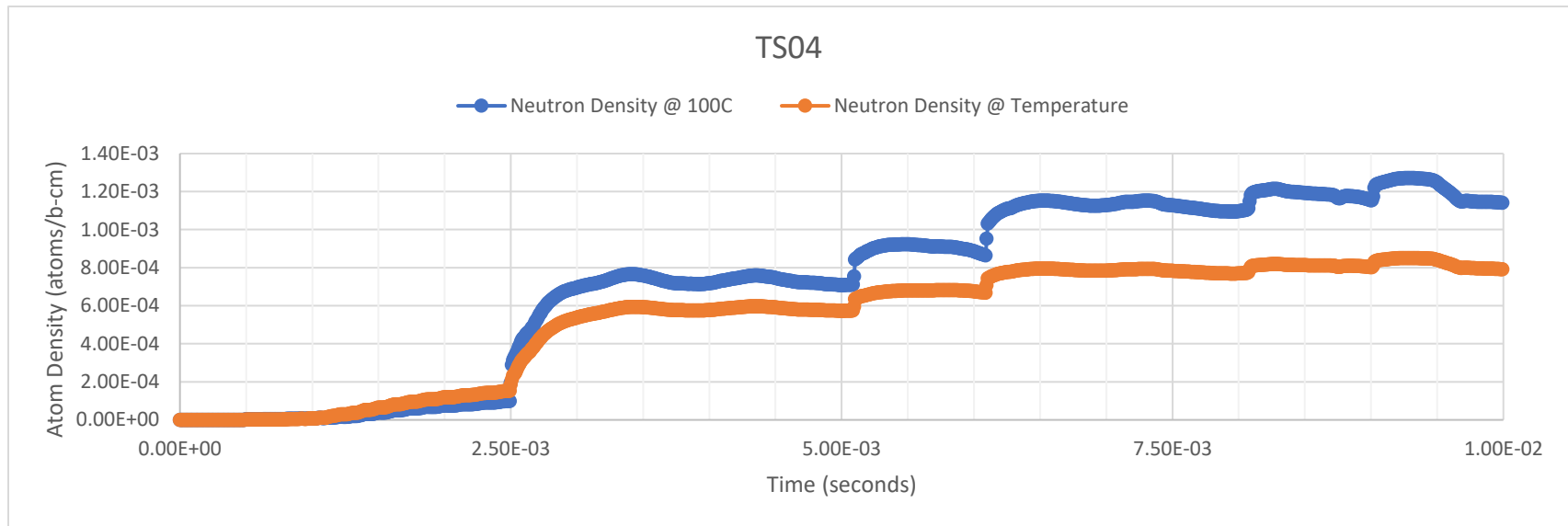


Figure 49: Neutron density comparison at TS04

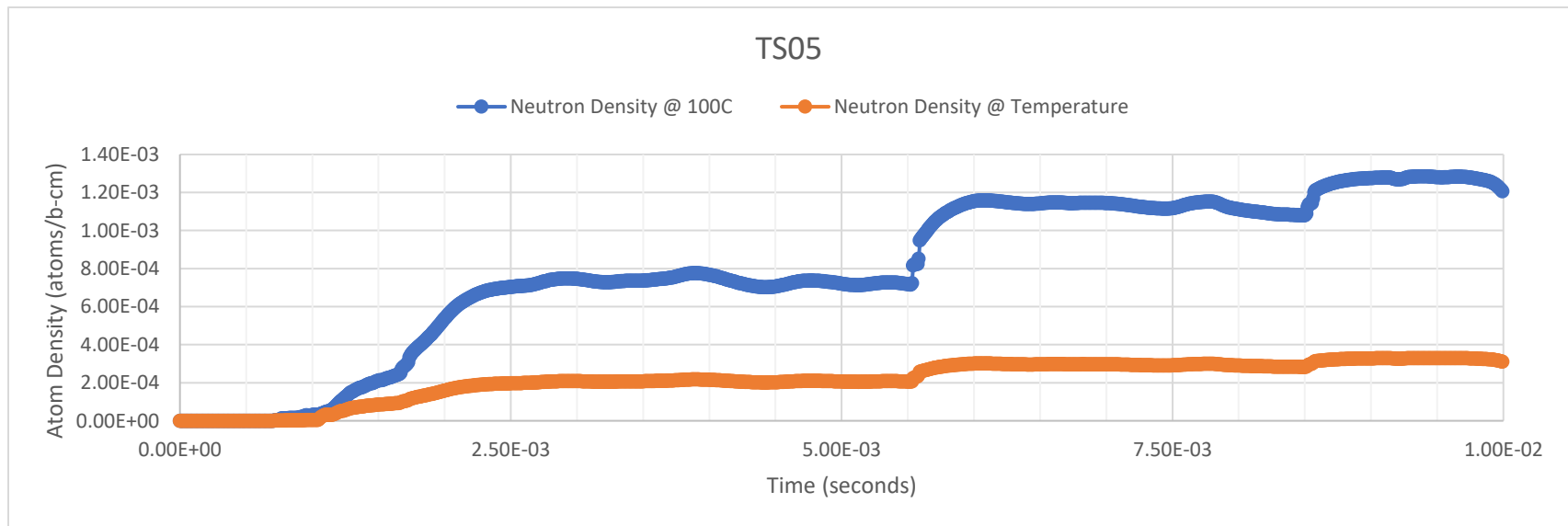


Figure 50: Neutron density comparison at TS04

After the atomic densities were found for each location and timestep, the data was truncated into millisecond timesteps for use in the MCNP modeling. The data was truncated using a MATLAB code that analyzed each row in the Excel file which contained the atomic density information for each location and timestep. If the row contained the desired timestep, every millisecond from 1 to 8 for example, it would copy that row and write it to a new sheet on the Excel file. The truncated data was then plotted against the original data set to determine if it was a good trend of the original. In some instances, the original CFD data had features that were not captured in the truncated data set and needed to be included, in these instances those timesteps were found from the original data and added to the truncated data manually. This datum was used to determine the number of runs that needed to be performed for each evaluation and was used to support the various cell cards that make up the helium-3 material in the HENRI MCNP files.

4.5 Reactivity Calculations

Reactivity calculations were evaluated by calculating the eigenvalues at two different core configurations and comparing them to obtain a reactivity difference, ρ . [Equation 2](#) was used for the following sections where reactivity was required to be calculated:

$$\Delta\rho \left[\% \frac{\Delta k}{k} \right] = \frac{k_2 - k_1}{k_2 k_1} * 100 \quad [2]$$

where

$\Delta\rho$ = change in reactivity

k_2 = k_{eff} at an altered state

k_1 = k_{eff} at the initial state

Temperature Assumptions for Reactivity Calculations

In addition to the temperature assumption made for the neutron densities described in the previous section, additional temperature assumptions were made for the MCNP reactivity calculations. This problem is ultimately a multi-physics problem in which as reactivity effects in the core change, so does the temperature. The temperature also changes differently between the core and the HENRI gas thimbles and the gas inside. MCNP alone is not suited for this type of evaluation as it only provides results on the eigenvalue and does not have the ability to also predict temperature. It is possible to force temperature effects in MCNP, however, by using temperature related cross section libraries. In order to do this accurately though a code such as RELAP, STAR-CCM+, or other thermal hydraulics code would have to be coupled to the neutronics to apply the correct cross section libraries.

Similar to ^{235}U , an increase in temperature results in the absorption cross section to decrease for helium-3. Figure 51 shows a comparison plot between the two. The lines in the graph represent the average neutron energies at 20°C and 600°C. In this temperature region the absorption cross section decreases linearly for both isotopes. Meaning that the ability for the helium-3 to absorb neutrons is decreased with higher temperatures. Note that the TREAT core itself, due to its negative temperature reactivity feedback, will also be reducing its ability to absorb and cause fissions within the fuel. While the impact negatively impacts the efficiency of the HENRI modules, the higher temperature also would reduce the reactivity in the core, ultimately leading to the end goal of a quicker reduction in reactivity and power in the reactor core.

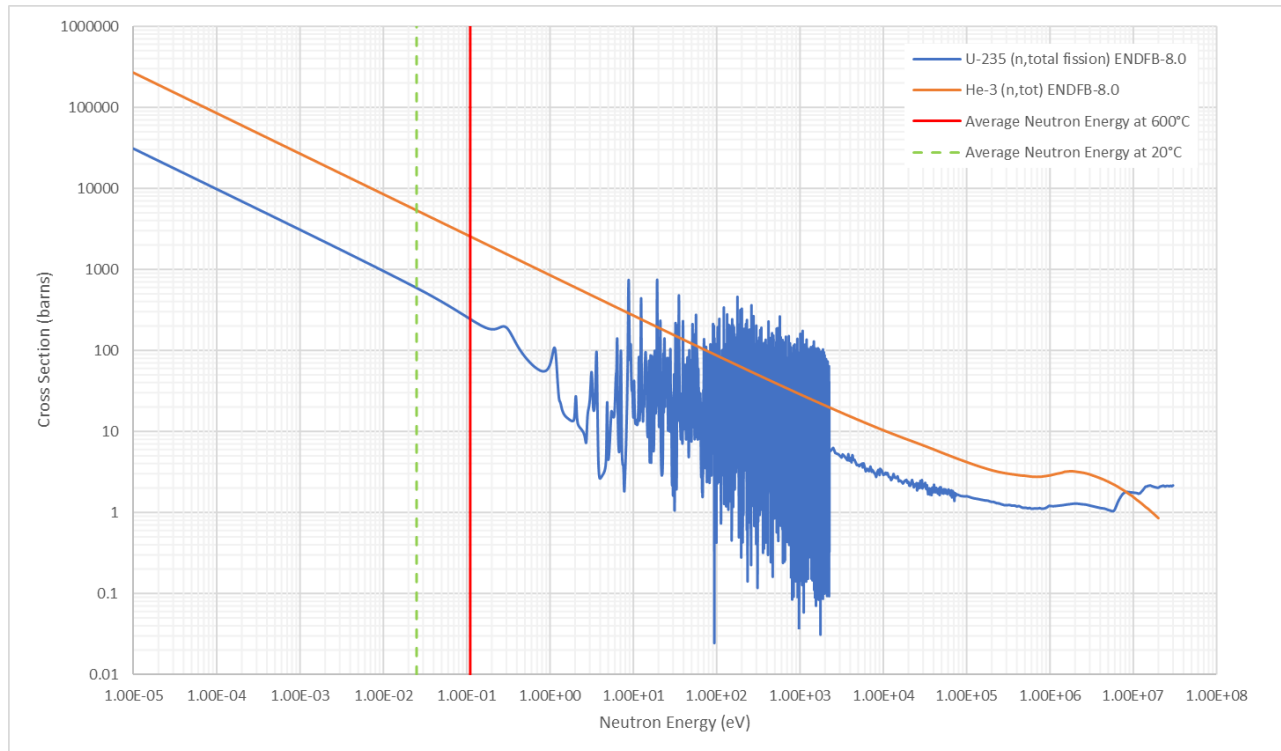


Figure 51: Temperature spectrum shift comparison for helium-3 and uranium-235

Since a thermal model has not been fully developed for the HENRI system at the time of this study to provide accurate temperatures of the core and the helium-3 gas, both of which impact the overall effectiveness of the HENRI modules, due to cross section changes, the results for this evaluation will be evaluated at cross sections at room temperature, 20°C. This will provide the desired information to support initial estimates and support initial design considerations. Further evaluation using coupled thermal and neutronics physics will be required for final results and safety evaluation but are outside the scope of this evaluation.

Rod Position Estimates

Rod position estimates were determined through MCNP simulation iterations to achieve k_{eff} close to 1.0000 for a steady state baseline, and 1.0466 for the 4.45% $\Delta k/k$ maximum pulse, when needed. For steady state and maximum pulse conditions, the compensation and transient rods were extended to their maximum position out of the TREAT core. Only the control rods are used to obtain the desired k_{eff} . All rod positions are rounded to the nearest hundredth of an inch as to be consistent with TREAT rod position readouts.

The HENRI modules were filled with air to simulate a steady state critical case and the 4.45% $\Delta k/k$ pulse case, both of which happen prior to initiation of the HENRI system. A 4.45% $\Delta k/k$ pulse was estimated to be the highest pulse based on reactor parameters and was used when a maximum pulse was needed in the simulations.

Quantity and Location of Modules Approach

A study was performed to look at the number of modules required to reach the desired negative reactivity insertion. In addition, the study included determining if location of the modules was important to the overall effectiveness of the system within the TREAT core. This study assumed a full slot core in order to provide maximum symmetry within the core.

To keep the core symmetrical for full or half slotted cores, it was determined an even number of HENRI modules should be used. Symmetry in the core ensures that the experiment location has sufficient number of neutrons for the desired testing at TREAT. Only two HENRI modules were used for the first two iterations and 1,000 psig helium-3 was assumed as the initial driver tank pressure for the STAR-CCM+ data provided. 1,000 psig was chosen based on a hand calculation and the original estimates for the in-core hardware volumes, see Appendix C, which

showed at that pressure the helium-3 atom density would be sufficient to reach the desired reduction in reactivity. Modules were placed in the F12 and O12 reactor grid locations for the first iteration of the double HENRI module system. The F12 and O12 locations were chosen based on the following:

- Each HENRI module would reside in a control rod fuel element
- The locations are symmetric east to west in the core
- The locations are near the highest flux locations for both a full and half slotted core.

The locations of the two HENRI modules for the second iteration are F10 and O10, similar to the initial iteration, these spots were chosen based on symmetry and high flux locations east to west as shown in Figure 52. Each block in the figure represents a location of a fuel element in the TREAT core with the numbers representing the fission tally from an MCNP run. The red to green color gradient in Figure 52 represents the flux profile within the TREAT core with red representing the highest flux locations and green representing the lowest flux locations. In addition to the flux map consideration the F10 and O10 locations were also chosen assuming they would be in RE fuel assemblies. As mentioned before, RE fuel assemblies are graphite filled fuel assemblies with an inner cavity. The letters are located at the north end of the core and the letters are shown on the west side of the core in Figure 52.

	A	B	C	D	E	F	G	H	J	K	L	M	N	O	P	R	S	T	U
1	0	0	2095	2099	2131	2140	2133	2122	2138	0	2155	2174	2219	2265	2284	2284	2320	0	0
2	0	2139	2110	2140	2150	2126	2067	2016	2125	0	2143	2069	2157	2254	2318	2342	2353	2438	0
3	2194	2181	2261	2326	2286	2179	2125	1365	2236	0	2253	1401	2221	2316	2471	2558	2541	2514	2615
4	2274	2337	2490	2587	2500	1545	2433	2496	2561	0	2586	2563	2542	1644	2710	2853	2807	2716	2763
5	2444	2542	2747	2899	2929	2890	2969	2994	2913	0	2944	3080	3101	3074	3174	3203	3096	2960	2975
6	2630	2740	2982	2226	3346	3422	3441	3373	3183	0	3215	3471	3597	3639	3621	2455	3370	3193	3187
7	2761	2902	3187	3458	3666	3769	3763	3630	3345	0	3376	3732	3930	3997	3950	3799	3596	3391	3366
8	2820	3003	2315	3649	3883	2773	3958	3770	3370	0	3400	3869	4131	2934	4164	3988	2613	3540	3507
9	2787	3053	3430	3779	4025	4131	4077	3810	3230	0	3247	3892	4244	4359	4281	4090	3867	3643	3604
10	2751	3072	3475	3835	4086	4191	4123	3818	3081	70	3089	3892	4294	4424	4333	4138	3916	3687	3643
11	2818	3077	3455	3806	4055	4164	4115	3858	3286	0	3314	3953	4287	4399	4328	4141	3903	3667	3622
12	2885	3059	2352	3703	3943	2819	4041	3871	3549	0	3587	3975	4213	2987	4242	4065	2657	3585	3543
13	2864	2988	3267	3537	3744	3861	3871	3768	3544	0	3580	3874	4042	4093	4043	3880	3665	3447	3416
14	2771	2856	3086	2292	3447	3533	3568	3528	3391	0	3428	3632	3730	3753	3721	2516	3451	3260	3248
15	2631	2678	2858	3007	3038	3004	3101	3167	3131	0	3162	3252	3245	3195	3285	3304	3190	3041	3049
16	2471	2478	2604	2696	2606	1617	2564	2666	2791	0	2817	2744	2688	1726	2830	2965	2907	2800	2844
17	2361	2307	2363	2419	2387	2293	2265	1481	2483	0	2507	1524	2380	2457	2604	2680	2647	2611	2706
18	0	2237	2184	2203	2232	2243	2226	2229	2422	0	2445	2301	2352	2423	2465	2475	2472	2550	0
19	0	0	2137	2120	2189	2264	2326	2394	2507	0	2538	2482	2472	2474	2460	2440	2460	0	0

Figure 52: Flux tally map of a full slot TREAT core.

Three more iterations were performed, this time using four HENRI modules in the core. Similar to the double HENRI module system, each HENRI module assumed a driver tank pressure of 1,000 psig. The locations were chosen based on symmetry and the relatively high surrounding flux. Table 7 provides a summary of the locations evaluated for the two HENRI and four HENRI configurations.

Table 7: Summary of configurations used in the study of location and quantity

Number of HENRI modules	Location
2	F12 & O12
2	F10 & O10
4	F9, F11, O9, & O11
4	E9, E11, P9, & P11
4	G9, G11, N9, & N11

The baseline full slot core MCNP model of TREAT was used in this evaluation. The model was modified for each iteration by placing the desired number of HENRI modules, filled with helium-3, in the respective locations to determine the impact of location and quantity of modules. Each iteration contained eight models to represent the helium-3 density changes, from the CFD modeling, in millisecond timesteps from 1 to 8. The only change between the set of models for each iteration was the associated helium-3 density occurring at each location within the HENRI module at the specified timestep. Each model was performed to produce a k_{eff} for the corresponding time step. Using the k_{eff} values from each model in the iteration as k_2 and then using the k_{eff} value from the critical baseline case as k_1 , [Equation 2](#) was used to determine the negative reactivity addition for each timestep.

For all the quantity and location models that were generated for the five cases the MCNP models were set up with an initial guess of one for the k_{eff} value, 110 total cycles skipping 10, and 1000 neutrons per generation. This was sufficient for all models and was verified by reviewing the Shannon entropy of the source distribution and the k_{eff} convergence plots. These plots can be used

to ensure the best calculations without contaminating the results from errors from initial kcode calculations. Figure 53 shows an example plot of the Shannon entropy of the source and k_{eff} convergence plot for one of the evaluations of four HENRI modules. Note that roughly 7 cycles are needed before convergence is met, skipping 10 cycles is therefore sufficient for the quantity and location analysis performed.

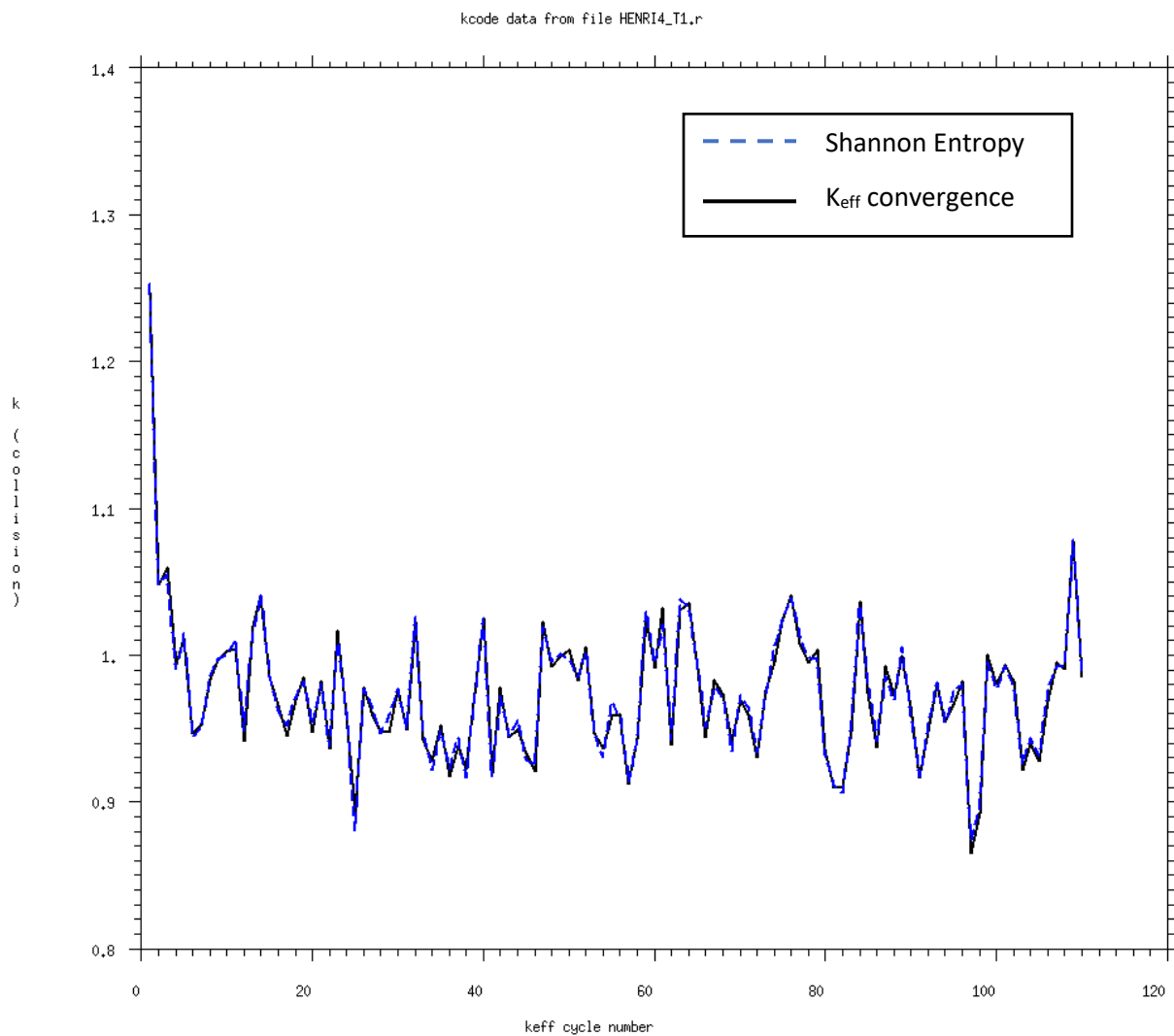


Figure 53: Example Shannon entropy and k_{eff} convergence plot for quantity and location models.

Reactivity Worth of the System

The objective of this study was to determine the effectiveness of the system during operation to validate that we are able to reach the negative insertion requirement. To determine the worth of the entire HENRI system during operations a pseudo pulse was performed using a timestep approach in MCNP. Initially a steady state model timestep approach was taken where the core was simulated, through the movement of the control rods in the model, to be at a critical state and each timestep from 1 to 5 milliseconds was ran from that critical location, similar to the approach used for the location and quantity study above. This resulted in a representation of the clip that started at the critical eigenvalue ($k_{\text{eff}} = 1$) and then decreased to be more and more subcritical as the timesteps went on. It was later determined that a pseudo pulse approach would be better because it was a closer representation of the actual use of the HENRI system, starting at the peak of a pulse, as well as it centered around the critical eigenvalue which provide less error in the results. This was determined through the bias study performed and discussed in greater detail below. The bias study compared the MCNP values to rod worth data that has been measured at TREAT to provide the bias between MCNP outputs and what can be measured at TREAT. A TREAT half-slotted core was used in this evaluation as that is the expected core configuration for experiments that will use the HENRI system. The half-slotted core is desired as it provides more reactivity in the beginning of the transient that is being clipped. In addition, the driver tank pressure was altered in the CFD model to provide inputs into the MCNP model to determine the lowest pressure required to get desired results.

The pulse test used the 4.45% $\Delta k/k$ maximum pulse MCNP model with a half slot core. This pulse was chosen based on the literature review presented in the Maximum Initiating Reactivity for a Pulse section above and is based on the hardware limit for reactor period of 0.023

seconds. Keeping the rods at the same location, to produce the 4.45% $\Delta k/k$ pulse, the model was modified by placing the HENRI modules in the desired locations. The HENRI modules were then filled with the helium-3 atom densities at their specific location and timestep, similar to the quantity and location study above. Each model in the iteration was then ran to provide a k_{eff} value. Reactivity effects for each timestep in the iteration were then determined by taking the k_{eff} for each timestep as the k_2 value and the baseline critical case was set to k_1 in [Equation 2](#) above. Figure 54 provides a summary of the approach taken to determine worth of the system.

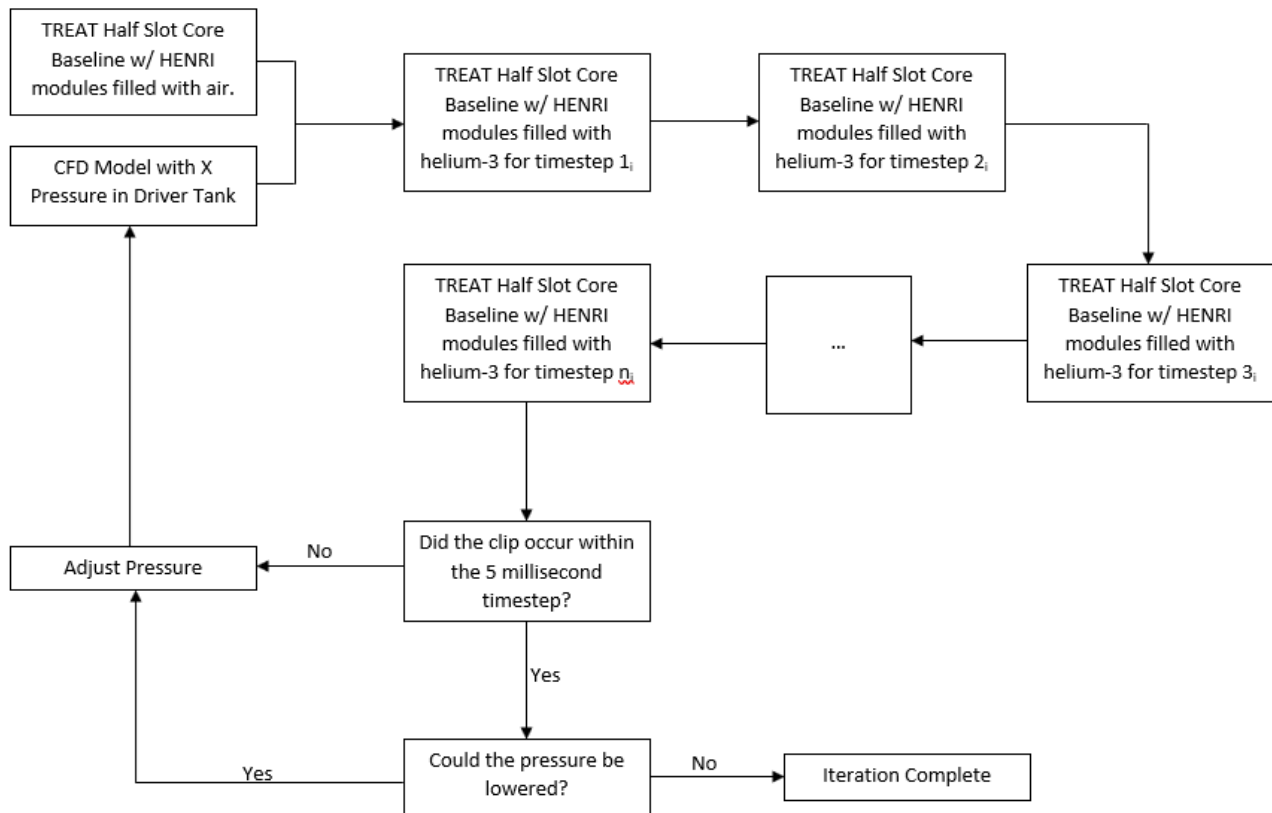


Figure 54: Flow of the iterative process used to determine the worth of the HENRI system along with the final driver tank pressures.

In addition to the above model changes, an fmesh neutron tally (fmesh14) was created, over the entire core, to provide images at each timestep in the iteration as a graphical representation

to check that reduction of the fissions in the core is actually occurring, which is what is expected to happen when firing HENRI. The fmesh is not intended to produce quantitative results, but it does provide qualitative evidence that the reactor is producing less neutrons and is useful for demonstrations. Figure 55 provides an example of the fmesh tally used in the model.

```
C
fmesh14:n   geom=xyz   origin=-100.0 -100.0 -122.0
            imesh=100.0   iints=100
            jmesh=100.0   jint=100
            kmesh=122.0   kints=100
C
```

Figure 55: Example fmesh tally for qualitative results.

For the reactivity worth iterations, the MCNP models were set up with an initial guess of one for the k_{eff} value, 250 total cycles skipping 150, and 3,500,000 neutrons per generation. This was sufficient for all models and was verified by reviewing the Shannon entropy of the source distribution and the k_{eff} convergence plots as mentioned above. Figure 56 shows an example plot of the Shannon entropy of the source and k_{eff} convergence plot for one of the pulse models. Note that it appears that after 5 to 10 cycles convergence is met but looking closely, there is a slight rise from 5 to 105. So approximately 105 cycles need to be skipped before convergence is met, skipping 150 cycles is therefore sufficient for the quantity and location analysis performed.

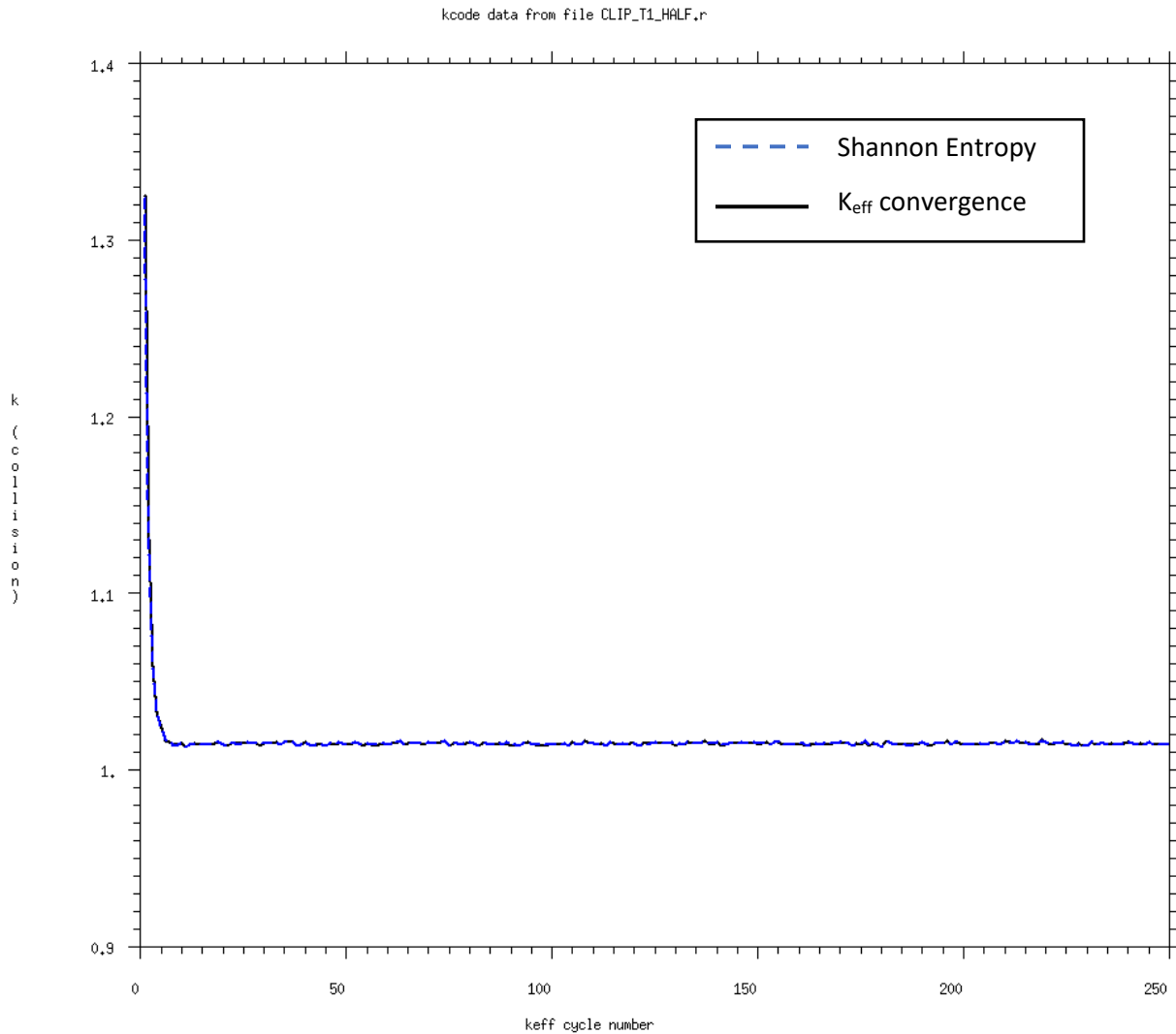


Figure 56: Example Shannon entropy and k_{eff} convergence plot for reactivity worth calculation models.

Annular Evaluation

This evaluation was performed to determine if, from a neutronics standpoint, an annular gas thimble design could be used in place of the cylindrical gas thimble design described earlier and determine the effectiveness of the attenuation per radial length of the helium-3. Helium-3 is known to have self-shielding and is very expensive to produce which makes any reduction in the amount of gas desirable from a programmatic cost standpoint.

As mentioned in the HENRI MCNP model description, the HENRI gas thimble was divided into 1/8-inch-thick radial zones within the gas portion of the model. This was done specifically to support the annular evaluation study. 1/8-inch-thick zones were chosen to keep pipe sizes consistent for ease of manufacturing the modules. F2 neutron tallies for the outer zircaloy pipe and each radial gas zone (F2 through F72) were used to determine the average neutron flux crossing each surface. The F2 tally tracks the flux contributions of particles that cross a surface of a certain weight and angle normal to the surface [34]. In other words, the tally provides the average number of neutrons passing each surface within the gas region of the HENRI module for each radial zone. The F2 tallies were also set up to group the neutrons based on their energies in order to evaluate only the neutrons at energies that could be captured by the system and exclude the tally of higher energies. Due to the radial length of the system, only neutrons at certain energies have the potential to be absorbed by the helium-3. One issue with the F2 tally, however, is that it averages all neutrons that cross the surface, both incoming and those scattered back across the surface. For this evaluation it was important to only add the incident neutrons to the tally and not include the backscattered neutrons, otherwise the results would not accurately represent the efficiency of each gas zone. To differentiate those neutrons that are incident from those that are backscattered, a cosine card was used in conjunction with each F2 tally. The cosine card can be used to create angular bins with respect to the positive normal to the surface at the entry point of the particle. The bins are set up from 180° to 0° . Due to the unfamiliarity of the cosine card, a simple MCNP model was created to ensure understanding of what angle bins would produce only the incident neutrons for each zone. This was done by taking a right circular cylinder normal to the z-axis, with arbitrary radius of 10 cm, and height of 20 cm. The cylinder was then divided with

a plane normal to the z-axis. This cylinder was then placed into a sphere of 40 cm. Figure 57 shows a schematic of the geometry and axis.

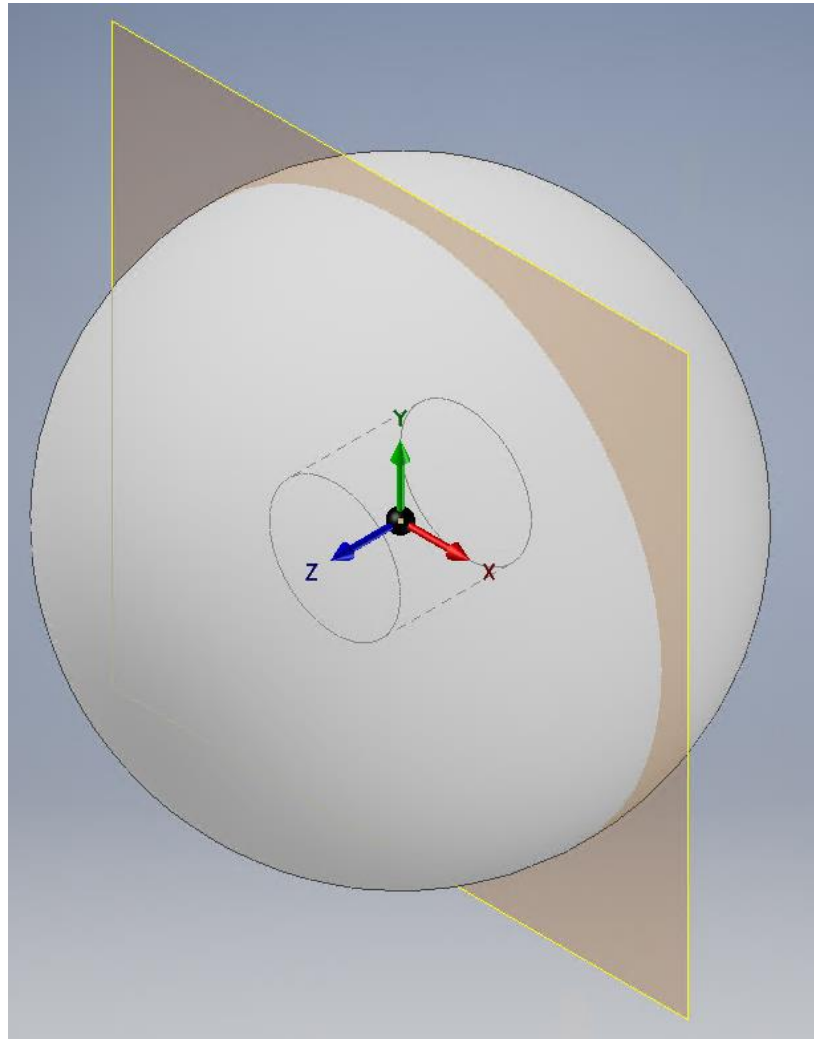


Figure 57: Computer generated geometry used for the cosine tally card test.

A source was placed at $(0,10.1,0)$ with a vector of $(0,-1,0)$. By setting a vector of -1 in the y-direction it ensures that the source can only act in that direction. This creates neutrons that are directed towards the center of the cylinder from outside the cylinder, similar to what would occur to the HENRI module inside the reactor core. An F2 tally was set up with the cosine card with angle bins, 180 to 90 and 90 to 0 across the radial cylinder surface, similar to what was proposed for the annular design MCNP cards. The cells were set up so that the sphere, not including the

cylinder, had importance of 1 and all other cells had an importance of 0. Giving the sphere an importance of 1 allows for the source to be distributed and traced through the surface of the cylinder, however, giving the cylinder an importance of 0 means that once the neutrons enter the cylinder they are no longer tracked or tallied, creating a “non-backscattering” zone. This, therefore, would provide a tally with a single angle bin having tally results and all other bins having no tally results. That angle could then be used in the actual HENRI MCNP model to determine the angle bins needed for the angular design study. Appendix D provides an example of the input MCNP model for this cosine test.

Once the MCNP model was set up with the correct angles, a mean free path evaluation was performed for neutrons in helium-3. As mentioned earlier, only specific neutron energies have the potential to be absorbed by the HENRI system based on the helium-3 being located in a cylinder with an axial diameter of 1.61 inches. To determine what energies could be captured in HENRI from the available volume of helium-3 the mean free path over all energies was determined based on [Equation 3](#).

$$\lambda = \frac{1}{\Sigma_{ti}} \quad [3]$$

where,

λ = mean free path (cm)

Σ_{ti} = macroscopic cross section per energy i (cm^{-1})

The macroscopic cross section, or the probability of interaction per path length, was determined using [Equation 4](#),

$$\Sigma_{ti} = (\sigma_i * 10^{-24}) * N \quad [4]$$

where,

σ = cross section per energy I (b)

N = atom density (atoms/b-cm)

ENDF/B-VII.1 helium-3 neutron total energy dependent cross-section data [35] was used to provide the cross-section data used in [Equation 4](#). The datum is graphed in Figure 58. The atom density value was determined by taking the average neutron density from the CFD model for the 5-millisecond timestamp at a driver tank pressure of 250 psig. The 5 millisecond timestamp data was used as this is anticipated to be the highest density of helium-3 during the desired clip time. The average was used for conservatism in the calculation because all atom densities will be seen over the timeframe of the HENRI clip.

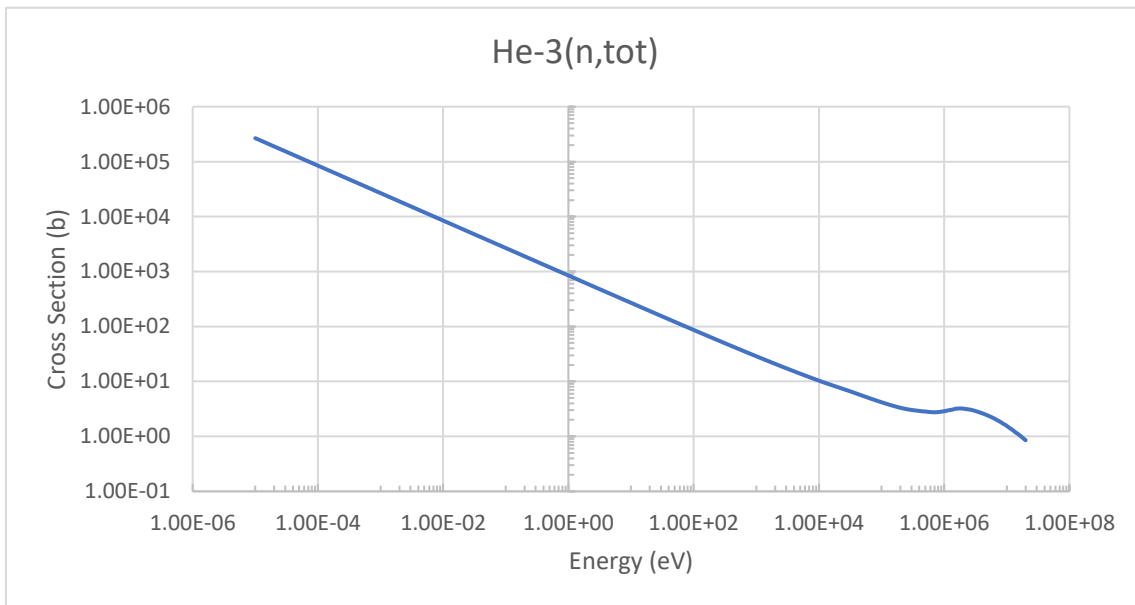


Figure 58: ENDF/B-VII.1 helium-3 neutron total energy dependent cross section data vs energy.

Once the macroscopic cross section was determined, [Equation 3](#) was used to determine the mean free path over the energies from 0.0002 eV to 2 eV. This range was chosen arbitrarily to capture enough data points that the cross sectional length of the HENRI thimble would be captured.

The values were then converted to inches to determine up to what energy, in eV, the HENRI system could potentially absorb.

The MCNP F2 tally results were summed up from 0 eV to the maximum energy that can be captured in the helium-3 at each surface. These values were then compared against one another to determine the max efficiency point. In other words, the amount of helium-3 needed to absorb an acceptable amount of neutrons compared to the volume of helium-3 in the system. An MCNP model was then created using the resulting module location, as determined by the quantity and location evaluation. The model was identical to the HENRI model described above with the exception that the inner zones, determined to not be needed, were filled with air.

To provide additional visuals, a fmesh of a single HENRI module (Fmesh4) was created to visualize the absorption of neutrons across each surface. The MCNP input can be seen in Figure 59.

```
c
fc4      Absorption within the HENRI system
fmesh4:n  geom=rzt  origin=20.32 40.64 -121.263
          imesh=2.8702  iints=400
          jmesh=242.526  jints=1000
          kmesh=1  kints=50
fm4      1  11  -2
c
```

Figure 59: Example fmesh used for as qualitative evidence for the annular evaluation.

For the annular evaluations, the MCNP models were set up with an initial guess of one for the k_{eff} value, 250 total cycles skipping 150, and 3,500,000 neutrons per generation. This was sufficient for all models and was verified by reviewing the Shannon entropy of the source distribution and the k_{eff} convergence plots as mentioned above. Figure 60 shows an example plot of the Shannon entropy of the source and k_{eff} convergence plot for one of the pulse models. Note

that it appears that after 5 to 10 cycles convergence is met but looking closely, there is a slight rise from 5 to 50. So approximately 50 cycles need to be skipped before convergence is met, skipping 150 cycles is therefore sufficient for the quantity and location analysis performed.

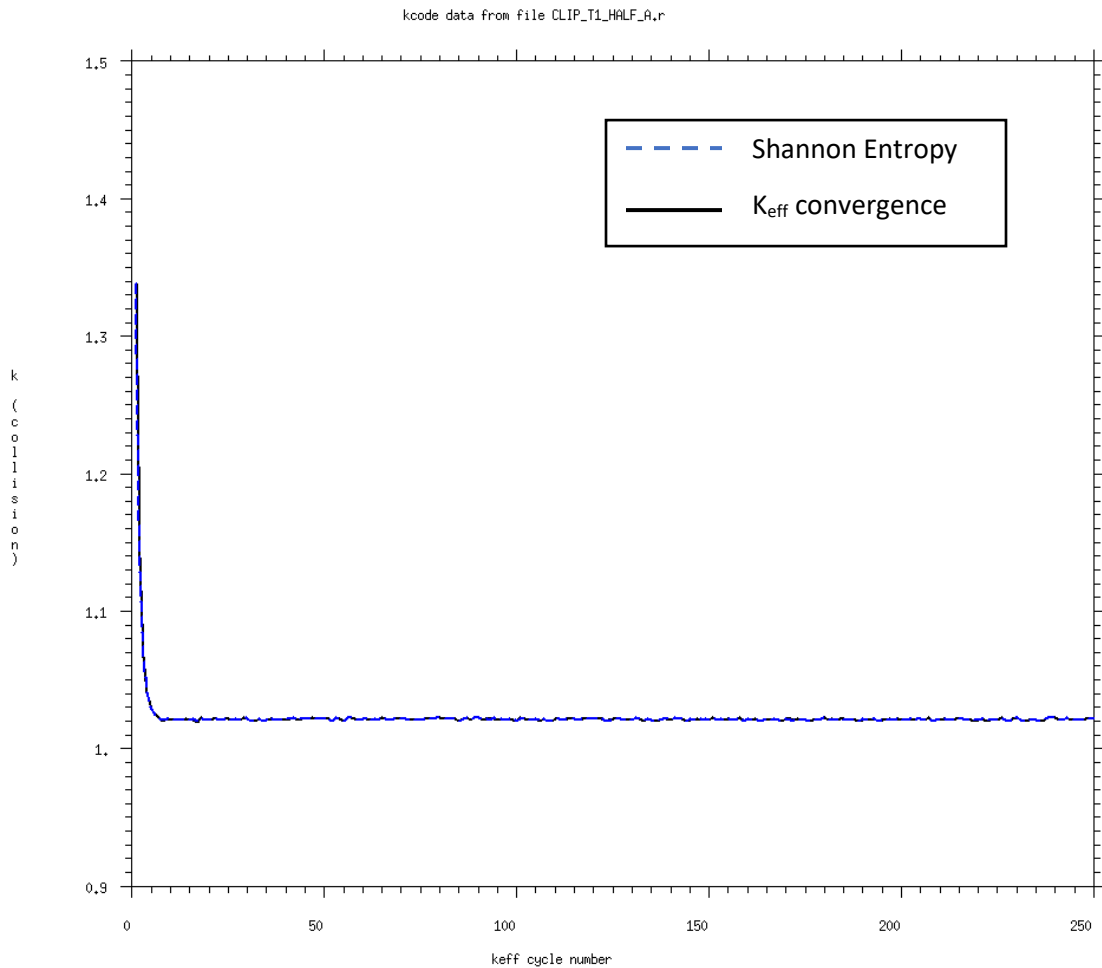


Figure 60: Example Shannon entropy and k_{eff} convergence plot for annular models

4.6 Model Inaccuracy Calculations

Any result, whether it be determined from a code or from actual instrumentation of a real-life event, there is always inaccuracies in measurements. In all these evaluations MCNP was used to evaluate the effect of a variable change in each specific study. During some of these studies it became very apparent that to have confidence in the results, there was an inaccuracy in the model

that needed to be determined and applied to the results to completely understand and be able to apply the values produced from MCNP for each of these studies. This inaccuracy was hypothesized to be the variation from actual measured results to the outputs from MCNP. Additionally, it is known that there will be some inaccuracies by the measurement tools used by TREAT to capture certain data that was used as a comparison, however, since the same instrumentation will be used to measure the effectiveness of the HENRI system, the inaccuracies of the measurement tools would be the same for the HENRI system and not a factor in the actual running of the HENRI system. As mentioned before, STAR-CCM+ was used to provide pressure and temperature data, which in some cases could also produce inaccuracies in the results, however, due to the validation of the models to a real-life experiment prototype, it was determined that the majority of the inaccuracies had to come from the MCNP evaluations, which was the focus for this model inaccuracy evaluation.

MCNP appeared to provide reasonable results for reactivity effects when close to the critical eigenvalue ($k_{\text{eff}}=1$), or the critical TREAT core. As the eigenvalues diverged from critical, the inaccuracies appeared to increase, when compared to as-measured data based on an initial study. The subcritical eigenvalues ($k_{\text{eff}}<1$) and supercritical eigenvalues ($k_{\text{eff}}>1$) varied in inaccuracies even being the same distance from the critical eigenvalue. Figure 64 and Figure 65 in section 5.2 show these differences. It is a common understanding that MCNP provides reliable results close to a critical eigenvalue, however, the further the eigenvalue diverges from one the more error is applied.

For a subcritical reactor the shape of the flux distribution is driven by the source. This impacts the rod worth in the system. In MCNP a KCODE calc moves the fission source as it computes each generation as if the system is critical and no source is present, even when using a

sub-critical model. In addition, a real subcritical reactor does not have a fundamental mode. When using MCNP, however, the KCODE calculation produces an artificial fundamental mode for subcritical configurations. This is a reason that the error for a subcritical system, removing reactivity, is in most cases larger than critical or super critical configurations using MCNP. When looking at why an error increase occurs the further away from the critical eigenvalue in the super-critical configuration, no literature could be found. The only comparison that could be found was the use of the dynamic method, used by MCNP, to that of the classroom taught k-static method [36]. Regardless of the evidence to support the causes of the bias, determining the model inaccuracies was still desired to support results.

Determining the best method to characterize the model inaccuracies in the MCNP models was not trivial and probably provided the most issues in this entire evaluation. Every core at TREAT is characterized before use to determine the worth of each control rod which is used for various calculations throughout operation of the facility. At least three different methods were investigated, using the rod worth data, to determine the best approach. Each approach is described below in enough detail to represent the issues encountered and the final approach.

Method #1

The first method used to characterize the model inaccuracies was a comparison between the compensation rod worth measurements, see Appendix F, measured at TREAT and the values produced by MCNP. A baseline full slotted core MCNP model was used to create a baseline, with a previously characterized vehicle, MIMIC-N, in the center location of the core. The transient rods and the control rods were banked at their maximum “out-of-core” location for this study. The four compensation rods were all placed at a critical baseline location of 26.5 inches into the core. This critical location had been verified based on operational data with MIMIC-N inside the core. The

compensation rods were used for this evaluation due to their close proximity radially, within the core to that of the expected HENRI modules. Room temperature cross sections were used for this evaluation as rod worth measurements performed at TREAT do not cause an increase in temperature as the core stays critical so no increased temperature cross sections were needed. The goal was to limit additional inaccuracies introduction that might appear from the other rods being located further from the center of the core. Additional MCNP models were created with the compensation rod locations at 21.5, 16.5, 11.5, 6.5, 1.5, and completely inserted into the core. Each k_{eff} value was compared to the baseline model to determine the reactivity of each configuration. These reactivity values were compared to the actual measured rod worth of all four compensation rods. A comparison plot was created based on the MCNP reactivity results and the deviation percentage between the MCNP reactivity values and actual measured rod worth data, see Figure 61. An equation was created to estimate the bias required to be applied for a given reactivity value from MCNP. This inaccuracy evaluation provided an outcome that was expected, as more negative reactivity was added to the core, the errors appeared to get larger, greater than 12%, for small deviations in reactivity. Based on the large uncertainties, it was determined that another method should be looked into to determine if a 12% inaccuracy was repeatable.

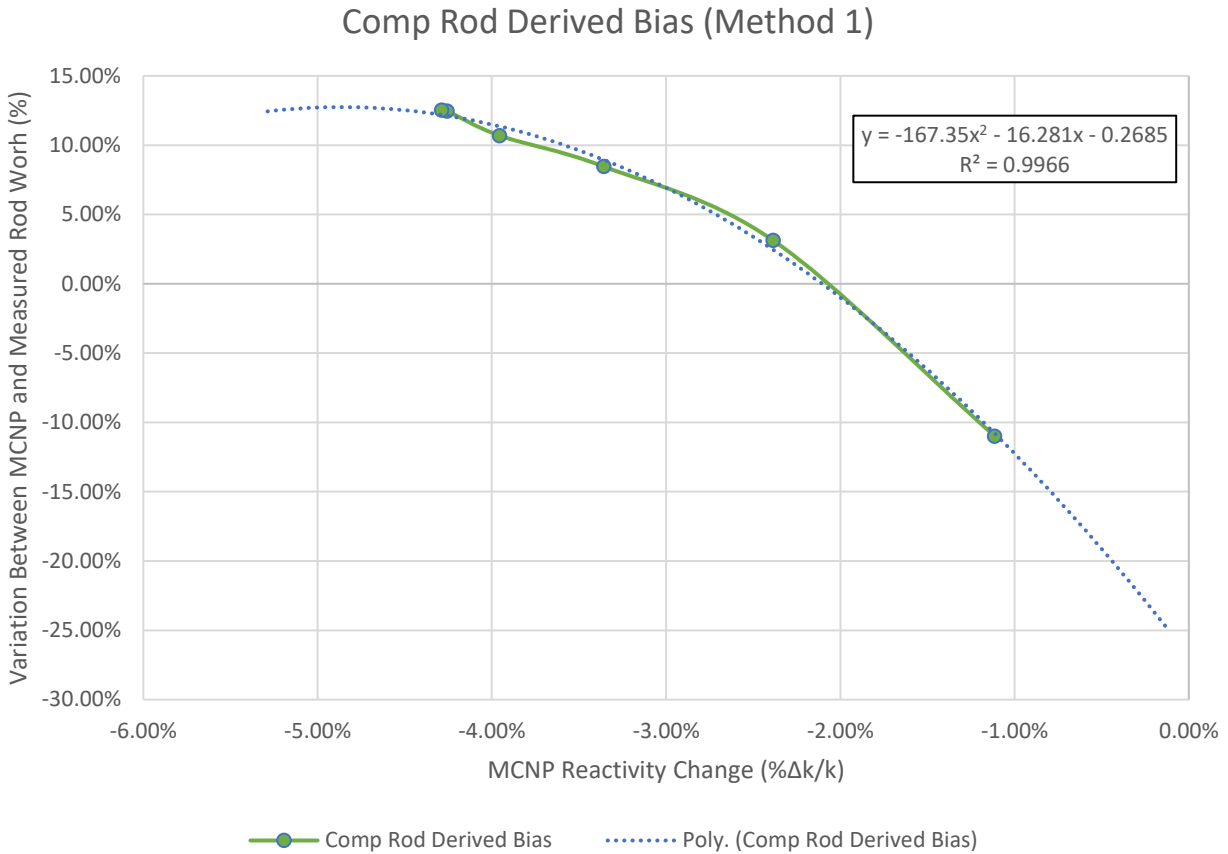


Figure 61: Compensation Rod Derived Bias (Method 1)

Method #2

Due to the very large bias for small variations, which did not appear to be a good representation of the actual bias, the next method was performed with the hopes to get a more accurate representation of the bias. This method similarly to Method #1, was a comparison of the MCNP results for the worth of the compensation rods to that of the compensation rod worth data. The difference between Method #1 and this method was the MCNP models were created to determine the worth of each rod individually, similar to how they actually measure each rod's worth when characterizing the core. For example, compensation rods 1 and 4 would be measured first. Each rod would be inserted at 30 inches, then compensation rod 1 would be withdrawn in increments of 4 inches until completely withdrawn while compensation rod 4 would be inserted in

increments of 4 inches to compensate for reactivity changes. Once compensation rod 1 is completely withdrawn both rods are placed back at the 30-inch insertion location and compensation rod 4 is withdrawn in a similar fashion while compensation 1 is inserted to compensate. Table 8 below shows the locations of the rods for each step. The benefit of doing it this way is that at each step, one rod is inserted and the other one is withdrawn providing worth for both rods. This process is repeated for compensation rods 2 and 3.

Table 8: Rod Locations for Bias Study, Method #2

Determining Worth of Comp 1				Determining Worth of Comp 4			
	#	Comp-1 Location (in)	Comp-4 Location (in)		#	Comp-1 Location (in)	Comp-4 Location (in)
Lower Portion of the Rod	1	30	30	Lower Portion of the Rod	1	30	30
	2	34	26		18	34	30
	3	38	22		19	38	26
	4	42	18		20	42	22
	5	46	14		21	46	18
	6	50	10		22	50	14
	7	54	6		23	54	10
	8	58	2		24	58	6
	9	58.5	0		25	58.5	2
Upper Portion of the Rod	1	30	30	Upper Portion of the Rod	1	30	30
	10	30	34		26	26	34
	11	26	38		27	22	38
	12	22	42		28	18	42
	13	18	46		29	14	46
	14	14	50		30	10	50
	15	10	54		31	6	54
	16	6	58		32	2	58
	17	2	58.5		33	0	58.5

The reactivity change for each rod position was determined by taking the k_{eff} for a specific change in compensation rod 1 and the k_{eff} for the alternate change for compensation rod 4 in equation 4. For example, to determine the reactivity of compensation rod 1 from 38 inches to 34

inches, you would take the k_{eff} from model 19 and k_{eff} from model 3, from the table above, and put it into [Equation 2](#). This was done for all positions along each compensation rod 1 through 4. The values were then compared to the original curve fit rod worth data as well as the measured rod worth data from the instrumentation at TREAT. No conclusive errors could be determined after analyzing this method. The data appeared to have no trend, as shown in Figure 62 and Figure 63 for compensation 1, and therefore was determined inconclusive leading to Method #3.

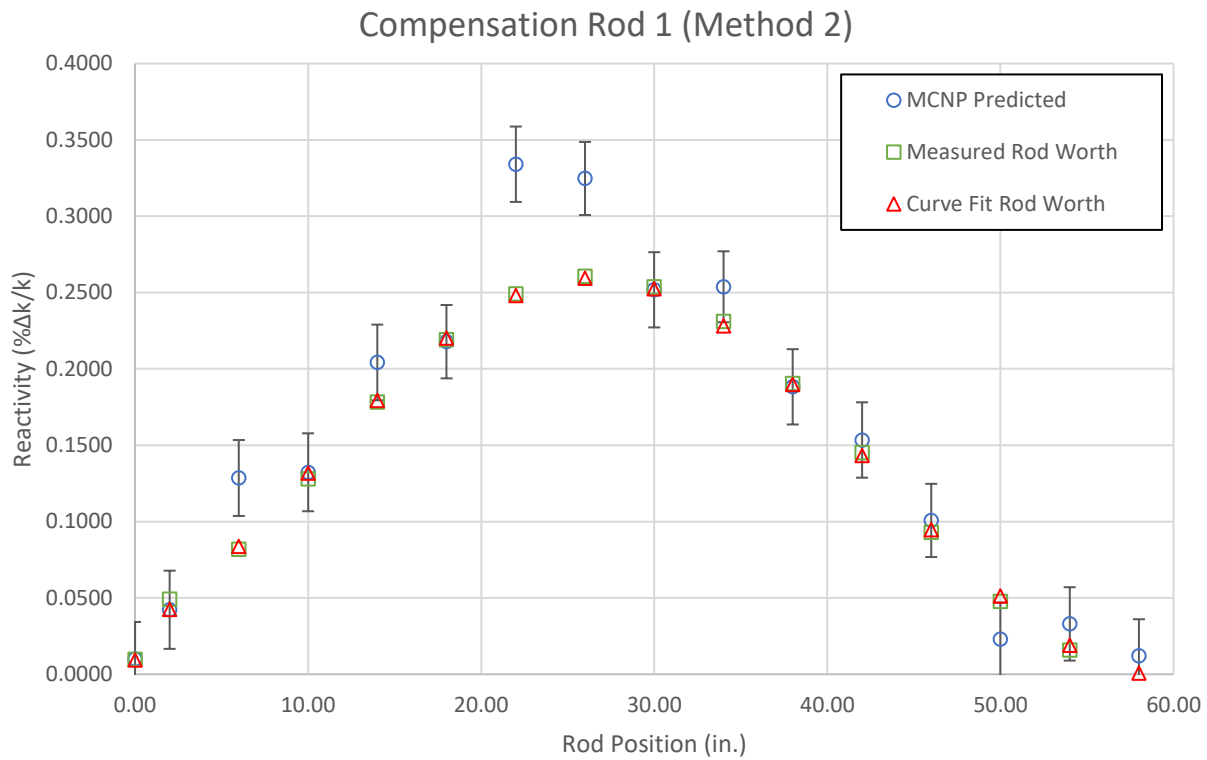


Figure 62: Compensation rod 1 comparison between MCNP predictions and measured rod worth.

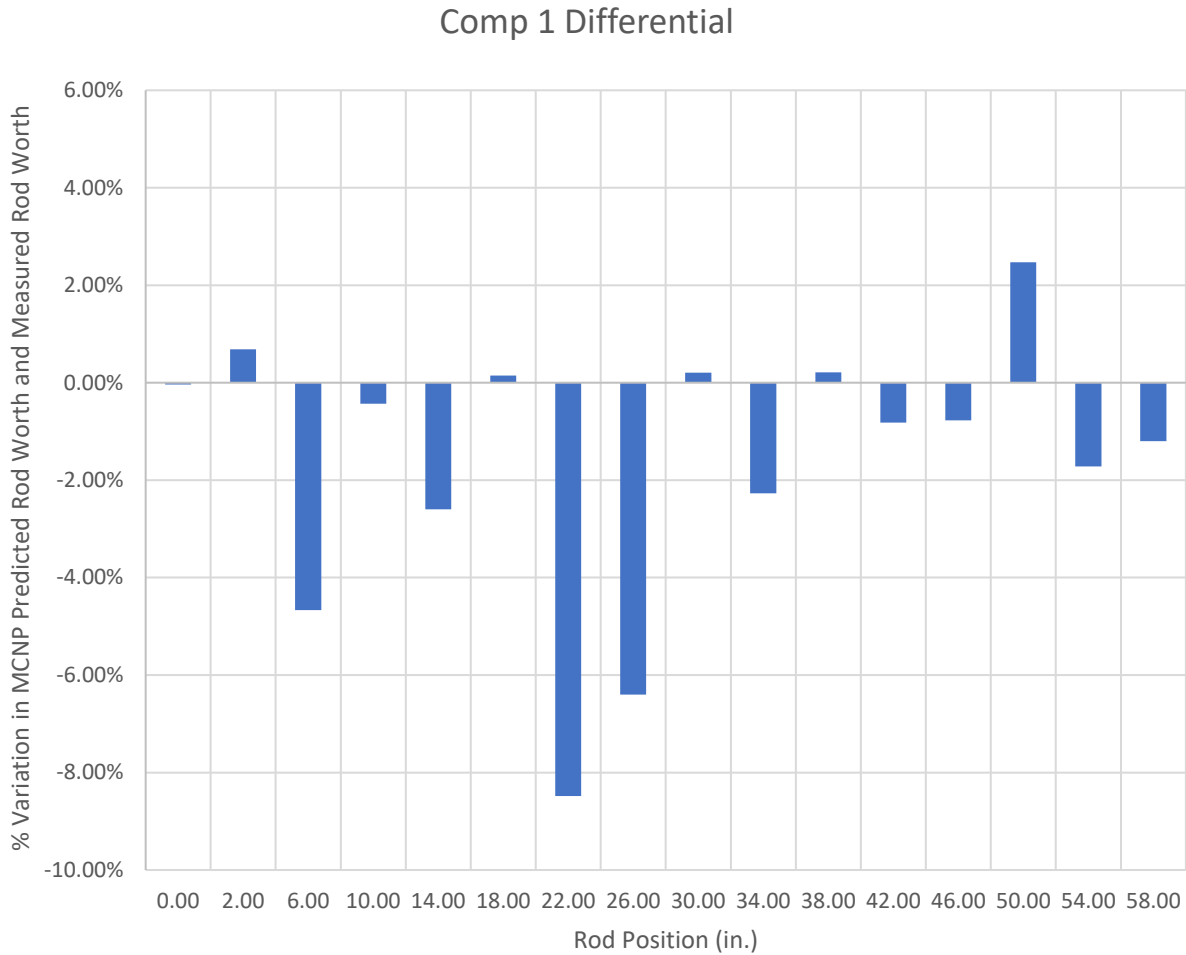


Figure 63: Percent deviation between MCNP predicted rod worth and measured rod worth data.

Method #3

After Method #2 resulted in inconclusive errors to apply to the results, Method #1 was re-evaluated to account for insertion ($k_{eff} < 1$) and withdrawal ($k_{eff} > 1$) of the rods and perform a direct comparison to the compensation rods. For Method #3 the same baseline full slotted core MCNP model was used as in Method #1, with the compensation rods placed at the critical position of 26.5 inches. Similarly, to Method #1, additional models were created at the following locations to represent insertion of rods, 21.5, 16.5, 11.5, 6.5, 1.5, and completely inserted into the core. This time another set of models were created to represent withdrawal of the rods, 31.5, 36.5, 41.5, 46.5,

51.5, and completely withdrawn. The reactivity values were determined by taking the k_{eff} for each step and the k_{eff} of the baseline model to use in [Equation 2](#). This provided a range of reactivities close to the critical eigenvalue ($k_{\text{eff}}=1$) as well as far from the critical eigenvalue in both the supercritical and subcritical directions. This data was then compared to the actual rod worth measurements from TREAT provided in Appendix F. This time, rather than creating a curve fit of the deviation, a curve was created comparing the MCNP values to that of the measured rod worth data. A linear curve fit was then created to produce an equation of uncertainty in the positive and negative reactivity direction. This was determined to provide the best results for the variation that MCNP model would create compared to what would be measured at TREAT. At the conclusion of this study, the possible errors introduced in the way that the rod worth data is gathered at TREAT was brought into question. It was determined after much thought that while there is known and unknown errors in how the data is gathered both in approach and the actual measurement itself, an evaluation of the error was not required as those errors should carry through when the actual HENRI system is used and measured. Meaning applying the model inaccuracies as is would produce results that TREAT should expect to measure using existing equipment and processes which would be the only way to show the actual effectiveness of the HENRI system at TREAT.

5 RESULTS & DISCUSSION

5.1 Rod Positions

Table 9 provides the rod positions of the control rods of the specific baseline or pulse used in the evaluations that follow. The positions correlate to the amount of rod pulled out of the core. All control rods were pulled to an identical level for each case.

Table 9: Rod Positions of Control Rods for Evaluations

Evaluation	Control Rods Position (cm)
HENRI Baseline (2 position - Critical)	47.5
HENRI 2 Position Runs	47.5
HENRI Baseline (4 position - Critical)	47.5
HENRI 4 Position Runs	47.5
Iterative Pulse Test Critical	21.336
Iterative Pulse Test 4.45% Pulse	73.152

5.2 Model Inaccuracies Evaluation

The inaccuracy results will be presented before the results of the other evaluations as these data impact the results of all the evaluations. Due to the complexity of the error results, only Method #3 results are presented in this thesis since it is the datum that was directly used in this evaluation. Table 10 provides the comparison between the MCNP results and the corresponding rod worth curve at various compensation rod positions for positive reactivity additions, pulling out the rods. Additionally, Table 11 provides the comparison between the MCNP results and the corresponding rod worth curve at various compensation rod positions for positive reactivity additions, insertion of the rods. For both sets of data, a compensation rod position of 26.5 inches was the baseline configuration. The data from both tables were plotted separately with rod worth data being the y-axis and the MCNP data being the x-axis. A linear fit produced an estimated actual measured value (EAMV) as a function of the MCNP value. The graph for the positive reactivity addition and negative reactivity addition can be seen in Figure 64 and Figure 65 respectively.

Table 10: MCNP Predicted Values vs Actual Rod Worth Measured Values (Positive Reactivity)

Adding Positive Reactivity (Rods are being Pulled out)		
Compensation Rod Position	MCNP	Rod Worth Curve
	Rho (%Δk/k)	Rho (%Δk/k)
26.50	--	--
31.50	1.347%	1.311%
36.50	2.604%	2.539%
41.50	3.597%	3.560%
46.50	4.332%	4.292%
51.50	4.756%	4.722%
56.50	4.968%	4.898%

Table 11: MCNP Predicted Values vs Actual Rod Worth Measured Values (Negative Reactivity)

Adding Negative Reactivity (Insertion of Rods)		
Compensation Rod Position	MCNP	Rod Worth Curve
	Rho (%Δk/k)	Rho (%Δk/k)
26.50	--	--
21.50	-1.439%	-1.251%
16.50	-2.661%	-2.312%
11.50	-3.652%	-3.095%
6.50	-4.253%	-3.573%
1.50	-4.583%	-3.785%
0.00	-4.596%	-3.810%

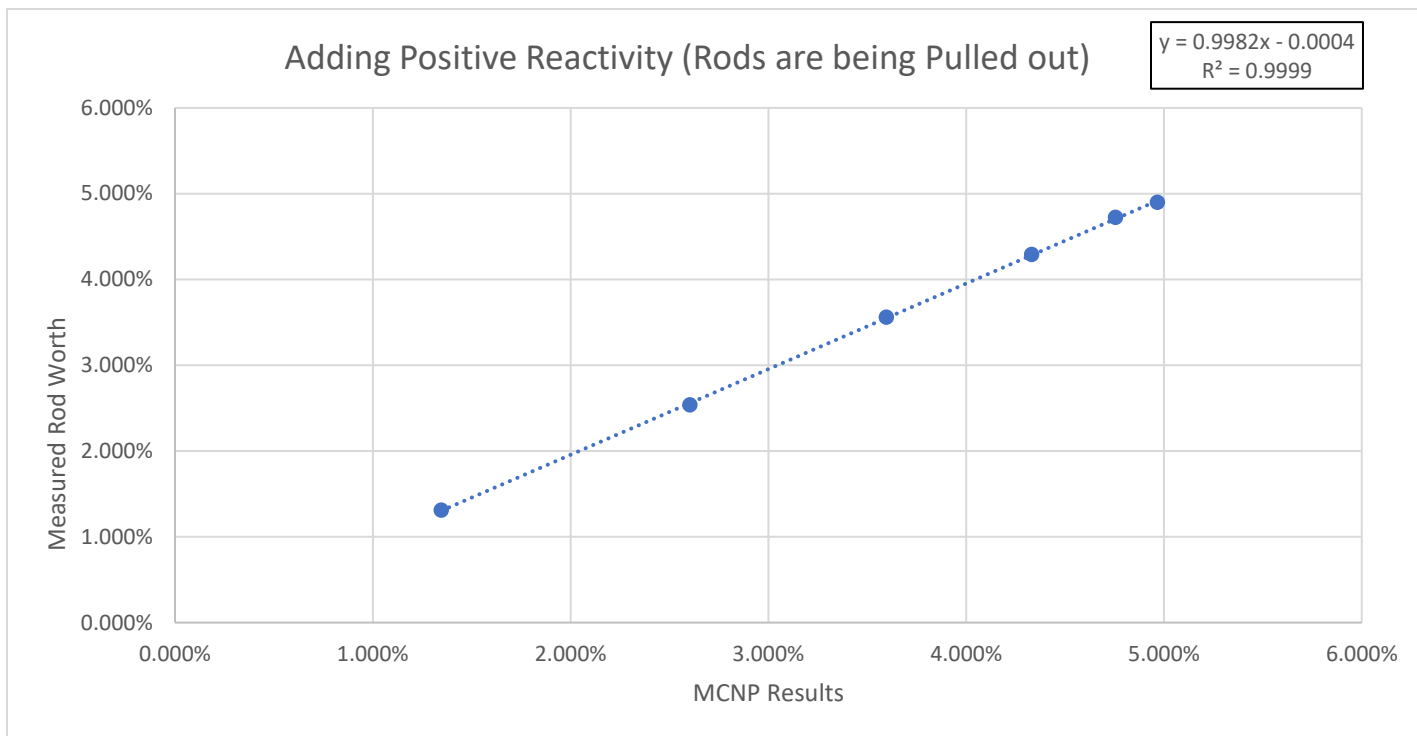


Figure 64: Relative inaccuracies for a positive reactivity addition for TREAT in MCNP compared to actual measured values.

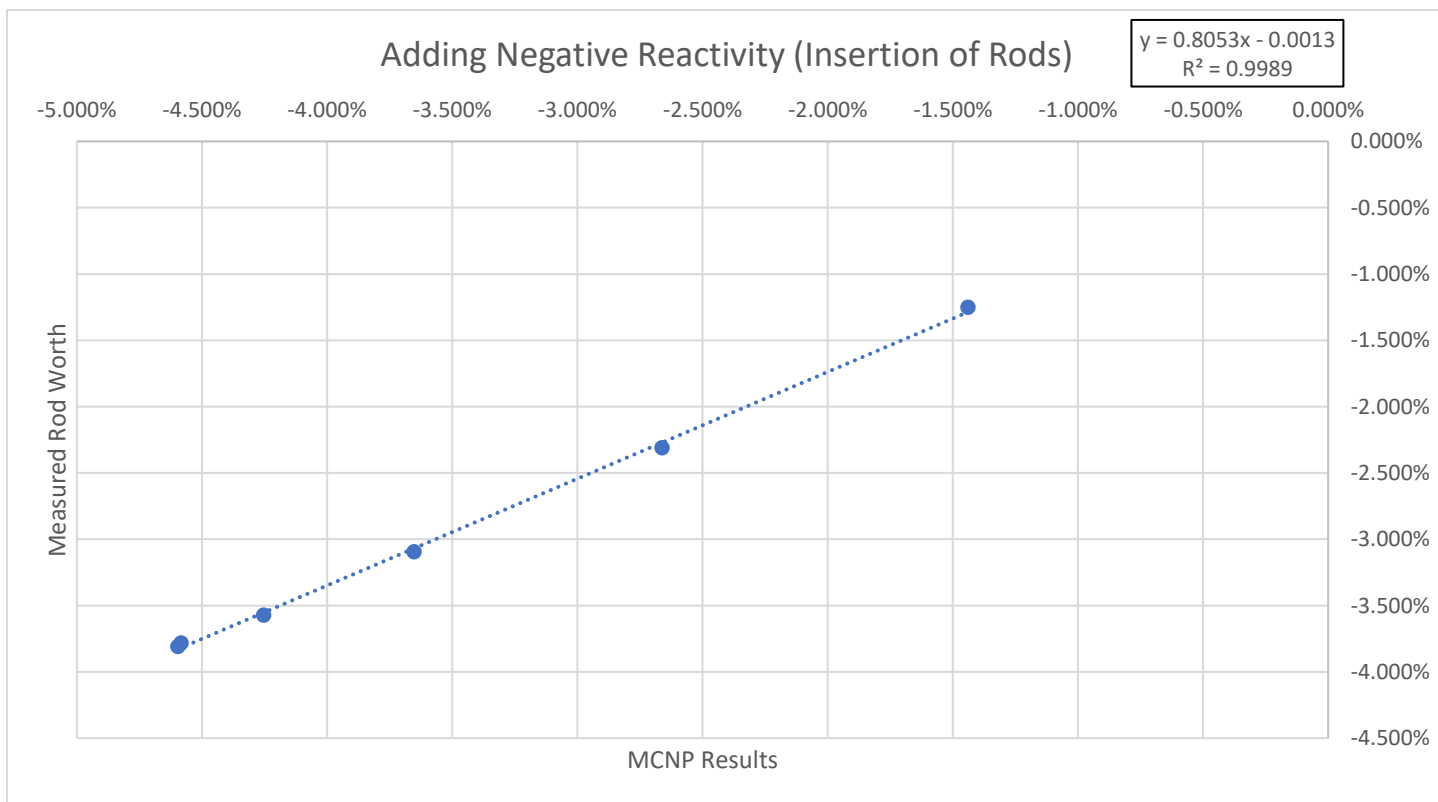


Figure 65: Relative inaccuracies for a negative reactivity addition for TREAT in MCNP compared to actual measured values.

The model inaccuracies were applied to the results based on the resulting reactivity. If the reactivity was a negative, [Equation 5](#) was used, if the reactivity was positive [Equation 6](#) was used.

$$EAMV = 0.8053 * MCNP \text{ Reactivity } (\%) - 0.0013 \quad [5]$$

$$EAMV = 0.9982 * MCNP \text{ Reactivity } (\%) - 0.0004 \quad [6]$$

It can be seen that the further you are from the critical eigenvalue in the negative reactivity addition direction the variation is much larger than deviations in the positive reactivity addition direction. As mentioned above, this is expected based on the way MCNP performs a KCODE evaluation through the artificial generation of a fundamental mode. This shows that MCNP is better at predicting reactivity for TREAT in critical evaluations rather than subcritical evaluations. In addition, the results provide a good argument for performing a more realistic pulse, centered around the critical eigenvalue, to determine effectiveness of the system.

5.3 Quantity and Location of Modules

As mentioned above, 1,000 psi helium-3 was used as an input for the five cases. Table 12 provides the pressure output from the CFD modeling as well as the converted atom density that were used as the input for each model producing the results described below.

Table 12: CFD pressure data with calculated atomic density for each timestep.

Time	TS00		TS01		TS02	
	Pressure (psi)	Atom Density (atoms/b-cm)	Pressure (psi)	Atom Density (atoms/b-cm)	Pressure (psi)	Atom Density (atoms/b-cm)
0	0.250	3.35E-07	0.250	3.35E-07	0.250	3.35E-07
0.001	21.145	2.80E-05	10.914	1.43E-05	8.939	1.17E-05
0.002	33.603	4.48E-05	37.088	4.95E-05	38.744	5.19E-05
0.003	36.418	4.87E-05	41.543	5.56E-05	43.842	5.87E-05
0.004	36.597	4.90E-05	296.526	3.97E-04	304.454	4.07E-04
0.005	391.320	5.24E-04	405.142	5.42E-04	398.339	5.33E-04
0.006	383.058	5.13E-04	396.009	5.30E-04	392.209	5.25E-04
0.007	377.649	5.05E-04	512.149	6.85E-04	509.555	6.82E-04
0.008	589.810	7.89E-04	582.219	7.79E-04	576.020	7.71E-04
Time	TS03		TS04		TS05	
	Pressure (psi)	Atom Density (atoms/b-cm)	Pressure (psi)	Atom Density (atoms/b-cm)	Pressure (psi)	Atom Density (atoms/b-cm)
0	0.250	3.35E-07	0.250	3.35E-07	0.250	3.35E-07
0.001	5.234	6.87E-06	4.222	5.86E-06	12.199	1.49E-05
0.002	37.286	4.98E-05	30.580	4.10E-05	208.190	2.75E-04
0.003	45.665	6.11E-05	271.681	3.64E-04	307.910	4.12E-04
0.004	305.873	4.09E-04	300.564	4.02E-04	309.566	4.14E-04
0.005	374.182	5.01E-04	298.908	4.00E-04	302.451	4.05E-04
0.006	389.304	5.21E-04	386.354	5.17E-04	498.714	6.67E-04
0.007	505.407	6.76E-04	494.861	6.62E-04	503.433	6.74E-04
0.008	558.278	7.47E-04	505.462	6.76E-04	523.819	7.01E-04

5.3.1 Double HENRI Locations

Table 13 and Table 14 show the results, without and with the measurement inaccuracies applied, from the dual HENRI locations (F12 & O12) and (F10 & O10) respectively. Additionally, a combined plot was produced to show the comparison of reactivity changes versus time for each case, see Figure 65.

Table 13: F12 & O12 Reactivity Change Results

Timestep (ms)	keff	Standard Deviation	$\Delta\rho$	$\Delta\rho$ w/Bias
0	0.99827	0.00266	0.000%	0.000%
0.001	0.98853	0.00286	-0.987%	-0.925%
0.002	0.97316	0.0029	-2.585%	-2.211%
0.003	0.96849	0.00243	-3.080%	-2.611%
0.004	0.96087	0.00272	-3.899%	-3.270%
0.005	0.95689	0.00266	-4.332%	-3.618%
0.006	0.9534	0.00243	-4.714%	-3.927%
0.007	0.95549	0.00262	-4.485%	-3.742%
0.008	0.95467	0.00294	-4.575%	-3.814%

Table 14: F10 & O10 Reactivity Change Results

Timestep (ms)	keff	Standard Deviation	$\Delta\rho$	$\Delta\rho$ w/Bias
0	0.99582	0.00263	0.000%	0.000%
0.001	0.99062	0.00229	-0.527%	-0.554%
0.002	0.97324	0.00242	-2.330%	-2.006%
0.003	0.96706	0.00244	-2.986%	-2.535%
0.004	0.94837	0.00293	-5.024%	-4.176%
0.005	0.94944	0.00293	-4.905%	-4.080%
0.006	0.95032	0.00285	-4.808%	-4.002%
0.007	0.94372	0.00247	-5.544%	-4.594%
0.008	0.94385	0.00237	-5.529%	-4.583%

Based on the above results, when measurement bias is applied, it is not certain that dual HENRI modules will be able to produce sufficient reduction in reactivity in the desired 5 millisecond timeframe. It can be seen that the reactivity is close to that desired and that a single HENRI module could be added, however, due to the desire for symmetry, and the potential desire for a full slot core, the 4 module core was evaluated.

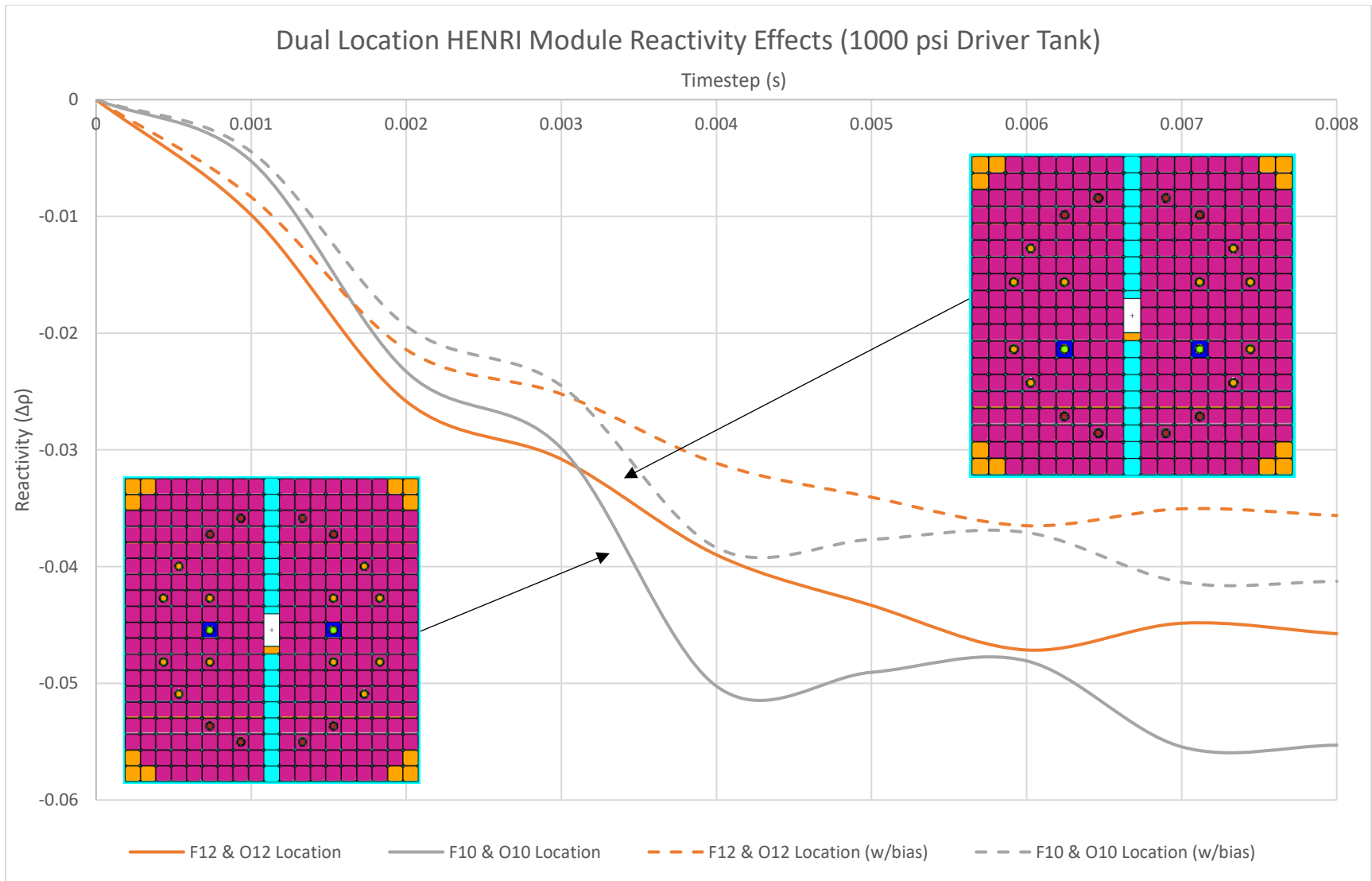


Figure 66: Reactivity effects from HENRI modules being placed in dual locations in TREAT.

5.3.2 Quad HENRI Locations

Table 15 provides the results from the quad HENRI locations (F9, F11, O9, & O11), (E9, E11, P9, & P11), and (G9, G11, N9, & N11). Additionally, a combined plot was produced to show the comparison of reactivity changes versus time for each case, see Figure 67.

Table 15: Quad HENRI Reactivity Reduction Results

F11, O11, F9 & O9					E11, P11, E9 & P9				
Timestep	keff	Standard Deviation	$\Delta\rho$	$\Delta\rho$ w/bias	Timestep	keff	Standard Deviation	$\Delta\rho$	$\Delta\rho$ w/bias
0	0.99095	0.00274	0.000%	0.000%	0	0.99243	0.00251	0.000%	0.000%
0.001	0.97662	0.00272	-1.481%	-1.322%	0.001	0.97571	0.00257	-1.727%	-1.521%
0.002	0.94468	0.00275	-4.943%	-4.110%	0.002	0.94949	0.00277	-4.557%	-3.800%
0.003	0.93395	0.00271	-6.159%	-5.090%	0.003	0.93712	0.00286	-5.947%	-4.919%
0.004	0.91266	0.00242	-8.657%	-7.101%	0.004	0.91929	0.00256	-8.017%	-6.586%
0.005	0.90997	0.00281	-8.980%	-7.362%	0.005	0.90661	0.00269	-9.538%	-7.811%
0.006	0.90949	0.00271	-9.038%	-7.409%	0.006	0.90803	0.00246	-9.366%	-7.672%
0.007	0.90217	0.00254	-9.931%	-8.127%	0.007	0.90421	0.00245	-9.831%	-8.047%
0.008	0.90684	0.00236	-9.360%	-7.667%	0.008	0.90871	0.00252	-9.283%	-7.606%
G11, N11, G9 & N9									
Timestep	keff	Standard Deviation	$\Delta\rho$	$\Delta\rho$ w/bias					
0	0.99487	0.0025	0.000%	0.000%					
0.001	0.97678	0.00265	-1.862%	-1.629%					
0.002	0.94557	0.00249	-5.241%	-4.350%					
0.003	0.93546	0.00261	-6.384%	-5.271%					
0.004	0.91416	0.00283	-8.874%	-7.277%					
0.005	0.91057	0.00255	-9.306%	-7.624%					
0.006	0.90967	0.0028	-9.414%	-7.711%					
0.007	0.91546	0.0027	-8.719%	-7.151%					
0.008	0.90245	0.00248	-10.294%	-8.420%					

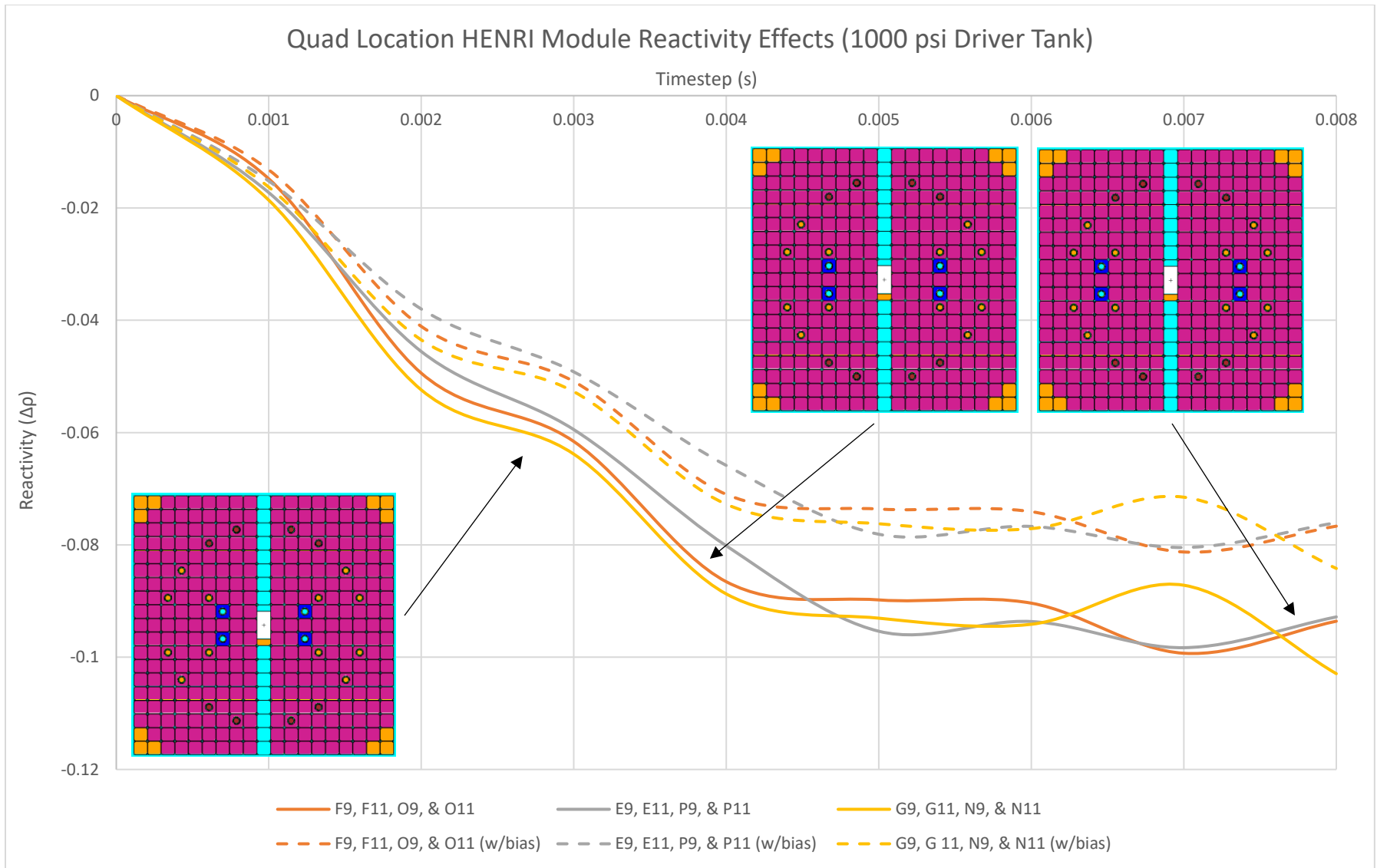


Figure 67: Reactivity effects of HENRI modules placed in a configuration of four in the TREAT core.

Based on the results from the HENRI modules located in four locations within the core, the desired reactivity reduction is plausible in the desired timeframe of 5 milliseconds. In addition, it was hypothesized that the location of the four HENRI modules did not have a strong impact on the efficiency of the reactivity reduction, as can be shown by these three locations reaching the desired reactivity in approximately the same time. For this reason, and for ease of core modification, it was determined that the HENRI modules could be placed inside control rod fuel elements in locations that were designed to contain control rods, the H6, H14, M6, & M14 locations. While these locations were not evaluated as part of this portion of the study, they were verified during the HENRI system worth evaluation. In addition, as mentioned above, all of these models were set up to evaluate at a critical core ($k_{\text{eff}} = 1$) rather than at a peak core as this study was performed early on in the project. As mentioned in the bias study, based on the behavior of the fundamental mode as calculated by MCNP, the error of this is expected to be larger and will be verified by the system worth evaluation which centers around the critical eigenvalue.

5.4 Worth of HENRI System

Varying pressures were evaluated using the pulse approach to determine what the lowest pressure in the driver tank was to achieve the desired reactivity reduction in the core at the H6, H14, M6, & M14 locations. Determining the lowest pressure was important as, at higher pressure there is a larger potential for leakage of the helium-3 in the system, additionally, the lower the pressure the safer the system is within the reactor. The pressures that were evaluated were 850 psig, 750 psig, 500 psig, and 250 psig. Appendix G provides the CFD input pressures and the converted atom densities for each driver tank pressure used for this study. To provide the results in a concise manner that is easier to compare, a comparison plot was created showing the results of the four pulses that were evaluated (Figure 68), the results in table form can be found in Appendix H.

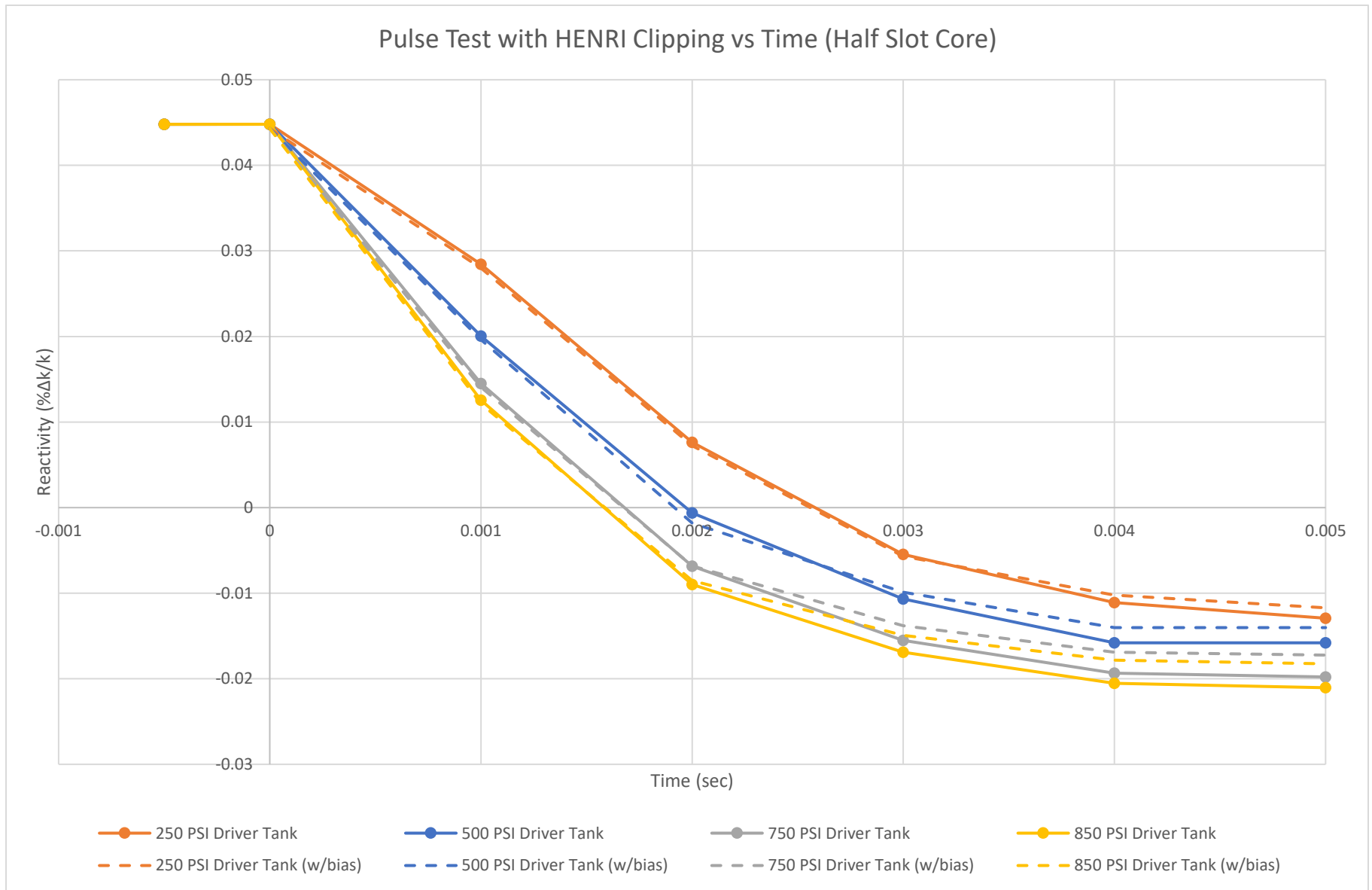


Figure 68: Comparison plot of the various driver tank pressures and their reactivity insertion ability over 5 milliseconds

The results show that at the lower bound of the evaluation, 250 psig, the HENRI system with four HENRI modules, produces the desired reactivity reduction well within the desired clip time. The system was not evaluated any lower than 250 psig, as it is expected that the 250 psig pressure would be the lowest pressure for the recovery system to work as desired. A final pressure of 500 psig was chosen for the system due to valve leakage evaluations using a prototype system. At an elevated pressure of 500 psig in the driver tank, the leak rate of the driver tank around the piston valve into the gas thimble was drastically reduced. An updated CFD model, which included temperature feedback and other gas dynamics feedback, was created after the worth evaluation was initially performed above. The 500 psig driver tank results were updated to provide a more realistic expectation of the system at 500 psig and can be seen in Table 16 and Figure 69 below. It should be noted that the pressure data had variations in it that required more than timesteps at every millisecond and a total of 10 models were required, this is shown in Figure 70. Additional plots of the flux were also included to show the variation in the core fissions during each timestep and can be found in Appendix I.

Table 16: 500 PSIG Driver Tank Reactivity Results as a Function of Time

Time Step	keff	std	MCNP $\Delta\rho$	MCNP $\Delta\rho$ (w/bias)
0.00000	1.04701	0.00004	4.49%	4.44%
0.00100	1.01487	0.00005	1.47%	1.42%
0.00234	0.98822	0.00005	-1.19%	-1.09%
0.00236	0.98717	0.00004	-1.30%	-1.18%
0.00265	0.9885	0.00004	-1.16%	-1.07%
0.00363	0.98684	0.00004	-1.33%	-1.20%
0.00451	0.98955	0.00005	-1.06%	-0.98%
0.00551	0.99198	0.00005	-0.81%	-0.78%
0.00651	0.9968	0.00004	-0.32%	-0.39%
0.00751	1.0004	0.00004	0.04%	0.00%
0.00851	0.99916	0.00005	-0.08%	-0.20%

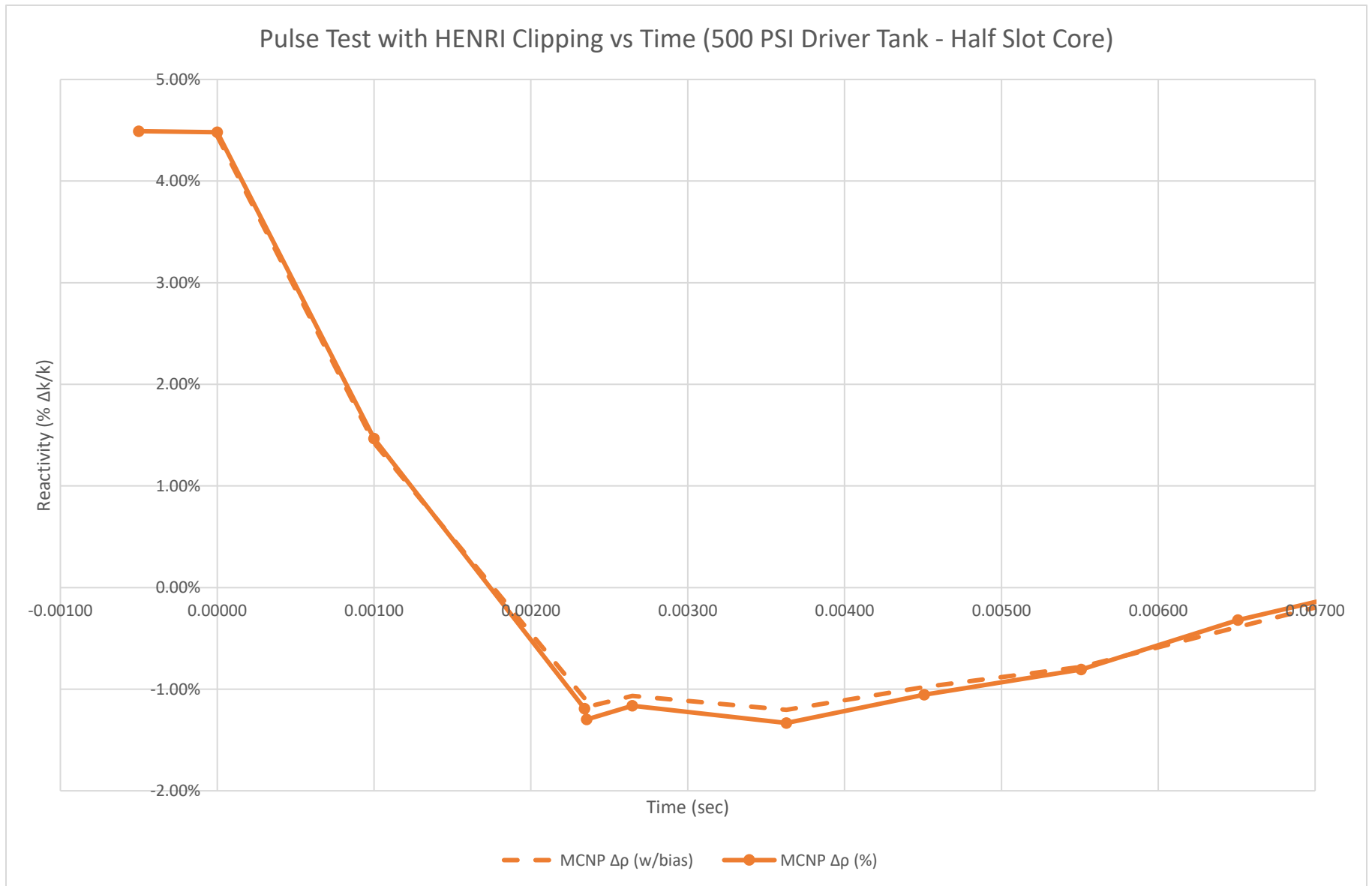


Figure 69: Reactivity worth of the HENRI system at 500 psig driver tank updated outputs from CFD.

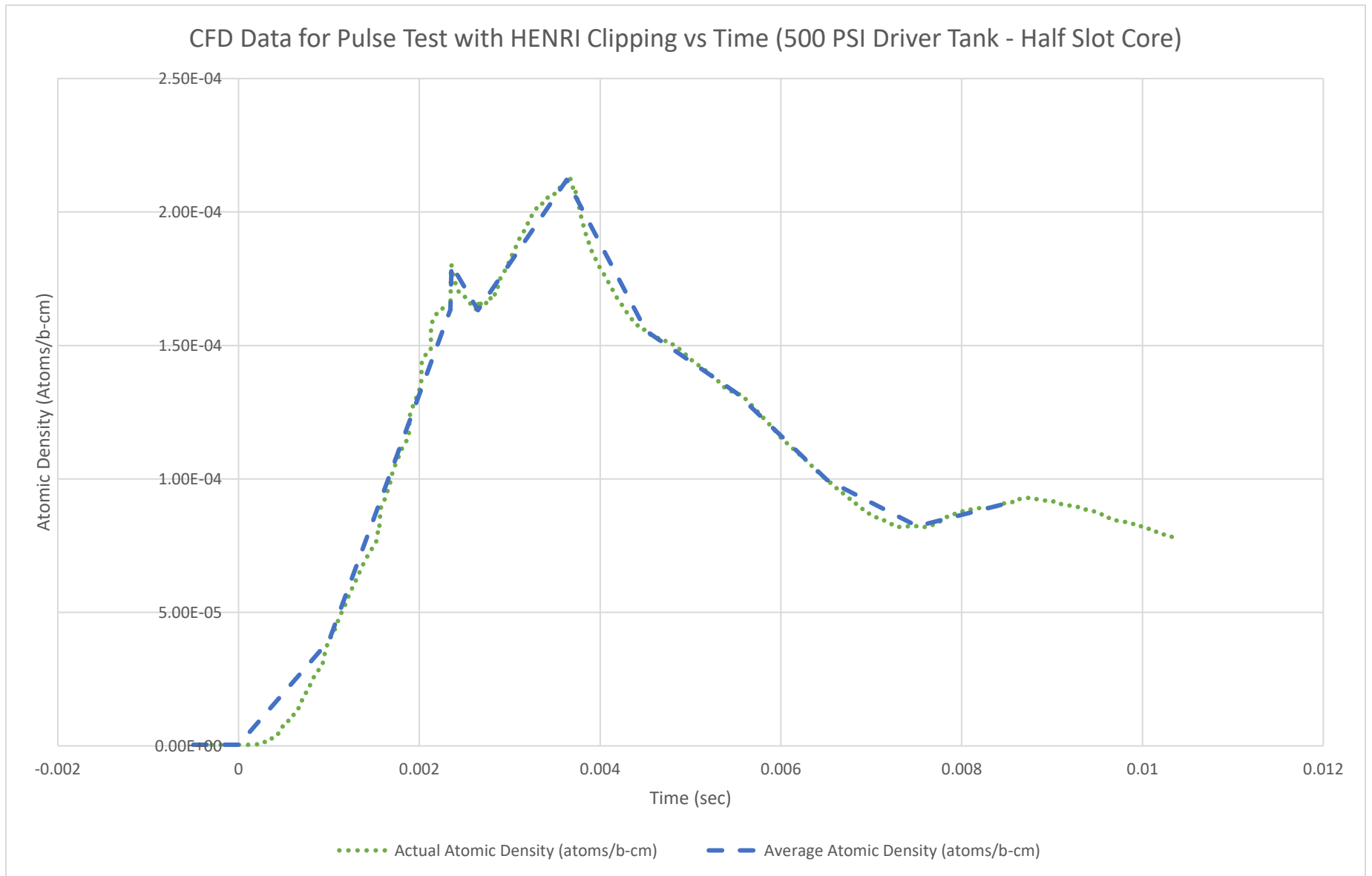


Figure 70: Comparison of the timestep truncated data used as compared to the output CFD data to show inclusion of deviations.

5.5 Annular Evaluation

The average neutron density value used in the macroscopic cross section determination, as discussed in section 4, that is later used in [Equation 3](#) to determine the mean free path was determined by using the 5 millisecond neutron density values in each zone. The 5 millisecond neutron density datum was taken from the CFD data provided by OSU at 250 psig, see Appendix G. The values along with their location, along with the average value used in the calculation is seen in Table 17.

Table 17: 5 Millisecond Neutron Density per Section with Average

TS00	TS01	TS02	TS03	TS04	TS05	N(avg)
2.08E+20	1.94E+20	1.67E+20	1.74E+20	1.58E+20	1.20E+20	1.70E+20

Table 18 summarizes the energy values, absorption cross sections at those energies, the macroscopic cross section, and the mean free path in inches for helium-3. A plot was created as a function of energy (eV) and the mean free path (inches), Figure 71.

As mentioned before, the helium-3 cross sectional area inside the HENRI module is 1.61 inches. It can be seen in the graph in Figure 71, that the region between a mean free path of 1.5 inches and 2 inches that there is a linear trend between mean free path and the energy that is able to be captured. Linearly interpolating values in Table 19 allows us to estimate the maximum energy that a 1.61 inch cross section of helium could absorb using [Equation 7](#).

$$\frac{y-y_0}{x-x_0} = \frac{y_1-y_0}{x_1-x_0} \quad [7]$$

The mean free path in inches was used for the x values and the energy in eV was used for the y values.

$$\frac{y - 0.35}{1.61 - 1.62} = \frac{0.35 - 0.275}{1.62 - 1.43} = y = 0.346$$

The resulting energy neutron energy range that the HENRI modules have the potential to absorb, using the 1.61-inch inner diameter for the gas thimble, is approximately 0 eV to 0.346 eV.

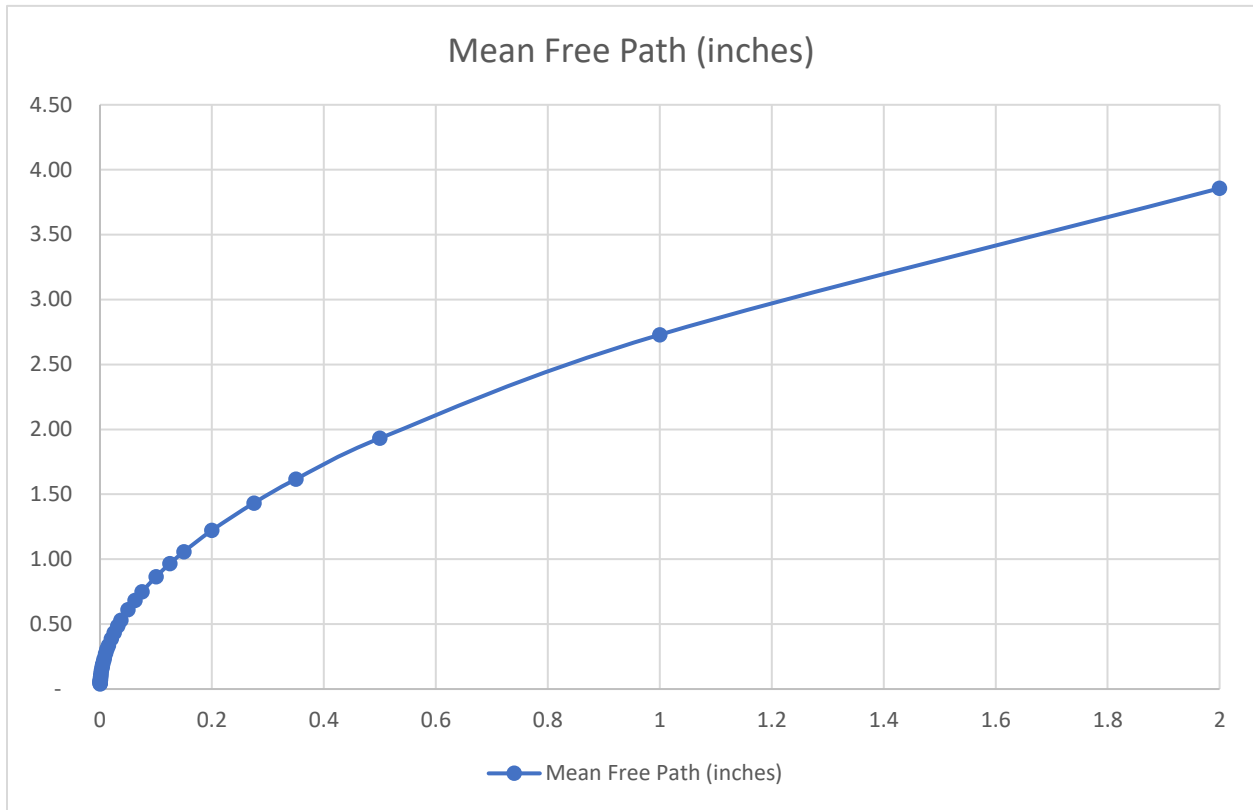


Figure 71: Mean free path compared to energy for helium-3.

Table 18: Helium-3 Mean Free Path vs. Energy

Energy (eV)	Absorption Cross Section (Thermal) – (b)	Macroscopic Cross Section (1/cm)	Mean Free Path (inches)
0.0002	59,807.80	10.1773	0.04
0.000275	51,004.30	8.6792	0.05
0.00035	45,210.60	7.6933	0.05
0.000425	41,028.00	6.9816	0.06
0.0005	37,826.10	6.4367	0.06
0.000625	33,832.80	5.7572	0.07
0.00075	30,885.10	5.2556	0.07
0.001	26,747.50	4.5515	0.09
0.00125	23,923.80	4.0710	0.10
0.0015	21,839.40	3.7163	0.11
0.002	18,913.60	3.2185	0.12
0.00275	16,129.80	2.7448	0.14
0.0035	14,297.70	2.4330	0.16
0.00425	12,975.10	2.2079	0.18
0.005	11,962.60	2.0356	0.19
0.00625	10,699.90	1.8208	0.22
0.0075	9,767.81	1.6622	0.24
0.01	8,459.48	1.4395	0.27
0.0125	7,566.62	1.2876	0.31
0.015	6,907.55	1.1754	0.33
0.02	5,982.43	1.0180	0.39
0.0253	5,319.31	0.9052	0.43
0.031475	4,769.23	0.8116	0.49
0.03765	4,360.78	0.7421	0.53
0.05	3,784.36	0.6440	0.61
0.0625	3,385.06	0.5760	0.68
0.075	3,090.32	0.5259	0.75
0.1	2,676.61	0.4555	0.86
0.125	2,394.15	0.4074	0.97
0.15	2,185.67	0.3719	1.06
0.2	1,893.05	0.3221	1.22
0.275	1,614.67	0.2748	1.43
0.35	1,431.48	0.2436	1.62
0.5	1,198.01	0.2039	1.93
1	847.84	0.1443	2.73
2	599.91	0.1021	3.86

Appendix J provides the results of all the surface tallies from the 5 millisecond, 250 psig driver tank MCNP model that was used for the annular evaluation. As shown above, each HENRI module, based on its axial cross section of helium-3 in the 1.61 diameter tube, has the potential to stop neutrons in the energy range from 0 eV to 0.346 eV energy range. The neutron tallies for the energy bins from 0 eV up to the 0.3261 eV from the MCNP outputs were summed in order to provide the neutrons that passed each region of the HENRI module. This provides the efficiency of each region of helium and how well it can capture neutrons in order to stop the chain reactions within the core. The overall results are provided in Table 19. Additionally, the amount of helium-3 that would be needed for each “annular” region was determined and provided in Table 19. Figure 72 provides a visual of the respective zones and the surfaces associated with each.

Table 19: Summation of MCNP F6 Tally up to 0.32609 eV Energy

Surface	Fuel Assembly Tube (676)	Metal/ He-3 Interface (100179)	1/8" Helium-3 Ring (100187)	1/4" Helium-3 Ring (100188)
Neutron Surface Tally	6.528224E-05	6.250702E-06	4.717732E-06	3.483412E-06
Helium-3 Needed (Liters)	N/A	N/A	1.98	2.97
Surface	3/8" Helium-3 Ring (100189)	1/2" Helium-3 Ring (100190)	3/4" Helium-3 Ring (100191)	Nearly Full Helium-3 (100192)
Neutron Surface Tally	2.715305E-06	2.198926E-06	1.829722E-06	1.560732E-06
Helium-3 Needed (Liters)	3.96	4.95	5.93	6.37

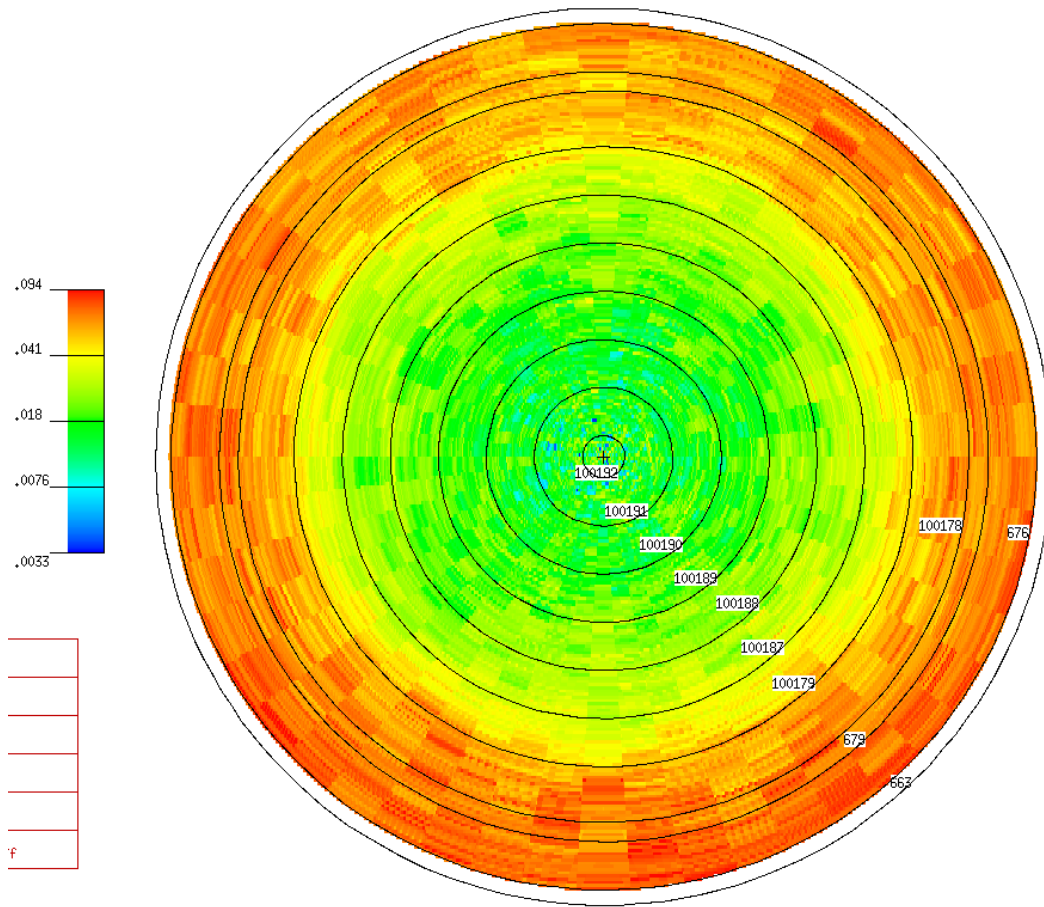


Figure 72: Visual of zones and the respective surfaces.

Figure 73 provides a chart for the amount of helium-3 savings compared to the neutron population that is seen at each surface.

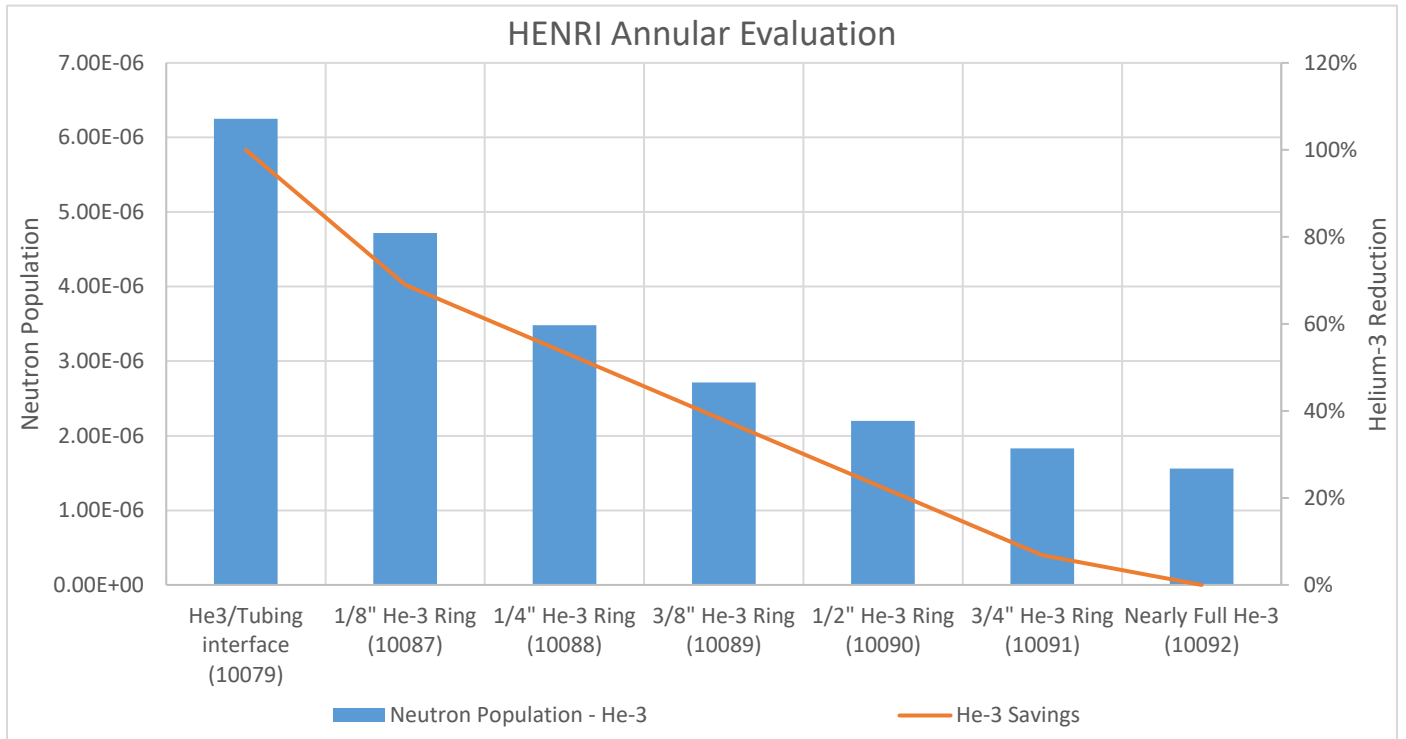


Figure 73: Helium-3 savings compared to the neutron population at each surface.

A graph was used to determine the most efficient annular design, by finding the efficiency point, based on the number of neutrons reduced at each helium-3 zone and the helium-3 savings that would be provided. Table 20 and Figure 74 provide the results of that evaluation.

Table 20: Helium-3 Savings vs Neutron Reduction

Surface	He-3 Thickness	n Reduction	Helium Savings
He3/Tubing interface (10079)	0.00	0.0%	100%
1/8" He-3 Ring (10087)	0.25	24.5%	69%
1/4" He-3 Ring (10088)	0.50	44.3%	53%
3/8" He-3 Ring (10089)	0.75	56.6%	38%
1/2" He-3 Ring (10090)	1.00	64.8%	22%
3/4" He-3 Ring (10091)	1.25	70.7%	7%
Nearly Full He-3 (10092)	1.61	75.0%	0%

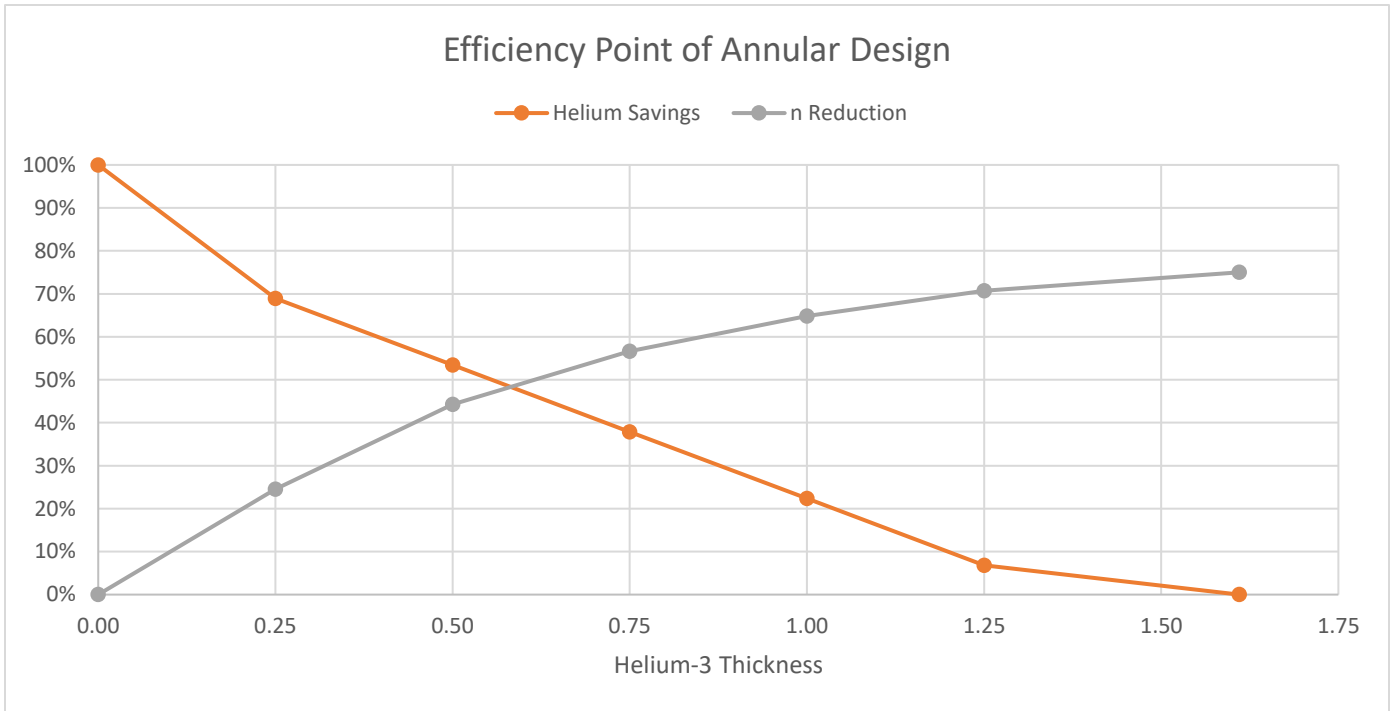


Figure 74: Efficiency curve for helium-3 usage vs reduction in neutrons.

Based on the above graph the most efficient point is before a total thickness of helium-3 of $\frac{3}{4}$ ". A $\frac{3}{4}$ " helium-3, $\frac{3}{8}$ " helium-3 ring, should have the most efficient helium-3 savings per neutron reduction. A verification of the $\frac{3}{8}$ " annular helium-3 section was performed to ensure that the target reduction in reactivity could still be achieved in the desired timeframe. Figure 75 provides a printout of the MCNP model with air in place of helium-3 to match the $\frac{3}{8}$ " helium-3 ring configuration as a validation of the above efficiency. Additionally, Figure 76 provides the resulting reduction in reactivity vs time for this annular case compared to a non-annular case as reported in Figure 69 above. As you can see from the results, an annular system with a $\frac{3}{8}$ " thickness of helium-3 is sufficient to reach the desired clip in the desired time. Additionally, a cylindrical test section doesn't take that much longer to reach the desired clip. Some things to consider, however, is the added manufacturer burden with an annular section.

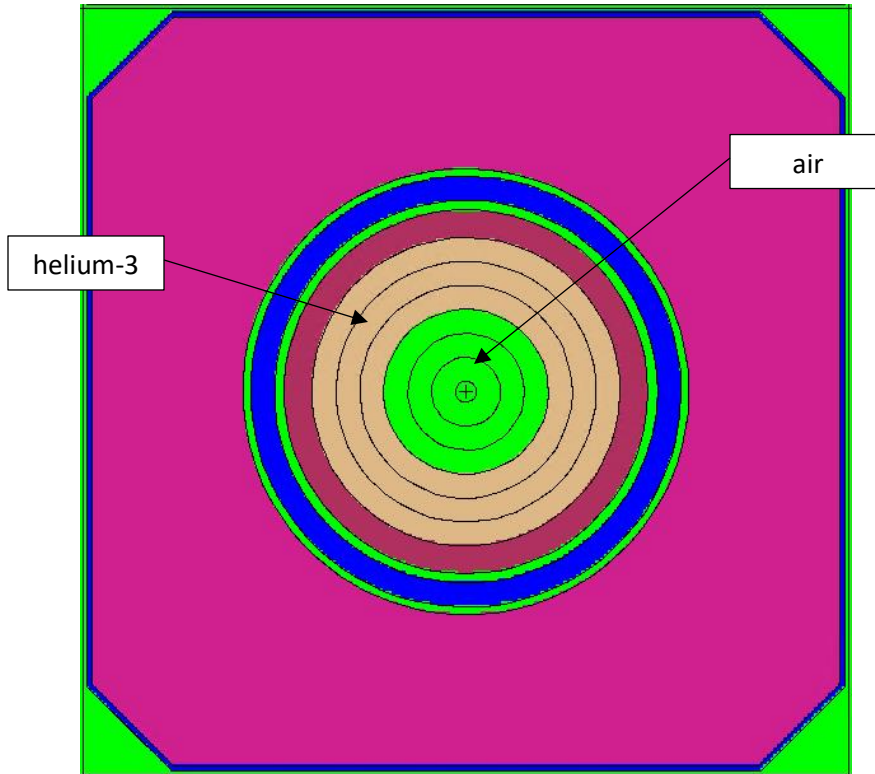


Figure 75: MCNP HENRI model cross section showing air zones and helium-3 zones.

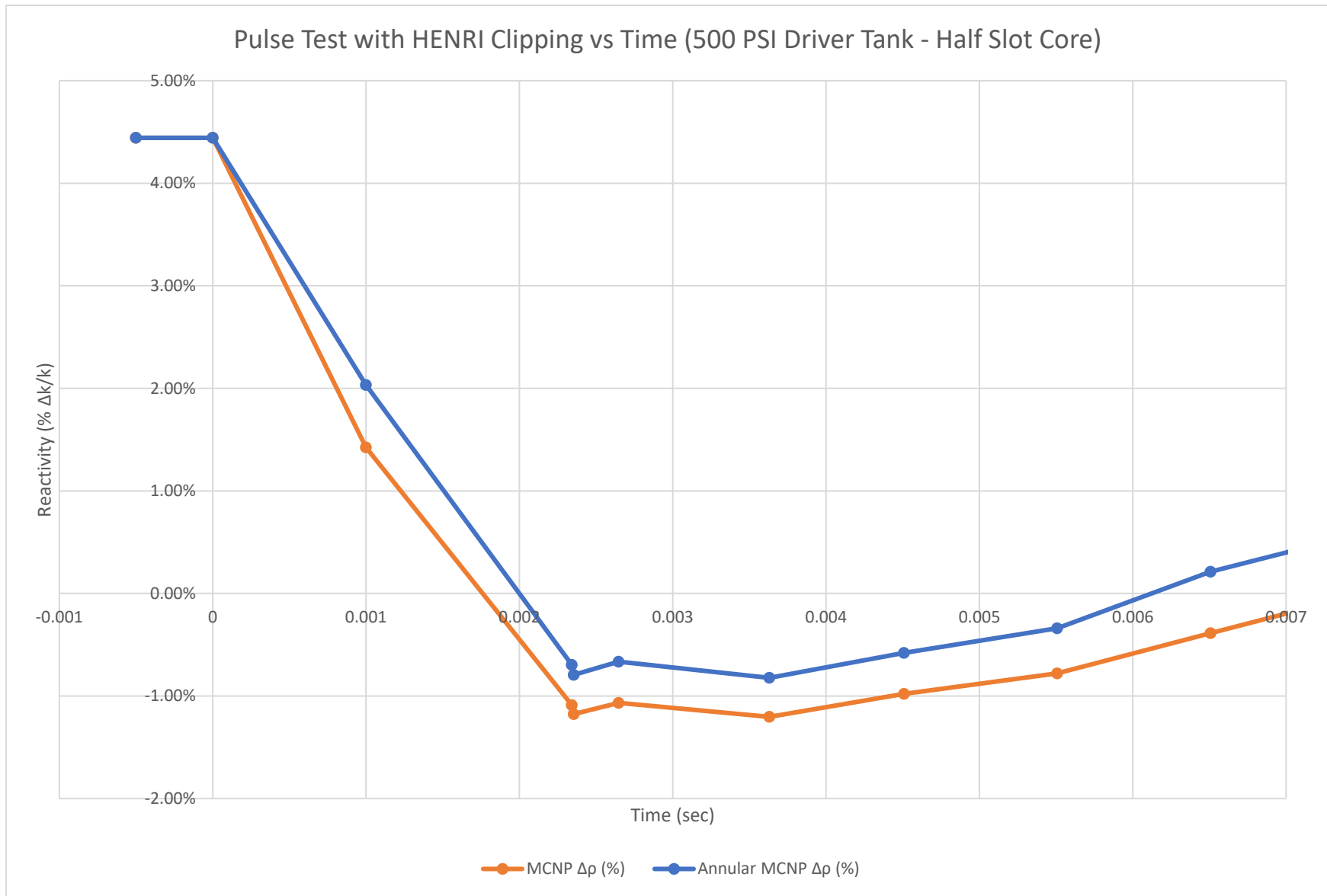


Figure 76: Annular HENRI evaluation compared to the non-annular HENRI worth evaluation.

6 SUMMARY AND CONCLUSIONS

TREAT's mission as early as the 1950's has been to understand the behaviors of reactor fuels under reactor accident conditions. In 2021 that need is no different after being restarted from a 23-year shutdown. In fact not only is the need still there but due to other facilities not meeting the current data needs, TREAT has been asked to perform an upgrade from its current 92 ms pulse width, induced by transient rods, to a 75 ms to 45 ms pulse width to support LWR studies. The system tasked with this pulse width decrease is a modular system composed of gas thimbles that will induce a clip through the rapid injection of helium-3 gas.

To support the design efforts, the behavior of a helium-3 injection system had to be understood. Using MCNP6, the evaluation concluded that the use of 4 HENRI modules would be necessary to maintain symmetry in the TREAT core while also offering a clip of -5% $\Delta k/k$ reactivity in a 5 millisecond timeframe. The evaluation also shows that even at a driving pressure of 250 psi, based on computational fluid dynamic predictions, the HENRI system as currently designed will exceed the desired clip of -5% $\Delta k/k$ in 5 milliseconds and actually reach the desired clip in just under 3 milliseconds. An annular gas thimble section design was also shown to perform within the desired requirements to support a reduction in the rare and expensive helium-3 gas.

7 FUTURE WORK

This report provides initial study of the feasibility of a helium-3 injection system at TREAT as well as supporting information to feed a final design of the system. Additional design efforts will be required to complete the system for use at TREAT including a thermal evaluation of the materials for use at TREAT. During the CFD work, it was determined that the gas dynamics cause an increase in temperature of the gas that exceeds the initial materials chosen for the gas thimble.

In addition, TREAT has limits the temperatures seen by the fuel. Any deviations of the final design, including, but not limited to use of the annular design, new materials, and various lengths and tube diameters will require re-evaluation of this work. In addition, fine tuning of the CFD models could provide additional inputs for the models to improve the output results to be more realistic including the use of coupled codes for a multi-physics approach in which the temperature and pressure can be fed directly into the time evolutions of the core reactivity changes. In addition, testing of the final system in the TREAT core will be required to validate the modeling performed in this analysis.

8 REFERENCES

- [1] Argonne National Laboratory, "TREAT Baseline Description Document," 1992.
- [2] B. K. Heath, C. C. Race and L. O. Nelson, "Transient Reactor Test Facility Restart 23 Years Later," in *Proceedings of the 2018 26th International Conference on Nuclear Engineering*, London, 2018.
- [3] D. R. McFarlane, G. A. Freund and J. F. Boland, "Hazards Summary Report on the Transient Reactor Test Facility," 1958.
- [4] C. L. Pope, C. B. Jensen, D. M. Gerstner and J. R. Parry, "Transient Reactor Test (TREAT) Facility Design and Experiment Capability," *Nuclear Technology*, vol. 205, no. 10, 2019.
- [5] Idaho National Laboratory, "Transient Reactor Test (TREAT) Facility FSAR. SAR-420," 2019.
- [6] Nuclear Regulatory Commission, "An Assessment of Postulated Reactivity-Initiated Accidents (RIAs) for Operating Reactors in the U.S.," March 2004.
- [7] L. O. Jernkvist and A. R. Massih, "Nuclear Fuel Behaviour under Reactivity-initiated Accidents (RIA) Condition," Nuclear Agency, Organisation for Co-operation and Development (OECD), Molnlycke, Sweden, 2010.
- [8] P. Rudling, L. O. Jernkvist, F. Garzarolli, R. Adamson, T. Mahmood, A. Strasser and C. Patterson, "Nuclear Fuel Behaviour under RIA Conditions," *Advanced Nuclear Technology International*, Molnlycke, Sweden, December, 2016.
- [9] D. C. Crawford, A. E. Wright and R. E. Holtz, "RIA Testing Capability of the Transient Reactor Test Facility," in *Om: Proc. IAEA Tech. Comm. Mtg. on Fuel Cycle Options for LWRs and HWRs. IAEA-TECDOC-1122*, Victoria, Canada, 1998.
- [10] J. D. Bess, N. E. Woolstenhulme, C. B. Davis, L. M. Dusanter, C. D. Folsom, J. R. Parry, T. H. Shorthill and H. Zhao, "Narrowing transient testing pulse widths to enhance LWR RIA experiment design in the TREAT facility," *Annals of Nuclear Energy*, vol. 124, pp. 548-571, 2019.
- [11] J. G. Crocker and L. A. Stephan, "Reactor Power Excursion Tests in the SPERT IV Facility," US Atomic Energy Commission, National Reactor Testing Station, 1964.
- [12] R. W. Miller, R. K. McCardell and T. F. Lagier, "Addendum to the SPERT IV Hazards Summary Report --- Capsule Driver Core," US Atomic Energy Commission National Reactor Testing Station, 1965.
- [13] A. A. Wasserman, S. O. Johnson, R. E. Heffner, R. S. Kern and A. H. Spano, "Power - Burst Facility Conceptual Design," US Atomic Energy Commission National Reactor Testing Station, 1963.
- [14] Aerojet Nuclear Company, "Final Safety Analysis Report for the Power Busrt Facility, ANCR-1011," Idaho Falls, 1971.

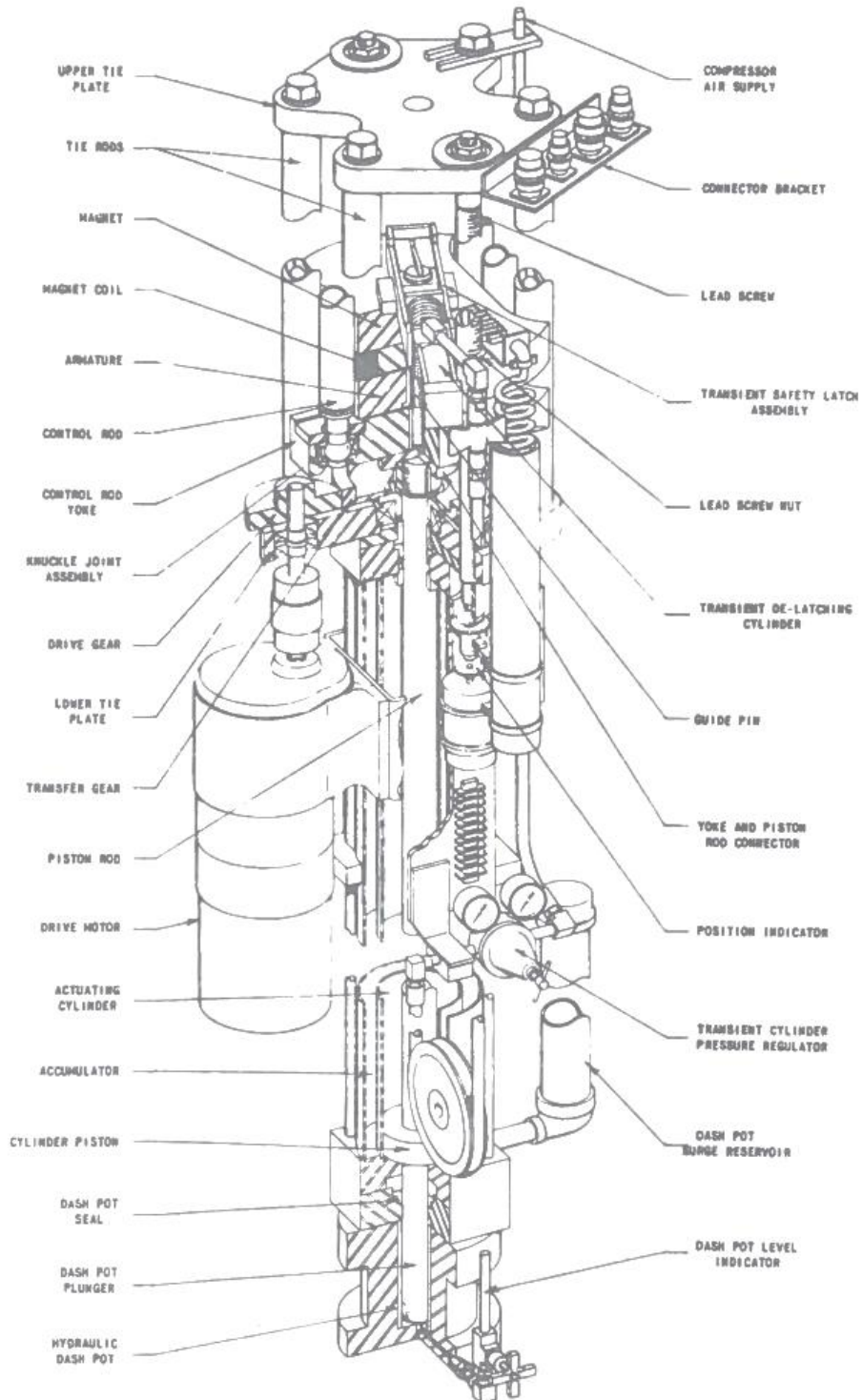
- [15] IAEA, [Online]. Available: https://www-pub.iaea.org/MTCD/Publications/PDF/SupplementaryMaterials/P1728/Summary_web.pdf. [Accessed 3 12 2020].
- [16] T. Nihara, M. Amaya and Y. Udagawa, "Experimental capability of Nuclear Safety Research Reactor (NSRR)," in *GAIN Fuel Safety Research Workshop*, Idaho Falls, 2017.
- [17] IRSN, "Research Reactor: CABRI," 2020. [Online]. Available: <https://www.irsn.fr/EN/Research/Research-organisation/Research-programmes/CABRI-International-program/Pages/CABRI-Facility.aspx>. [Accessed 10 January 2021].
- [18] R. C. Singleterry Jr. , "TREAT versus CABRI Comparison for the DOE Fuel Minimization Project," Argonne National Laboratory, 1997.
- [19] K. R. DePriest and P. J. Cooper, "MCNP/MCNPX Model of the Annular Core Research Reactor," Sandia National Laboratory, Albuquerque, New Mexico, 2006.
- [20] Sandia National Laboratory, "Experiment Handbook: Annular Core Research Reactor," Albuquerque, New Mexico, 2015.
- [21] P. Royl, W. Breitung, E. A. Fischer, G. Schumacher, R. O. Gaunt and S. A. Wright, "Contributions from the ACRR In-Pile Experiments to the Understanding of Phenomena Influencing Unprotected Loss of Flow Accident Simulations in LMFBRs," *Nuclear Engineering and Design*, no. 100, pp. 387-408, 1987.
- [22] L. W. Deitrich, C. E. Dickerman, A. E. Klickman and A. E. Wright, "A Review of Experiments and Results from the Transient Reactor Test (TREAT) Facility," in *ANS Winter Meeting*, Washington, D.C., 1998.
- [23] C. B. Jensen, N. E. Woolstenhulme and D. M. Wachs, "The TREAT Experiment Legacy Supporting LWR Fuel Technology," in *Top Fuel*, Prague, Czech Republic, 2018.
- [24] Idaho National Laboratory, *Validation of the Methodology Used at the TREAT Reactor to Calculate Reactivity Addition From Reactor Period*, TEV-2146, 2015.
- [25] L. f. R. M. t. L. Harrison, *Request for Technical Feasibility Evaluation of the Fast Shutdown System Verification Tests*, Idaho National Laboratory: RWN-11-89, 1989.
- [26] X.-5. M. C. Team, "MCNP-A General Monte Carlo N-Particle Transport Code," Los Alamos National Laboratory, Los Alamos, 2008.
- [27] J. D. Bess, T. Ivanova, I. Hill and L. Scott, The 2020 Edition of the IRPhEP Handbook.
- [28] J. D. Bess, T. Ivanova, L. Scott and I. Hill, The 202 Edition of the ICSBEP Handbook.
- [29] Idaho National Laboratory, *MCNP Model Validation for TREAT Source Term Generation*, TEV-2326, Idaho Falls, 2015.

- [30] Idaho National Laboratory, *Neutronics Analysis of Baseline Configuration Multi-SERTTA Experiment Vehicle in TREAT, ECAR-3372*, Idaho Falls, 2017.
- [31] Idaho National Laboratory, *Neutronics Analysis of the MARCH-SERTTA Capsule*, Idaho Falls, 2020.
- [32] Siemens, "Simcenter STAR-CCM+," Siemens, 2021. [Online]. Available: <https://www.plm.automation.siemens.com/global/en/products/simcenter/STAR-CCM.html>. [Accessed May 2021].
- [33] S. Balderrama, G. Mignot, W. Marcum and N. Woolstenhulme, "CFD Modeling of the Gas Injection System for the Out-of-Pile HENRI Facility," in *18th International Topical Meeting on Nuclear Reactor Thermal Hydraulics - NURETH*, Portland Oregon, 2019.
- [34] J. K. Shultis and R. E. Faw, "An MCNP Primer," 2011. [Online]. Available: <https://www.mne.k-state.edu/~jks/MCNPprmr.pdf>. [Accessed 14 11 2021].
- [35] "Nuclear Data Center at KAERI," 2018. [Online]. Available: <http://atom.kaeri.re.kr/>. [Accessed September 2018].
- [36] D. E. Cullen, C. J. Clouse, R. Procassini and R. C. Little, "Static and Dynamic Criticality: Are They Different? (UCRL-TR-201506)," Lawrence Livermore National Laboratory, Livermore, CA, 2003.
- [37] B. Heath, "Parametric Thermal Models of the Transient Reactor Test Facility (TREAT)," 2014.
- [38] R. O. Meyer, R. K. McCardell, H. M. Chung, D. J. Diamond and H. H. Scott, "A Regulatory Assessment of Test Data for Reactivity-Initiated Accidents," in *Nuclear Safety*, 1996.
- [39] E. Yang, "Topical Report on Reactivity Initiated Accident: Bases for RIA Fuel and Core Coolability Criteria," EPRI, Palo Alto, Ca., 2002.
- [40] J. I. M. Damian, A. Weir, V. L. Putman and J. D. Bess, "Power Burst Facility: U(18)O₂-CaO-ZrO₂ Fuel Rods in Water (INL/EXT--09-15446)," Idaho National Laboratory, Idaho Falls, 2009.
- [41] *Transient Analysis and Determination of Core Characterization Limits*, Idaho Falls, Idaho: Idaho National Laboratory, 2018.
- [42] A. Laporta, *Validation of the Methodology Used at the TREAT Reactor to Calculate Reactivity Addition from Reactor Period*, Idaho Falls, Idaho: Idaho National Laboratory, 2015.

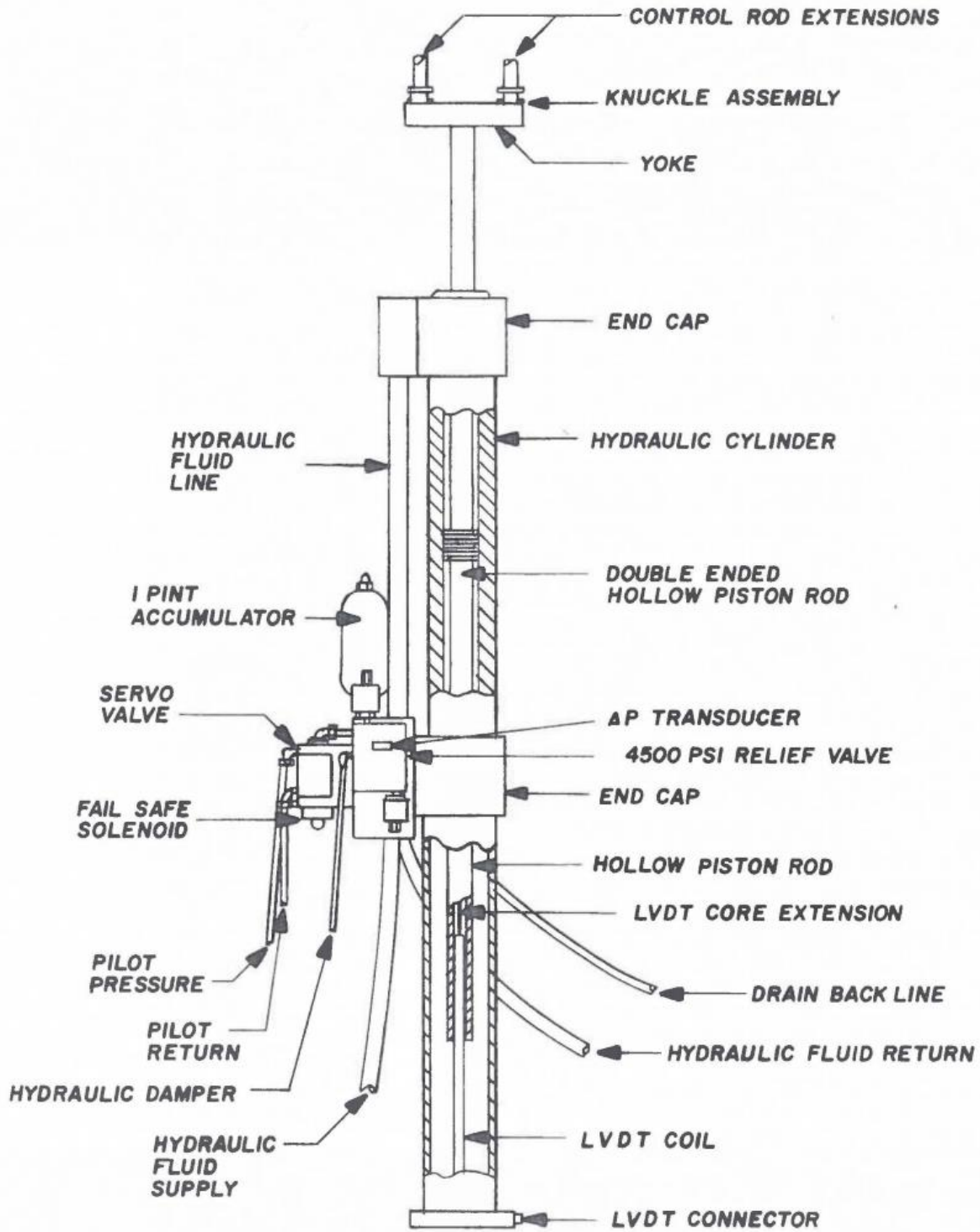
9 APPENDICES

Appendix A: Detailed Diagrams of the TREAT Control Rod Drives

Control Rod Drives

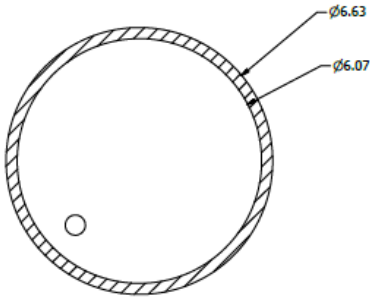
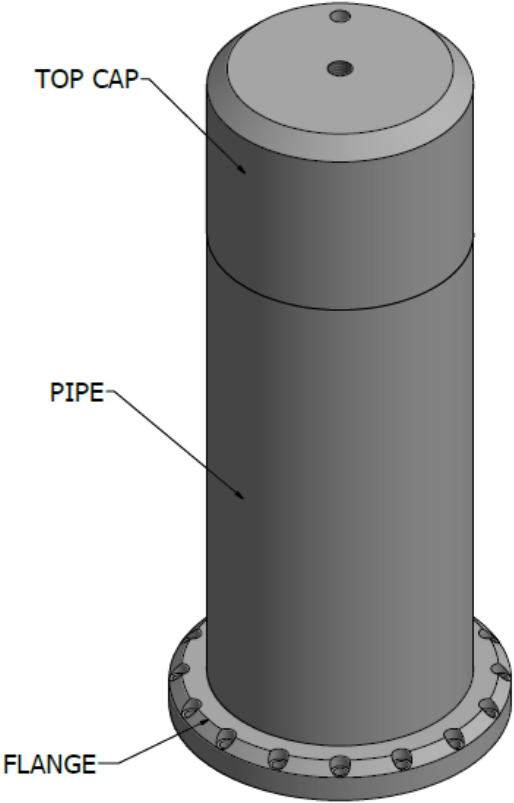
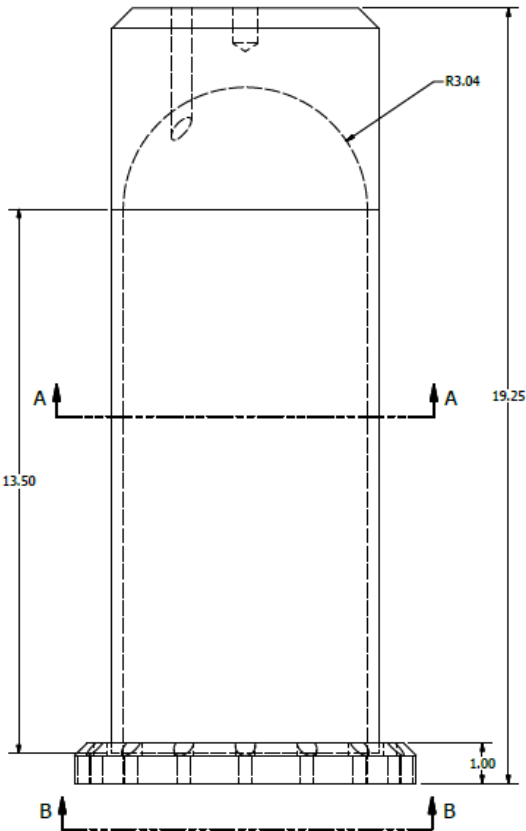


Transient Rod Drives

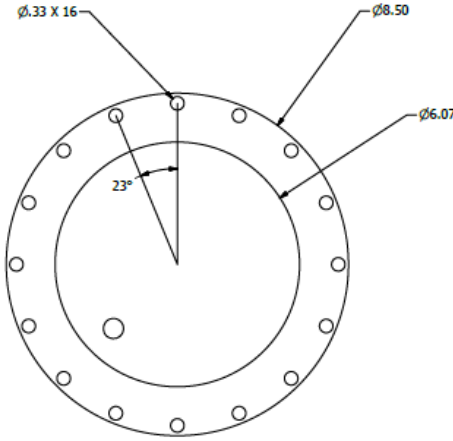


Appendix B: Detailed Design used for the HENRI Concept in this Evaluation.

Driver Tank

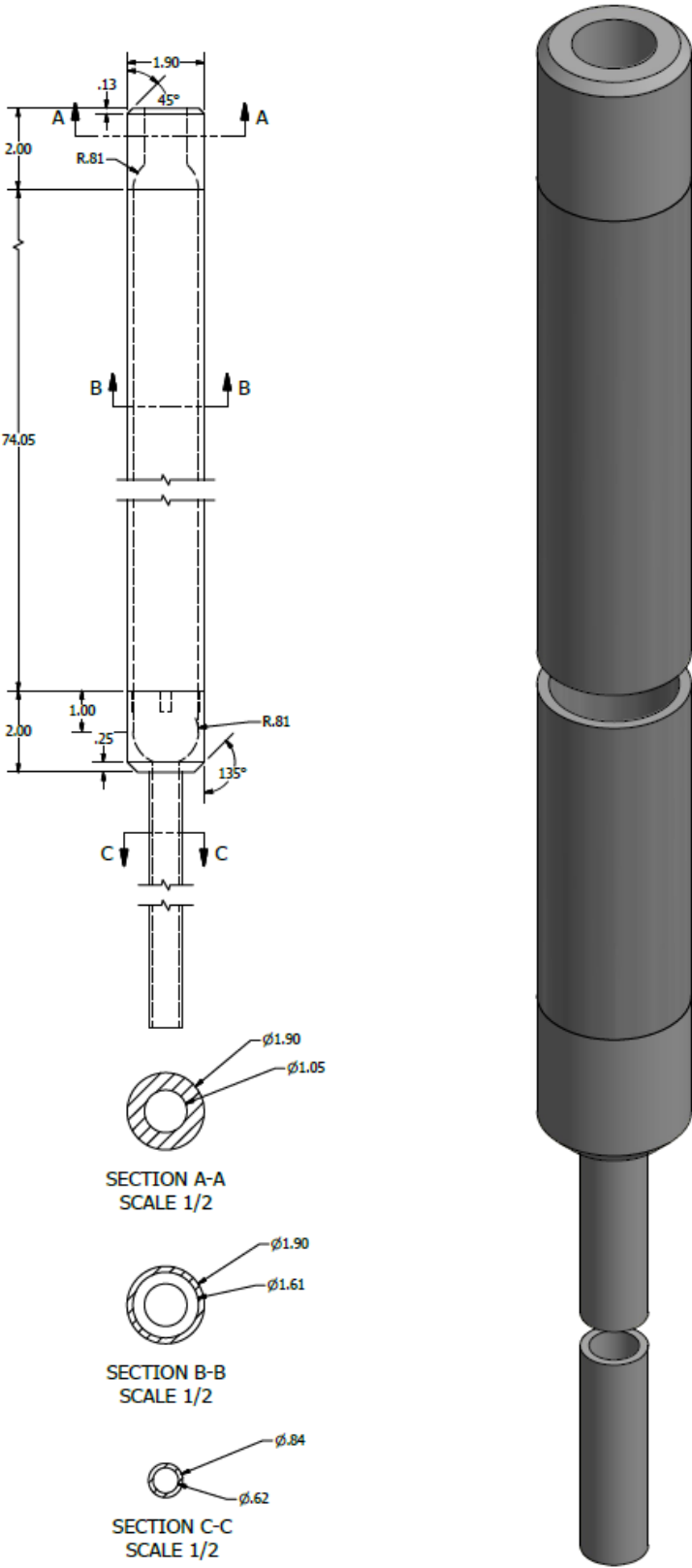


SECTION A-A
SCALE 1 / 2

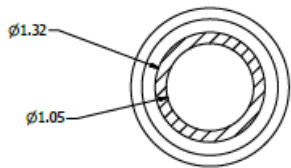
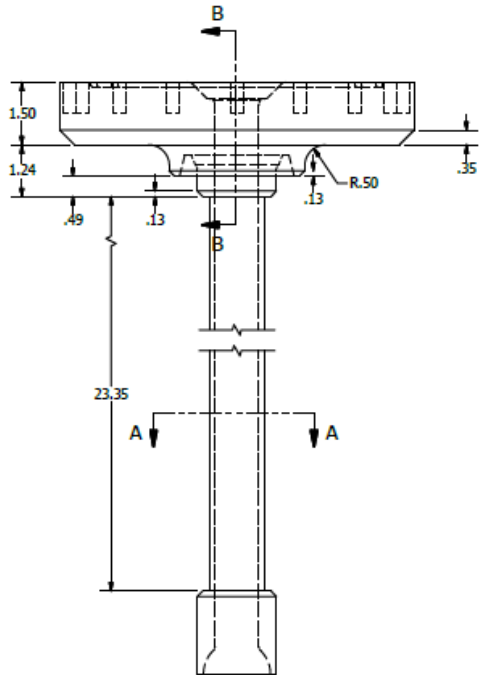
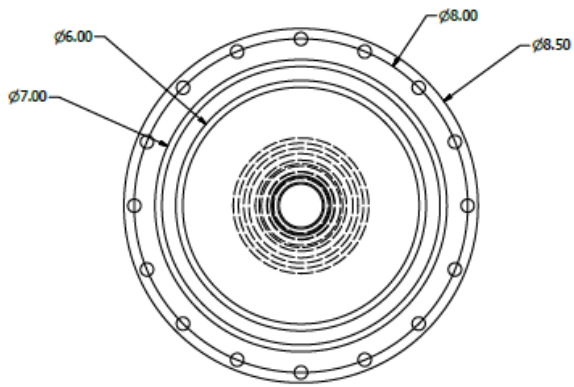


VIEW B-B
SCALE 1 / 2

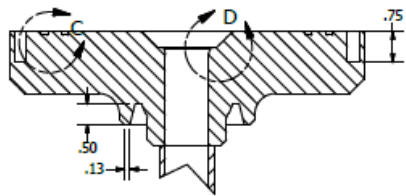
Gas Thimble with Vacuum Line



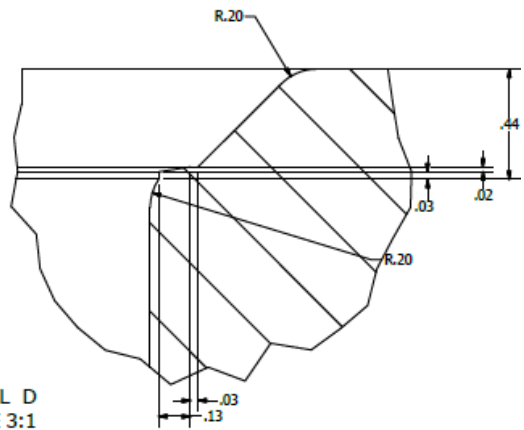
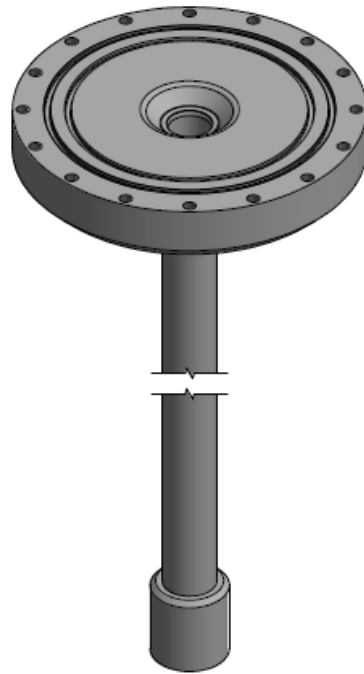
Transfer Line



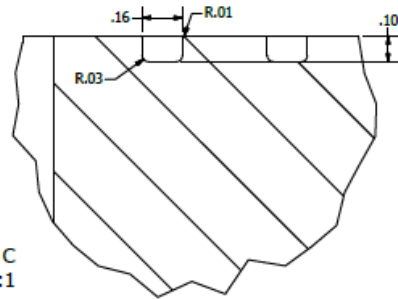
SECTION A-A
SCALE 1:1



SECTION B-B
SCALE 1/2



DETAIL D
SCALE 3:1



DETAIL C
SCALE 3:1

Appendix C: Initial Hand Calculations to Determine Driver Tank Pressure

NOTE: These calculations are based on initial estimates of the in core hardware and do not represent what is shown in Appendix B.

Initial Conditions used for the Evaluation:

Temperature	
C	K
100	373.15
Volume	
cm ³	m ³
1167	0.001167
Ideal Gas Const. (J/mol-K)	
8.314	
Atmospheric Pressure	
psi	Pa
14.6959	101325
MW	
g/mol	kg/mol
3.016	0.003016
Avogadro's No.	
6.02E+23	

Desired Atomic Density:

NOTE: This was determined prior to involvement in the project to provide an initial estimate.

Desired atomic density	
3.35E+20	atoms/cm ³

Created a table that provides moles of gas and atomic density based on the pressure. Used the ideal gas law to get the moles per volume and multiplied by Avogadro's number to get the atomic density.

Pressure		Atomic Density (N)			
psi	Pa	atoms/m ³	atoms/cm ³	moles/m ³	moles/cm ³
1	6894.75729	1.34E+24	1.33834E+18	2.222416827	2.2224E-06
100	689475.729	1.33834E+26	1.33834E+20	222.2416827	2.2224E-04
200	1378951.458	2.67668E+26	2.67668E+20	444.4833653	4.4448E-04
300	2068427.187	4.01502E+26	4.01502E+20	666.725048	6.6673E-04
400	2757902.916	5.35336E+26	5.35336E+20	888.9667306	8.8897E-04
500	3447378.645	6.6917E+26	6.6917E+20	1111.208413	1.1112E-03
600	4136854.374	8.03004E+26	8.03004E+20	1333.450096	1.3335E-03
700	4826330.103	9.36838E+26	9.36838E+20	1555.691779	1.5557E-03
800	5515805.832	1.07067E+27	1.07067E+21	1777.933461	1.7779E-03
900	6205281.561	1.20451E+27	1.20451E+21	2000.175144	2.0002E-03
1000	6894757.29	1.33834E+27	1.33834E+21	2222.416827	2.2224E-03

Linearly interpolated to get the pressure required in the gas thimble to get desired atomic density.

$$\text{Required Pressure} = 300 - (300 - 200) * \frac{(4.01502 * 10^{20} - 3.35 * 10^{20})}{(4.01502 * 10^{20} - 2.67668 * 10^{20})}$$

$$\text{Required Pressure} = 250.31 \text{ psi} = 1725.828 \text{ kPa}$$

Initially it was estimated that the chamber would be three times larger than the driver tank.

$$\text{Pressure Tank} = \frac{250.31 * (1 + \frac{1}{3})}{\frac{1}{3}} = 1001.24 \text{ psi}$$

To create a more reasonable number 1000 psig was assumed for the driver tank pressure.

Appendix D: MCNP Input File for Cosine Tally Card Test

Cosine Angle Test

c The objective of this model is to determine what angles are needed to verify incident neutrons coming into a surface but not the back scatter.
C To do this, cells were created with 0 importance to ensure there was no backscatter out of the cylinder once they went into the cylinder.

C

1 1 -1E-20 -10 -11 13 imp:n=0 \$ Setting importance to 0 allows for no back scatter to be observed in the results.

2 1 -1E-20 -10 -13 12 imp:n=0 \$ Setting importance to 0 allows for no back scatter to be observed in the results

3 0 -14 #1 #2 imp:n=1 \$ This allows for the source to be present and track all particles going into the cylinder from outside the cylinder (inside the sphere)

4 0 14 imp:n=0 \$ Empty Space!

10 cz 10 \$ Cylinder in center of sphere with radius

10 cm

11 pz 10 \$ Top of cylinder enclosure

12 pz -10 \$ Bottom of cylinder enclosure

13 PZ 0 \$ Plane dividing the cylinder in half

14 so 40 \$ Outer sphere to house the source and create an environment where neutrons can be tracked into the cylinder

m1 92238 1

SDEF POS=0 10.1 0 VEC=0 -1 0 \$ Source located on the y-axis (.1 cm from cylinder) directed at the cylinder

c

F2:n 10 \$ Surface tally to tally neutrons coming into the cylinder on the outside edge (radially)

fs2 -12 -11 \$ The upper and lower bounds of where we want the tally to count

*c2 90 0 \$ Captures all angle bins from 180 to 0 and puts it in angle bins from 180 to 90 and 90 to 0.

Sd2 3.142 3.142 1

c

nps 10000

Appendix E: Example MCNP Input File for HENRI Evaluations

NOTE: Some portions of the MCNP input file were removed to shorten the length of the appendix. Places where that was done are documented in the body of the input file.

```
Model of the TREAT Reactor with Half Slot and HENRI (Filled) - HENRI Project
c Model of the maximum pulse at TREAT ~ 4.45%dk/k with clip T=1
c
c Conversion of TREAT reactor model created by A. W. LaPorta in SCALE6.1.1 to
c MCNP6.1 by A. S. Chipman March-July 2017.
c Added BUSTER Experiment Vehicle for MARCH System May 2018.
c Added MARCH-SERTTA Capsule June 2018.
c Updated materials May-June 2018.
c Removed experiment attributes and added HENRI April 2020
c
c *****
c *****
c *          u=1      Standard Fuel Assembly          *
c *          u=2      Zircaloy Dummy Assembly         *
c *          u=3      Half Zircaloy Dummy Assembly (South) *
c *          u=4      Half Slotted Zircaloy Dummy Assembly (North) *
c *          u=5      48" Access Hole(Slotted) Assembly Zircaloy 3 *
c *          u=6      Aluminum Dummy Assembly         *
c *          u=7      M8 Calibration Experiment        *
c *          u=8      Air Void for M8 Calibration Experiment *
c *          u=9      Air Void for Fuel Assembly with Grid Plate *
c *          u=10     48" Access Hole(Slotted) Assembly Zircaloy 4 *
c *          u=15     HENRI Control Rod Assembly      *
c *          u=47     Half Slotted Zircaloy Dummy Assembly (South) *
c *
c *          u=11     Control Rod Assemblies 1 Northeast *
c *          u=12     Control Rod Assemblies 2 Southeast *
c *          u=13     Control Rod Assemblies 3 Southwest *
c *          u=14     Control Rod Assemblies 4 Northwest *
c *
c *          u=21     Compensation Rod Assembly 1 Northeast *
c *          u=22     Compensation Rod Assembly 2 Southeast *
c *          u=23     Compensation Rod Assembly 3 Southwest *
c *          u=24     Compensation Rod Assembly 4 Northwest *
c *
c *          u=31     Transient Rod Assemblies 1 Northeast *
c *          u=32     Transient Rod Assemblies 2 Southeast *
c *          u=33     Transient Rod Assemblies 3 Southwest *
c *          u=34     Transient Rod Assemblies 4 Northwest *
c *
c *
c *          u=41     Standard Fuel Assembly with Northeast Pedestal *
c *          u=42     Standard Fuel Assembly with East Pedestal *
c *          u=43     Standard Fuel Assembly with Southeast Pedestal *
c *          u=44     Standard Fuel Assembly with Northwest Pedestal *
c *          u=45     Standard Fuel Assembly with West Pedestal *
c *          u=46     Standard Fuel Assembly with Northwest Pedestal *
c *
c *
c *****
c *****
c
c
c *****
c *****Cell Cards*****
c *****
c
```

Removal of portions of the TREAT baseline model cell cards that were not added as part of this evaluation or do not impact the HENRI analysis to reduce the size of the document.

c

```

C *****HENRI*****
C
1005 22  4.3461E-02  (-100178 100179 -100123 100180):(100180 -100181 -100179)  $ HENRI Tube
                                     imp:n,p=1
                                     u=15
1006 11  6.77697E-5  (-100179 100187 -100123 100182)      imp:n,p=1 $ TS1
                                     u=15
1012 11  6.77697E-5  (-100187 100188 -100123 100182)      imp:n,p=1 $ TS1 D-1
                                     u=15
1013 11  6.77697E-5  (-100188 100189 -100123 100182)      imp:n,p=1 $ TS1 D-2
                                     u=15
1014 11  6.77697E-5  (-100189 100190 -100123 100182)      imp:n,p=1 $ TS1 D-3
                                     u=15
1015 11  6.77697E-5  (-100190 100191 -100123 100182)      imp:n,p=1 $ TS1 D-4
                                     u=15
1016 11  6.77697E-5  (-100191 100192 -100123 100182)      imp:n,p=1 $ TS1 D-5
                                     u=15
1017 11  6.77697E-5  (-100192 -100123 100182)      imp:n,p=1 $ TS1 D-6
                                     u=15
1007 11  5.64487E-5  (-100179 100187 -100182 100183)      imp:n,p=1 $ TS2
                                     u=15
1018 11  5.64487E-5  (-100187 100188 -100182 100183)      imp:n,p=1 $ TS2 D-1
                                     u=15
1019 11  5.64487E-5  (-100188 100189 -100182 100183)      imp:n,p=1 $ TS2 D-2
                                     u=15
1020 11  5.64487E-5  (-100189 100190 -100182 100183)      imp:n,p=1 $ TS2 D-3
                                     u=15
1021 11  5.64487E-5  (-100190 100191 -100182 100183)      imp:n,p=1 $ TS2 D-4
                                     u=15
1022 11  5.64487E-5  (-100191 100192 -100182 100183)      imp:n,p=1 $ TS2 D-5
                                     u=15
1023 11  5.64487E-5  (-100192 -100182 100183)      imp:n,p=1 $ TS2 D-6
                                     u=15
1008 11  4.15639E-5  (-100179 100187 -100183 100184)      imp:n,p=1 $ TSC
                                     u=15
1024 11  4.15639E-5  (-100187 100188 -100183 100184)      imp:n,p=1 $ TSC D-1
                                     u=15
1025 11  4.15639E-5  (-100188 100189 -100183 100184)      imp:n,p=1 $ TSC D-2
                                     u=15
1026 11  4.15639E-5  (-100189 100190 -100183 100184)      imp:n,p=1 $ TSC D-3
                                     u=15
1027 11  4.15639E-5  (-100190 100191 -100183 100184)      imp:n,p=1 $ TSC D-4
                                     u=15
1028 11  4.15639E-5  (-100191 100192 -100183 100184)      imp:n,p=1 $ TSC D-5
                                     u=15
1029 11  4.15639E-5  (-100192 -100183 100184)      imp:n,p=1 $ TSC D-6
                                     u=15
1009 11  2.77052E-5  (-100179 100187 -100184 100185)      imp:n,p=1 $ TS3
                                     u=15
1030 11  2.77052E-5  (-100187 100188 -100184 100185)      imp:n,p=1 $ TS3 D-1
                                     u=15
1031 11  2.77052E-5  (-100188 100189 -100184 100185)      imp:n,p=1 $ TS3 D-2
                                     u=15
1032 11  2.77052E-5  (-100189 100190 -100184 100185)      imp:n,p=1 $ TS3 D-3
                                     u=15
1033 11  2.77052E-5  (-100190 100191 -100184 100185)      imp:n,p=1 $ TS3 D-4
                                     u=15
1034 11  2.77052E-5  (-100191 100192 -100184 100185)      imp:n,p=1 $ TS3 D-5
                                     u=15
1035 11  2.77052E-5  (-100192 -100184 100185)      imp:n,p=1 $ TS3 D-6
                                     u=15
1010 11  1.54799E-5  (-100179 100187 -100185 100186)      imp:n,p=1 $ TS4
                                     u=15
1036 11  1.54799E-5  (-100187 100188 -100185 100186)      imp:n,p=1 $ TS4 D-1
                                     u=15
1037 11  1.54799E-5  (-100188 100189 -100185 100186)      imp:n,p=1 $ TS4 D-2
                                     u=15
1038 11  1.54799E-5  (-100189 100190 -100185 100186)      imp:n,p=1 $ TS4 D-3
                                     u=15
1039 11  1.54799E-5  (-100190 100191 -100185 100186)      imp:n,p=1 $ TS4 D-4
                                     u=15

```

```

1040 11 1.54799E-5 (-100191 100192 -100185 100186) imp:n,p=1 $ TS4 D-5
                                         u=15
1041 11 1.54799E-5 (-100192 -100185 100186) imp:n,p=1 $ TS4 D-6
                                         u=15
1011 11 2.75037E-5 (-100179 100187 -100186 100181) imp:n,p=1 $ TS5
                                         u=15
1042 11 2.75037E-5 (-100187 100188 -100186 100181) imp:n,p=1 $ TS5 D-1
                                         u=15
1043 11 2.75037E-5 (-100188 100189 -100186 100181) imp:n,p=1 $ TS5 D-2
                                         u=15
1044 11 2.75037E-5 (-100189 100190 -100186 100181) imp:n,p=1 $ TS5 D-3
                                         u=15
1045 11 2.75037E-5 (-100190 100191 -100186 100181) imp:n,p=1 $ TS5 D-4
                                         u=15
1046 11 2.75037E-5 (-100191 100192 -100186 100181) imp:n,p=1 $ TS5 D-5
                                         u=15
1047 11 2.75037E-5 (-100192 -100186 100181) imp:n,p=1 $ TS5 D-6
                                         u=15

```

Removal of portions of the TREAT baseline model cell cards that were not added as part of this evaluation or do not impact the HENRI analysis to reduce the size of the document.

```

c
c *****core fuel lattice
100700 0 -13631 13630 -13633 13632 -13635 13634 $ for fuel and grid plate
                                         lat=1
                                         tmp=2.530048E-8
                                         u=90
                                         fill=-9:9 -9:9 0:0
c
c
c A B C D E F G H J K L M N O P R S T U
2 2 1 1 1 1 1 1 1 1 1 1 1 1 1 1 1 1 2 2 $ 19
2 1 1 1 1 1 1 1 1 1 1 1 1 1 1 1 1 1 1 2 $ 18
1 1 1 1 1 1 1 13 1 1 1 12 1 1 1 1 1 1 1 $ 17
1 1 1 1 1 1 13 1 1 1 1 1 1 1 12 1 1 1 1 1 $ 16
1 1 1 1 1 1 1 1 1 1 1 1 1 1 1 1 1 1 1 1 $ 15
1 1 1 33 1 1 1 15 1 1 1 15 1 1 1 32 1 1 1 $ 14
1 1 1 1 1 1 1 1 1 1 1 1 1 1 1 1 1 1 1 1 $ 13
1 1 33 1 1 23 1 1 1 1 1 1 1 22 1 1 32 1 1 $ 12
1 1 1 1 1 1 1 1 1 46 3 43 1 1 1 1 1 1 1 1 $ 11
1 1 1 1 1 1 1 1 45 0 42 1 1 1 1 1 1 1 1 1 $ 10
1 1 1 1 1 1 1 1 44 4 41 1 1 1 1 1 1 1 1 1 $ 09
1 1 34 1 1 24 1 1 1 5 1 1 1 21 1 1 31 1 1 $ 08
1 1 1 1 1 1 1 1 1 1 5 1 1 1 1 1 1 1 1 1 $ 07
1 1 1 34 1 1 1 15 1 5 1 15 1 1 1 31 1 1 1 $ 06
1 1 1 1 1 1 1 1 1 5 1 1 1 1 1 1 1 1 1 1 $ 05
1 1 1 1 1 1 14 1 1 5 1 1 1 11 1 1 1 1 1 1 $ 04
1 1 1 1 1 1 1 1 14 1 5 1 11 1 1 1 1 1 1 1 $ 03
2 1 1 1 1 1 1 1 1 5 1 1 1 1 1 1 1 1 2 $ 02
2 2 1 1 1 1 1 1 1 5 1 1 1 1 1 1 2 2 $ 01
c
c A B C D E F G H J K L M N O P R S T U
c
                                         imp:n,p=1
c *****fuel area of reactor core
100800 0 (13636 -13637 13638 -13639 13640 -13641)
(-13648:13649:-13650:13651:-13652:13653) $ cutout for experiment from fuel
lattice
(-60205:60206:-60145:60152:-2381:13653) $ 2381 not 8247
                                         fill=90
                                         imp:n,p=1
                                         tmp=2.530048E-8
                                         u=100
c *****experiment area of reactor core
100801 0 (13648 -13649 13650 -13651 13652 -13653): $ section removed from fuel
lattice for experiment
(60205 -60206 60145 -60152 2381 -13653) $ 2381 not 8247
                                         imp:n,p=1
                                         tmp=2.530048E-8
                                         u=100
c *****biological shield exterior boundary

```

```

c 100900 0          (-13424:13425:-13426:13427:-13428:13429)  $ edge of biological shield and
area of importance (cut off grid plate top, assembly top)
c                  : (13430:13431:13432:13433:-13434:13435)
c
c                  imp:n,p=0
c                  tmp=2.530048E-8
c                  u=0
c *****cut off window for reactor core only*****
c 101000 0          (13118 -13119 13120 -13121 741 -2381) $13428 -13429)  $ cut off window
outer reflector steel liner, grid plate top, assembly top
c
c                  fill=100
c                  imp:n,p=1
c                  tmp=2.530048E-8
c                  u=0
c 101001 0          (-13118:13119:-13120:13121:-741:2381) $-13428:13429)  $ outside of cut
off window
c
c                  imp:n,p=0
c                  tmp=2.530048E-8
c                  u=0
c *****cut off window for reactor with bioshield*****
101010 0          (13424 -13425 13426 -13427 741 -2381 $13428 -13429):  $ cut off window
grid plate top, assembly top
-13430 -13431 -13432 -13433)$ 741 -2381)
c
c                  fill=100
c                  imp:n,p=1
c                  tmp=2.530048E-8
c                  u=0
101011 0          (-13424:13425:-13426:13427:-741:2381):  $-13428:13429):  $ outside of cut
off window
(13430:13431:13432:13433:-741:2381)
c
c                  imp:n,p=0
c                  tmp=2.530048E-8
c                  u=0
c
c --- for geometry error/volumes checks ---
c
c 101011 0          ((-13424:13425:-13426:13427:-741:13429): $2381):  $-13428:13429):  $
outside of cut off window for geometry check/volumes
c
c                  (13430:13431:13432:13433:-741:13429)) $2381)
c
c                  (-70000)
c
c                  imp:n,p=1
c                  tmp=2.530048E-8
c                  u=0
c 101012 0          (70000)  $ for
geometry check/volumes
c
c                  imp:n,p=0
c                  tmp=2.530048E-8
c                  u=0
c
c *****
c *****Surface Cards*****
c *****
c

```

Removal of portions of the TREAT baseline model surface cards that were not added as part of this evaluation or do not impact the HENRI analysis to reduce the size of the document.

```

c
c %%%%%%%%%%%%%%%%%%%%%%%%%%%%%%
c %%%%%%%%%%%%%%%%%%%%%%%%%% HENRI Surfaces %%%%%%%%%%%%%%%%%%%%%%%%%%
c %%%%%%%%%%%%%%%%%%%%%%%%%%%%%%
c
c
c *****Fuel Section Control Rod Element*****
c
100100 PX 5.0292
100101 PX 4.9657
100102 PX -5.0292
100103 PX -4.9657
100104 PY 5.0292
100105 PY 4.9657

```

```

100106 PY -5.0292
100107 PY -4.9657
100108 P -5.0292 -3.906774 0 -4.46786 -4.46786 1 -3.906774 -5.0292 0
100109 P -4.9657 -3.880358 0 -4.423156 -4.423156 1 -3.880358 -4.9657 0
100110 P 5.0292 3.906774 0 4.46786 4.46786 1 3.906774 5.0292 0
100111 P 4.9657 3.880358 0 4.423156 4.423156 1 3.880358 4.9657 0
100112 P 5.0292 -3.906774 0 4.46786 -4.46786 1 3.906774 -5.0292 0
100113 P 4.9657 -3.880358 0 4.423156 -4.423156 1 3.880358 -4.9657 0
100114 P -5.0292 3.906774 0 -4.46786 4.46786 1 -3.906774 5.0292 0
100115 P -4.9657 3.880358 0 -4.423156 4.423156 1 -3.880358 4.9657 0
100116 PZ 62.70625
100117 PZ -62.70625
100118 CZ 2.8575
100119 CZ 2.54
100120 PZ -130.4131
100121 PZ 70.485
c *****Fuel Block*****
c
100122 CZ 2.9591
100123 PZ 61.11875
100124 PZ -61.11875
c *****Bearing Tube*****
100125 CZ 3.15595
100126 CZ 2.8702
100127 PZ 75.40625
100128 PZ 61.75375
100129 CZ 2.54
100130 PZ 135.6519
100131 TRC 0 0 133.1119 0 0 2.54 3.81 3.175
100132 PZ 133.1119
c *****Base Fuel Assembly*****
100133 PZ -121.8406
100134 PZ -119.9356
100135 CZ 2.87782
c *****Plug-Long Lower*****
100136 PZ -83.4231
100137 CZ 2.877344
c *****Plug-Short Lower*****
100138 PZ -61.35685
100139 PZ -70.24685
100140 PX 4.1656
100141 PY 4.1656
100142 PX -4.1656
100143 PY -4.1656
c *****Plug-Long Upper*****
100144 PZ 124.0631
100145 PZ 83.42313
100146 CZ 3.25755
c *****Plug-Short Upper*****
100147 PZ 70.24688
100148 PZ 61.35688
c *****Upper Clad*****
100149 PZ 125.9681
c *****Head Fuel Assembly*****
100150 CZ 3.37312
100151 PZ 124.0631
100152 PX 5.08
100153 PX -5.08
100154 PY 5.08
100155 PY -5.08
100156 PX 4.9657
100157 PX -4.9657
100158 PY 4.9657
100159 PY -4.9657
100160 PZ 130.89
c 100145 C/Y 0 127.715 0.51054 $ Small hole on side of assembly
100161 TRC 0 0 130.89 0 0 -1.169 3.731 3.15595
100162 P 5.08 0 128.35 5.08 1 128.35 3.81 0 130.89
100163 P -5.08 0 128.35 -5.08 1 128.35 -3.81 0 130.89
100164 P 0 5.08 128.35 1 5.08 128.35 0 3.81 130.89
100165 P 0 -5.08 128.35 1 -5.08 128.35 0 -3.81 130.89

```

```

100166 P 3.9688 5.08 128.35 5.08 3.9688 128.35 3.81 3.4427 130.89
100167 P 3.9688 -5.08 128.35 5.08 -3.9688 128.35 3.81 -3.4427 130.89
100168 P -5.08 3.9688 128.35 -3.9688 5.08 128.35 -3.4427 3.81 130.89
100169 P -5.08 -3.9688 128.35 -3.9688 -5.08 128.35 -3.4427 -3.81 130.89
100170 P 3.9688 5.08 128.35 5.08 3.9688 128.35 3.9688 5.08 129
100171 P 3.9688 -5.08 128.35 5.08 -3.9688 128.35 3.9688 -5.08 129
100172 P -5.08 3.9688 128.35 -3.9688 5.08 128.35 -5.08 3.9688 129
100173 P -5.08 -3.9688 128.35 -3.9688 -5.08 128.35 -5.08 -3.9688 129
100174 P 3.9161 4.9530 128.35 4.9531 3.9161 128.35 3.9161 4.9530 127
100175 P 3.9161 -4.9530 128.35 4.9531 -3.9161 128.35 3.9161 -4.9530 127
100176 P -4.9530 3.9161 128.35 -3.9161 4.9531 128.35 -4.9530 3.9161 127
100177 P -4.9530 -3.9161 128.35 -3.9161 -4.9531 128.35 -4.9530 -3.9161 127
c *****HENRI*****
100178 CZ 2.413
100179 CZ 2.0447
100180 PZ -121.7613
100181 PZ -121.393
100182 PZ 31.90875 $ TS1
100183 PZ 8.41375 $ TS2
100184 PZ -8.09625 $ TSC
100185 PZ -31.59125 $ TS3
100186 PZ -79.21625 $ TS4
100187 CZ 1.7272 $ He-3 Division 1
100188 CZ 1.4097 $ He-3 Division 2
100189 CZ 1.0922 $ He-3 Division 3
100190 CZ 0.7747 $ He-3 Division 4
100191 CZ 0.4572 $ He-3 Division 5
100192 CZ 0.1397 $ He-3 Division 6
c #####
c #####

c *****
c *****Data Cards*****
c *****
c
c *****
c *****Material Cards*****
c *****
c
c --- Reactor Materials ---
c
c --- Urania-Graphite Fuel 6.781 ppm Boron--- Web Elements Data
c
c atom density 8.6538E-02
c
m999 5010.80c 1.3004E-07 5011.80c 5.2342E-07
      6000.80c 8.6503E-02
      8016.80c 1.8645E-05 8017.80c 4.5417E-08
      23050.80c 1.5338E-09 23051.80c 6.1200E-07
      26054.80c 2.9114E-07 26056.80c 4.5702E-06
      26057.80c 1.0555E-07 26058.80c 1.4046E-08
      92234.80c 8.5471E-08 92235.80c 8.7200E-06
      92236.80c 3.9858E-08 92238.80c 4.9985E-07
c
mt999 grph.20t o2-u.20t u-o2.20t fe56.22t
c
c --- Urania-Graphite Fuel --- Web Elements Data
c
c atom density 8.6536E-02
c
m1 5010.80c 1.1315E-07 5011.80c 4.5546E-07
   6000.80c 5.1033E-02 6000.80c 3.5463E-02 $ carbon split for possible
carbon/graphite treatment
   8016.80c 2.4035E-05 8017.80c 5.8547E-08
   23050.80c 1.5338E-09 23051.80c 6.1199E-07
   26054.80c 2.9114E-07 26056.80c 4.5702E-06
   26057.80c 1.0555E-07 26058.80c 1.4046E-08
   92234.80c 8.5471E-08 92235.80c 8.7200E-06
   92236.80c 3.9859E-08 92238.80c 4.9985E-07
c
mt1 grph.20t o2-u.20t u-o2.20t fe56.22t

```

```

c
c --- Zircaloy 3 --- Web Elements Data
c
c atom density 4.3473E-02
c
m2      1001.80c 8.5821E-05      1002.80c 9.8705E-09
        3006.80c 4.3001E-08      3007.80c 5.2354E-07
        4009.80c 4.3634E-07
        5010.80c 7.2384E-08      5011.80c 2.9135E-07
        6000.80c 3.9289E-05
        7014.80c 1.4265E-05      7015.80c 5.2691E-08
        8016.80c 2.2557E-04      8017.80c 5.4947E-07
        11023.80c 1.7105E-06
        12024.80c 1.2780E-07      12025.80c 1.6179E-08
        12026.80c 1.7813E-08
        13027.80c 7.2871E-07
        14028.80c 1.2913E-06      14029.80c 6.5571E-08
        14030.80c 4.3225E-08
        15031.80c 1.2696E-06
        19039.80c 9.3796E-07      19040.80c 1.1767E-10
        19041.80c 6.7690E-08
        20040.80c 9.5116E-07      20042.80c 6.3482E-09
        20043.80c 1.3246E-09      20044.80c 2.0467E-08
        20046.80c 3.9247E-11      20048.80c 1.8348E-09
        21045.80c 8.7472E-06
        22046.80c 5.4220E-08      22047.80c 4.8897E-08
        22048.80c 4.8450E-07      22049.80c 3.5555E-08
        22050.80c 3.4044E-08
        23050.80c 1.9298E-10      23051.80c 7.7001E-08
        24050.80c 3.2860E-09      24052.80c 6.3368E-08
        24053.80c 7.1854E-09      24054.80c 1.7886E-09
        25055.80c 7.1578E-08
        26054.80c 1.0701E-05      26056.80c 1.6798E-04
        26057.80c 3.8795E-06      26058.80c 5.1629E-07
        27059.80c 6.6726E-08
        28058.80c 4.5610E-08      28060.80c 1.7569E-08
        28061.80c 7.6372E-10      28062.80c 2.4351E-09
        28064.80c 6.2014E-10
        29063.80c 4.2804E-08      29065.80c 1.9078E-08
        30064.80c 2.9249E-08      30066.80c 1.6781E-08
        30067.80c 2.4660E-09      30068.80c 1.1277E-08
        30070.80c 3.7291E-10
        31069.80c 3.3901E-08      31071.80c 2.2499E-08
        32070.80c 1.1286E-08      32072.80c 1.4915E-08
        32073.80c 4.1864E-09      32074.80c 1.9648E-08
        32076.80c 4.1214E-09
        33075.80c 5.2486E-08
        34074.80c 4.4623E-10      34076.80c 4.6664E-09
        34077.80c 3.7999E-09      34078.80c 1.1838E-08
        34080.80c 2.4707E-08      34082.80c 4.3477E-09
        37085.80c 3.3205E-08      37087.80c 1.2805E-08
        38084.80c 2.5133E-10      38086.80c 4.4251E-09
        38087.80c 3.1416E-09      38088.80c 3.7062E-08
        39089.80c 4.4231E-07
        40090.80c 2.2019E-02      40091.80c 4.8018E-03
        40092.80c 7.3396E-03      40094.80c 7.4381E-03
        40096.80c 1.1983E-03
        41093.80c 4.2326E-07
        42092.80c 6.0813E-09      42094.80c 3.7906E-09
        42095.80c 6.5239E-09      42096.80c 6.8353E-09
        42097.80c 3.9135E-09      42098.80c 9.8883E-09
        42100.80c 3.9463E-09
        44096.80c 2.1555E-09      44098.80c 7.2757E-10
        44099.80c 4.9646E-09      44100.80c 4.9023E-09
        44101.80c 6.6376E-09      44102.80c 1.2275E-08
        44104.80c 7.2445E-09
        45103.80c 3.8213E-08
        46102.80c 3.7690E-10      46104.80c 4.1164E-09
        46105.80c 8.2512E-09      46106.80c 1.0099E-08
        46108.80c 9.7773E-09      46110.80c 4.3307E-09
        47107.80c 2.8342E-06      47109.80c 2.6336E-06

```

48106.80c	4.3728E-10	48108.80c	3.1134E-10
48110.80c	4.3693E-09	48111.80c	4.4777E-09
48112.80c	8.4412E-09	48113.80c	4.2748E-09
48114.80c	1.0050E-08	48116.80c	2.6202E-09
49113.80c	1.0285E-08	49115.80c	2.2946E-07
50112.80c	9.6396E-07	50114.80c	6.5589E-07
50115.80c	3.3788E-07	50116.80c	1.4449E-05
50117.80c	7.6322E-06	50118.80c	2.4069E-05
50119.80c	8.5365E-06	50120.80c	3.2377E-05
50122.80c	4.6012E-06	50124.80c	5.7540E-06
51121.80c	1.8477E-08	51123.80c	1.3819E-08
52120.80c	2.7736E-11	52122.80c	7.7045E-10
52123.80c	2.7428E-10	52124.80c	1.4608E-09
52125.80c	2.1788E-08	52126.80c	5.8061E-09
52128.80c	9.7816E-09	52130.80c	1.0503E-08
55133.80c	2.9588E-08		
56130.80c	3.0353E-11	56132.80c	2.8921E-11
56134.80c	6.9211E-10	56135.80c	1.8876E-09
56136.80c	2.2490E-09	56137.80c	3.2163E-09
56138.80c	2.0531E-08		
57138.80c	2.5479E-11	57139.80c	2.8284E-08
58136.80c	5.1920E-11	58138.80c	7.0443E-11
58140.80c	2.4824E-08	58142.80c	3.1192E-09
59141.80c	2.7907E-08		
60142.80c	7.4154E-09	60143.80c	3.3260E-09
60144.80c	6.4885E-09	60145.80c	2.2628E-09
60146.80c	4.6892E-09	60148.80c	1.5540E-09
60150.80c	1.5267E-09		
62144.80c	8.0290E-10	62147.80c	3.9203E-09
62148.80c	2.9396E-09	62149.80c	3.6143E-09
62150.80c	1.9301E-09	62152.80c	6.9959E-09
62154.80c	5.9498E-09		
63151.80c	1.2372E-08	63153.80c	1.3505E-08
64152.80c	5.0014E-11	64154.80c	5.4515E-10
64155.80c	3.7011E-09	64156.80c	5.1190E-09
64157.80c	3.9136E-09	64158.80c	6.2118E-09
64160.80c	5.4666E-09		
65159.80c	2.4743E-08		
66156.80c	1.4520E-11	66158.80c	2.4199E-11
66160.80c	5.6626E-10	66161.80c	4.5761E-09
66162.80c	6.1732E-09	66163.80c	6.0256E-09
66164.80c	6.8193E-09		
67165.80c	2.3843E-08		
68162.80c	3.2915E-11	68164.80c	3.7852E-10
68166.80c	7.9019E-09	68167.80c	5.3910E-09
68168.80c	6.2961E-09	68170.80c	3.5101E-09
69169.80c	2.3277E-08		
71175.80c	2.1893E-08	71176.80c	5.8210E-10
72174.80c	2.7848E-09	72176.80c	9.0505E-08
72177.80c	3.2373E-07	72178.80c	4.7480E-07
72179.80c	2.3705E-07	72180.80c	6.1073E-07
73180.80c	2.6078E-12	73181.80c	2.1729E-08
74180.80c	2.5668E-11	74182.80c	5.6684E-09
74183.80c	3.0224E-09	74184.80c	7.0724E-09
74186.80c	6.0812E-09		
75185.80c	7.8982E-09	75187.80c	1.3220E-08
77191.80c	7.6308E-09	77193.80c	1.2827E-08
78000.42c	2.0158E-08		
79197.80c	1.9965E-08		
80196.80c	2.9406E-11	80198.80c	1.9545E-09
80199.80c	3.3072E-09	80200.80c	4.5285E-09
80201.80c	2.5838E-09	80202.80c	5.8538E-09
80204.80c	1.3468E-09		
81203.80c	5.6778E-09	81205.80c	1.3560E-08
82204.80c	1.5942E-09	82206.80c	2.7443E-08
82207.80c	2.5166E-08	82208.80c	5.9669E-08
83209.80c	1.8817E-08		
90232.80c	1.6947E-08		
92234.80c	9.0863E-13	92235.80c	1.1895E-10
92238.80c	1.6401E-08		

c

```

mt2      al27.22t  fe56.22t
c
c --- Zircaloy 2 --- Web Elements Data
c
c atom density  4.3448E-02
c
m3      1001.80c  7.8267E-05    1002.80c  9.0007E-09
        7014.80c  8.4172E-06    7015.80c  3.1090E-08
        8016.80c  2.1888E-04    8017.80c  5.3318E-07
        12024.80c 2.5638E-06    12025.80c 3.2458E-07
        12026.80c 3.5736E-07
        13027.80c 8.7714E-06
        14028.80c 9.0671E-06    14029.80c 4.6041E-07
        14030.80c 3.0350E-07
        24050.80c 1.6481E-06    24052.80c 3.1781E-05
        24053.80c 3.6037E-06    24054.80c 8.9704E-07
        25055.80c 1.4359E-06
        26054.80c 8.2568E-06    26056.80c 1.2961E-04
        26057.80c 2.9934E-06    26058.80c 3.9836E-07
        28058.80c 1.3725E-05    28060.80c 5.2869E-06
        28061.80c 2.2982E-07    28062.80c 7.3275E-07
        28064.80c 1.8661E-07
        40090.80c 2.1825E-02    40091.80c 4.7595E-03
        40092.80c 7.2751E-03    40094.80c 7.3726E-03
        40096.80c 1.1878E-03
        50112.80c 4.8346E-06    50114.80c 3.2895E-06
        50115.80c 1.6946E-06    50116.80c 7.2469E-05
        50117.80c 3.8278E-05    50118.80c 1.2071E-04
        50119.80c 4.2813E-05    50120.80c 1.6238E-04
        50122.80c 2.3076E-05    50124.80c 2.8858E-05
        82204.80c 5.3303E-09    82206.80c 9.1757E-08
        82207.80c 8.4142E-08    82208.80c 1.9950E-07

```

```

c
mt3      al27.22t  fe56.22t
c
c --- Air --- Web Elements Data
c
c atom density  5.0109E-05
c
m4      1001.80c  4.9600E-07    1002.80c  5.7046E-11
        2003.80c  1.7798E-16    2004.80c  1.2991E-10
        6000.80c  9.4635E-09
        7014.80c  3.8576E-05    7015.80c  1.4248E-07
        8016.80c  1.0627E-05    8017.80c  2.5887E-08
        10020.42c 4.5074E-10
        18036.80c 7.7922E-10    18038.80c 1.4635E-10
        18040.80c 2.3064E-07
        36078.80c 9.8924E-14    36080.80c 6.4442E-13
        36082.80c 3.2730E-12    36083.80c 3.2475E-12
        36084.80c 1.6110E-11    36086.80c 4.8897E-12

```

```

c
mt4      lwtr.20t  hwtr.20t
c
c --- CP-2 Graphite --- Web Elements Data
c
c atom density  8.3709E-02
c
m5      1001.80c  2.2391E-05    1002.80c  2.5753E-09
        2003.80c  2.3036E-17    2004.80c  1.6815E-11
        3006.80c  7.3680E-09    3007.80c  8.9708E-08
        4009.80c  5.5795E-09
        5010.80c  6.4791E-09    5011.80c  2.6079E-08
        6000.80c  8.3657E-02
        7014.80c  4.9928E-06    7015.80c  1.8441E-08
        8016.80c  1.2513E-05    8017.80c  3.0481E-08
        9019.80c  5.2935E-09
        10020.42c 5.8338E-11
        11023.80c 2.1872E-09
        12024.80c 1.9610E-09    12025.80c 2.4826E-10
        12026.80c 2.7334E-10
        13027.80c 8.2000E-08

```

14028.80c	2.3118E-06	14029.80c	1.1739E-07
14030.80c	7.7382E-08		
15031.80c	2.1105E-08		
16032.80c	1.3398E-06	16033.80c	1.0726E-08
16034.80c	6.0546E-08	16036.80c	2.8226E-10
17035.80c	9.6733E-09	17037.80c	3.0917E-09
18036.80c	1.0085E-10	18038.80c	1.8942E-11
18040.80c	2.9851E-08		
19039.80c	2.3988E-09	19040.80c	3.0094E-13
19041.80c	1.7311E-10		
20040.80c	3.8921E-06	20042.80c	2.5976E-08
20043.80c	5.4201E-09	20044.80c	8.3750E-08
20046.80c	1.6059E-10	20048.80c	7.5078E-09
21045.80c	2.2370E-10		
22046.80c	2.0800E-08	22047.80c	1.8758E-08
22048.80c	1.8586E-07	22049.80c	1.3640E-08
22050.80c	1.3060E-08		
23050.80c	5.9225E-09	23051.80c	2.3631E-06
24050.80c	4.2019E-10	24052.80c	8.1030E-09
24053.80c	9.1881E-10	24054.80c	2.2871E-10
25055.80c	3.6611E-10		
26054.80c	6.5260E-09	26056.80c	1.0244E-07
26057.80c	2.3659E-09	26058.80c	3.1486E-10
27059.80c	1.7065E-10		
28058.80c	1.6330E-08	28060.80c	6.2904E-09
28061.80c	2.7344E-10	28062.80c	8.7185E-10
28064.80c	2.2203E-10		
29063.80c	1.6420E-09	29065.80c	7.3187E-10
30064.80c	3.7401E-10	30066.80c	2.1458E-10
30067.80c	3.1533E-11	30068.80c	1.4421E-10
30070.80c	4.7684E-12		
31069.80c	8.6699E-11	31071.80c	5.7540E-11
32070.80c	1.4432E-10	32072.80c	1.9072E-10
32073.80c	5.3532E-11	32074.80c	2.5125E-10
32076.80c	5.2701E-11		
33075.80c	6.7115E-10		
34074.80c	5.7060E-12	34076.80c	5.9671E-11
34077.80c	4.8590E-11	34078.80c	1.5137E-10
34080.80c	3.1593E-10	34082.80c	5.5595E-11
35079.80c	6.3799E-10	35081.80c	6.2062E-10
36078.80c	1.2803E-14	36080.80c	8.3406E-14
36082.80c	4.2361E-13	36083.80c	4.2032E-13
36084.80c	2.0851E-12	36086.80c	6.3286E-13
37085.80c	4.2460E-10	37087.80c	1.6373E-10
38084.80c	7.7130E-11	38086.80c	1.3580E-09
38087.80c	9.6412E-10	38088.80c	1.1374E-08
39089.80c	5.6558E-10		
40090.80c	1.9285E-09	40091.80c	4.2055E-10
40092.80c	6.4282E-10	40094.80c	6.5144E-10
40096.80c	1.0495E-10		
41093.80c	5.4123E-10		
42092.80c	7.7763E-11	42094.80c	4.8471E-11
42095.80c	8.3422E-11	42096.80c	8.7404E-11
42097.80c	5.0043E-11	42098.80c	1.2644E-10
42100.80c	5.0462E-11		
44096.80c	2.7562E-11	44098.80c	9.3035E-12
44099.80c	6.3483E-11	44100.80c	6.2687E-11
44101.80c	8.4876E-11	44102.80c	1.5697E-10
44104.80c	9.2637E-11		
45103.80c	9.7728E-11		
46102.80c	4.8195E-12	46104.80c	5.2637E-11
46105.80c	1.0551E-10	46106.80c	1.2913E-10
46108.80c	1.2502E-10	46110.80c	5.5377E-11
47107.80c	2.4161E-10	47109.80c	2.2451E-10
48106.80c	5.5915E-12	48108.80c	3.9811E-12
48110.80c	5.5870E-11	48111.80c	5.7257E-11
48112.80c	1.0794E-10	48113.80c	5.4663E-11
48114.80c	1.2852E-10	48116.80c	3.3504E-11
49113.80c	1.8788E-11	49115.80c	4.1915E-10
50112.80c	4.1088E-12	50114.80c	2.7957E-12
50115.80c	1.4402E-12	50116.80c	6.1589E-11

50117.80c	3.2531E-11	50118.80c	1.0259E-10
50119.80c	3.6386E-11	50120.80c	1.3800E-10
50122.80c	1.9612E-11	50124.80c	2.4526E-11
51121.80c	2.3626E-10	51123.80c	1.7671E-10
52120.80c	3.5467E-13	52122.80c	9.8518E-12
52123.80c	3.5072E-12	52124.80c	1.8679E-11
52125.80c	2.7861E-10	52126.80c	7.4243E-11
52128.80c	1.2508E-10	52130.80c	1.3430E-10
53127.80c	7.9247E-11		
55133.80c	3.7834E-10		
56130.80c	3.8813E-13	56132.80c	3.6982E-13
56134.80c	8.8501E-12	56135.80c	2.4137E-11
56136.80c	2.8758E-11	56137.80c	4.1127E-11
56138.80c	2.6253E-10		
57138.80c	3.2580E-13	57139.80c	3.6167E-10
58136.80c	6.6391E-13	58138.80c	9.0077E-13
58140.80c	3.1742E-10	58142.80c	3.9885E-11
59141.80c	3.5686E-10		
60142.80c	9.4822E-11	60143.80c	4.2531E-11
60144.80c	8.2969E-11	60145.80c	2.8935E-11
60146.80c	5.9961E-11	60148.80c	1.9871E-11
60150.80c	1.9522E-11		
62144.80c	2.0534E-12	62147.80c	1.0026E-11
62148.80c	7.5178E-12	62149.80c	9.2434E-12
62150.80c	4.9361E-12	62152.80c	1.7892E-11
62154.80c	1.5216E-11		
63151.80c	3.1640E-11	63153.80c	3.4539E-11
64152.80c	1.2791E-13	64154.80c	1.3942E-12
64155.80c	9.4652E-12	64156.80c	1.3091E-11
64157.80c	1.0009E-11	64158.80c	1.5886E-11
64160.80c	1.3980E-11		
65159.80c	6.3280E-11		
66156.80c	3.7133E-14	66158.80c	6.1888E-14
66160.80c	1.4482E-12	66161.80c	1.1703E-11
66162.80c	1.5788E-11	66163.80c	1.5410E-11
66164.80c	1.7440E-11		
67165.80c	6.0976E-11		
68162.80c	8.4177E-14	68164.80c	9.6803E-13
68166.80c	2.0208E-11	68167.80c	1.3787E-11
68168.80c	1.6102E-11	68170.80c	8.9769E-12
69169.80c	5.9531E-11		
71175.80c	5.5989E-11	71176.80c	1.4887E-12
72174.80c	9.0149E-14	72176.80c	2.9299E-12
72177.80c	1.0480E-11	72178.80c	1.5370E-11
72179.80c	7.6740E-12	72180.80c	1.9771E-11
73180.80c	6.6694E-11	73181.80c	5.5571E-07
74180.80c	3.2822E-13	74182.80c	7.2482E-11
74183.80c	3.8648E-11	74184.80c	9.0436E-11
74186.80c	7.7761E-11		
75185.80c	2.0199E-11	75187.80c	3.3809E-11
77191.80c	1.9515E-11	77193.80c	3.2804E-11
78000.42c	5.1552E-11		
79197.80c	5.1058E-10		
80196.80c	7.5204E-13	80198.80c	4.9985E-11
80199.80c	8.4579E-11	80200.80c	1.1581E-10
80201.80c	6.6079E-11	80202.80c	1.4971E-10
80204.80c	3.4443E-11		
81203.80c	7.2602E-11	81205.80c	1.7339E-10
82204.80c	3.3975E-12	82206.80c	5.8486E-11
82207.80c	5.3633E-11	82208.80c	1.2717E-10
83209.80c	2.4061E-10		
90232.80c	2.1670E-10		
92234.80c	1.1619E-14	92235.80c	1.5210E-12
92238.80c	2.0972E-10		
c			
mt5	al27.22t	fe56.22t	grph.20t
c			
c	Al-2 alloy (SCALE Composition)		
m66	13027.80c	5.9477E-2	
	50112.80c	4.2433E-6	50114.80c 2.8872E-6 \$ only Sn-112,120 yes GPD
	50115.80c	1.4873E-6	50116.80c 6.3605E-5

50117.80c	3.3596E-5	50118.80c	1.0595E-4
50119.80c	3.7577E-5	50120.80c	1.4252E-4
50122.80c	2.0254E-5	50124.80c	2.5328E-5

c
c --- Aluminum 6063 --- Web Elements Data

c
c atom density 5.9986E-02

m6	12024.80c	4.7558E-04	12025.80c	6.0208E-05
	12026.80c	6.6289E-05		
	13027.80c	5.8755E-02		
	14028.80c	3.2036E-04	14029.80c	1.6267E-05
	14030.80c	1.0724E-05		
	22046.80c	2.8023E-06	22047.80c	2.5272E-06
	22048.80c	2.5041E-05	22049.80c	1.8377E-06
	22050.80c	1.7595E-06		
	24050.80c	1.3587E-06	24052.80c	2.6201E-05
	24053.80c	2.9710E-06	24054.80c	7.3955E-07
	25055.80c	2.9596E-05		
	26054.80c	5.9562E-06	26056.80c	9.3500E-05
	26057.80c	2.1593E-06	26058.80c	2.8737E-07
	27059.80c	1.3795E-05		
	28058.80c	9.4294E-06	28060.80c	3.6322E-06
	28061.80c	1.5789E-07	28062.80c	5.0342E-07
	28064.80c	1.2821E-07		
	29063.80c	1.7698E-05	29065.80c	7.8884E-06
	30064.80c	1.2094E-05	30066.80c	6.9385E-06
	30067.80c	1.0196E-06	30068.80c	4.6630E-06
	30070.80c	1.5419E-07		
	50112.80c	6.6429E-08	50114.80c	4.5199E-08
	50115.80c	2.3284E-08	50116.80c	9.9575E-07
	50117.80c	5.2595E-07	50118.80c	1.6587E-06
	50119.80c	5.8827E-07	50120.80c	2.2312E-06
	50122.80c	3.1708E-07	50124.80c	3.9652E-07

c
mt6 al27.22t fe56.22t

c
c --- Boron Carbide --- Web Elements Data

c
c atom density 8.7032E-02

m7	5010.80c	1.3881E-02	5011.80c	5.5871E-02
	6000.80c	1.7187E-02		
	11023.80c	4.1911E-07		
	13027.80c	3.5710E-05		
	14028.80c	3.1641E-05	14029.80c	1.6067E-06
	14030.80c	1.0591E-06		
	20040.80c	2.3306E-06	20042.80c	1.5555E-08
	20043.80c	3.2456E-09	20044.80c	5.0150E-08
	20046.80c	9.6164E-11	20048.80c	4.4957E-09
	22046.80c	1.6607E-06	22047.80c	1.4976E-06
	22048.80c	1.4839E-05	22049.80c	1.0890E-06
	22050.80c	1.0427E-06		
	25055.80c	1.7538E-07		

c
mt7 grph.20t al27.22t

c
c --- Mild, Low Carbon Steel 1018 --- Web Elements Data

c
c atom density 8.5498E-02

m8	6000.80c	7.8918E-04		
	15031.80c	4.5903E-05		
	16032.80c	4.9107E-05	16033.80c	3.9314E-07
	16034.80c	2.2192E-06	16036.80c	1.0346E-08
	22046.80c	2.0421E-07	22047.80c	1.8416E-07
	22048.80c	1.8248E-06	22049.80c	1.3391E-07
	22050.80c	1.2822E-07		
	23050.80c	1.8607E-08	23051.80c	7.4241E-06
	24050.80c	5.9405E-06	24052.80c	1.1456E-04
	24053.80c	1.2990E-05	24054.80c	3.2335E-06

	25055.80c	7.7640E-04		
	26054.80c	4.8714E-03	26056.80c	7.6471E-02
	26057.80c	1.7660E-03	26058.80c	2.3503E-04
	28058.80c	1.0994E-04	28060.80c	4.2349E-05
	28061.80c	1.8409E-06	28062.80c	5.8695E-06
	28064.80c	1.4948E-06		
	29063.80c	1.0318E-04	29065.80c	4.5987E-05
	41093.80c	4.0809E-06		
	42092.80c	4.3975E-06	42094.80c	2.7411E-06
	42095.80c	4.7176E-06	42096.80c	4.9428E-06
	42097.80c	2.8300E-06	42098.80c	7.1505E-06
	42100.80c	2.8537E-06		
c				
c	mt8	fe56.22t		
c				
c	Inconel (SCALE Composition)			
m9	14028.80c	4.1032E-3	14029.80c	2.0845E-4
	14030.80c	1.3757E-4		
	22046.80c	2.1537E-4	22047.80c	1.9422E-4
	22048.80c	1.9245E-3	22049.80c	1.4123E-4
	22050.80c	1.3522E-4		
	24050.80c	6.2651E-4	24052.80c	1.2082E-2
	24053.80c	1.3699E-3	24054.80c	3.4101E-4
	26054.80c	3.6620E-4	26056.80c	5.7486E-3
	26057.80c	1.3275E-4	26058.80c	1.7668E-5
	28058.80c	4.2321E-2	28060.80c	1.6302E-2
	28061.80c	7.0863E-4	28062.80c	2.2594E-3
	28064.80c	5.7541E-4		
c				
c	Fuel Pin T-433 Fuel U-10 wt% Zr (SCALE Composition)			
m10	92234.80c	2.2296E-4	92235.80c	2.3656E-2
	92236.80c	1.2959E-4	92238.80c	1.0401E-2
	40090.80c	4.9524E-3	40091.80c	1.0800E-3
	40092.80c	1.6508E-3	40094.80c	1.6729E-3
	40096.80c	2.6952E-4		
c				
c	Helium-3			
m11	2003.80c	1		
c				
c	Sodium Bonding (SCALE Composition)			
m12	11023.80c	2.5408E-2		
c				
c	--- Stainless Steel 304 --- Web Elements Data			
c				
c	atom density	8.8333E-02		
c				
m13	6000.80c	4.0111E-04		
	7014.80c	3.4268E-04	7015.80c	1.2657E-06
	14028.80c	1.1865E-03	14029.80c	6.0249E-05
	14030.80c	3.9717E-05		
	15031.80c	6.9992E-05		
	16032.80c	4.2787E-05	16033.80c	3.4255E-07
	16034.80c	1.9336E-06	16036.80c	9.0144E-09
	24050.80c	8.0516E-04	24052.80c	1.5527E-02
	24053.80c	1.7606E-03	24054.80c	4.3825E-04
	25055.80c	1.7538E-03		
	26054.80c	3.2763E-03	26056.80c	5.1430E-02
	26057.80c	1.1877E-03	26058.80c	1.5807E-04
	28058.80c	6.7054E-03	28060.80c	2.5829E-03
	28061.80c	1.1228E-04	28062.80c	3.5799E-04
	28064.80c	9.1169E-05		
c				
c	mt13	fe56.22t		
c				
c	Fuel Cladding HT-9 (SCALE Composition)			
m14	26054.80c	4.1689E-3	26056.80c	6.5439E-2
	26057.80c	1.5113E-3	26058.80c	2.0112E-4
	24050.80c	4.7108E-4	24052.80c	9.0844E-3
	24053.80c	1.0301E-3	24054.80c	2.5641E-4
	28058.80c	3.3951E-4	28060.80c	1.3078E-4
	28061.80c	5.6849E-6	28062.80c	1.8126E-5

28064.80c	4.6162E-6			
42092.80c	7.4848E-5	42094.80c	4.6774E-5	
42095.80c	8.0575E-5	42096.80c	4.4528E-5	
42097.80c	4.8446E-5	42098.80c	1.2259E-4	
42100.80c	4.9004E-5			\$ Mo-100 no GPD
14028.80c	4.6510E-4	14029.80c	2.3627E-5	
14030.80c	1.5594E-5			
23050.80c	6.9510E-7	23051.80c	2.7734E-4	
6000.80c	1.1006E-3			
25055.80c	5.9297E-4			
74184.80c	1.2327E-4			
c				
c	Dysprosium (SCALE Composition)			
m15	66156.80c	1.8492E-4	66158.80c	3.0973E-5
	66160.80c	7.4983E-4	66161.80c	6.0435E-3
	66162.80c	8.1004E-3	66163.80c	7.8676E-3
	66164.80c	8.8761E-3		
c				
c	Plenum Gas (SCALE Composition)			
m16	2003.80c	2.0053E-6	2004.80c	2.0053E-2 \$ He-3, 4 no GPD
	18036.80c	2.2635E-5	18038.80c	4.2511E-6 \$ Ar-36, 38, 40 no GPD
	18040.80c	6.6996E-3		
c				
c	--- Lead --- Web Elements Data			
c				
c	atom density	3.2965E-02		
c				
m17	26054.80c	7.1475E-08	26056.80c	1.1220E-06
	26057.80c	2.5912E-08	26058.80c	3.4484E-09
	28058.80c	3.9604E-07	28060.80c	1.5255E-07
	28061.80c	6.6313E-09	28062.80c	2.1144E-08
	28064.80c	5.3847E-09		
	29063.80c	1.1150E-06	29065.80c	4.9697E-07
	30064.80c	5.0794E-07	30066.80c	2.9142E-07
	30067.80c	4.2825E-08	30068.80c	1.9574E-07
	30070.80c	6.4759E-09		
	33075.80c	9.1148E-07		
	47107.80c	3.2813E-06	47109.80c	3.0490E-06
	50112.80c	5.5801E-09	50114.80c	3.7967E-09
	50115.80c	1.9559E-09	50116.80c	8.3643E-08
	50117.80c	4.4180E-08	50118.80c	1.3933E-07
	50119.80c	4.9415E-08	50120.80c	1.8942E-07
	50122.80c	2.6635E-08	50124.80c	3.3308E-08
	51121.80c	3.2086E-07	51123.80c	2.3999E-07
	82204.80c	4.6111E-04	82206.80c	7.9376E-03
	82207.80c	7.2789E-03	82208.80c	1.7259E-02
	83209.80c	1.6339E-05		
c				
mt17	fe56.22t			
c				
c	--- High Density Concrete (Hematite/Magnetite) --- Web Elements Data			
c				
c	atom density	1.0082E-01		
c				
m20	1001.80c	2.4759E-02	1002.80c	2.8476E-06
	8016.80c	4.9393E-02	8017.80c	1.2032E-04
	11023.80c	3.4241E-05		
	12024.80c	9.9820E-04	12025.80c	1.2637E-04
	12026.80c	1.3913E-04		
	13027.80c	1.2488E-03		
	14028.80c	1.5962E-03	14029.80c	8.1052E-05
	14030.80c	5.3430E-05		
	16032.80c	5.0325E-05	16033.80c	4.0290E-07
	16034.80c	2.2743E-06	16036.80c	1.0603E-08
	19039.80c	2.1011E-05	19040.80c	2.6360E-09
	19041.80c	1.5163E-06		
	20040.80c	2.7148E-03	20042.80c	1.8119E-05
	20043.80c	3.7806E-06	20044.80c	5.8418E-05
	20046.80c	1.1202E-07	20048.80c	5.2369E-06
	22046.80c	6.3574E-05	22047.80c	5.7332E-05
	22048.80c	5.6808E-04	22049.80c	4.1689E-05

```

22050.80c 3.9917E-05
23050.80c 4.2478E-08 23051.80c 1.6949E-05
24050.80c 1.2134E-07 24052.80c 2.3398E-06
24053.80c 2.6532E-07 24054.80c 6.6044E-08
25055.80c 2.9917E-05
26054.80c 1.0853E-03 26056.80c 1.7036E-02
26057.80c 3.9344E-04 26058.80c 5.2360E-05

```

```

c
mt20    al27.22t  fe56.22t
c
c --- Aluminum 1100 --- Web Elements Data
c

```

```

c atom density 6.0148E-02
c
m21     13027.80c 5.9607E-02
        14028.80c 2.5456E-04 14029.80c 1.2926E-05
        14030.80c 8.5209E-06
        25055.80c 1.4853E-05
        26054.80c 8.1134E-06 26056.80c 1.2736E-04
        26057.80c 2.9414E-06 26058.80c 3.9144E-07
        27059.80c 1.3846E-05
        28058.80c 9.4643E-06 28060.80c 3.6456E-06
        28061.80c 1.5847E-07 28062.80c 5.0528E-07
        28064.80c 1.2868E-07
        29063.80c 3.5528E-05 29065.80c 1.5835E-05
        30064.80c 1.2139E-05 30066.80c 6.9642E-06
        30067.80c 1.0234E-06 30068.80c 4.6802e-06
        30070.80c 1.5476E-07
        50112.80c 6.6675E-08 50114.80c 4.5367E-08
        50115.80c 2.3371E-08 50116.80c 9.9944E-07
        50117.80c 5.2790E-07 50118.80c 1.6648E-06
        50119.80c 5.9045E-07 50120.80c 2.2395E-06
        50122.80c 3.1825E-07 50124.80c 3.9799E-07

```

```

c
mt21    al27.22t  fe56.22t
c
c --- Zircaloy 4 ---
c

```

```

c atom density 4.3461E-02
c
m22     1001.80c 9.7972E-05 1002.80c 1.1268E-08
        5010.80c 3.6358E-08 5011.80c 1.4635E-07
        6000.80c 8.8806E-05
        7014.80c 2.2480E-05 7015.80c 8.3032E-08
        12024.80c 2.5677E-06 12025.80c 3.2507E-07
        12026.80c 3.5790E-07
        13027.80c 1.0981E-05
        14028.80c 1.5567E-05 14029.80c 7.9047E-07
        14030.80c 5.2108E-07
        20040.80c 2.8666E-06 20042.80c 1.9132E-08
        20043.80c 3.9920E-09 20044.80c 6.1684E-08
        20046.80c 1.1828E-10 20048.80c 5.5297E-09
        22046.80c 3.4043E-07 22047.80c 3.0701E-07
        22048.80c 3.0420E-06 22049.80c 2.2324E-07
        22050.80c 2.1375E-07
        24050.80c 4.2915E-06 24052.80c 8.2757E-05
        24053.80c 9.3840E-06 24054.80c 2.3359E-06
        25055.80c 3.5954E-06
        26054.80c 9.9233E-06 26056.80c 1.5577E-04
        26057.80c 3.5975E-06 26058.80c 4.7876E-07
        27059.80c 1.3406E-06
        28058.80c 3.2074E-06 28060.80c 1.2355E-06
        28061.80c 5.3706E-08 28062.80c 1.7124E-07
        28064.80c 4.3609E-08
        29063.80c 2.1500E-06 29065.80c 9.5830E-07
        40090.80c 2.1792E-02 40091.80c 4.7523E-03
        40092.80c 7.2640E-03 40094.80c 7.3614E-03
        40096.80c 1.1860E-03
        41093.80c 4.2521E-06
        42092.80c 3.0546E-07 42094.80c 1.9040E-07
        42095.80c 3.2769E-07 42096.80c 3.4334E-07

```

```

42097.80c 1.9657E-07 42098.80c 4.9669E-07
42100.80c 1.9822E-07
48106.80c 2.1964E-10 48108.80c 1.5639E-10
48110.80c 2.1947E-09 48111.80c 2.2491E-09
48112.80c 4.2400E-09 48113.80c 2.1472E-09
48114.80c 5.0483E-09 48116.80c 1.3161E-09
50112.80c 5.4875E-06 50114.80c 3.7338E-06
50115.80c 1.9235E-06 50116.80c 8.2257E-05
50117.80c 4.3448E-05 50118.80c 1.3702E-04
50119.80c 4.8596E-05 50120.80c 1.8431E-04
50122.80c 2.6193E-05 50124.80c 3.2756E-05
72174.80c 3.5412E-09 72176.80c 1.1509E-07
72177.80c 4.1166E-07 72178.80c 6.0377E-07
72179.80c 3.0144E-07 72180.80c 7.7663E-07
74180.80c 2.5786E-09 74182.80c 5.6944E-07
74183.80c 3.0363E-07 74184.80c 7.1049E-07
74186.80c 6.1092E-07
92234.80c 3.1948E-12 92235.80c 4.1823E-10
92238.80c 5.7666E-08

```

```

c
mt22 al27.22t fe56.22t
c
c --- Aluminum 6061 --- Web Elements Data
c
c atom density 5.9634E-02
c

```

```

m23 12024.80c 6.3411E-04 12025.80c 8.0277E-05
12026.80c 8.8385E-05
13027.80c 5.7760E-02
14028.80c 4.2715E-04 14029.80c 2.1690E-05
14030.80c 1.4298E-05
22046.80c 4.2035E-06 22047.80c 3.7908E-06
22048.80c 3.7562E-05 22049.80c 2.7565E-06
22050.80c 2.6393E-06
24050.80c 4.7554E-06 24052.80c 9.1704E-05
24053.80c 1.0399E-05 24054.80c 2.5884E-06
25055.80c 4.4394E-05
26054.80c 1.1912E-05 26056.80c 1.8700E-04
26057.80c 4.3187E-06 26058.80c 5.7473E-07
27059.80c 1.3795E-05
28058.80c 9.4294E-06 28060.80c 3.6322E-06
28061.80c 1.5789E-07 28062.80c 1.5789E-07
28064.80c 1.2821E-07
29063.80c 7.0794E-05 29065.80c 3.1554E-05
30064.80c 3.0235E-05 30066.80c 1.7346E-05
30067.80c 2.5491E-06 30068.80c 1.1657E-05
30070.80c 3.8547E-07
50112.80c 6.6429E-08 50114.80c 4.5199E-08
50115.80c 2.3284E-08 50116.80c 9.9575E-07
50117.80c 5.2595E-07 50118.80c 1.6587E-06
50119.80c 5.8827E-07 50120.80c 2.2312E-06
50122.80c 3.1708E-07 50124.80c 3.9652E-07

```

```

c
mt23 al27.22t fe56.22t
c

```

```

c *****
c *****Tally Cards*****
c *****

```

```

c --- Reactor Tallies ---
c

```

```

c fc9984 fission density for core fuel (fiss/cc)
c fm9984 -1 999 -6
c f9984:n (3000 11000 12000 13000 14000 15000 16000)
c (20000 21000 22000 23000)
c (30000 31000 32000 33000)
c (40000 41000 42000 43000)
c
c T

```

```

c sd9984      3.402963E6
c             6.1197184E4
c             3.0598592E4
c             6.1197184E4
c             3.55595596E6
c
c --- HENRI Tallies ---
c
c
fc4           Absorption within the HENRI system
fmesh4:n     geom=rzt   origin=20.32 40.64 -121.263
             imesh=2.8702   iints=400
             jmesh=242.526  jints=1000
             kmesh=1   kints=50
fm4      1    11    -2
c
fmesh14:n    geom=xyz   origin=-100.0 -100.0 -122.0
             imesh=100.0   iints=100
             jmesh=100.0   jints=100
             kmesh=122.0   kints=100
c
fc2           Flux across the surface (#/cm^2)
f2:n         676
e2           0 45I 1E-06 5I 1E-01 1I 1
sd2          1 1.4428E04 1
fs2          -100120 -100121
*C2          90 0
c
fc12         Flux across the He-3 surface (#/cm^2)
f12:n        100179
e12          0 45I 1E-06 5I 1E-01 1I 1
sd12         1 1.11E04 1
fs12         -100180 -100123
*C12         90 0
c
fc22         Flux across the He-3 surface 1 (#/cm^2)
f22:n        100187
e22          0 45I 1E-06 5I 1E-01 1I 1
sd22         1 7.94E03 1
fs22         -100180 -100123
*C22         90 0
c
fc32         Flux across the He-3 surface 2 (#/cm^2)
f32:n        100188
e32          0 45I 1E-06 5I 1E-01 1I 1
sd32         1 6.48E03 1
fs32         -100180 -100123
*C32         90 0
c
fc42         Flux across the He-3 surface 3 (#/cm^2)
f42:n        100189
e42          0 45I 1E-06 5I 1E-01 1I 1
sd42         1 5.02E03 1
fs42         -100180 -100123
*C42         90 0
c
fc52         Flux across the He-3 surface 4 (#/cm^2)
f52:n        100190
e52          0 45I 1E-06 5I 1E-01 1I 1
sd52         1 3.56E03 1
fs52         -100180 -100123
*C52         90 0
c
fc62         Flux across the He-3 surface 5 (#/cm^2)
f62:n        100191
e62          0 45I 1E-06 5I 1E-01 1I 1
sd62         1 2.10E03 1
fs62         -100180 -100123
*C62         90 0
c
fc72         Flux across the He-3 surface 6 (#/cm^2)

```

```

f72:n      100192
e72        0 45I 1E-06 5I 1E-01 1I 1
sd72       1 6.42E02 1
fs72       -100180 -100123
*C72       90 0
c
fc6        HENRI Heat Generation Rate
f6:n,p     1005
c
fc16       HENRI Heat Generation Rate each
f16:n,p    (1005<100700 [2 4 0])
           (1005<100700 [2 -4 0])
           (1005<100700 [-2 4 0])
           (1005<100700 [-2 -4 0])
           T
c
fc26       Helium-3 Heat Generation Rate each
f26:n,p    (1006<100700 [2 4 0])
           (1007<100700 [2 4 0])
           (1008<100700 [2 4 0])
           (1009<100700 [2 4 0])
           (1010<100700 [2 4 0])
           (1011<100700 [2 4 0])
           T
c
fc36       Helium-3 Heat Generation Rate each
f36:n,p    (1006<100700 [-2 4 0])
           (1007<100700 [-2 4 0])
           (1008<100700 [-2 4 0])
           (1009<100700 [-2 4 0])
           (1010<100700 [-2 4 0])
           (1011<100700 [-2 4 0])
           T
c
fc46       Helium-3 Heat Generation Rate each
f46:n,p    (1006<100700 [2 -4 0])
           (1007<100700 [2 -4 0])
           (1008<100700 [2 -4 0])
           (1009<100700 [2 -4 0])
           (1010<100700 [2 -4 0])
           (1011<100700 [2 -4 0])
           T
c
fc56       Helium-3 Heat Generation Rate each
f56:n,p    (1006<100700 [-2 -4 0])
           (1007<100700 [-2 -4 0])
           (1008<100700 [-2 -4 0])
           (1009<100700 [-2 -4 0])
           (1010<100700 [-2 -4 0])
           (1011<100700 [-2 -4 0])
           T
c
c
c c --- Core Fuel Assemblies ---
c c
c c fc106 (n) energy deposition in assemblies (MeV/g)
c c f106:n (100700<100700[-9:9 -9:9 0:0]<100800)
c c sd106 1 $ Convert MeV/g to total MeV
c c
c c fc116 (p) energy deposition in assemblies (MeV/g)
c c f116:p (100700<100700[-9:9 -9:9 0:0]<100800)
c c sd116 1 $ Convert MeV/g to total MeV
c c
c c
c c *****
c c *****Criticality Control Cards*****
c c *****
c c
c c hsrc 32 -162.8775 162.8775 32 -162.8775 162.8775 32 -122.0787 135.6519
mode n p

```

```

c kcode 1000 1.0 10 110
kcode 3500000 1.0 150 250
c kcode 30000 1.0 120 800
  ksrc -20.32 -20.32 0
  kopts kinetics=yes PRECURSOR=YES
c lost 1000
  prdmp 0 50 1 2 0
  print
c
c sdef sur=70000 nrm=-1 wgt=7.85398E5 par=1
c nps 20E9
c prdmp 1E9 1E9 1 2 2E9
c void
c
c
c
c
c *****Control Rod Bank Position*****
c *****Max of 58.0" or 147.32 cm*****
c
c 73.152 cm = 28.8 inches
c
c TR11 0 0 73.152
c TR12 0 0 73.152
c TR13 0 0 73.152
c TR14 0 0 73.152
c
c
c *****Compensation Rod Bank Position*****
c *****Max of 58.5" or 148.59 cm*****
c
c TR21 0 0 148.59
c TR22 0 0 148.59
c TR23 0 0 148.59
c TR24 0 0 148.59
c
c
c *****Transient Rod Bank Position*****
c *****Max of 40.0" or 101.60 cm*****
c
c TR31 0 0 101.60
c TR32 0 0 101.60
c TR33 0 0 101.60
c TR34 0 0 101.60

```

Appendix F: Measured Compensation Rod Worth for TREAT[Error! Not a valid link.](#)

Position (in)	Position (cm)	Comp-1	Comp-2	Comp-3	Comp-4	Comp-Bank (% Δ k/k)
18.0	45.72	1.7084	1.8063	1.7650	1.6668	6.9462
18.5	46.99	1.6829	1.7797	1.7389	1.6422	6.8435
19.0	48.26	1.6567	1.7525	1.7121	1.6170	6.7383
19.5	49.53	1.6300	1.7247	1.6848	1.5913	6.6306
20.0	50.80	1.6027	1.6963	1.6568	1.5649	6.5205
20.5	52.07	1.5749	1.6672	1.6282	1.5381	6.4082
21.0	53.34	1.5465	1.6376	1.5991	1.5107	6.2937
21.5	54.61	1.5176	1.6075	1.5694	1.4828	6.1772
22.0	55.88	1.4882	1.5768	1.5393	1.4545	6.0587
22.5	57.15	1.4584	1.5457	1.5087	1.4257	5.9384
23.0	58.42	1.4282	1.5142	1.4776	1.3965	5.8164
23.5	59.69	1.3976	1.4822	1.4462	1.3670	5.6929
24.0	60.96	1.3667	1.4498	1.4144	1.3371	5.5679
24.5	62.23	1.3354	1.4171	1.3822	1.3069	5.4416
25.0	63.50	1.3039	1.3841	1.3498	1.2764	5.3141
25.5	64.77	1.2721	1.3508	1.3171	1.2457	5.1856
26.0	66.04	1.2401	1.3173	1.2841	1.2147	5.0562
26.5	67.31	1.2079	1.2836	1.2510	1.1836	4.9260
27.0	68.58	1.1756	1.2497	1.2177	1.1523	4.7952
27.5	69.85	1.1432	1.2157	1.1843	1.1209	4.6640
28.0	71.12	1.1107	1.1816	1.1508	1.0894	4.5324
28.5	72.39	1.0781	1.1475	1.1172	1.0579	4.4006
29.0	73.66	1.0456	1.1133	1.0837	1.0264	4.2689
29.5	74.93	1.0131	1.0792	1.0502	0.9949	4.1372
30.0	76.20	0.9807	1.0451	1.0167	0.9634	4.0058
30.5	77.47	0.9484	1.0111	0.9834	0.9321	3.8749
31.0	78.74	0.9162	0.9773	0.9502	0.9009	3.7445
31.5	80.01	0.8842	0.9436	0.9171	0.8698	3.6148
32.0	81.28	0.8525	0.9101	0.8843	0.8390	3.4859
32.5	82.55	0.8209	0.8769	0.8518	0.8084	3.3581
33.0	83.82	0.7897	0.8440	0.8195	0.7780	3.2313
33.5	85.09	0.7588	0.8114	0.7876	0.7480	3.1058
34.0	86.36	0.7283	0.7792	0.7560	0.7183	2.9817
34.5	87.63	0.6981	0.7474	0.7248	0.6889	2.8592
35.0	88.90	0.6683	0.7159	0.6940	0.6599	2.7383
35.5	90.17	0.6390	0.6850	0.6637	0.6314	2.6191
36.0	91.44	0.6102	0.6545	0.6339	0.6033	2.5019
36.5	92.71	0.5819	0.6245	0.6046	0.5757	2.3867

Error!
valid

Position (in)	Position (cm)	Comp-1	Comp-2	Comp-3	Comp-4	Comp-Bank (%Δk/k)
37.0	93.98	0.5541	0.5951	0.5758	0.5485	2.2735

Not a link.

Error!
valid

Position (in)	Position (cm)	Comp-1	Comp-2	Comp-3	Comp-4	Comp-Bank (%Δk/k)
37.5	95.25	0.5568	0.5968	0.5785	0.5512	2.1627
38.0	96.52	0.5595	0.5995	0.5812	0.5539	2.0519
38.5	97.79	0.5622	0.6022	0.5839	0.5566	1.9411
39.0	99.06	0.5649	0.6049	0.5866	0.5593	1.8303
39.5	100.33	0.5676	0.6076	0.5893	0.5620	1.7195
40.0	101.60	0.5703	0.6103	0.5920	0.5647	1.6087
40.5	102.87	0.5730	0.6130	0.5947	0.5674	1.4979
41.0	104.14	0.5757	0.6157	0.5974	0.5701	1.3871
41.5	105.41	0.5784	0.6184	0.6001	0.5728	1.2763
42.0	106.68	0.5811	0.6211	0.6028	0.5755	1.1655
42.5	107.95	0.5838	0.6238	0.6055	0.5782	1.0547
43.0	109.22	0.5865	0.6265	0.6082	0.5809	0.9439
43.5	110.49	0.5892	0.6292	0.6109	0.5836	0.8331
44.0	111.76	0.5919	0.6319	0.6136	0.5863	0.7223
44.5	113.03	0.5946	0.6346	0.6163	0.5890	0.6115
45.0	114.30	0.5973	0.6373	0.6190	0.5917	0.5007
45.5	115.57	0.6000	0.6400	0.6217	0.5944	0.3899
46.0	116.84	0.6027	0.6427	0.6244	0.5971	0.2791
46.5	118.11	0.6054	0.6454	0.6271	0.5998	0.1683
47.0	119.38	0.6081	0.6481	0.6298	0.6025	0.0575
47.5	120.65	0.6108	0.6508	0.6325	0.6052	-0.0533
48.0	121.92	0.6135	0.6535	0.6352	0.6079	-0.1641
48.5	123.19	0.6162	0.6562	0.6379	0.6106	-0.2749
49.0	124.46	0.6189	0.6589	0.6406	0.6133	-0.3857
49.5	125.73	0.6216	0.6616	0.6433	0.6160	-0.4965
50.0	127.00	0.6243	0.6643	0.6460	0.6187	-0.6073
50.5	128.27	0.6270	0.6670	0.6487	0.6214	-0.7181
51.0	129.54	0.6297	0.6697	0.6514	0.6241	-0.8289
51.5	130.81	0.6324	0.6724	0.6541	0.6268	-0.9397
52.0	132.08	0.6351	0.6751	0.6568	0.6295	-1.0505
52.5	133.35	0.6378	0.6778	0.6595	0.6322	-1.1613
53.0	134.62	0.6405	0.6805	0.6622	0.6349	-1.2721
53.5	135.89	0.6432	0.6832	0.6649	0.6376	-1.3829
54.0	137.16	0.6459	0.6859	0.6676	0.6403	-1.4937
54.5	138.43	0.6486	0.6886	0.6703	0.6430	-1.6045
55.0	139.70	0.6513	0.6913	0.6730	0.6457	-1.7153
55.5	140.97	0.6540	0.6940	0.6757	0.6484	-1.8261

Not a link.

Appendix G: CFD Data for Various Driver Tank Pressures and Associated Atom Density Values

250 PSIG Driver Tank						
Time	TS00		TS01		TS02	
	Pressure (psi)	Atom Density (atoms/b-cm)	Pressure (psi)	Atom Density (atoms/b-cm)	Pressure (psi)	Atom Density (atoms/b-cm)
0.000	0.169	2.88E-07	0.169	2.88E-07	0.169	2.88E-07
0.001	19.503	2.84E-05	13.797	1.73E-05	11.908	1.50E-05
0.002	46.805	5.89E-05	39.605	4.32E-05	37.051	3.84E-05
0.003	190.205	1.37E-04	186.436	9.51E-05	184.200	1.08E-04
0.004	277.227	1.92E-04	275.620	1.56E-04	274.703	1.54E-04
0.005	348.739	2.08E-04	355.448	1.94E-04	355.681	1.67E-04
Time	TS03		TS04		TS05	
	Pressure (psi)	Atom Density (atoms/b-cm)	Pressure (psi)	Atom Density (atoms/b-cm)	Pressure (psi)	Atom Density (atoms/b-cm)
0.000	0.169	2.88E-07	0.169	2.88E-07	0.169	2.88E-07
0.001	9.135	1.14E-05	20.163	7.59E-06	6.619	1.17E-05
0.002	82.767	5.73E-05	105.121	5.34E-05	99.210	5.38E-05
0.003	172.260	1.15E-04	150.460	1.00E-04	147.704	7.04E-05
0.004	269.938	1.52E-04	270.493	1.47E-04	269.837	9.74E-05
0.005	377.461	1.74E-04	380.983	1.58E-04	382.593	1.20E-04

500 PSIG Driver Tank						
Time	TS00		TS01		TS02	
	Pressure (psi)	Atom Density (atoms/b-cm)	Pressure (psi)	Atom Density (atoms/b-cm)	Pressure (psi)	Atom Density (atoms/b-cm)
0.000	0.169	2.88E-07	0.169	2.88E-07	0.169	2.88E-07
0.001	42.422	6.50E-05	28.356	3.31E-05	22.622	2.53E-05
0.002	95.637	1.17E-04	80.376	8.07E-05	73.928	7.17E-05
0.003	328.956	2.41E-04	286.115	1.61E-04	268.159	1.47E-04
0.004	418.428	3.18E-04	401.432	2.08E-04	410.551	1.90E-04
0.005	600.311	3.51E-04	607.199	2.49E-04	619.404	2.23E-04
Time	TS03		TS04		TS05	
	Pressure (psi)	Atom Density (atoms/b-cm)	Pressure (psi)	Atom Density (atoms/b-cm)	Pressure (psi)	Atom Density (atoms/b-cm)
0.000	0.169	2.88E-07	0.169	2.88E-07	0.169	2.88E-07
0.001	16.421	1.81E-05	40.334	1.41E-05	11.321	2.18E-05
0.002	68.006	6.17E-05	186.035	9.37E-05	170.679	1.14E-04
0.003	264.730	1.33E-04	269.170	1.27E-04	261.435	1.73E-04
0.004	470.952	1.90E-04	470.064	2.10E-04	476.052	2.38E-04
0.005	627.654	2.01E-04	654.121	1.73E-04	644.087	3.60E-04

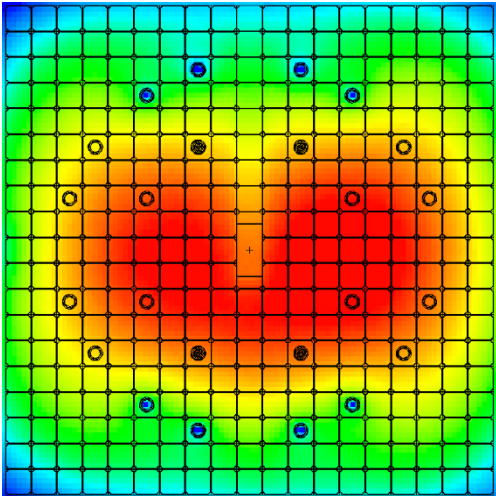
750 PSIG Driver Tank						
Time	TS00		TS01		TS02	
	Pressure (psi)	Atom Density (atoms/b-cm)	Pressure (psi)	Atom Density (atoms/b-cm)	Pressure (psi)	Atom Density (atoms/b-cm)
0.000	0.169	2.88E-07	0.169	2.88E-07	0.169	2.88E-07
0.001	60.520	9.42E-05	43.503	5.03E-05	34.091	3.64E-05
0.002	143.943	1.75E-04	124.302	1.21E-04	116.672	1.05E-04
0.003	497.065	3.58E-04	459.169	2.41E-04	407.710	2.17E-04
0.004	639.800	4.71E-04	611.248	2.98E-04	719.205	2.89E-04
0.005	909.044	5.07E-04	927.698	3.55E-04	947.226	3.20E-04
Time	TS03		TS04		TS05	
	Pressure (psi)	Atom Density (atoms/b-cm)	Pressure (psi)	Atom Density (atoms/b-cm)	Pressure (psi)	Atom Density (atoms/b-cm)
0.000	0.169	2.88E-07	0.169	2.88E-07	0.169	2.88E-07
0.001	24.798	2.60E-05	63.905	1.76E-05	15.936	3.04E-05
0.002	106.468	8.96E-05	280.258	1.35E-04	259.803	1.56E-04
0.003	403.780	1.99E-04	411.655	1.76E-04	399.256	2.40E-04
0.004	722.851	2.78E-04	715.559	2.93E-04	727.089	3.15E-04
0.005	958.993	2.84E-04	992.552	2.50E-04	984.080	4.66E-04

850 PSIG Driver Tank						
Time	TS00		TS01		TS02	
	Pressure (psi)	Atom Density (atoms/b-cm)	Pressure (psi)	Atom Density (atoms/b-cm)	Pressure (psi)	Atom Density (atoms/b-cm)
0.000	0.169	2.88E-07	0.169	2.88E-07	0.169	2.88E-07
0.001	68.169	1.07E-04	50.408	5.86E-05	38.814	4.12E-05
0.002	163.793	1.99E-04	141.073	1.37E-04	131.888	1.19E-04
0.003	565.807	4.05E-04	526.745	2.70E-04	465.961	2.42E-04
0.004	729.022	5.32E-04	694.804	3.35E-04	821.119	3.22E-04
0.005	1045.577	5.72E-04	1061.769	4.02E-04	1084.402	3.60E-04
Time	TS03		TS04		TS05	
	Pressure (psi)	Atom Density (atoms/b-cm)	Pressure (psi)	Atom Density (atoms/b-cm)	Pressure (psi)	Atom Density (atoms/b-cm)
0.000	0.169	2.88E-07	0.169	2.88E-07	0.169	2.88E-07
0.001	28.256	2.91E-05	74.341	1.90E-05	17.933	3.47E-05
0.002	122.660	1.02E-04	317.347	1.62E-04	297.399	1.67E-04
0.003	460.946	2.23E-04	469.835	1.97E-04	455.086	2.61E-04
0.004	824.373	3.12E-04	816.901	3.25E-04	828.682	3.44E-04
0.005	1094.157	3.17E-04	1200.424	2.82E-04	1122.024	5.21E-04

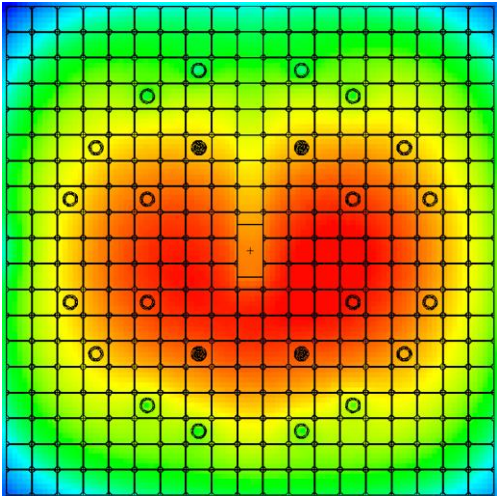
Appendix H: Tabular Results for the Reactivity Addition for Various Starting Driver Tank Pressures

250 PSI Driver Tank					500 PSI Driver Tank				
Timestep	keff	Standard Deviation	$\Delta\rho$	$\Delta\rho$ w/ Error	Timestep	keff	Standard Deviation	$\Delta\rho$	$\Delta\rho$ w/ Error
0	0.9999	0.00007	0.00%	0.00%	0	0.9999	0.00007	0.00%	0.00%
Pulse	1.04678	0.00007	4.48%	4.43%	Pulse	1.04678	0.00007	4.48%	4.43%
0.001	1.02917	0.00006	2.84%	2.80%	0.001	1.02035	0.00005	2.00%	1.96%
0.002	1.00759	0.00007	0.76%	0.72%	0.002	0.99929	0.00006	-0.06%	-0.18%
0.003	0.99447	0.00007	-0.55%	-0.57%	0.003	0.98935	0.00006	-1.07%	-0.99%
0.004	0.98893	0.00006	-1.11%	-1.02%	0.004	0.98435	0.00007	-1.58%	-1.40%
0.005	0.98714	0.00006	-1.29%	-1.17%	0.005	0.98435	0.00007	-1.58%	-1.40%
750 PSI Driver Tank					850 PSI Driver Tank				
Timestep	keff	Standard Deviation	$\Delta\rho$	$\Delta\rho$ w/ Error	Timestep	keff	Standard Deviation	$\Delta\rho$	$\Delta\rho$ w/ Error
0	0.9999	0.00007	0.00%	0.00%	0	0.9999	0.00007	0.00%	0.00%
Pulse	1.04678	0.00007	4.48%	4.43%	Pulse	1.04678	0.00007	4.48%	4.43%
0.001	1.01462	0.00006	1.45%	1.41%	0.001	1.01262	0.00006	1.26%	1.21%
0.002	0.99309	0.00007	-0.69%	-0.68%	0.002	0.991	0.00007	-0.90%	-0.85%
0.003	0.98463	0.00007	-1.55%	-1.38%	0.003	0.98328	0.00007	-1.69%	-1.49%
0.004	0.98092	0.00007	-1.94%	-1.69%	0.004	0.97978	0.00007	-2.05%	-1.78%
0.005	0.9805	0.00006	-1.98%	-1.72%	0.005	0.97929	0.00006	-2.10%	-1.82%

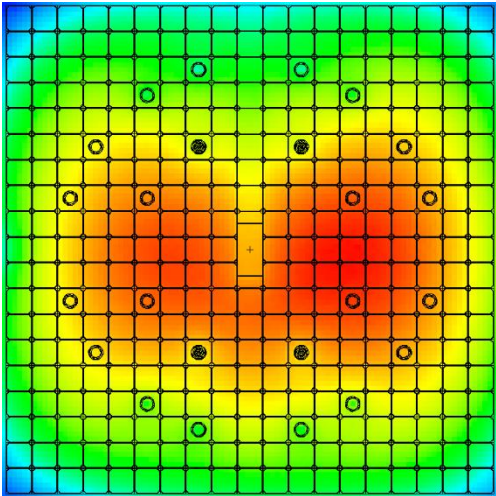
Appendix I: Tally 14 Flux Images Over the Clip of the HENRI System (250 psi – Driver Tank)



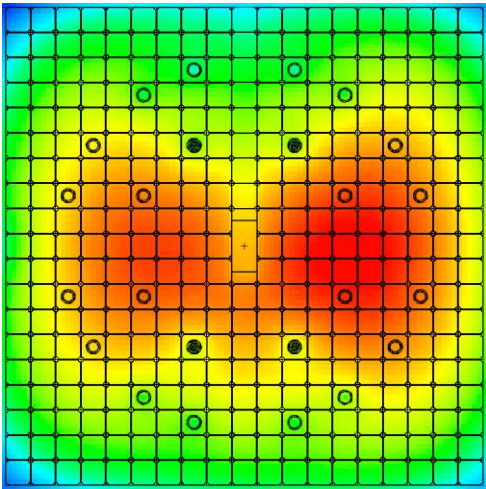
Critical Core



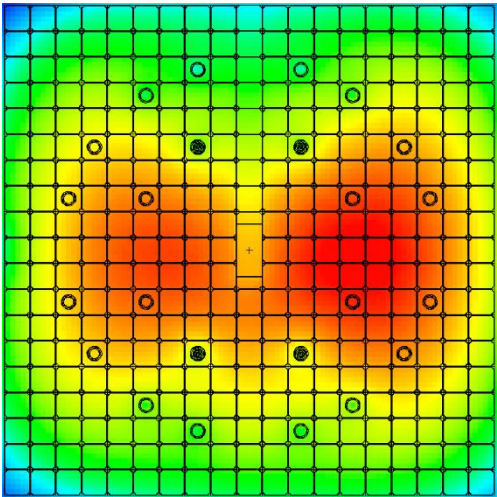
4.5% $\Delta k/k$ Pulse Core



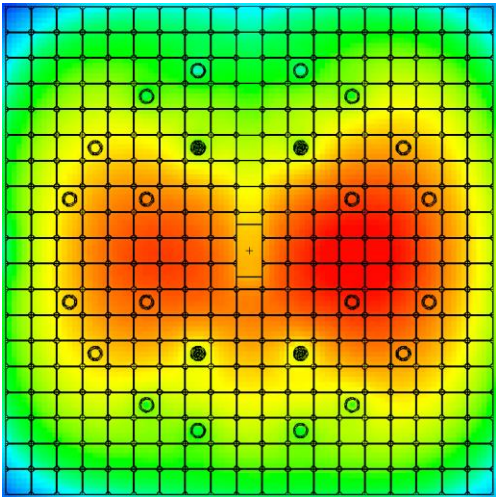
HENRI Clip ($T=1\text{ms}$)



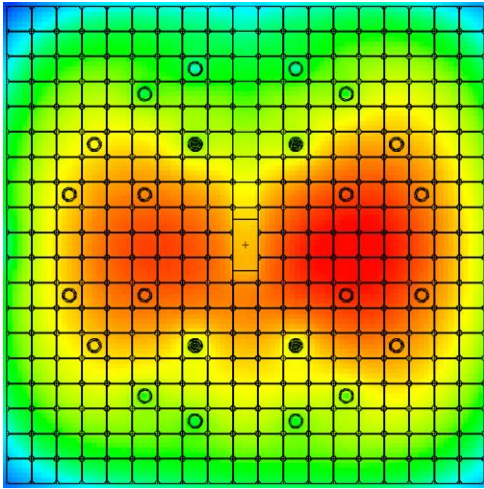
HENRI Clip ($T=2.34\text{ms}$)



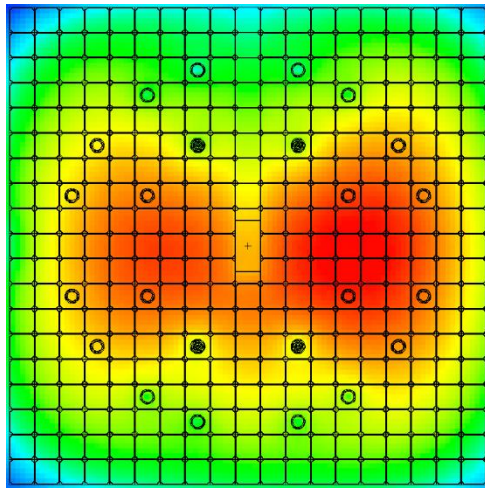
HENRI Clip ($T=2.36\text{ms}$)



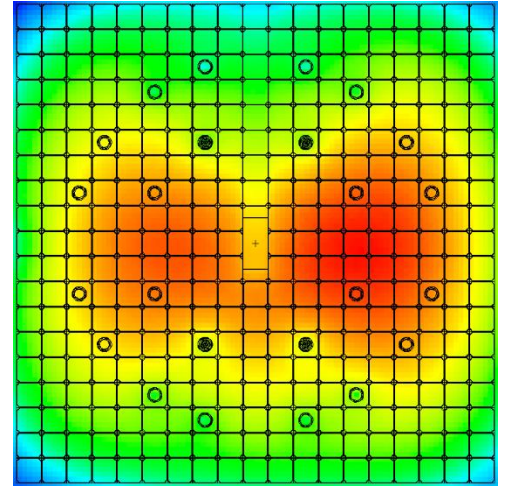
HENRI Clip ($T=2.65\text{ms}$)



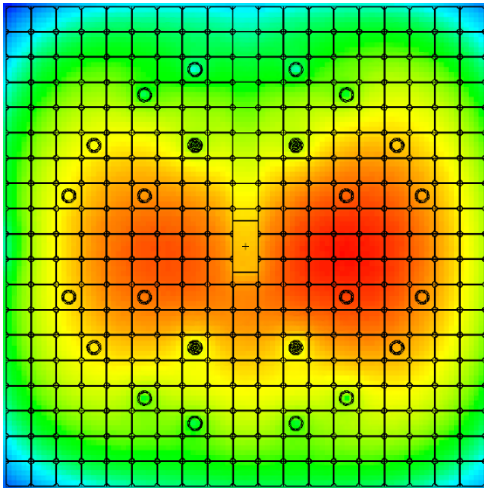
HENRI Clip (T=3.63 ms)



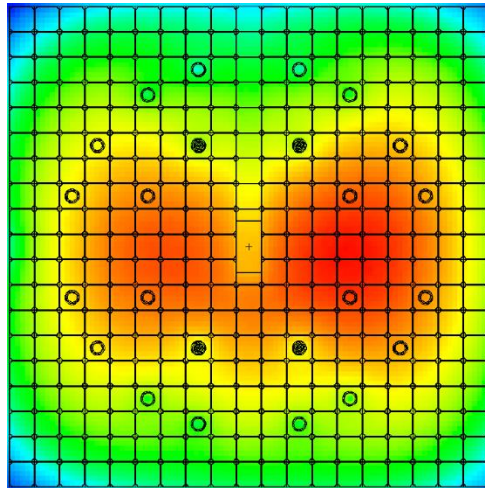
HENRI Clip (T=4.51 ms)



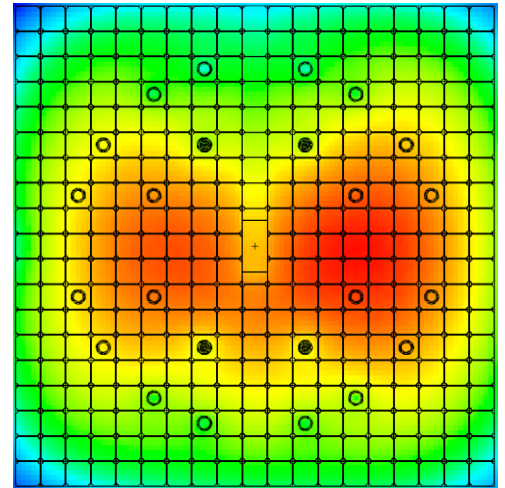
HENRI Clip (T=5.51 ms)



HENRI Clip (T=6.51 ms)



HENRI Clip (T=7.51 ms)



HENRI Clip (T=8.51 ms)

Appendix J: Surface Tally Results for the Annular Evaluation

energy	eV	Surface Tally (676)	Surface Tally (100179)	Surface Tally (100187)	Surface Tally (100188)
0	0	0	0	0	0
2.17E-08	0.021739	7.2584E-06	6.35703E-07	3.04329E-07	1.63496E-07
4.35E-08	0.043478	1.3786E-05	1.23065E-06	8.06726E-07	5.30996E-07
6.52E-08	0.065217	1.2589E-05	1.15519E-06	8.51808E-07	6.08151E-07
8.7E-08	0.086957	9.3676E-06	8.92195E-07	7.05895E-07	5.28769E-07
1.09E-07	0.1087	6.4736E-06	6.36216E-07	5.26822E-07	4.06437E-07
1.3E-07	0.13043	4.3688E-06	4.41435E-07	3.76941E-07	2.98698E-07
1.52E-07	0.15217	2.987E-06	3.11161E-07	2.71142E-07	2.17272E-07
1.74E-07	0.17391	2.1068E-06	2.25466E-07	2.01448E-07	1.64833E-07
1.96E-07	0.19565	1.5508E-06	1.69515E-07	1.52938E-07	1.25831E-07
2.17E-07	0.21739	1.1924E-06	1.34098E-07	1.22709E-07	1.01795E-07
2.39E-07	0.23913	9.5616E-07	1.08786E-07	1.01214E-07	8.57762E-08
2.61E-07	0.26087	8.033E-07	9.29744E-08	8.70395E-08	7.41335E-08
2.83E-07	0.28261	6.8921E-07	8.07779E-08	7.68095E-08	6.49323E-08
3.04E-07	0.30435	6.0708E-07	7.14704E-08	6.88089E-08	5.82393E-08
3.26E-07	0.32609	5.4685E-07	6.50641E-08	6.31023E-08	5.40523E-08
3.48E-07	0.34783	4.9535E-07	6.02533E-08	5.80846E-08	5.02549E-08
3.7E-07	0.36957	4.5458E-07	5.52291E-08	5.32116E-08	4.63771E-08
3.91E-07	0.3913	4.208E-07	5.10678E-08	5.02367E-08	4.3753E-08
4.13E-07	0.41304	3.9234E-07	4.84359E-08	4.72976E-08	4.17521E-08
4.35E-07	0.43478	3.6633E-07	4.5527E-08	4.54011E-08	3.98538E-08
4.57E-07	0.45652	3.4533E-07	4.20507E-08	4.16827E-08	3.64255E-08
4.78E-07	0.47826	3.23E-07	3.97471E-08	3.97689E-08	3.53922E-08
5E-07	0.5	3.0452E-07	3.80824E-08	3.82007E-08	3.36589E-08
5.22E-07	0.52174	2.9164E-07	3.63848E-08	3.66782E-08	3.28499E-08
5.43E-07	0.54348	2.7736E-07	3.54383E-08	3.53925E-08	3.15472E-08
5.65E-07	0.56522	2.6309E-07	3.28729E-08	3.33753E-08	2.97069E-08
5.87E-07	0.58696	2.5154E-07	3.18295E-08	3.24233E-08	2.85364E-08
6.09E-07	0.6087	2.3982E-07	3.06841E-08	3.12371E-08	2.78862E-08
6.3E-07	0.63043	2.301E-07	2.91245E-08	3.00597E-08	2.683E-08
6.52E-07	0.65217	2.2119E-07	2.83684E-08	2.9049E-08	2.63689E-08
6.74E-07	0.67391	2.1383E-07	2.75744E-08	2.77653E-08	2.53131E-08
6.96E-07	0.69565	2.0556E-07	2.64968E-08	2.68934E-08	2.40395E-08
7.17E-07	0.71739	1.9833E-07	2.52838E-08	2.62649E-08	2.38959E-08
7.39E-07	0.73913	1.9237E-07	2.48298E-08	2.55232E-08	2.29305E-08
7.61E-07	0.76087	1.8555E-07	2.38778E-08	2.49374E-08	2.27521E-08
7.83E-07	0.78261	1.7973E-07	2.31347E-08	2.41459E-08	2.15512E-08
8.04E-07	0.80435	1.7415E-07	2.27216E-08	2.39818E-08	2.14949E-08
8.26E-07	0.82609	1.6902E-07	2.18485E-08	2.24818E-08	2.08101E-08

energy	eV	Surface Tally (676)	Surface Tally (100179)	Surface Tally (100187)	Surface Tally (100188)
8.48E-07	0.84783	1.6344E-07	2.12673E-08	2.25318E-08	2.03365E-08
8.7E-07	0.86957	1.5989E-07	2.08573E-08	2.18941E-08	1.99378E-08
8.91E-07	0.8913	1.5513E-07	1.99681E-08	2.13462E-08	1.94672E-08
9.13E-07	0.91304	1.4984E-07	1.98044E-08	2.05391E-08	1.8677E-08
9.35E-07	0.93478	1.4747E-07	1.91948E-08	2.0517E-08	1.84917E-08
9.57E-07	0.95652	1.4359E-07	1.83724E-08	1.97011E-08	1.81502E-08
9.78E-07	0.97826	1.4096E-07	1.88478E-08	1.90548E-08	1.7487E-08
0.000001	1	1.3629E-07	1.80344E-08	1.89932E-08	1.76044E-08
0.016668	16668	6.3397E-05	9.48307E-06	1.09543E-05	1.07814E-05
0.033334	33334	5.1528E-06	7.47569E-07	8.82258E-07	8.84446E-07
0.050001	50001	3.0503E-06	4.439E-07	5.2377E-07	5.23726E-07
0.066667	66667	2.2211E-06	3.27625E-07	3.86028E-07	3.86905E-07
0.083334	83334	1.7478E-06	2.51966E-07	2.96048E-07	2.97123E-07
0.1	100000	1.4338E-06	2.0896E-07	2.46479E-07	2.46801E-07
0.55	550000	1.4854E-05	2.16997E-06	2.55891E-06	2.55387E-06
1	1000000	6.007E-06	8.67409E-07	1.02227E-06	1.02176E-06
total		0.00017074	2.17084E-05	2.25565E-05	2.10436E-05

energy	eV	Surface Tally (100189)	Surface Tally (100190)	Surface Tally (100191)	Surface Tally (100192)
0	0	0	0	0	0
2.1739E-08	0.021739	9.77202E-08	6.1519E-08	4.1736E-08	2.94568E-08
4.3478E-08	0.043478	3.70939E-07	2.70677E-07	2.03338E-07	1.6097E-07
6.5217E-08	0.065217	4.57716E-07	3.5623E-07	2.85015E-07	2.37243E-07
8.6957E-08	0.086957	4.12417E-07	3.34333E-07	2.76856E-07	2.34942E-07
1.087E-07	0.1087	3.26719E-07	2.69778E-07	2.26287E-07	1.95156E-07
1.3043E-07	0.13043	2.43331E-07	2.04916E-07	1.74809E-07	1.51506E-07
1.5217E-07	0.15217	1.79867E-07	1.52084E-07	1.34262E-07	1.15289E-07
1.7391E-07	0.17391	1.38853E-07	1.18836E-07	1.04349E-07	8.96608E-08
1.9565E-07	0.19565	1.06855E-07	9.33969E-08	8.14901E-08	7.13026E-08
2.1739E-07	0.21739	8.71838E-08	7.68034E-08	6.6976E-08	5.97834E-08
2.3913E-07	0.23913	7.33752E-08	6.56671E-08	5.77822E-08	5.32543E-08
2.6087E-07	0.26087	6.41639E-08	5.6491E-08	5.06404E-08	4.50287E-08
2.8261E-07	0.28261	5.73257E-08	4.97971E-08	4.59999E-08	4.32113E-08
3.0435E-07	0.30435	5.13932E-08	4.59777E-08	4.16608E-08	3.94868E-08
3.2609E-07	0.32609	4.7446E-08	4.24195E-08	3.85203E-08	3.44417E-08
3.4783E-07	0.34783	4.37615E-08	4.01158E-08	3.62829E-08	3.18066E-08
3.6957E-07	0.36957	4.10134E-08	3.67765E-08	3.38337E-08	3.18554E-08
3.913E-07	0.3913	3.90888E-08	3.46264E-08	3.13977E-08	2.99848E-08
4.1304E-07	0.41304	3.7074E-08	3.29803E-08	3.102E-08	2.82197E-08
4.3478E-07	0.43478	3.56253E-08	3.25128E-08	2.99929E-08	2.73727E-08
4.5652E-07	0.45652	3.3118E-08	3.01364E-08	2.81563E-08	2.44136E-08
4.7826E-07	0.47826	3.1681E-08	2.94937E-08	2.67484E-08	2.47301E-08
0.0000005	0.5	3.0336E-08	2.79562E-08	2.54268E-08	2.38234E-08
5.2174E-07	0.52174	2.91553E-08	2.73962E-08	2.54182E-08	2.45382E-08
5.4348E-07	0.54348	2.80567E-08	2.51107E-08	2.34553E-08	2.22587E-08
5.6522E-07	0.56522	2.64602E-08	2.51063E-08	2.32007E-08	2.07762E-08
5.8696E-07	0.58696	2.56904E-08	2.36508E-08	2.21478E-08	2.02726E-08
6.087E-07	0.6087	2.56293E-08	2.30724E-08	2.08067E-08	2.12599E-08
6.3043E-07	0.63043	2.40777E-08	2.25686E-08	2.10766E-08	1.94301E-08
6.5217E-07	0.65217	2.39453E-08	2.14684E-08	2.00459E-08	1.93834E-08
6.7391E-07	0.67391	2.27482E-08	2.12286E-08	1.99422E-08	1.79804E-08
6.9565E-07	0.69565	2.22559E-08	2.00383E-08	1.89165E-08	1.72616E-08
7.1739E-07	0.71739	2.21818E-08	2.02476E-08	1.87349E-08	1.75421E-08
7.3913E-07	0.73913	2.09001E-08	1.96708E-08	1.84803E-08	1.71485E-08
7.6087E-07	0.76087	2.11582E-08	1.95686E-08	1.75608E-08	1.67794E-08
7.8261E-07	0.78261	2.00332E-08	1.86548E-08	1.69326E-08	1.68065E-08
8.0435E-07	0.80435	1.94477E-08	1.83029E-08	1.73268E-08	1.57475E-08
8.2609E-07	0.82609	1.83725E-08	1.76222E-08	1.67961E-08	1.62073E-08
8.4783E-07	0.84783	1.86759E-08	1.74369E-08	1.60699E-08	1.47734E-08

energy	eV	Surface Tally (100189)	Surface Tally (100190)	Surface Tally (100191)	Surface Tally (100192)
8.6957E-07	0.86957	1.84837E-08	1.64611E-08	1.5735E-08	1.48594E-08
8.913E-07	0.8913	1.77776E-08	1.68541E-08	1.6042E-08	1.42222E-08
9.1304E-07	0.91304	1.72981E-08	1.62432E-08	1.50306E-08	1.35155E-08
9.3478E-07	0.93478	1.68567E-08	1.59727E-08	1.47954E-08	1.39369E-08
9.5652E-07	0.95652	1.65288E-08	1.51117E-08	1.39456E-08	1.42711E-08
9.7826E-07	0.97826	1.60878E-08	1.54187E-08	1.45676E-08	1.35296E-08
0.000001	1	1.62863E-08	1.54415E-08	1.46082E-08	1.39293E-08
0.016668	16668	1.06383E-05	1.05233E-05	1.04079E-05	1.03021E-05
0.033334	33334	8.78409E-07	8.83344E-07	8.82517E-07	8.71264E-07
0.050001	50001	5.24745E-07	5.22725E-07	5.17299E-07	5.16884E-07
0.066667	66667	3.83127E-07	3.83883E-07	3.86723E-07	3.81482E-07
0.083334	83334	2.97248E-07	2.96708E-07	2.95435E-07	2.93832E-07
0.1	100000	2.43991E-07	0.000000245	2.49933E-07	2.51254E-07
0.55	550000	2.55443E-06	2.5561E-06	2.56117E-06	2.56429E-06
1	1000000	1.0184E-06	1.0184E-06	1.01128E-06	1.02475E-06
total		2.00337E-05	1.93456E-05	1.88064E-05	1.83852E-05